UNIVERSITY OF SOUTHAMPTON

FACULTY OF ENGINEERING, SCIENCE AND MATHEMATICS

School of Chemistry

Synthesis, Structure and Properties of Heavy Metal Pyrochlore Oxides

A thesis submitted for the Degree of Doctor of Philosophy

by

ROSA GALATI

MARCH 2010

Dedicated to the memory of Elisa

Per aspera ad virtutem

ABSTRACT

Many interesting and often exotic magnetic phenomena have been observed over the past twenty years in the family of the heavy metal pyrochlore oxides, $A_2B_2O_6O'$. In these systems, competing interactions are common and tend to emerge mainly at low temperatures. Magnetic properties are related to the contribution of *d* orbitals that transition metal (TM) offer and their interplay with the positive contribution coming from the cation sitting on the *A* site.

The work described in this thesis explores the effects of chemical substitution of the *A* site cation on the symmetry and the properties of a number of pyrochlores containing TM of the second and third transition row, such as Ir, Ru, Mo and Os. Depending if this site is fully occupied and on the radius size the behaviour of the resulting material can change significantly. The defect pyrochlore family AOs_2O_6 (A = Cs, Rb, K) was studied in detail following the attention that its members attracted for having been the first materials, belonging to this subgroup, to exhibit superconducting properties [1, 2, 3] and for the diversity in their properties. In these compounds, the smaller the ionic radius of an element, the weaker is the bond to the structure. As a result, the temperature dependence of their energy becomes quite different from normal lattice vibrations and gives interesting low temperature behaviours [4].

The effect of replacing the weak bonded potassium ions on the structures and superconducting properties of the AOs_2O_6 phases has also been studied. The ability to exchange the *A*-type in pyrochlores is well known and leads to applications for example in nuclear clean-up. Thus the ion exchange of K^+ by smaller cations such as Li^+ or Na^+ has been investigated with the aim of synthesising compounds which cannot be obtained by direct synthesis. New defect pyrochlore materials, $AA'Os_2O_6$ (A' = Li^+, Na^+) have been synthesised together with hydrated derivatives, $AA'OsO_6{\cdot}nH_2O$. Parent materials were obtained by ion exchange in non-aqueous solvents under strictly dry conditions. A Ba-based osmium oxide pyrochlore, $Ba(Os_2O_6)_2{\cdot}H_2O$ was also synthesised, for the first time, from the K-osmate starting material by ion-exchange methods in aqueous medium.

In this work, diffraction techniques, X- ray and neutron powder diffraction, were employed and found suitable for detecting the change in cation and anion location and general structure investigation.These structural descriptions are correlated with the measured superconducting properties and theoretical descriptions of variations in the T_c in these systems as a function of cation size and rattling.

CONTENTS

LIST OF FIGURES

LIST OF TABLES

DECLARATION OF AUTHORSHIP

This thesis is the result of work done wholly while I was in registered candidature for a Ph.D. degree at this University. The material presented herein is based on work mostly done by myself, with the following exceptions. Powder neutron diffraction data used in Sn. 3.4.1 and in Sn. 6.1 were collected by Dr P.F. Henry at the Institut Laue-Langevin (ILL) in Grenoble, France. Thermogravimetric analysis of KOs_2O_6 in Sn. 5.2.1 was carried out by Dr C.S. Knee at the University of Gothenburg. Magnetic data were recorded by Mr. C.F. Simon, Sn. 6.1 and by Dr E.A. Young at Southampton and further analysed by them. The material contained herein has not been submitted by the author for a degree at any other institution.

Date: 22 March 2010

Signed:

LIST OF PAPERS

This thesis discusses the work published in the following papers:

1. **R. Galati**, R. W. Hughes, C. S. Knee, P. F. Henry, and M. T.Weller *J. Mater. Chem.* 17, 160, 2007.

2. **R. Galati**, C. Simon, C. S. Knee, P. F. Henry, B. D. Rainford, and M. T. Weller *Chem. Mater.* 20, 1652, 2008.

3. **R. Galati**, C. Simon, P. F. Henry, and M. T.Weller *Phys. Rev. B* 77, 104523, 2008.

4. **R. Galati**, E.A. Young and M. T. Weller, submitted to *J. Phys.: Condens. Matter*.

ACKNOWLEDGMENTS

First and foremost I would like to thank my supervisor, Prof. M. T. Weller for his constant guidance and support throughout this project. A special thanks to my advisor, Dr. A.L.Hector, for the constant help and technical support provided, and to P. Henry and C.S. Knee for many synergistic interactions and continued interest in our structural studies.

I would also to thank the following people for making the last few years both memorable and enjoyable. The Weller group members past and present, encompassing Ben, Holly, Florian, Charlie, Bob, Pete, and many others of the inorganic floor who have been good company along the way. My thanks to Eleni, Jess, Kate and Valeska, Jenny, Marina, Ole, Pietro, Alex and all the 'Levitt's group' past and present, for the great time I had with them. I enjoyed the atmosphere, their friendship, and their support. Particular thanks must go to Dr. Valeska Ting for diligently proof reading this work and for providing helpful suggestions. This thesis has been supported by the EPSRC. Their support is gratefully acknowledged.

This work would not have been possible without the help and support of many people:

A Mamma, Papà e Gerardo un grazie speciale, per essere sempre stati, nonostante i limiti geografici, costante guida e supporto in questo *iter vitae* e nei momenti difficili che mi hanno portato giorno dopo giorno, momento dopo momento a costruire la persona che sono oggi. Ai miei fratelli Luigi e Vincenzo, a Nonna e Zia Nella. A tutti loro la gioia di questo traguardo.

Un pensiero caro a Maria e Peppe, per essere stati fantastici compagni di casa, la loro vicinanza costante ha diminuito tanto la nostalgia di casa e molto di più. Questo viaggio nella scienza non sarebbe stato lo stesso senza l'amicizia e la presenza costante di Maria, 'bella' nel suo semplice modo di essere e paziente ascoltatrice. Mai dimen-

ticherò il lento e rilassante inizio delle nostre giornate, dietro una calda tazzina da caffè, intente a discutere, l'una di fronte all'altra, delle nostre preoccupazioni, delle nostre scadenze, dei nostri traguardi e del nostro futuro. Aver concluso la scrittura della tesi nello stesso periodo e' stato il modo migliore di segnare la fine di questo viaggio. L' avventura Southampton non sarebbe stata la stessa senza le parole di conforto di persone care come Salvo e Giulia.

Questa tesi lo dedico ad Elisa, che non ha avuto il tempo di vederne la fine; lei che mi ha insegnato che nella vita bisogna osare sempre.

1. INTRODUCTION

Heavy metal oxide compounds have many industrial applications which result from the chemical and physical properties of the materials [7] and that may be exploited; these are often dependent on their structure that, generally, consists of multi-dimensional units made from metal-oxygen polyhedra, MO_n. Combinations of such MO_n units form extended structures, which facilitate cooperative electronic effects that result in materials displaying electrical and magnetic properties, that can have variable oxygen stoichiometry and that find application in solid state devices such as capacitors, heating elements and rechargeable batteries. Examples of the applications of complex metal oxides include fast ion transporters [8, 9, 10], semiconductors, [11], superconductors [12] ferroelectrics [13, 14], piezoelectrics [15] and catalysts [16, 17, 18]. Consequently, an understanding of the connection between the structural chemistry of such phases and the physical properties are of fundamental importance to the development of new materials and have been the focus of many studies in the last fifty years.

A key structure-type that has been shown to demonstrate a vast range of useful physical properties, is the family of formula $A_2B_2X_6X'$ adopting the pyrochlore structure. This structure-type is generally assumed by a large number of oxides, fluorides, oxyfluorides, oxysulfides [19] and oxynitrides [20, 21, 22] isostructural to the mineral pyrochlore, $(NaCa)(NbTa)O_6F/(OH)$, the structure of which was first reported by Gaertner in 1930 [23]. The name derives from the Greek *pyros* - a fire and *chloros* - green, as it turns green upon ignition. Materials belonging to this structure-type have great technological importance and varied physical properties, a direct consequence of the wide range of chemical substitution at the *A*, *B* sites as long as ionic radius and charge neutrality requirements are satisfied. Phases are known where the *A* cation is an alkali metals, alkaline earth or a rare earth ion and where the *B* cation is a transition metal. This huge combination results in materials with interesting physical properties ranging from highly insulating to semiconducting to metallic, or from paramagnetic, ferromagnetic to anti-ferromagnetic and with applications such as pigments [24, 25],

as traps for radioactive waste or as materials in gas turbines and diesel engines [26, 27].

In the literature, compounds of ionic charge (A^{3+}, B^{4+}), (A^{2+}, B^{5+}), ($A^{+}A'^{2+}$, B^{4+}), (A^{+}, B^{6+}), (A^{+}, $B^{5+}B'^{6+}$) are numerous, but also many other combination of these [5] can result in more complex stoichiometry. Phases where vacancies (□) can occur on both anion and cation arrangements, giving compounds of stoichiometry (A□) B_2(O_6O'), (A□) B_2(O_6□), are common. Empty sites often create good pathways for ionic conduction as has been reported for systems such as K$B_x$$W_{2-x}$$O_6$ (B = Al, Ti and Ta) [28] and $Sr_2Os_2O_{6.4}$ [29]. Heavy metal compounds of formula $A_2B_2X_6X'$ comprises a large number of cubic oxides, $A_2B_2O_6O'$, mainly forming pyrochlore of composition (3+, 4+) and (2+, 5+), although numerous other cations are known to exist within the oxide group. When both A and B are occupied by magnetic ions, as it happens in pyrochlore compounds where heavy transition metals combine with rare earths, interesting magnetic features arise. In such systems, magnetic moments due to the combination of f electron of rare earths, d of transition metal (TM) and coupling between f and d can form structures that support geometrical frustration in three dimensions [30, 31, 32], magnetic ordering, and can result in interesting phenomena, such as the anomalous Hall effect in $Nd_2Mo_2O_6O'$ [33], the underscreened Kondo effect in $Pr_2Ir_2O_{7.7}$ [34] or the superconductivity in $Cd_2Re_2O_6O'$ [35, 36] and AOs_2O_6 (A = K, Rb, Cs) [1, 2, 3]. Many of the oxide pyrochlores containing rare earths elements also exhibit interesting fluorescent and phosphorescent behaviour and can find potential application as laser host materials [37]. Such a wide range of properties are very interesting from the electronic point of view [5] and still very poorly understood and this has prompted a large amount of interest in the pyrochlore structure type. The recent attention that this family of compounds has received, however, depends also on the challenging possibility of tuning the electronic properties by changing the A-site cation, which in turn influences the B–O–B electronic interaction of the pyrochlore framework generating varied unconventional and interesting properties. Each of these properties depends on the structure, as subtle changes alter symmetry considerations, bond overlap, and band energy levels.

Understanding and predicting the structure of these compounds becomes, therefore, essential for the design of new materials and the pyrochlore structure represents an interesting example of a highly symmetric and a highly complex structure at the same time. The structural and chemical complexity which can arise in such a simple

pyrochlore lattice offers the potential for observing interesting properties allowing the structure/property relationships of materials to be investigated and perhaps optimised for a specific application. The structural investigation, hence, is expected to improve the understanding of the structure-properties interactions in these systems for which the electronic state is often the result of subtle coupling between electronic and structural degrees of freedom deriving from the intermediate character between localized and itinerant orbitals.

1.1 Scope of the Work

This thesis will explore various structural aspects of selected pyrochlore compounds that offer many interesting and often exotic magnetic phenomena, the nature of which is still unclear and a motive of literature debates. The aim is to prepare oxides containing heavy transition metals in combination with rare earths or alkali metals and to correlate the structures to their physical properties in a joint effort with other members of the project. Large importance will be dedicated to the investigation of the local rearrangement of the cations following the synthetic process. Many different experimental techniques exist for the characterisation of materials, giving information on both the local, and long-range structure. Such techniques are utilised in this study, and mainly involve diffraction, in combination with standard solid state preparation methods. Powder X-ray diffraction (PXD) represents an important tool for routine structure. Powder neutron diffraction (PND) measurements overcome many of the sensitivity limitations experienced in PXD, becoming a powerful probe to understand structural and dynamical features of the local environment of light atoms, such as oxygen, lithium or sodium. Heavy metals from the transition series in the Periodic Table- such as osmium or iridium- often have unpaired electrons in their compounds and this leads to very interesting properties such as superconductivity, magnetism and electrical conductivity. The compositions selected for analysis are expected to give insight into the effect of structure change upon the properties of some systems which were, until now, poorly understood and which contained 4*d* and 5*d* transition elements, in order to obtain new materials with potential useful applications in electronic, sensor and data storage systems.

The detailed investigation of the pyrochlore superconductor AOs_2O_6 (A = Cs, Rb,

and K) represents the main focus of this thesis. This system represents a real melting pot of anomalous physical behaviour, exotic properties and literature disputes, features that have been partly associated with the highly anharmonic motion of the *A* cation, in the large Os_2O_6 framework [38, 4]. In this way, the present research is expected to enrich the structural understanding of the pyrochlore osmate, AOs_2O_6, adding detailed information on the local structure that is needed and contributing to the elucidation of the superconducting mechanism that is still not completely understood. Pyrochlores of composition $R_2B_2O_6O'$, where *R* is a rare earth oxide and *B* is a transition metal oxide (Ru, Ir, Mo) in the oxidation state 4+ were also investigated. What motivated the study of such systems was the lack of detailed structural studies able to give a clear understanding of the interaction resulting from subtle coupling between electronic and structural degrees of freedom.

1.2 Thesis Outline

This chapter contains a short **Introduction** to the topology of the pyrochlores, a necessary tool for a better understanding of those structural behaviours that are discussed in the further chapters. **Chapter 2** contains a detailed description of the experimental techniques and procedures used in these studies. **Chapter 3** mainly focuses on the AOs_2O_6 family by analyzing its structures in detail and correlating trends. Starting from earlier published works, this part also discusses the relevant results on the KOs_2O_6 phase. The fact that the pyrochlore structure is able to accommodate a wide variety of cations leads to the possibility of studying structure/property variations with doping. This possibility is explored in **Chapter 4**, where the effect of using an *A*-cation of ionic radius smaller than K^+ prompts important changes in structure and the properties. Incorporation of water is a common phenomenon in structures such as the defect pyrochlore family that have cavities where easily exchangeable or mobile species reside. Description of structural changes following hydration of KOs_2O_6 represents the focus of **Chapter 5** whereas **Chapter 6** describes how the same phenomenon influences the exchanged compounds investigated in Chapter 4. A correlation between structure and properties of the osmate defect pyrochlore family is also discussed. The chapter also reports the synthesis of a new Ba-based osmium pyrochlore, obtained by an ion-exchange method. To our knowledge this is the first barium pyrochlore belonging to the osmate family. **Chapter 7** describes the structural investigation of a series of

rare earth pyrochlores. Structural trends were associated with the use of different TMs on the *B* site and within the group of *R* cations. A conclusive chapter summarizes the main achievements of this work.

1.3 Structure of the Pyrochlore

The pyrochlore oxide structure contains four crystallographically non equivalent atoms, *A*, *B*, O and O' which mainly crystallises in the cubic space group $Fd\bar{3}m$, arranged in interconnected AO_8 and BO_6 polyhedra [39]. Although there are four possible choices of origin as a consequence of the four non-equivalent lattice atoms, a common way of describing the pyrochlore structure is by fixing its origin on the *B* site, with the four atoms described (according to the Wyckoff notation) occupying the sites: 16*d* (*A*), 16*c* (*B*), 48*f* (O) and 8*b* (O') of the ideal cubic space group [40, 41, 42]. Throughout this work, *B* was always chosen as the origin of the cell. The lattice contains eight atoms per unit cell. The lattice parameter for the cubic cell is usually $\sim$10 Å. The atomic parameter coordinates for a cubic pyrochlore cell with origin at the *B* site are reported in Table 1.1.

Tab. 1.1: Atomic parameter coordinates for a pyrochlore cell with origin at 16*c*, *B* site. Crystal symmetry is cubic, $Fd\bar{3}m$.

Atom	Site	Site Symmetry	Coordinate
A	16*d*	$\bar{3}m$ (D_{3d})	$\frac{1}{2}, \frac{1}{2}, \frac{1}{2}$
B	16*c*	$\bar{3}m$ (D_{3d})	0, 0, 0
x (O)	48*f*	mm (C_{2v})	$x, \frac{1}{8}, \frac{1}{8}$
O'	8*b*	$\bar{4}3m$ (T_d)	$\frac{3}{8}, \frac{3}{8}, \frac{3}{8}$

x for regular octahedra = 0.3125 (5/6)

A number of systems of notation have been developed to describe the pyrochlore lattice and these were detailed in a review published by Subramanian *et al.* [5]. Only two of the four descriptions will be briefly introduced in this chapter because of their informative relation to the purpose of this research. Among these, one widely accepted description considers the pyrochlore-family as a superstructure of the ideal defect *fluorite*, (*Fd3m* space group), a description obtained by removing one eighth of the anions in an ordered fashion [43, 44], see Fig. 1.1.

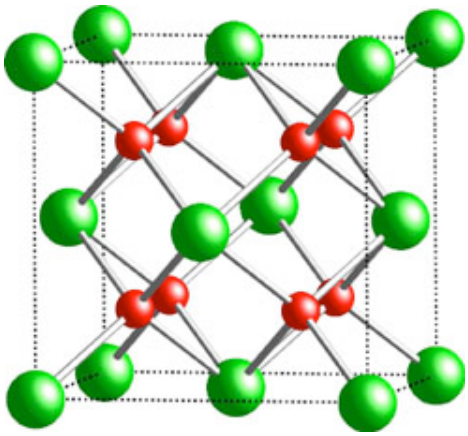

Fig. 1.1: Unit cell of fluorite. Green spheres represent 4^+ cations and red spheres represent 2^- anions. Source: http://www-ssrl.slac.stanford.edu

Although, there are no known materials that meet the requirements of the ideal defect fluorite lattice, this structure-type represents a good starting point for understanding the pyrochlore lattice. In the fluorite structure, *e.g.* CaF_2 depicted in Fig. 1.1, each cation is coordinated to eight anions, thus *A* will be cubically coordinated by F^- anions. *A* cations are FCC packed and form a tetrahedron about each F atom. Conversely to the defect fluorite, the pyrochlore structure is ordered on both the cation and anion sublattice due to a relaxation of the oxygens along the edges of the coordination cube, from positions at $\frac{1}{8}, \frac{1}{8}, \frac{1}{8}$, corresponding to the 8*a* site, toward the vacant anion, on the 8*b* site, to form a trigonal antiprism of oxygen atoms around the *B* cation. Following this ordering two distinct crystallographic anion sites form: one on the 48*f* at coordinate *x*, $\frac{1}{8}, \frac{1}{8}$ and the other on the 8*b* leaving the 8*a* sites. The pyrochlore structure has, therefore, only one variable atomic coordinate, the *x* coordinate of the framework O (O *x*), 48*f* site. All the other atoms sit on special positions ruled by the cubic $Fd\overline{3}m$ space group. This *x* parameter is accurately determined by Rietveld refinement of X-ray and neutron diffraction data [45] although Chakoumakous' relationships (see Table 1.2) can be used to calculate the interatomic distances for the atoms of an ideal cubic pyrochlore [46].

The principal interatomic distances are therefore determined as a function of O *x* and the lattice constant. The value O *x* was found to be strictly influenced by the size of the *A* cation and increases with the increase in the ion size as a consequence of the relaxation toward the empty 8a site. Variation of O *x* determines changes in *B*-O bond length, and in turn determines the *A*–O bond length and the *B*–O–*B* angles and, hence, the shape of the *A* and *B* cation polyhedra. The cell, thus expands or contracts to

Tab. 1.2: Atomic distances for a pyrochlore cell with origin at the A cation on the 16c as from [46]. Crystal symmetry is cubic, $Fd\bar{3}m$.

Atom pair	Distance	
A. . . .A	$a\sqrt{2}/4$	Cub-cub cation separation
A. . . .B	$a\sqrt{2}/4$	Cub-oct cation separation
B. . . . B	$a\sqrt{2}/4$	Oct-oct cation separation
A– O	$a(x^2-\frac{1}{2}x+\frac{3}{32})^{0.5}$	Cub-bond (equatorial)
A– O'	$a\sqrt{3}/8$	Cub-bond (axial)
B– O	$a(x^2-x+\frac{9}{32})^{0.5}$	Oct bond
O. . . .O'	$a(x-\frac{1}{8})$	Shared cub-cub edge
O. . . .O	$a(2x^2-\frac{3}{2}x+\frac{11}{32})^{0.5}$	Shared cub-oct edge
O. . . .O	$a\sqrt{2}(\frac{5}{8}-x)$	Unshared oct edge)

For the alternative origin choice at B site x has to be replaced by $(\frac{3}{4}-x)$.

accommodate differently sized cations. A is in cubic and B in octahedral arrangement respectively as shown in Fig. 1.2. (i) For x value = 0.375 the O' anions will have the same defect fluorite arrangement where A adopts trigonally flattened octahedra and the B-site is in a regular cubic coordination. (ii) For x values increasing to *e.g.* 0.4375, B will have oxygen in a regular octahedral coordination whereas the cubic A site distorts into a trigonal scalenohedron. (iii) If x increases further, the B-site elongates along a threefold axis and the A site becomes a hexagonal bipyramid.

In $A_2B_2O_6O'$ pyrochlores, the larger (8-fold coordinated) A cation has eight nearest neighbour oxygens arranged in a distorted cubic (scalenohedral) geometry, six of which are equidistant at a slightly longer distance with two shorter bonds to O' from the central cation[47, 48]. Each 8b oxygen is surrounded by four A cations arranged at the vertex of a tetrahedron whereas each oxygen atom sitting on the 48f site has two A and two B cations around it. A schematic representation of the coordination around the A site is shown in figure Fig. 1.2(a). The smaller B atoms, on the other side, are six-fold coordinated (in a trigonal antiprism arrangement to oxygen) as showed in Fig. 1.2(b). BO_6 octahedra, sharing corners, form the rigid tridimensional network B_2O_6 which form hexagonal holes along the [111] direction, as shown in Fig. 1.3. The term octahedral is commonly used to describe the cation arrangement of the B site,

although this is not technically correct as the BO_6 units do not form symmetrical octahedra as implied by the space group requirements. A–O and B–O are the shortest bond distances in the structure and their values are usually comparable with those found in A and B binary or ternary oxides having eight, and six-fold coordination respectively. The unit cell of the pyrochlore is shown in Fig. 1.2 and highlights the coordination around the two cations with each cube containing vacancies at two opposing corners.

The second most common description considers the structure as being made by two interpenetrating networks: one resulting from the corner sharing of four BO_6 octahedra arranged to form a rigid tetrahedral cluster with channels, including one made of A_2O' units in *anticrystobalite* arrangement [49, 5], accommodated in the channels made by the B_2O_6 network, as shown in Fig. 1.3. In the A_2O' units, the A cation is in linear coordination, while the O' occupies the centre of an A_4 tetrahedron. This second way of looking at the pyrochlore structure highlights the independence of the two networks. The rigid BO_6 unit is structurally stable whereas A cations mainly satisfy charge-balance requirements [50]. A–O bond distances are significantly longer than the A–O' and the A_2O' network only weakly interacts with the B_2O_6 framework. Cation and/or anion vacancies on this network do not, therefore, significantly affect the stability of the lattice [51]. Indeed, certain pyrochlore compounds occur with partial occupancy of the 16*d* site and partial or empty 8*b* sites [5, 52, 53].

1.3.1 Defect Pyrochlores

The relationship between pyrochlore stability and composition is extensively described in the literature as summarised by Subramanian *et al.* [5]. It is found that each possible pyrochlore composition is ruled by the ionic radii and charge of the ions forming the lattice. The ratio r_A/r_B needs to satisfy certain requirements, below which a non-stoichiometric fluorite phase would form [5]. If the ratio r_A/r_B results in a big mismatch, then the system is expected to undergo complete disorder with the cation adjusting to accommodate the loss of stoichiometry.

As was outlined at the beginning of the chapter, if vacancies occur defect phases such as $(A\square)B_2(O_6O')$, $(A\square)B_2(O_6\square)$ form. A previous study conducted by Hyman *et al.* [41] showed that in defect phases, lattice defects do not occur at 16*c* and 48*f* and that the only lattice positions affected are the 16*d* and 8*b*. The fractional occupancy for

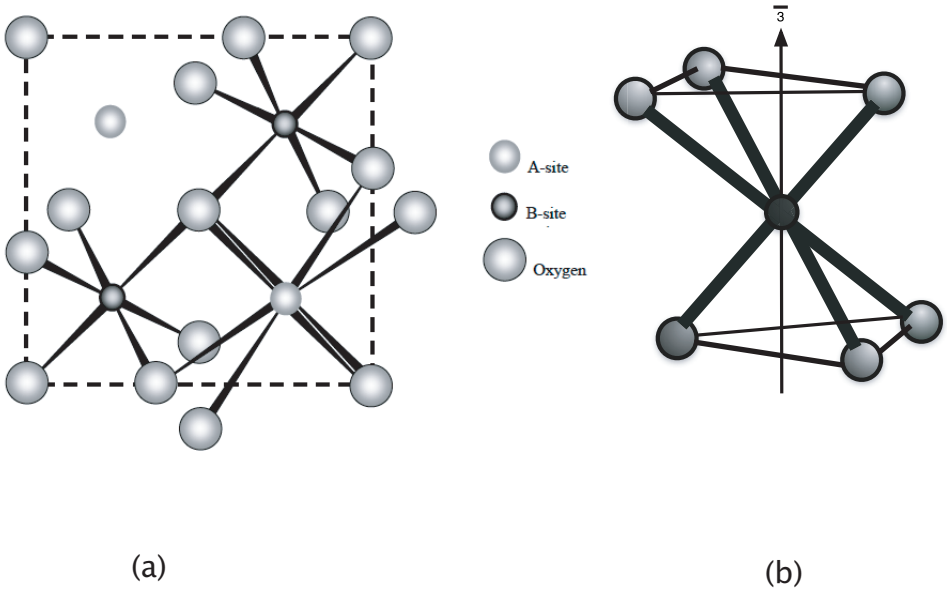

Fig. 1.2: Unit cell of pyrochlore showing the coordination of the A atoms (a) and the 6-fold coordination around the B cation: figure (a) has been adapted from [5].

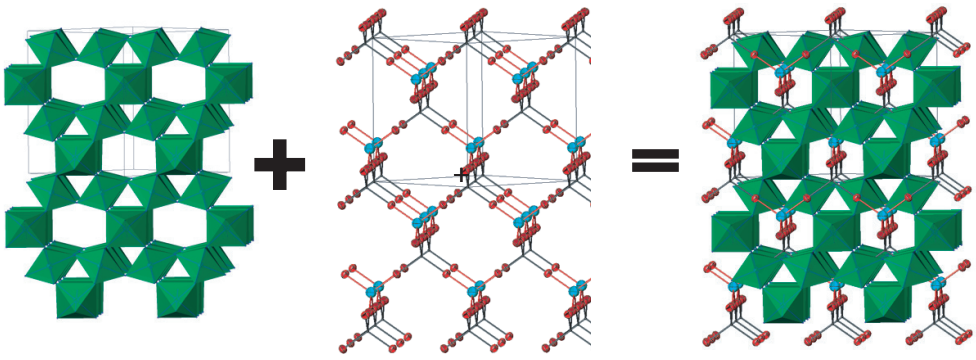

Fig. 1.3: Interpenetrating sublattices of B_2O_6 (left) and the A_2O' sublattice (centre) results in the $A_2B_2O_6O$' pyrochlore structure (right), where red spheres represent oxygen atoms and blue spheres are A cations. The B_2O_6 sublattice is made of corner-sharing BO_6 octahedra.

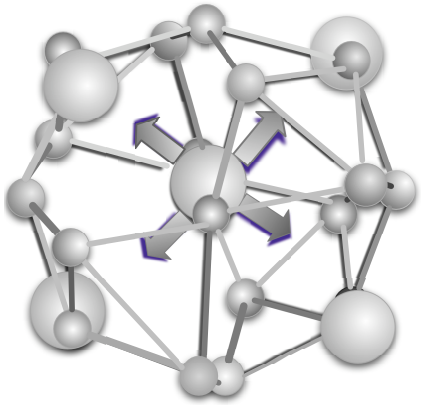

Fig. 1.4: Pyrochlore cavity delimited by a framework of 18 oxygens, smaller spheres. Bigger spheres are A cations sitting on the 8b lattice position, $\frac{3}{8}, \frac{3}{8}, \frac{3}{8}$. The four arrows identify the four [111] directions along which the smaller A^+ cations can be displaced.

these sites varies in the range $0.5 \leq 16d \geq 1$ and $0 \leq 8b \geq 1$. In non-stoichiometric compounds, disorder and structural energy as well as entropy are increased compared to a stoichiometric phase (also identified in the course of the work as α-phases), which can result in interesting cation rearrangements and unpredictable as well as intriguing properties. So, although occupancy of the 16d site is electrostatically more favored, as it appears from electrostatic potential calculations [54], structural studies of several defect materials by powder diffraction showed that if the O' site is empty then the A cation prefers the 8b position or a displacement from this site toward the near empty 32e site which connects to the furthest 16d positions, at coordinate x, x, x. The structure is still easily described in terms of corner-shared octahedral networks made by B_2O_6 units, as in the stoichiometric compounds. In compounds in which the 16d site is partially occupied or empty, the closely coordinated O' anions are missing, so the A cations are surrounded only by a puckered ring of 6 O anions. In such cases the framework built from B and O atoms remains intact and bears an excess negative charge, which is compensated by the lower valence A cations [55]. The difference in cation and anion arrangement between the α - and β -type is shown in Fig. 1.5.

The smaller the ionic radius of an element, the weaker the bond to the structure, and the more enhanced displacements can be. Displacement of the cation toward the 8b or the 32e position is favored by the degree of freedom that the atom is allowed toward the four empty cavities (along the [111] directions) formed by the framework where four big cavities between the 8b and 16d can accommodate cations and /or an-

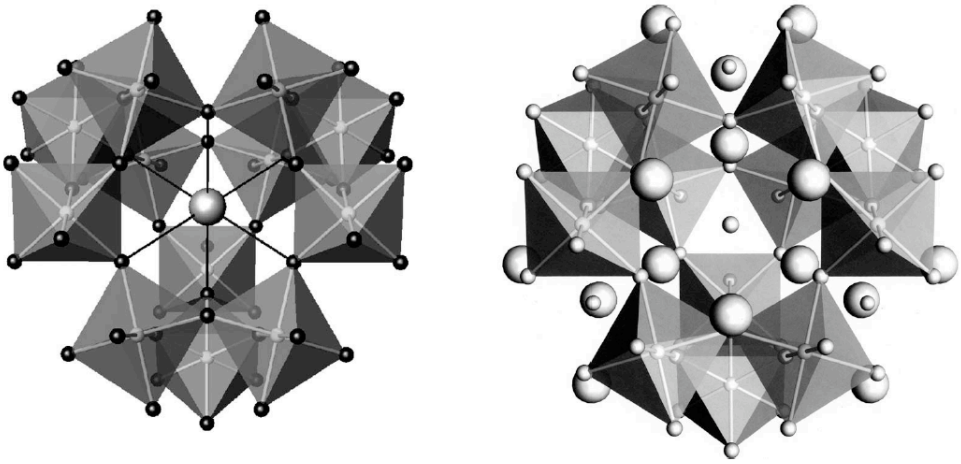

Fig. 1.5: The β-pyrochlore (left) and α-pyrochlore (right) structures as viewed along the [111] direction and centred on $(\frac{3}{8}, \frac{3}{8}, \frac{3}{8})$. For AB_2O_6, B_2O_6 octahedra are shown shaded grey, oxygen are small pale grey spheres, and large grey spheres are A cations

ions. Influenced by charge, polarizability and size, any of the three possible sites can result in full or partial occupancy. A spatial representation of the anion and cation coordinations around the sites of interest is shown in Fig. 1.6. Purple arrows highlight the hypothetical cation displacement from the 8*b* toward the empty 32*e* positions when the O' oxygens (shown as grey spheres) are missing and the 16*d* site is empty. In the defect subgroup where O' is vacant, its original site is often occupied by the smaller A^+ cation, (see Fig. 1.4), located in the middle of the cage identified by 18 oxygen.

An important part in the next few chapters is reserved for discussion of non-stoichiometric pyrochlore oxides, $A\square B_2O_6\square$-type, displaying this last cation arrangement. This subgroup of defect materials will be referred to as β-*pyrochlores*, to use the name used by Yonezawa *et al.* to describe the osmate family AOs_2O_6 and to distinguish their cation arrangement from conventional defect pyrochlores [56]. This defect variant is also known in literature as an *inverse* pyrochlore [57]. The first defect structure to appear in the literature within the pyrochlore family was reported by Babel *et al.* [58, 59]. In this subgroup, the A ion could be a monovalent cation whereas the B cation could be any transition metal of suitable size and oxidation state able to adopt the octahedral coordination. For smaller ions, such as K^+ and Li^+, the structure easily incorporates water molecules.

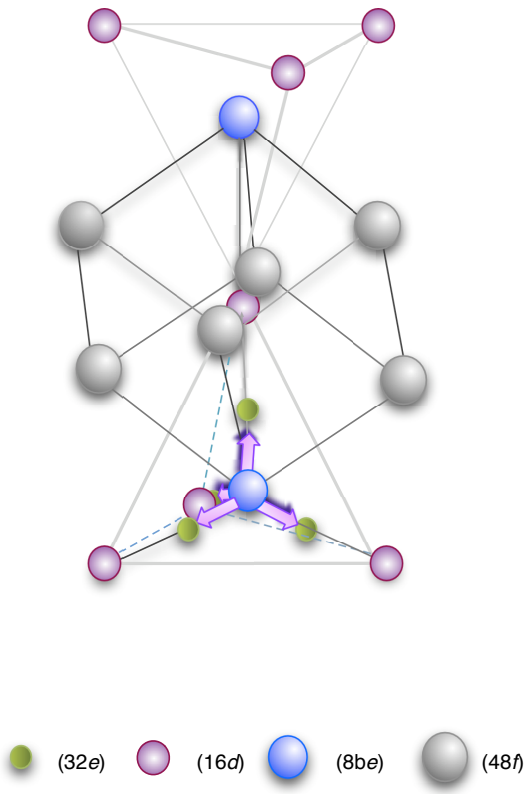

Fig. 1.6: Cation and anion coordination in pyrochlores. Possible atomic displacement from the 8*b* to adjacent 32*e* sites are represented as purple arrows. Grey spheres are oxygens.

1.3.2 Crystal Structure Determination and Symmetry Allowed Distortion

As earlier described, the ideal pyrochlore structure has only one variable atom position coordinate, the x coordinate of the framework O, 48f site. All the other atoms sit on special positions within the cubic $Fd\bar{3}m$ space group. The interaction of X-rays with a pyrochlore-type material generates a diffraction pattern containing two different subsets of intensity maxima [60]: i) one characteristic of the fluorite cell, complying with the conditions where h+k and k+l and l+h must be a multiple of four (hkl: h+k = 4n k+l = 4 n, and l+h = 4n) [60, 61] and ii) one coming from the supercell of the ordered pyrochlore structure, and influenced by the difference between the scattering powers of the cations sitting on both A and B sites, and by the occupancy of the cation and anion sites, by the displacements of the O x from the ideal 8a fluorite site. Extra conditions are allowed and dependent on the specific atom; namely A and B cations allow extra diffraction maxima for hkl: = h = 2n + 1 or h,k,l = 4n + 2 or h,k,l = 4 n, whereas for the oxygens extra conditions allowed are hkl: h = 2n + 1 or h + k+ l = 4n [62].

Although $Fd\bar{3}m$ represents the ideal space group, deviations from cubic symmetry, by way of tetragonal, rhombohedral or triclinic distortion are possible. These deviations are mainly ascribed to the critical ratio of radii between the A and the B cations. The three main symmetry forbidden reflection are usually associated with the violation of i) the lattice-centering extinction rule of the $Fd\bar{3}m$ space group [63]; ii) violations of the d-glide extinction rule of $Fd\bar{3}m$ [64, 65, 66, 67, 68, 69, 70] and iii) violation of the special extinction rules [50] that apply to the pyrochlore structure because of the atoms in special positions in $Fd\bar{3}m$.

As earlier mentioned, the study of defect AOs_2O_6 phases represents the main focus of this work and space group investigation will play an important role in that. The aim is to resolve discrepancies between literature descriptions by Schuck *et al.* [71] and Rogacki *et al.* [72], that described KOs_2O_6 in $F\bar{4}3m$, and those by Hiroi *et al.* [1, 2]. To investigate this further, a series of model independent structure refinements were carried out using space groups from the subgrouping as described by Hiroi in work on symmetry-lowering structural transitions of $Cd_2Re_2O_6O$' [70]. A simplified diagram of the group-subgroup symmetry reductions from the parent pyrochlore $Fd\bar{3}m$ space group is shown in Fig. 1.7. Space group, symbol and the number of unique atomic

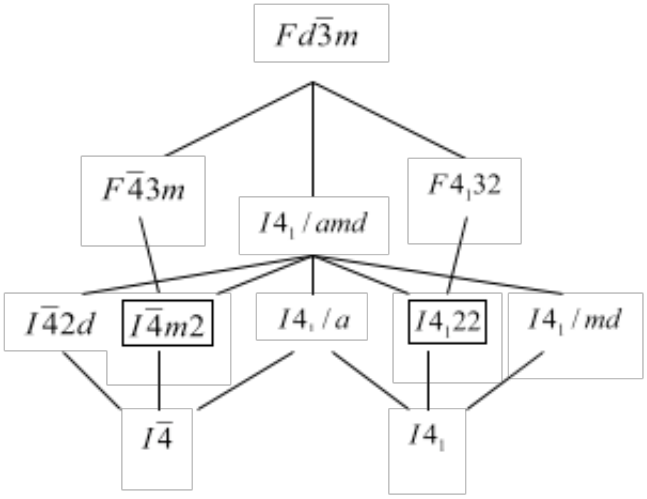

Fig. 1.7: Simplified diagram of the group-subgroup symmetry reductions from the standard pyrochlore space group. Space group, symbol and the number of unique atomic positions in the asymmetric unit of the structure are given.

positions in the asymmetric unit of the structure are given. The subgrouping follows reductions in the pyrochlore symmetry from a face-centred to a body-centred lattice.

2. EXPERIMENTAL

Heavy metal oxides described in this thesis were synthesised either by standard solid state methods, or by ion exchange reactions. A full range of appropriate techniques was used in the characterisation and structure solution of the various synthesised materials.

Powder X-ray diffraction (PXD) was the most widely used technique in this work. This allowed initial phase identification, reactions to be monitored, and detailed structural characterisation using the Rietveld method [73, 45] on a routine basis. Powder neutron diffraction (PND) was also employed to conduct variable temperature diffraction studies and to provide accurate structural information. PND allowed a more accurate determination of the position of lighter atoms, particularly on features involving the coordination of oxygen and alkali metals cations.

Several other analytical techniques were also employed. Thermogravimetric analysis (TGA) was used to study stability and structural changes in materials and as a basis for thermal diffraction experiments, it also gave information about the amount of adsorbed water in a sample. Energy Dispersive X-ray Spectroscopy (EDS) was carried out on the novel materials to show, qualitatively, that the stated elements were present in the new structures produced, whereas atomic absorbance spectroscopy (AAS) was employed for quantitatively determining the concentration of a particular metal element in a specific sample. The magnetic properties of selected materials have been investigated using a vibrating sample magnetometer (VSM). This chapter provides a summary of the experimental methods used in this thesis and describes their application to a range of polycrystalline compounds.

2.1 Synthetic Methods to Solid State Products

2.1.1 High Temperature Solid State Reactions

Many of the polycrystalline materials investigated in the course of this work were prepared by conventional solid state routes. This procedure involves heating together a mixture of components at high temperatures. The high temperatures overcome the activation energies of the reactions and help to satisfy both thermodynamic and kinetic solid state reaction requirements [74]. The rate of reaction is governed by the diffusion of the ions forming the lattice which is in turn facilitated by a reasonably high temperature. To ensure a greater contact surface area between starting materials, these were intimately mixed in an agate mortar, before heating in an alumina crucible at the desired temperature. The rate of the reaction is often increased by pressing of the starting materials into pellets or by several regrindings of the mixture; both procedures help to maximise the interfacial contact of the reacting ions.

Controlling the reaction environment is important for the success of the synthesis, particularly if the starting materials require oxidation states that are not stable at ambient pressure. In these cases the use of evacuated quartz tubes, or of a furnace either involving the passage of a reducing gas (such as nitrogen or argon) or an oxidising gas (such as oxygen), must be used to complete the reaction.

2.1.2 Ion-exchange Reactions

Polycrystalline phases investigated in Chapter 4 and Chapter 6 were prepared by ion-exchange methods. This method allows the synthesis of compounds well below their sintering temperatures and unaccessible *via* direct synthesis. Pyrochlores are materials known to exhibit ion exchange properties due to their rigid frameworks that form tunnel structures where the mobile cations occupy only some of the sites allowing transport into empty sites. In a general exchange reaction:

$$R - A^+ + B^+ \rightleftharpoons R - B^+ + A^+ \tag{2.1}$$

where *R*- is the ion exchanger matrix and A^+ and B^+ are the monovalent exchanging ions, two type of interaction energies are involved: (i) the free energies involved in the changes in hydration of the counterions and the grouping of the matrix and (ii) the electrostatic interactions between the same [75]. Thermodynamic, kinetic, and structural factors are all very important and all the diffusion processes require an activation

energy, E_a, to overcome the barrier to diffusion. However, the maximum uptake of ions by ion exchangers are generally less than their ion-exchange capacities, and is influenced by the nature of the species involved, temperature, and concentration of the ions in solution. If the concentration of the entering ions is high enough and the outgoing ions do not accumulate at the surface of the exchanger, then the reaction rate will depend on counterdiffusion of ions within the solid [76]. The pore size of the cavity and the rigidity of the matrix are considered the controlling parameters causing the hindrance to the entry of the larger ions, and hence partial ion-exchange. Often exchange reactions are accompanied by a phase change or vacancy formation.

2.2 Powder X-ray Diffraction (PXD)

X-ray diffraction is a structurally probing technique, which is used to measure the atomic arrangement of atoms in a structure. A monochromatic beam of electromagnetic radiation, such as X-rays, interacting with a crystalline material, can be scattered or deflected away from its initial direction of propagation. If the energy of the scattered protons results unchanged from that of the incident beam, then it can produce a coherent scattering; conversely it will give rise incoherent scattering. For a specific sample, the coherent interaction is a function of the electron density distribution. Scattering from an ordered material can form a distinct diffraction pattern which represents the fingerprint of the material. For the diffraction phenomenon the choice of the radiation is important as its wavelength has to be comparable to interatomic distances. Copper $K_\alpha 1$ ($\lambda = 1.5406\ \AA$) represents the best choice for many crystals if the diffraction data are recorded.

2.2.1 Theory

Diffraction is conventionally described using Bragg's Law [77]. By definition, a crystal is a solid made of a series of planes of atoms which are arranged in unit cells spaced at regular intervals in three independent directions. The perpendicular distance between each set of planes is known as the *d* spacing. Each set of planes in a crystalline structure is described by a unique set of integers, which are known as Miller indices. In a three dimensional structure three indices are required to completely identify the family of

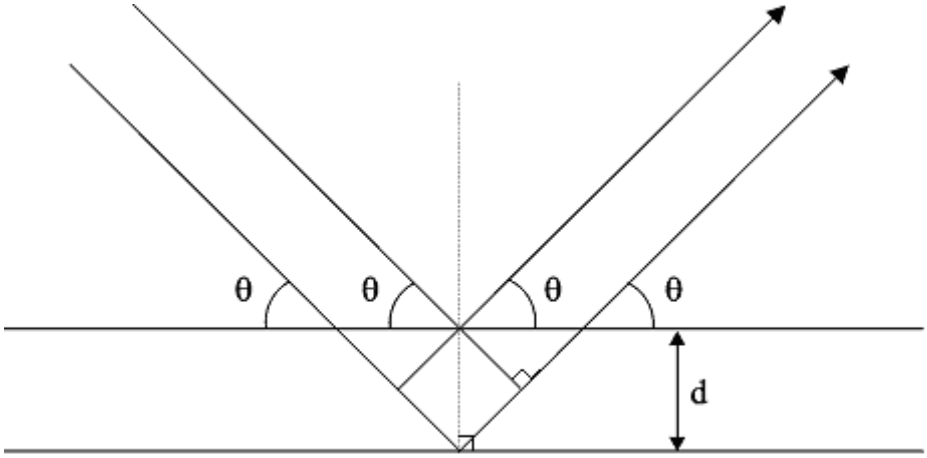

Fig. 2.1: Schematic representation of scattering from parallel planes of point scatterers which can be used to derive the Bragg equation.

planes; these are conventionally associated with the letters h, k and l and are derived from the reciprocal relationship from the lattice parameters a, b and c.

Any wave of X-ray radiation impinging on a regular array of scattering points will produces diffraction only if the X-rays scattered from the adjacent planes will combine constructively. This concept is well described by considering a scattering situation as shown in Fig. 2.1 in which a plane wave with an angle of incidence θ (Bragg angle) and wavelength λ, separated by a perpendicular distance d, is incident on two parallel planes of atoms. For constructive interference the path difference between the two diffracted beams must correspond to an integer number of wavelengths. Simple trigonometry leads to the Bragg equation [78]:

$$n\lambda = 2dsin\theta \tag{2.2}$$

where n is an integer (1, 2, 3..).

When a set of planes *hkl* satisfy the Bragg condition, the scattered radiation will emerge from the crystal in a well-defined direction. In the case of a polycrystalline material, the sample is made by a very large number of small, randomly oriented single crystals, such that for any reflection *hkl* there will always be a finite number of planes inclined satisfying the Bragg's conditions.

However, because the orientation of these crystallites around the incident beam is

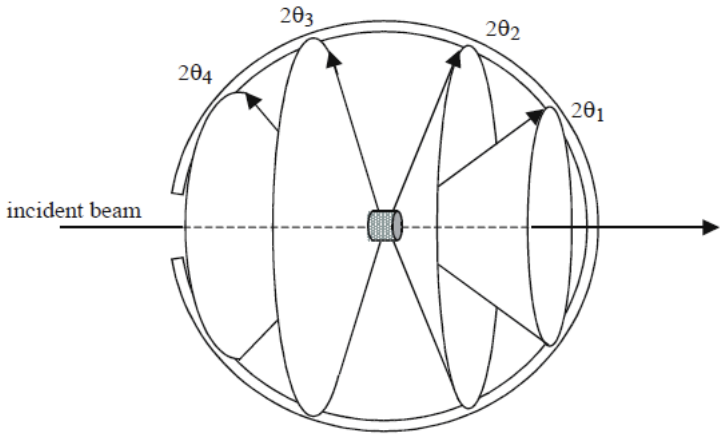

Fig. 2.2: Diffraction cones arising from the scattering of a polycrystalline compound.

not fixed, the scattered radiation emerges not as a single, narrow beam but as a continuous cone of intensity at an angle 2θ the axis of which lies along the incident beam direction as it is shown in Fig. 2.2. Because the crystallites are oriented randomly, at angles of incidence other than the Bragg angle, destructive interference will also occur and discrete cones of scattered radiation will be generated simultaneously for all the *hkl* reflections.

It might be considered that diffraction maxima should be seen for all the planes in a crystalline structure, but in practice the intensity of an observed reflection depends on reflection conditions or systematic absences dictated by the symmetry of the structure (*i.e.* glide planes or screw axes) [79], by the space symmetry elements, by the electron density, as well as thermal vibrations of the atoms within a structure, which can contribute to a decrease in the observed intensity. Measurements of the diffraction maxima allows the interplane distance *d* to be calculated and give, in turn, information on the unit cell and the crystal system (Table 2.1). Table 2.1 reports the crystal systems into which all crystal structures can be classified. Each of these has distinctive symmetry requirements, allowing further division into fourteen Bravais lattices, including the lattice types primitive, P, body-centred, I, or face-centred, F, (or C when only one face is centred).

Tab. 2.1: Equations for d-spacings in the different crystal systems

Crystal System	Expression for d_{hkl}
Cubic	$\frac{1}{d_{hkl}^2} = \frac{h^2+k^2+l^2}{a}$
Tetragonal	$\frac{1}{d_{hkl}^2} = \frac{h^2+k^2}{a^2} + \frac{l^2}{c^2}$
Orthorombic	$\frac{1}{d_{hkl}^2} = \frac{h^2}{a^2} + \frac{k^2}{b^2} + \frac{l^2}{c^2}$
Hexagonal	$\frac{1}{d_{hkl}^2} = \frac{4}{3}\left(\frac{h^2+hk+k^2}{a^2}\right) + \frac{l^2}{c^2}$
Monoclinic	$\frac{1}{d_{hkl}^2} = \frac{1}{sin^2\beta}\left(\frac{h^2}{a^2} + \frac{k^2 sin^2\beta}{b^2}\right) + \frac{l^2}{c^2} - \frac{2hlcos\beta}{ac}$
Triclinic	$\frac{1}{d_{hkl}^2} = \frac{1}{V^2}\left[h^2b^2c^2sin^2\alpha + K^2a^2c^2sin^2\beta + l^2a^2b^2sin^2\gamma\right)$
	$+2hkabc^2(cos\alpha cos\beta - cos\gamma) + 2kla^2bc(cos\beta cos\gamma - cos\alpha)$
	$+2hlab^2c(cos\alpha cos\gamma - cos\beta)$
	where $V = abc(1 - cos^2\alpha - cos^2\beta - cos^2\gamma + 2cos\alpha cos\beta cos\gamma)^{1/2}$

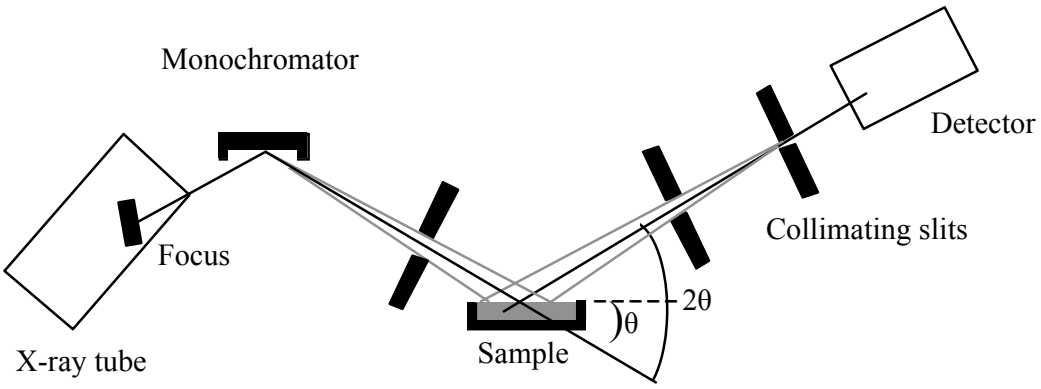

Fig. 2.3: Schematic of the Siemens D5000 diffractometer

2.2.2 PXD Instrumentation

The majority of the PXD data collected for this thesis were recorded out using a Siemens D5000 diffractometer. X-rays are generated by accelerating an electron beam at a copper target which removes core electrons from the copper plate and produces copper wavelength X-rays. A single crystal monochromator selects only X-rays of λ = 1.54056 *Å* (copper $K_{\alpha 1}$). The radiation is then collimated by aperture slits before hitting the sample which is mounted in a recessed aluminum or plastic sample holder. The diffracted beam then passes through a further set of slits before reaching a standard scintillation detector. The detector on the D5000 is a conventional scintillation counter, consisting of a crystal that fluoresces when exposed to X-ray radiation and a photomultiplier tube that measures light from the crystal and can only observe a small cross section of the diffraction cone diffracted from the sources. The incident beam, sample and detector are positioned according to the Bragg Brentano geometry. The sample is rotated at a constant angular velocity, where the detector rotates exactly at velocity double that of the sample, maintaining a fixed relationship between the incident angle, θ, and the diffraction angle, 2θ, through the angular range to be studied. A computer controls the instrument, which also collects and stores the data (fingerprints) collected. A schematic of the D5000 diffractometer is shown in Fig. 2.3.

Further diffraction data analysed in this thesis were collected using a Bruker D8 Advance diffractometer. The X-ray source, main components and geometry are the same as for the D5000 diffractometer. The D8, however, differs from the Siemens in-

strument in the detector and the sample environments. For data collected in this work a Paar HTK-1200 furnace stage was used. This allows the collection of data at up to 1473 K from a sample placed under vacuum or gas flow. The sample is mounted on a recessed alumina holder which is loaded inside a sealed chamber. Kapton windows allow the incident and diffracted X-ray beams to pass into and out of the chamber. The temperature of the furnace can be controlled by a PC. For the purpose of the research the instrument was fitted with a positive sensitive detector (PSD). It is composed of an anode (at which an intense electrical field is applied) and a cathode, separated by a work gas (argon) which is ionised by the diffracted X-ray photons. The electrons ionised are immediately accelerated, and gain sufficient energy to ionise other argon atoms. The position of the charge can be calculated by the time which it takes to reach each end of the detector wire. The main advantage of the PSD is that the detector wire covers approximately 8 degrees in 2θ. This allows a much greater number of data points to be sampled at the same time, making the collection of powder patterns much faster. The disadvantage is that the resolution is not as good, giving a broader peak shape in the diffraction pattern.

The diffraction data collected using both instruments was initially analysed using the Diffrac^{plus} evaluation program (EVA) [80] for the identification of the phases and their indexing. The diffraction pattern can also be matched against diffraction patterns of known compounds maintained by the Joint Commitee on Powder Diffraction Standards (JCPDS) [81].

Following these initial steps a further set of data was generally collected for a longer period of time and over a large 2θ range to be used in a full structural refinement by the Rietveld method [73, 45]. In addition to providing information about the structure and cell of the compound investigated, X-ray diffraction allows the resolution of atoms within the cell *via* consideration of peak intensities. X-ray photons are scattered by electrons thus atoms with a high atomic number will dominate the diffraction pattern. This scattering is strongly dependent on the term 'sinθ', where θ is the angle of diffraction, and decreases as sinθ increases. The consequence of this is that the scattering is stronger at low angle and weak at high angle. The intensity of each diffraction maximum is related to the structure factor, F. For any regular arrangement of stationary atoms, F results from the sum of the contribution of the scattering amplitudes, f,

and the phases, ϕ:

$$F = \sum_{j=1}^{N} f_j exp[i\phi_j] \tag{2.3}$$

In a unit cell, the total phase shift of an atom, j, at a point (x_j, y_j, z_j) from the origin, is the sum of the phase shift in each direction. When the phase shift is evaluated, the structure factor for one unit cell becomes:

$$F_{jkl} = \sum_{j=1}^{N} f_j exp[2\pi i(hx_j + ky_j + lz_j)] \tag{2.4}$$

h, k and *l* are the Miller indices defining the plane from which the reflection occurs. For very small crystals, it may be shown that the intensity of the scattered beam is proportional to the square of the structure factor:

$$I_{hkl} = kL^2 |F_{hkl}|^2 \tag{2.5}$$

where k is a scaling constant and L is the Lorentz factor, a geometric function of the method used in collecting the data and hence the instrument used [82].

In real situations, the scattered intensity is modified due to imperfections in the lattice structure. Defects and substitutional disorder, especially in non-stoichiometric compounds, can cause local structure irregularities. In addition, thermal motion also reduces the scattered intensity as a consequence of time dependent vibrations of the atoms about their mean positions, which contribute to the disruption of the in-phase behaviour of their combined scattering.

The structure factor, reflected by a plane *h,k,l* can be corrected according to:

$$T_{hkl} = exp\left[-B_{hkl}\frac{sin^2\theta}{\lambda^2}\right] \tag{2.6}$$

where T_{hkl} is the thermal motion correction and B is equal to $8\pi^2 U$, where U is the root mean square thermal displacement. The structure factor for a unit cell, can be written therefore:

$$F_{hkl} = \sum_{j=1}^{N} f_j n_j exp\left[-B_{hkl}\frac{sin^2\theta}{\lambda^2}\right] exp[2\pi i(hx_j + ky_j + lz_j)] \tag{2.7}$$

where n_j is the occupation factor of the j^{th} atom; this factor is one in a structure free

from defects. From Eqn. 2.7 the displacements due to thermal motion are assumed isotropic, which is usually only the case in some highly symmetric positions of cubic space groups [83]. In all other cases, anisotropic thermal motion can be described in the form of an ellipsoid, replacing the above equation with:

$$T_{hkl} = exp\left[-\frac{1}{4}(B_{11}h^2a^{*2} + B_{22}k^2b^{*2} + B_{33}l^2c^{*2} + 2B_{12}hka^*b^* + 2B_{23}hlb^*c^* + 2B_{13}hla^*c^*)\right] \tag{2.8}$$

The intensities of the diffracted beams are also governed by the multiplicity of an *h,k,l* reflection. In a given crystal symmetry class, thus, for a specific *h,k,l* reflections there are a number of equivalent planes diffracting at the same angle and resulting in an increased density.

Using these principles a simulated pattern of diffraction can be calculated from a reference model using cell parameters, atomic positions and symmetry elements. This represents the basis of the Rietveld method for the analysis of the diffraction data.

2.2.3 The Rietveld Method

In a single crystal diffraction experiment, the intensity of the reflections produced by each point can be routinely measured. Powder diffraction data, on the other hand, often contain many overlapping peaks which make the structure factor extraction rather difficult and in some cases impossible. For this reason the amount of information that could be obtained from powder data was limited until the Rietveld method was proposed by H.M. Rietveld [73]. Rietveld realised that although many reflections did overlap, and thus could not be modelled as single intensities, they could be fitted using simple shape parameter giving structural information about the total intensity and the peak shape of a cluster of reflections. The method was further developed following the advent of computers and now permits the solution of increasingly complex structural problems. The method is the same for both PND and PXD data.

A typical structural refinement begins with a starting model, usually obtained from a similar crystal system. The choice of the model is very important as the method is one of structure refinement rather than structure solution. Scale factors and backgrounds are then introduced, followed by lattice parameters, zero point correction and sample displacement to accurately locate Bragg reflections. Atom positions are then varied, modifying the peak intensities, followed by the refinement of the temperature factors

which define their thermal motion. Finally, the peak shape is refined. Variation of the anisotropic temperature factors is also possible in some cases for neutron data. The instrument parameters that can be varied are also usually dependant on the kind of experiment carried out. The method is a least square best fit process aimed at to minimise the function M:

$$M = \sum_i w_i (y_i^{obs} - y_i^{calc})^2 \tag{2.9}$$

where w_i is a weighting factor given by $1/y_i^{obs}$, y_i^{calc} is the observed intensity at each step/point i (2θ for PXD), y_i^{calc} is the calculated intensity at each step.

For PXD, the calculated intensities are determined from the $|F_K|^2$ values obtained by the sum of the calculated contributions from neighbouring Bragg reflections (K) plus background b_i:

$$y_i^{calc} = s \sum_k L_k |F_k|^2 \phi(2\theta_i - 2\theta_k) P_k A + y_{bi} \tag{2.10}$$

where s is the scale factor, L_k contains Lorentz polarisation and multiplicity factors, ϕ is a reflection profile function, F_k is the structure factor for the K^{th} Bragg reflection, P_k is the preferred orientation function, A is an absorption factor and y_{bi} is the background intensity at the i^{th} step.

The background intensity, y_{bi} is modelled by a function that is a cosine Fourier series with a leading constant term:

$$y_{bi} = B_i + \sum_{j=2}^{N} B_j cos[P * (j - l)] \tag{2.11}$$

For X-ray diffraction, P represents the position of the step in 2θ, while for TOF the times are scaled by 180/TMAX; TMAX is the maximum allowed by the incident spectrum. B_i and B_j are determined by least squares during the refinement.

A comparison of intensities is carried out at every point so it is essential for the calculation of the calculated profile to accurately describe the peak shape of the Bragg reflections. The peak shape is generally dictated by the instrument. For both D5000 and D8 diffractometers the peak shape is pseudo-Voigt as described by the expression:

$$\eta L + (1 - \eta) G \tag{2.12}$$

where L and G are the Lorenzian and Gaussian contribution to the peak shape and

η is the mixing parameter which can be refined as a linear function of 2θ. L and G contributions to the peak shape are described by:

$$G = \frac{(4ln2)^{1/2}}{H_k\sqrt{\pi}} exp\left[-4ln2(2\theta_i - 2\theta_k)^2\right] \tag{2.13}$$

and

$$L = \frac{2}{\pi H_k} 1/\left[1 + 4\frac{(2\theta_i - 2\theta_k)^2}{H_k^2}\right] \tag{2.14}$$

where $2\theta_k$ is the calculated position for the k^{th} Bragg reflections corrected for the counter zero-point and H_k is the full-width-at-half-maximum (FWHM) of the k^{th} Bragg reflection. This last term is dependent on the scattering angle $2\theta_k$ and is modelled as:

$$H_k^2 = Utan^2\theta + Vtan\theta + W \tag{2.15}$$

where U, V, W are the refinable and are instrument and sample dependent.

The least squares parameters essentially fall into two distinct groups. The first defines the structural parameters and describe the content of the unit cell, including the overall temperature factors, atomic coordinates and fractional occupancies of each site. The second includes the profile parameters, which describe the position, shape and FWHM of each peak. This includes the scale factor, unit cell parameters and U, V, W correction. A quantitative assessment of the agreement between the observed and calculated profiles is defined by a number of reliability factors identified as $R_{profile}$ (R_p), $R_{expected}$ (R_{exp}) and $R_{weightedprofile}$ (R_{wp}) and are given by:

$$R_{profile} = R_p = 100\left[\frac{\sum_i \left|y_i^{obs} - y_i^{calc}\right|}{\sum_i y_i^{obs}}\right] \tag{2.16}$$

$$R_{expected} = R_{exp} = 100\left[\frac{(N - P + C)}{\sum_i w_i (y_i^{obs})^2}\right]^{1/2} \tag{2.17}$$

R_{exp} is defined from the statistics of the refinement, N is the number of observations, P is the number of refinable parameters, C is the number of constraints.

$R_{weightedprofile}$, from a mathematical point, is the most significant between the R factors because the numerator is the residual being minimised. By the same reasoning

it is also the factor that best reflects the progress of the refinement. It is given by:

$$R_{weightedprofile} = R_{wp} = 100 \left[\frac{\sum_i (y_i^{obs} - y_i^{calc})^2}{\sum_i w_i (y_i^{obs})^2} \right]^{1/2} \tag{2.18}$$

The final parameter being minimised during the refinement is the chi-squared value, defined as:

$$\chi^2 = \left[\frac{R_{wp}}{R_{exp}} \right]^2 \tag{2.19}$$

This value is used as a measure of how well the calculated model fits the actual observed data in conjunction with a visual analysis of the difference between the patterns.

For a good fit $R_{weightedprofile}$ should approach statistically the R_{exp} factor which can also be estimated by examining the plot of the profile fit; for a good fit, the difference line between the calculated and the observed value should be as flat as possible. All the Rietveld refinements reported in this thesis were performed using the Generalised Structure Analysis Suite, GSAS, of von Dreele and Larson [84].

2.3 Powder Neutron Diffraction (PND)

The wave-like properties of the neutron were first demonstrated, by means of diffraction, in 1936. From the de Broglie relationship,

$$\lambda = \frac{h}{mv} \tag{2.20}$$

(where λ is the wavelength, h is Planck's constant, m is the mass of a neutron, v is the velocity of a neutron), it can be seen that neutrons with thermal energies have associated wavelengths of approximately 1.6 $\AA$, comparable to interatomic separations. In fact, as the mean square of a Boltzmann distribution of neutron velocities is 2200 ms^{-1} at 273 K, this means that moderate velocity neutrons are suitable for diffraction. The use of PND has several advantages that compensate for cost and level of complexity over X-ray diffraction experiments with respect to instrumental set up. While X-rays are diffracted by the electron density surrounding nuclei, neutrons are scattered by the nuclei of the atoms. This means that the scattering power of neutrons from a sample is not dependent on atomic number, but on the potential scattering and resonant scattering of a nucleus, which varies across the periodic table giving neighbouring element and

isotopes markedly different scattering lengths. As this scattering power can be very different for atoms of a similar atomic weight, a PND experiment can often distinguish between elements close to each other in the periodic table and can give accurate information about light atoms in the presence of heavier ones; this is of particular significance in this work, since it permits accurate determination of oxygen positions, or light alkali metals in the presence of heavy transition metals. With neutrons there is no angular dependence on scattering such as that seen in X-ray diffraction, which allows observation of high angle diffraction maxima that would not be seen by X-ray. Another advantage is that the neutron sample environment can be controlled by the use of either furnace or cryostat. This allows both the *in-situ* study of phase transitions and permits, at low temperature, due to the decrease of thermal motion, very accurate structural determination. For these reasons, and despite the high cost and the complex instrumental set up neutron, diffraction represents an invaluable tool for the detailed investigation of many materials.

The two principal sources of neutron radiation available for diffraction techniques, and both used in this work, are: constant wavelength and time of flight (TOF). The first uses a reactor source, such as found at the Institut Laue-Langevin (ILL) in Grenoble, France. The neutrons here are generated by fission in a nuclear reactor. In the second pulsed neutrons are generated from a spallation source, such as ISIS at the Rutherford Appleton Laboratories in Oxford. In this method the neutrons are generated by firing high energy protons, at a heavy metal target. In this thesis data were collected on the D2B, D1A and D20 high resolution diffractometers at the high flux reactor at the ILL, and on the HRPD diffractometer at the ISIS, Oxford.

2.3.1 Constant Wavelength PND

The instrumentation and the general principles of the constant wavelength diffractometer are essentially similar to those of the PXD experiment, described in Sn. 2.2. In such conventional diffraction experiments, a monochromatic beam of known wavelength, λ, is used. The scattered radiation is measured as a function of scattering angle, 2θ, by using a large PSD which covers a range of scattering angles. The high flux and the stationary large PSD allow several short-time measurements giving opportunities for the investigation of phase transitions as the temperature changes. D2B and D1A are both high-resolution powder diffractometers able to provide high resolution at long

wavelengths. The nearly perfect gaussian peaks in the 2θ range 3–160° permit the refinement of complex structures with a volume up to 2000 and 1000 $Å^3$ for D2B and D1A respectively.

Instrumentation

The D2B instrument has a white neutron beam monochromated from 300 to 50 mm (selected using a germanium monochromator) with a take off angle of 135° which gives a resolution of $\Delta d/d \approx 5 \times 10^{-4}$. The resolution of D1A is lower than D2B ($\Delta d/d \approx 2 \times 10^{-3}$); the height of the beam is of 150 mm. D1A is particularly well suited to magnetic structures and large d-spacing studies. The samples examined run on these instruments were mounted in vanadium cans of 5 mm of diameter. The D2B detector uses a bank of 128 three inch collimators and ^{3}He counters at 2.5° intervals sweeping from 0-160° in 0.025° steps. Although a range of wavelengths can be selected, for this work λ = 1.594 $Å$ was used. D1A utilises a 60° bank of ^{3}He detectors which sweep in 0.05°; and longer wavelength, 1.909 $Å$. Data collection on D2B was performed between 2 K and room temperature over a period of 4-8 hours (chapter 3, 4), where D1A data were collected at 2 K over a period of 4-5 hours (Chapter 6). D20 is a very high intensity 2-axis diffractometer equipped with a large microstrip detector. Due to the extremely high neutron flux it permits experiments on very small samples with a medium to high resolution. The complete diffraction pattern covers a scattering range of 153.6° in a matter of seconds. Studies as a function of temperature, pressure or other parameter can be performed. Different monochromators and take-off angles, plus optional Soller collimators and secondary slits, permit a wide choice in the Q-space range, wavelength, resolution and flux. A high-resolution configuration ($\Delta d/d \approx 2 \times 10^{-3}$) is obtained for a take-off angle of 120° [85].

A schematic representation of a conventional neutron diffractometer at a reactor source is shown in Fig. 2.4. The neutron beam coming from the moderator at a reactor covers a wide range of wavelengths and does not change with time. A monochromator is therefore necessary to produce a monochromatic beam.

2.3.2 Time of Flight (TOF) PND

TOF PND, as anticipated section Sn. 2.3, uses neutrons generated from a spallation source. Initially, H^- are produced by an ion source, deprived of electrons to create a proton beam, accelerated into an 800 MeV synchrotron and directed onto a heavy metal

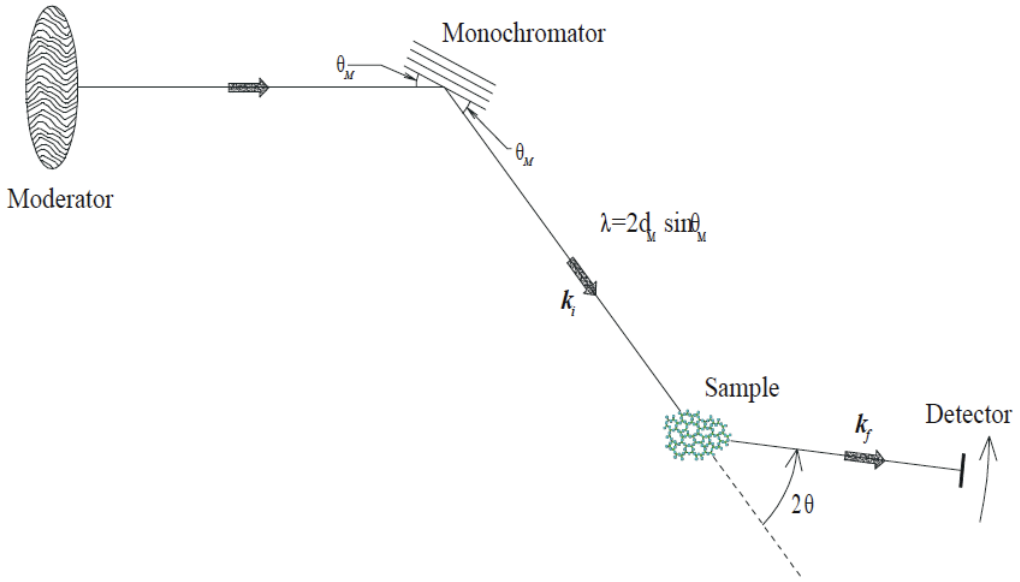

Fig. 2.4: Schematic of a neutron diffractometer for constant wavelength neutron source.

target. The collision between high energy protons and the metal target, usually a mixture of tungsten and tantalum, produces high energy neutrons. The pulses of neutrons produced have short wavelengths (not suitable for diffraction) and are slowed down by moderators, before they reach the experimental beam lines. Moderators containing hydrogenated materials, such as water or methane, slow the incident neutrons by collision; these finally arrive at the beam lines with a suitable wavelength for diffraction experiments. Each pulse provides a consistent range of neutron velocities and, hence, of neutron wavelengths covering the entire neutron spectrum.

Pulsed neutron source diffractometers operate in a fundamentally different way to a conventional constant wavelength instrument. In a conventional diffractometer the wavelength, λ, is fixed, while the angle of diffraction, θ, and d are the variables. In a TOF experiment, θ is fixed and the variables are d and the wavelength of the neutron. The relationship between d-spacing and TOF is linear as it is derived from the combination of the de Broglie relationship (Eqn. 2.20) and Bragg's law (Eqn. 2.2):

$$\lambda = \frac{h}{m_n v_n} = 2dsin\theta \tag{2.21}$$

In a TOF experiment, the velocity can be considered a function of the the primary

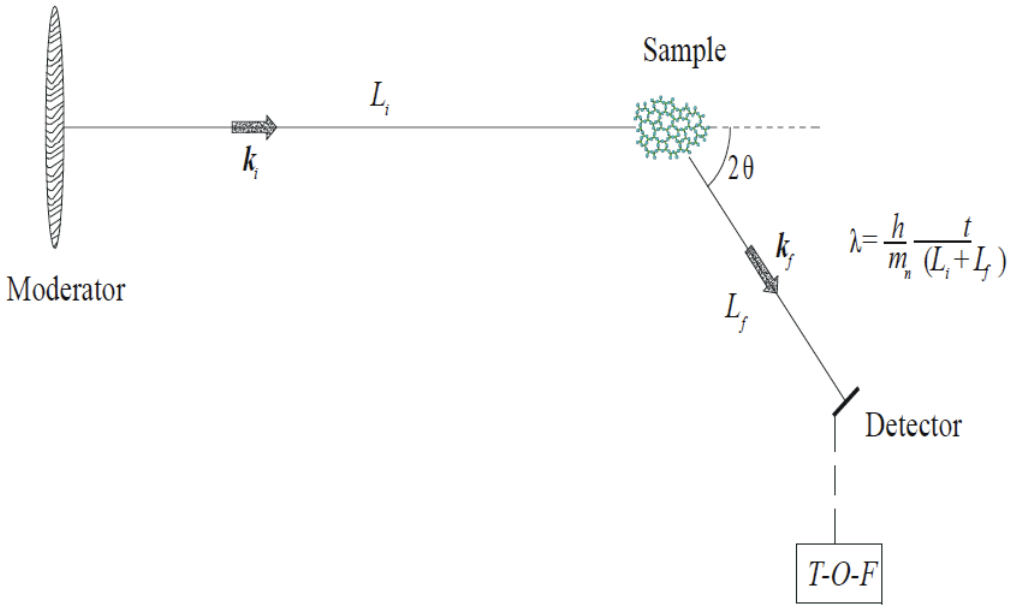

Fig. 2.5: Schematic of a neutron diffractometer for a pulsed neutron source

flight path distance (the distance from moderator to the sample, L_i), and of the secondary flight path distance (the distance from the sample to the detector, L_f) and of their respective flight times, t_i and t_f. By substitution of these variables in Eqn. 2.21:

$$\frac{h}{m_n}\left[\frac{t_i+t_f}{L_i+L_f}\right] = 2dsin\theta \tag{2.22}$$

For a total neutron flight path $L_i + L_f = L$ and a total time of flight $t_i + t_f = t$ then:

$$t = 2dL\left(\frac{m_n}{h}\right)sin\theta \tag{2.23}$$

Eqn. 2.23 shows the proportionality between t and d.

The schematic of a typical neutron diffractometer at a pulsed neutron source is shown in Fig. 2.5.

Instrumentation

For this work TOF data were collected on the High Resolution Powder Diffractometer (HRPD). HRPD is the highest resolution powder diffractometer in the world with a resolution of $\Delta d/d$ = 4-5 $\times$ 10^{-4}. An array of zinc sulphide scintillation detectors at fixed scattering angles of 160° $\leq$ 2θ $\leq$176° forms the backscattering bank. As a re-

sult of the instrument path length of 95 m, which gives long time of flight, the highest resolution for the HRPD is available in the d-spacing range of 0.6-4.6 $\AA$. Collection times are, however, rather long (8-12) hours, as the beam line only uses one in five of the pulses from the source to avoid overlap. This instrument is ideal for the study of complicated structures, and was designed for materials with large cell volumes up to 2500 $\AA^3$). In this work high-resolution data were required to accurately determine the atomic positions for the pyrochlore phases investigated in Chapter 7 and to investigate possible phase changes. The samples were loaded into a vanadium can which is mounted within an evacuated sample tank before being exposed to the neutron beam. It is also possible to mount specialised sample environments within the sample tank, such as a furnace and a cryostat. The furnace allows the collection of data up to 1073 K where the cryostat uses liquid helium to operate down to a base temperature of $\sim$ 2 K.

2.3.3 Thermogravimetric Analysis (TGA)

Thermal analysis of samples in this work was performed using a Polymer Laboratories STA-1500 simultaneous thermal analysis system. Thermogravimetric analysis (TGA) and differential thermal analysis (DTA) can be performed simultaneously.

TGA measures the mass of a pre-weighed sample as a function of temperature.Typically a small amount of sample is heated at a ramp rate of 1-20 $^\circ$ per minute up to a maximum of 1500° C. The experiment can be conducted in air or in a controlled atmosphere. This technique is particularly useful for studying transitions that involve a change in mass, such as the dehydration or decomposition of a sample.

To identify those transitions, such as phase changes, that do not result in a change of mass, DTA can be used in conjunction with TGA. In a DTA experiment the sample is heated along with a thermally inert standard, usually alumina. The temperatures of both are recorded, the rate of change of which will be identical if no thermal event, such as a phase change is happening to the sample. If a decomposition or phase change occurs then the temperature will differ. An exothermic process will give the sample a higher temperature than the reference, whereas for an endothermic transition it will be lower. Data can also be collected as the sample cools to see if any observed thermal events are reversible.

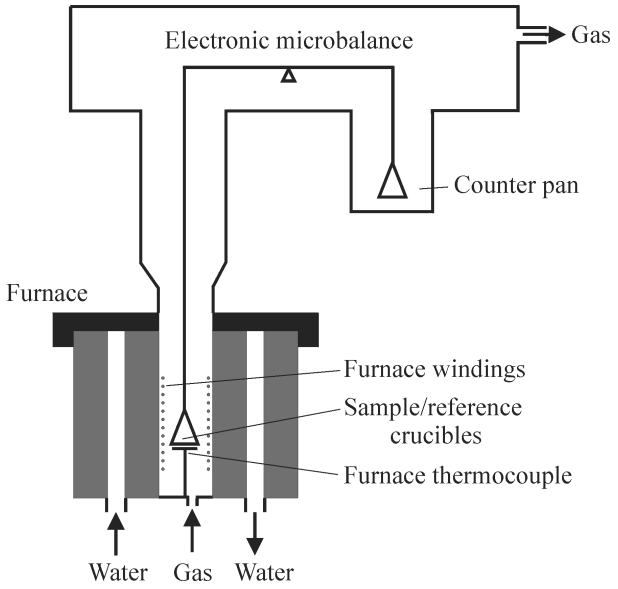

Fig. 2.6: Schematic representation of the STA-1500 instrument

2.3.4 *Energy Dispersive Spectroscopy*

Energy Dispersive X-Ray Spectroscopy (EDX) were carried out on a JEOL JSM 5910 Scanning Electron Microscope fitted with an Oxford Instruments Inca Energy 300 Energy-Dispersive X-ray Spectrometry analysis system. The principle on which EDX is based is the same as SEM.

The acceleration of electrons over a potential gives a beam of monochromatic electron according to:

$$\lambda \left[\frac{1.5}{(V + 10^{-6}V^2)} \right]^{1/2} nm \tag{2.24}$$

where V is the accelerating voltage.

The incident high-energy electron beam can interact with the sample elastically or inelastically. Elastically scattered electrons leave with the same energy as the incident electron. Inelastic scattering will leave the electrons with a different energy after interacting with atoms within the sample, generating a range of signals.

In SEM, the three signals that provide the majority of the information come from the backscattered electrons and X-rays. The secondary electrons leaving the sample have a relatively low energy, below 50eV, and can be used to create an image of the surface. The backscattered electrons keep almost all the energy upon interaction with the sample and can be used for imaging or diffraction experiments. The morphology

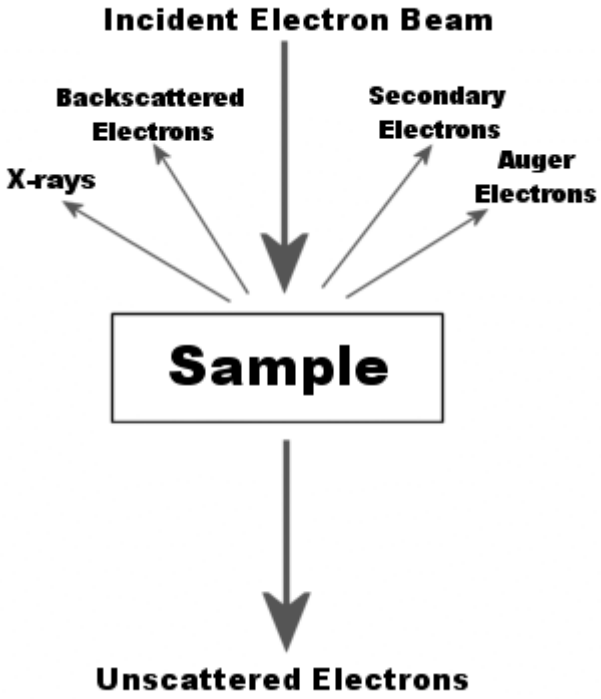

Fig. 2.7: Typical interaction-scattering situation arising during SEM/EDX experiments.

of the sample is also very important and will determine the contrast that is seen in the image.

In some cases the incident electron beam will remove a core electron from an atom in the sample, which upon relaxation will emit either an X-ray photon or an Auger electron. These are both characteristic of the atom and can be used for EDX or Auger electron spectroscopy (AES). By detecting and measuring the energy of these X-rays, elemental analysis, or EDS, data can be collected. It is also possible to use the emitted X-rays to form maps or line profiles, which show the elemental distribution in the surface of a sample. These signals are produced by the reflection of high energy electrons and are a consequence of the energy exchange between the electron beam and the sample. It is the detection of specific signals which produces an image of the sample and also the elemental composition of the sample.

EDX is generally carried out with a sampling depth of 1-2 μm. This technique can provide rapid qualitative analysis of the elements which are present within a sample although, if the sample does not contain elements lighter than sodium or elements that have very similar X-ray energies, it can also quantitatively analyse the elemental

composition of the sample. If quantitative results are possible, the percentage weight of each element present is given in the EDX data, which may be used to study the structural formula of a material.

2.3.5 VSM

The magnetic properties of a number of the materials described in the course of this work were characterised using the technique of vibrating sample magnetometry. The magnetic data used in the following chapters were collected by Dr. E. Young (Chapter 3 and Chapter 4) and by Mr. Charles Simon (Chapter 5). Heat capacity (HC) measurements were collected on a Quantum Design Physical Property Measurements System. The sample was mixed with a small amount of n-grease and placed in PVC sleeving with nylon end caps to exclude moisture. The temperature dependent contribution of the n-grease to the HC was subtracted by mass. VSM measurements were collected at 10 Oersted, in the Field Cooled (FC) condition. The data obtained reveal the magnetic behaviour of the material investigated, *i.e.* ferromagnetic, antiferromagnetic, paramagnetic or superconductivity. For paramagnetic materials, the molar magnetic susceptibility, χ (a parameter related to the number of unpaired electrons present within the compounds), can be obtained using the Curie-Weiss equation:

$$\chi = \frac{C}{(T-\theta)} \tag{2.25}$$

C is the Curie constant, θ is the Weiss constant and T is the temperature. This equation can also be written as:

$$\chi = \frac{N_A \mu_B^2 \mu_{eff}^2}{3K_B(T-\theta)} \tag{2.26}$$

where N_A is the Avogadro number, μ_B the Bohr magneton, μ_{eff} is the magnetic moment of the ion(s) and K_B is the Boltzmann constant. From this, the determination of the gradient of a plot of $\chi - 1$ *vs* T yield the magnetic moment μ_{eff} of the compound.

3. THE SUPERCONDUCTING FAMILY $A\mathrm{Os_2O_6}$, (A = Cs, Rb, K)

In the early 2000s, pyrochlore-containing A–Os–O materials ($A = \mathrm{Cs^+}$, $\mathrm{Rb^+}$, $\mathrm{K^+}$) attracted considerable attention as they were found to be the first members belonging to the β-pyrochlore subgroup to exhibit superconducting properties [1, 2, 3]. The composition of the pyrochlore phase was reported as $A\mathrm{Os_2O_6}$, and its structure and the study of its properties incited considerable attention and controversy in view of their interesting structural and physical phenomena; for the first time the osmium cation was observed with oxidation state of 5.5^+ on the B sites of the structure, combined with oxygen to form the pyrochlore framework, a relatively rigid framework where the alkali metal A^+ is accommodated.

Initial considerations on the compounds pointed out the dependence of the superconducting properties on the Os oxidation state that arises from the combination of $5d^3$ and $5d^2$ orbitals (for a total of two and a half electrons) and plays a leading role in dictating the electronic properties of this family. Recent low temperature studies assigned to the A cation and its strong vibrations within the voids created by the $\mathrm{OsO_6}$, the characteristic features exhibited by the family [86, 6, 87, 88]

A deep structural study started on these phases confirmed that the $\mathrm{CsOs_2O_6}$ compound behaved as a normal β-pyrochlore, although $\mathrm{RbOs_2O_6}$, from a structural point of view, reveals some features which will become more evident in $\mathrm{KOs_2O_6}$. $\mathrm{KOs_2O_6}$ appears to be quite unusual, and, indeed is the most interesting among the range of compounds investigated. These differences are quite relevant at low temperature and are often ascribed to the high motion of the potassium in the cage formed by the three dimensional rearrangement of the framework atoms [38]; this feature opens up an interesting discussion on the role played by the combination of phonon modes and electrons on the unusual $\mathrm{KOs_2O_6}$ lattice dynamic. It becomes, therefore, very important to investigate the local crystal chemistry underlying this arrangement in order to obtain insight into its effect upon the superconductive properties of Os-based pyrochlore systems. The focus of the current Chapter is upon the $A\mathrm{Os_2O_6}$ pyrochlore

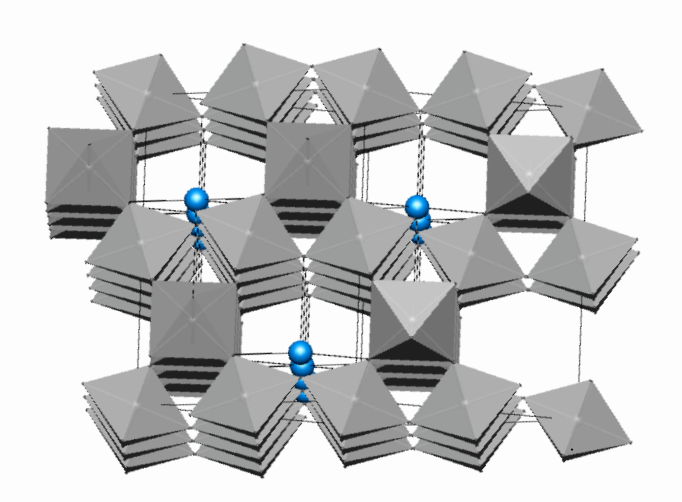

Fig. 3.1: The β-pyrochlore unit cell viewed along [011]. OsO_6 octahedra shaded grey and A ions shown in blue

compounds, their structural behaviour across a wide temperature range, and the interactions between their local crystal structure and peculiar properties manifested by them. Structural studies on the β-osmate family discussed in this Chapter include both X-ray powder diffraction (PXD) and neutron powder diffraction (PND) for cation and anion location.

3.1 General features of AOs_2O_6 pyrochlores

The structure adopted by the members of the family of superconductors AOs_2O_6 first reported by Hiroi *et al.* [1, 2, 3] is normally described in the space group $Fd\bar{3}m$ with the diffraction pattern containing no extra reflections that preclude cubic indexing. As typical examples of defect pyrochlores, AOs_2O_6 structures can be thought of as formed by nearly invariant Os_2O_6 units, composed of corner shared OsO_6 octahedra, interleaved with larger A cations, linearly coordinated by four A, which replace the A_2O' units, forming the α-type pyrochlore structure as highlighted in Fig. 3.1. The O ions of the Os_2O_6 framework form cavities connected by channels in three dimensions (Fig. 3.2). Normally O occupies the 48f sites, Os the 16c whilst the A cation is distributed along the 8b sites. In contrast to the α-pyrochlore phases, as outlined in the introductory chapter, in these β-structures the A cation is shifted from the 16d to the 8b position, replacing O', while the BO_6 framework remains unchanged.

The distribution of the alkali metals in the β lattice, $Fd\bar{3}m$, resembles the diamond

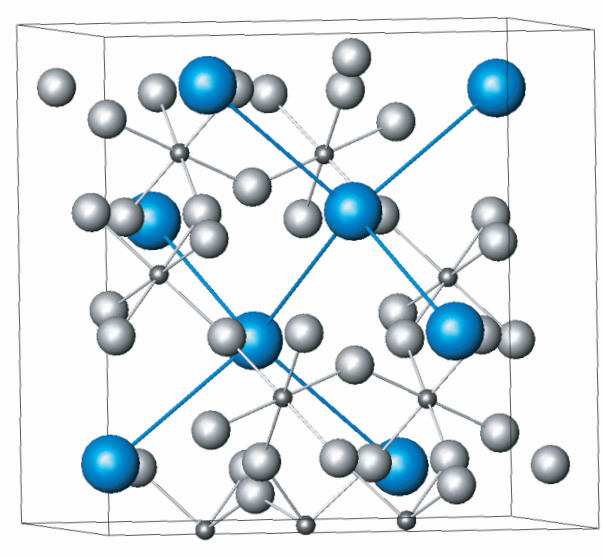

Fig. 3.2: The β-pyrochlore unit cell. Blue spheres represent the A^+ cations. Small dark spheres are Os, coordinated octahedrally by oxygen (grey larger spheres).

structure, with the A atoms occupying the diamond sublattice. Interaction between the atoms forming the diamond lattice, in the bond directions of the diamond sublattice (made possible by the channels formed by the Os–O cage) are very important and account for unconventional features in AOs_2O_6 [4].

The Os cations present slightly distorted octahedral coordination to the oxygen (because of the shift of the positional x parameter from its ideal value based on a regular octahedron) and share corners to form an Os_2O_6 three dimensional network with hexagonal holes along the [111] directions wherein K, Rb and Cs, having the right size to satisfy the charge balance which the system requires, are located.

The cubic unit cell parameter for KOs_2O_6, $RbOs_2O_6$ and $CsOs_2O_6$ follows the expected trend; it increases linearly with the A ion radius, r_R, and O x parameter, as reported in Fig. 3.3.

The smaller the ionic radius of an element, the weaker is the bond to the structure which can result in displacements towards the nearby empty sites connecting to the furthest 16*d* positions. Recent density functional calculations [38], *de facto*, showed that the bond between the alkali metal ions and the framework is relatively weak and that the effective potential they undergo is sensitive to the radius of the ion. In particular the potassium ion, due to its smaller size, can move along the the [111] directions with a maximum displacement of 1 Å. In general if the coupling between ions, lying in

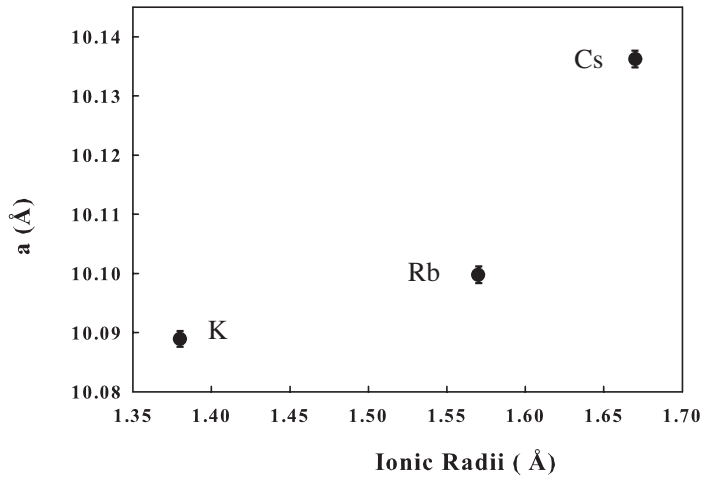

Fig. 3.3: Variation of the cubic lattice parameter of AOs_2O_6 as a function of the ionic radii of A (A = K^+, Rb^+ and Cs^+).

the cavity formed by the large framework sublattice, is rather weak, their energies are greatly influenced by large anharmonic (flat) potentials wells. As a result, the temperature dependence of their energy becomes quite different from normal lattice vibrations and can give interesting anharmonic phenomena as the ionic radius of the guest atom decreases. KOs_2O_6, especially, with the smallest alkali metal ionic radius, differs from the other two members of the β-pyrochlore osmate superconductors. It shows several interesting low temperature physical behaviours, such as a second anomaly in the specific heat [89, 90] unusual temperature dependence of the electrical resistivity [88], and uncommon pressure dependence of T_c [91], mainly associated with the active movement, called *rattling*, of the alkali metal ions in the big cavities [4].

Several studies, using a variety of methods, have ascribed this interesting low temperature lattice dynamic as a potentially important factor in the superconducting properties of KOs_2O_6 [92]. Furthermore, this is consistent with the X-ray observation of an anomalously large atomic displacement for the K ions [93, 94], and the low-frequency phonon structures seen in photoemission spectra [86]. All of these studies agree with earlier work [4] on the temperature dependence of phonon modes of AOs_2O_6 [6, 95, 96] and structural behaviour analysis reported in Sn. 3.4 [94]. They provide further information on the issues related to the vibrational dynamics of the osmates and explain some phenomena including cation displacive disorder (Sn. 3.4) and cell expansion (Sn. 3.4.1).

Recent structural work on these β-pyrochlores has concentrated on KOs_2O_6 with two groups proposing different crystal structures from single crystal X-ray data. Schuck *et al.* [71] have stated that between 100 and 400 K weak additional reflections are observed which violate $Fd\bar{3}m$ symmetry and suggest a symmetry reduction to $F\bar{4}3m$. This is in contrast to Yamaura *et al*. [93] who found no extra reflection in their data collected between 5 and 300 K (partial data sets collected using oscillation photographs only below 100 K) and concluded that the structure is best described in $Fd\bar{3}m$. Both groups have demonstrated that the modeled atomic displacement parameter (or ADP) of the potassium ion at room temperature is unusually large when compared to those of other ions. These observations agree with the band structure calculations of Kuneš *et al*. where an instability in the optic mode of the K^+ ion was found to result in the *rattling* behaviour [38] which seems also to be the cause of the second anomaly recently discovered in the KOs_2O_6 heat capacity at Tp = 7.5 K by Hiroi and co-workers [89]. The transition was believed to be associated with the rattling of K^+ located in an anharmonic potential created by the Os–O units and may have a structural origin, but neither symmetry change nor cell doubling was detected in that work. The previous studies of the thermal dependence of the structures of AOs_2O_6 phases were all undertaken using single crystal X-ray diffraction with the limitations inherent in that method. These include the relative insensitivity to light atom positions and difficulties in determining accurate and precise lattice parameters; furthermore, very low temperature studies, below 20 K, are problematic with X-rays due to absorption by the cryogenic equipment.

The above considerations represent a starting point for studies carried out in the present chapter which were undertaken with the threefold objective of i) searching for symmetry reduction as reported for the related KOs_2O_6 phase (Sn. 3.3), ii) investigating the unusually high ADP for A-type cation rubidium in $RbOs_2O_6$ and potassium in KOs_2O_6, as reported by Yamaura *et al.* [93] (Sn. 3.4) and iii) determining precisely the structure of a β-pyrochlore below its superconducting critical temperature (Sn. 3.4, Sn. 3.4.1). In order to answer the various issues associated with the structures of these materials as a function of temperature, a detailed powder neutron diffraction study of each of the materials KOs_2O_6, $RbOs_2O_6$, and $CsOs_2O_6$ has been undertaken between 1.5 and 500 K 350 K and will be discussed in the following sections.

3.2 Experimental

Polycrystalline KOs_2O_6 was prepared by reaction of appropriate quantities of high-purity OsO_2 (0.862 g, Alfa aesar, 99.99%) and KO_2 (0.138 g, Aldrich 99.99%). These materials were ground together thoroughly in a dry box, pressed into a pellet, and placed into a silica ampoule together with a small gold tube containing 0.13 g of Ag_2O to create an oxidizing atmosphere. The ampoule was sealed under vacuum and heated to 723 K at a rate of 100 K h^{-1} and maintained at this temperature for 16 h before furnace cooling. Bulk KOs_2O_6 can be reliably synthesised using this method but is not single phase and contains small amounts of OsO_2 ($\sim$5%), $KOsO_4$ ($\sim$20%), and OsO_4 (visibly observed as coating the wall of the tube and some crystallites). OsO_4 rapidly evaporates from the product at room temperature in a stream of air, though caution is required, as OsO_4 is very toxic by inhalation, ingestion, or skin contact. $RbOs_2O_6$ was prepared by reaction of RbO_2 (0.41 g, synthesized from Rb metal and O_2 in liquid ammonia) and OsO_2 (1.59 g, Alfa aesar, 99.99%) at an elevated oxygen pressure by inclusion of 0.13 g Ag_2O; the silica tube was heated at 100 K h^{-1} to 873 K and maintained at this temperature for 14 h before furnace cooling. $CsOs_2O_6$ was prepared by reaction of CsO_2 (0.135 g, synthesized from Cs metal and O_2 in liquid ammonia) and OsO_2 (0.365 g, Alfa aesar, 99.99%) in the presence of 0.13 g of Ag_2O. The silica tube was heated at 100 K h^{-1} to 943 K and maintained at this temperature for 14 h before furnace cooling. All $AOsO_4$ phases, A = K^+, Rb^+, and Cs^+, could be removed from the mixed-phase products by washing with water or other polar solvents, though exposure to water, air, or wet solvents can results in the rapid, reversible, uptake of water into the KOs_2O_6 pyrochlore structure channels (Chapter 5). For A = Rb^+ and Cs^+, no uptake of water occurs. In order to produce a near pure polycrystalline sample of each AOs_2O_6 phase, the products from the sealed tube reactions were washed with distilled water and then dried in a nitrogen atmosphere at 600 K for 12 h; the products from such washing-drying protocols have been shown to be structurally identical to pyrochlore materials handled only in dry conditions. [97]. Following this procedure, all handling was undertaken in strictly dry 2 ppm H_2O atmospheres. The 2-3 g samples of each osmate pyrochlore, were obtained by combining the products from several syntheses under identical conditions and used for powder neutron diffraction studies.

Preliminary PXD inspection at room temperature considered the description in the $Fd\bar{3}$m space group, with the origin at *3m*. PXD data for all samples were collected as

described in Sn. 4.1.3, over a 2 θ range of 10°–110° with a step size of 0.02°. Profiles indicated that for all the washed and dried samples the main observed peaks could be indexed using a cubic cell with $a \sim 10$ Å with the space group $Fd\bar{3}$m; a few very weak peaks (I/I° = 0.04) could be assigned to OsO_2.

A more complete description of the experimental set up used to characterise each feature investigated are reported at beginning of the corresponding sections.

3.3 Space Group Investigation

As mentioned in Sn. 3.1, the space group of KOs_2O_6 has been the focus of debate in the literature, with Schuck *et al.* [71] stating that weak additional reflections violate $Fd\bar{3}m$ symmetry and suggesting a symmetry reduction to $F\bar{4}3m$ and Yamaura *et al.* [93] who found no extra reflections in their data collected between 5 and 300 K and concluded that the structure is best described in $Fd\bar{3}m$.

In order to answer the questions related to the space group associated with these structures, a detailed powder neutron diffraction study was undertaken on KOs_2O_6 and $RbOs_2O_6$, between 1.5 and 350 K.

High resolution NPD was used for this study as it is far more sensitive to any small displacement in the oxygen atom positions associated with any symmetry changes. Also, data can be easily obtained below the superconducting transition and ADP extracted (for high symmetry structures where the background is well defined across the full data range) as there is no form factor contribution to the data. It is noteworthy that the previous structural work was unable to delineate any trends in bond lengths or angles with temperature [93]. Neutron diffraction data were recorded either on the high flux D20 or on the high resolution D2B diffractometer.

$RbOs_2O_6$

The first sample to be synthesised, and hence fully characterised by means of NPD, was $RbOs_2O_6$. Polycrystalline $RbOs_2O_6$ was cooled in an Orange Cryostat to 2 K and data were collected for 8 h ($\lambda = 1.59432$ Å). The sample was then heated with data sets collected at 5 K, 10 K, 20 K, 50 K (4 h each), 100 K, 200 K (3 h each) and finally 300 K (8 h). All data were refined using the GSAS/EXPGUI suite of programs [84, 98].

The initial model investigated was the standard β-pyrochlore description in $Fd\bar{3}$m with Os (0, 0, 0), Rb ($\frac{3}{8}$, $\frac{3}{8}$, $\frac{3}{8}$) and O (x, $\frac{1}{8}$, $\frac{1}{8}$). Inspection of the background showed some weak oscillations possibly due to a small amorphous component, such as could

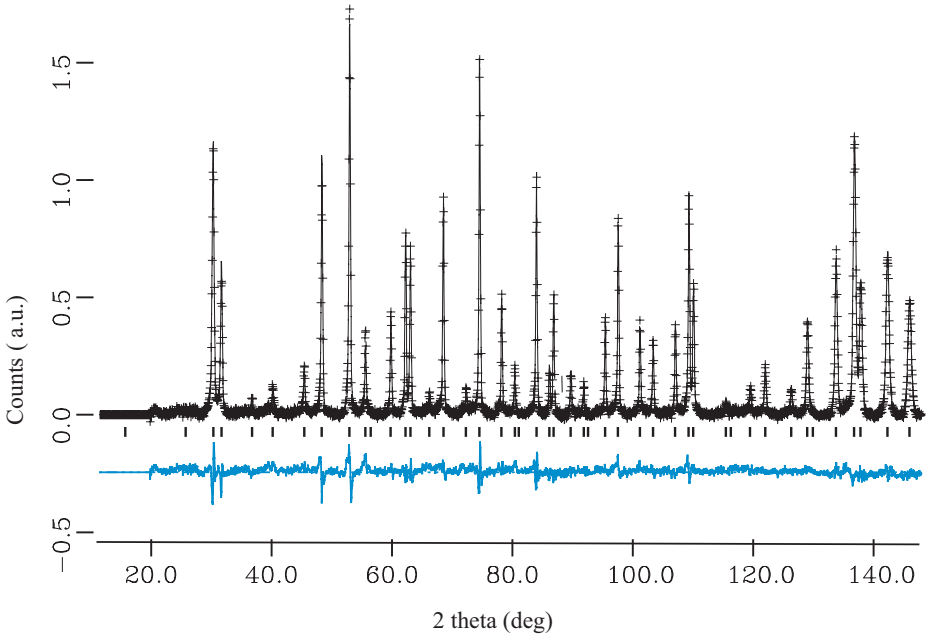

Fig. 3.4: Final profile fit achieved in $Fd\bar{3}m$ to the data collected at 2K from $RbOs_2O_6$. Crosses represent observed data, upper continuous line the calculated profile and lower continuous line the difference. Tick marks show the reflection positions.

originate through contamination with particles of the shattered silica ampoules, and it was therefore decided to determine the background manually. 105 background points were selected in the range 20–150° 2θ. These points were then fitted with a 30 term, shifted Chebyschev function. In order to ensure consistency, the same 2θ background points were used for data collected at each temperature. The structure refinement in $Fd\bar{3}m$ using the 2 K data proceeded smoothly, with the introduction of the cell constant, peak shape coefficients, atom positions and anisotropic atomic displacement parameters (AADPs). Finally, variation of atomic site occupancies revealed no statistically significant deviations supporting the expected $RbOs_2O_6$ stoichiometry. The profile fit achieved is shown diagrammatically in Fig. 3.4.

Data collected at all higher temperatures were analysed sequentially using the preceding refinement as the starting point for the next temperature. Careful inspection of the diffraction profiles showed no obvious extra reflections or tetragonal peak splitting, though in order to investigate the possible symmetry reduction, as reported for KOs_2O_6 by Schuck *et al.* [99], comparative refinements were carried out, initially on the 2 K data set, using models in $F\bar{4}3m$, $F23$, $I\bar{4}m2$ and $I4_122$. Results, in terms of the

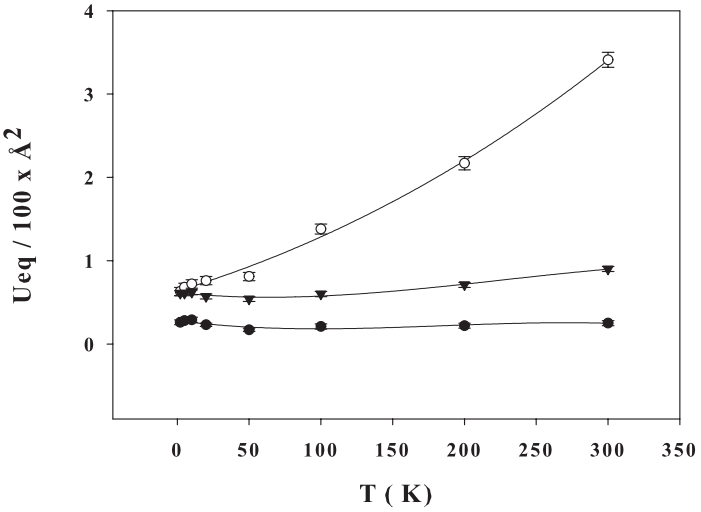

Fig. 3.5: Evolution of the U_{eq} isotropic atomic displacement parameters with temperature of Rb (circle), Os (filled circle) and O (black triangle) in $RbOs_2O_6$

Tab. 3.1: Summary of profile fits achieved as a function of space group choice, 2 K data.

Space Group	R_p	R_{wp}	χ^2	Total No. of Parameters
$Fd\bar{3}m$	4.56	5.83	1.04	4
$F\bar{4}3m$	4.44	5.72	0.99	8
$I\bar{4}m2$	4.88	6.13	1.15	13
$F23$	4.45	5.70	0.99	8
$I4_122$	4.42	5.62	0.96	9

profile fits achieved and numbers of refined parameters obtained, are summarised in Table 3.1. Note that χ^2 values close to, and just below, unity were obtained; these unusually small values result, in part, from fitting accurately a relatively high background, originating from the silica contaminant across a significant part of the diffraction pattern. Modelling in $F\bar{4}3m$ produced a very slightly improved profile fit over $Fd\bar{3}m$ (R_{wp} decreasing from 5.83 to 5.72%) at the expense of introducing four additional atomic variables, see Table 3.3.

In order to investigate this space group further profiles were inspected for evidence of intensity associated with the additional allowed reflections (*0 k l: k + l* $\neq$ *4n*: 024, 046 and *00l:l* $\neq$ *4n*: 002, 006, 00 10). No evidence of diffraction corresponding to these reflections was observed and the marginal improvement in profile fit

Tab. 3.2: Derived bond lengths (Å) and angle (°) of interest for $RbOs_2O_6$ between 2 and 300 K, $Fd\bar{3}m$.

T/K	Os–O[a]	∠ O–Os–O	∠ O–Os–O	Rb–O	Rb–O'	∠ O–Os–O
2	1.9104(5)	91.76(6)	88.24(6)	3.114(2)	3.6216(1)	138.55(9)
5	1.9110(5)	91.82(6)	88.18(6)	3.113(2)	3.6214(1)	138.47(8)
10	1.9118(5)	91.90(6)	88.10(6)	3.111(2)	3.6211(3)	138.35(8)
20	1.9111(5)	91.83(6)	88.17(6)	3.113(2)	3.6214(2)	138.45(8)
50	1.9111(5)	91.79(6)	88.21(6)	3.114(2)	3.6218(2)	138.51(8)
100	1.9110(6)	91.77(6)	88.23(6)	3.115(2)	3.6221(3)	138.54(9)
200	1.9110(6)	91.75(7)	88.25(7)	3.116(2)	3.6227(3)	138.56(10)
300	1.9114(6)	91.74(7)	88.26(7)	3.117(2)	3.6239(3)	138.58(10)

[a] Os–O distance from Os at (0,0,0) to O at (0.25 - x, $^1/_8$,$^1/_8$).

derives solely from additional flexibility in fitting some high angle reflections with the additional ADPs. Calculations of dummy histograms using the positional parameters given by Schuck *et al* [99] indicate that the additional reflections allowed in $F\bar{4}3m$ should have been observable in our data sets if this model was correct for $RbOs_2O_6$. Similarly with $F23$ and $I4_122$ the slightly improved profile fits achieved are not significant in terms of the additional number of variables. No evidence for a change in structural description from that of $Fd\bar{3}m$ was found in any of the analyses of data sets collected above 2 K, showing that $RbOs_2O_6$ adopts the same structure above and below the superconducting critical temperature. On this basis all further data sets were analysed using the description in $Fd\bar{3}m$; the results of these refinements are summarised in Table 3.3 and Table 3.4. Fig. 3.5 shows the evolution of the U_{eq} ADPs of the different ions with increasing temperature. The osmium and oxygen ADPs increase by a small amount between 2 K and room temperature (RT). Overall the oxygen ADPs increase by a factor of 1.5 times between 2 K and RT, while the values for the osmium site barely change and remain within the estimated standard deviations (esds) over the same temperature range. In sharp contrast, the rubidium ADP increases from 0.63 to 3.14; a 5.5 fold increase. This behaviour reflects that observed by both Schuck *et al.* [71] and Yamaura *et al.* [93] for the potassium analogue and has been interpreted in terms of a large anharmonic optic mode for this ion [38].

Tab. 3.3: Refined lattice parameters, atomic coordinates and ADPs and profile fit factors for $RbOs_2O_6$ between 2 and 300 K, $Fd\bar{3}m$. Estimated standard deviations in parentheses

T(K)	a (Å)	O_x	Rb $U_{11}\times$ 100 Å^2	Os $U_{11}\times$ 100 Å^2	Os $U_{12}\times$ 100 Å^2	O $U_{11}\times$ 100 Å^2	O $U_{22}\times$ 100 Å^2	Os U_{23} 100 Å^2	R_p	R_{wp}	χ^2
2	10.10786(5)	0.3169(2)	0.63(5)	0.26(3)	0.23(3)	0.50(6)	0.68(4)	-0.09(6)	4.48	5.75	1.01
5	10.10789 (5)	0.3170 (1)	0.68(5)	0.28(3)	0.19(3)	0.54(6)	0.64(4)	-0.08(6)	4.30	5.62	0.96
10	10.10794(5)	0.3172(1)	0.72(5)	0.29(3)	0.15(3)	0.53(6)	0.67(4)	-0.18(6)	4.41	5.72	1.00
20	10.10815 (5)	0.3171(1)	0.76(5)	0.23 (2)	0.20(3)	0.48(6)	0.62(4)	-0.18(6)	4.29	5.60	0.96
50	10.10857 (5)	0.3170(1)	0.81(5)	0.17(3)	0.17(3)	0.43(6)	0.60(4)	-0.07(5)	4.35	5.63	0.96
100	10.10931(5)	0.3169(2)	1.38(6)	0.21(3)	0.17(3)	0.61	0.60(4)	0.02(6)	4.54	5.83	0.63
200	10.11085(6)	0.3169(2)	2.17(8)	0.22(3)	0.19(3)	0.62(8)	0.76(5)	0.01(7)	5.19	6.55	0.81
300	10.11393(5)	0.3168(2)	3.41(9)	0.25(3)	-0.01(3)	0.94(8)	0.88(5)	0.16(6)	4.73	6.08	1.19

[a] Rb: $U_{12} = U_{22} = U_{33}.U_{12}, U_{13}, U_{23} = 0, Os : U_{11} = U_{22} = U_{33}.U_{12} = U_{13} = U_{23}, O : U_{22} = U_{33} \neq U11.U12, U13 = 0$.

KOs_2O_6

A similar study to that conducted on $RbOs_2O_6$ was performed on KOs_2O_6. The intention was, again, to investigate the models developed by Schuck *et al.* [71], in $F\bar{4}3m$, from single crystal X-ray diffraction data in the temperature range of 80–400 K and, furthermore, to analyse in detail the 1.5 K data set with the aim of finding evidence for a possible low temperature structural transition as proposed by Hiroi *et al.* [89]. Analysis of the structure of KOs_2O_6 required neutron diffraction and data were recorded in the 1.5–500 K temperature range using a cryofurnace. An initial data set was collected in the $2\theta = 10°$–$150°$ range with wavelength $\lambda = 1.87$ Å; thereafter, a continuous ramp rate of between 1 and 2 K min^{-1} was used between 10 and 500 K with data collections in 1 min blocks. A second set of data was collected between 2 and 12 K with a 0.2 K min^{-1} ramp rate.

Initial data analysis for the material was undertaken in the $Fd\bar{3}m$ space group using the standard β-pyrochlore description. Least squares refinement gave a good fit to the data, reported in Fig. 3.6, and allowed extraction of the structural model independent parameters (see Table 3.4), identified as model 1. Fig. 3.7 shows the plot of the lattice parameters as a function of temperature for KOs_2O_6. Although absolute values were in accordance with previous studies [1], it was soon noticed that the small thermal expansion of the cell was not perfectly in accordance with simple Grüneisen theory [100]. This behaviour will be investigated in more detail in Sn. 3.4.

Although the $Fd\bar{3}m$ group was found to be appropriate to fit all the cell reflections, additional models in the $F\bar{4}3m$ space group [71] were also tested using an ordered potassium ion distribution (model 2) and then allowing one potassium ion (which showed a large ADP when on a special site) to become displaced (model 3), as often it is found high ADPs to be associated with local static displacements.

For both refinements simultaneously varying the positional and atomic displacement parameters produced an unstable refinement, so these were varied only in alternate cycles. Table 3.5 and Table 3.6 summarise the results of these analyses. For the model of Schuck *et al.* [71] Table 3.5, the quality of the fit to the data was similar to that obtained with the ordered $Fd\bar{3}m$ model described in Table 3.4 and with an elevated atomic displacement parameter for the potassium ion on the 4c site. However the increased number of refinable parameters and instability in the refinement does not

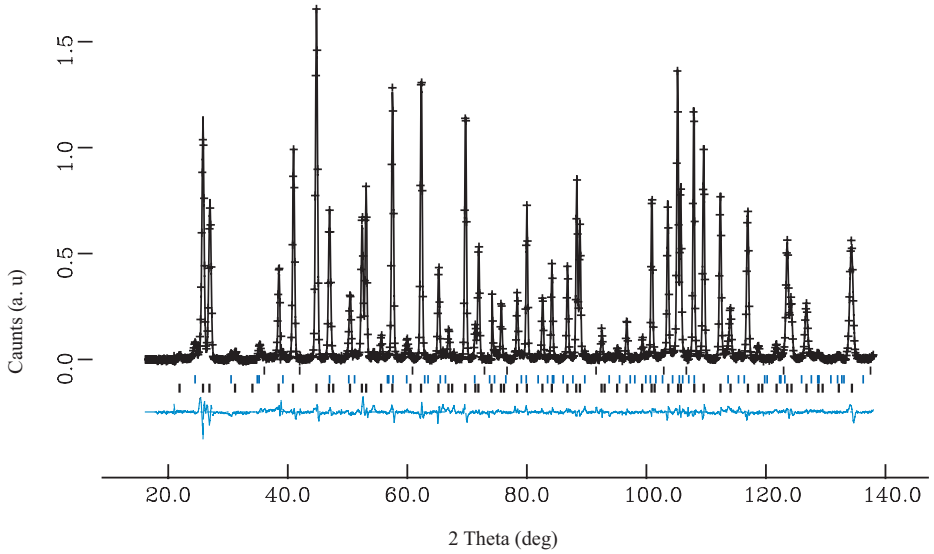

Fig. 3.6: Profile fit obtained to the 1.5 K data set obtained from KOs_2O_6 data set (model 1). Cross marks are observed intensities, upper continuous line is the calculated profile, and lower continuous line is the difference. Tick marks, from top to bottom, are calculated reflection positions for vanadium (sample can), OsO_2 and KOs_2O_6 respectively.

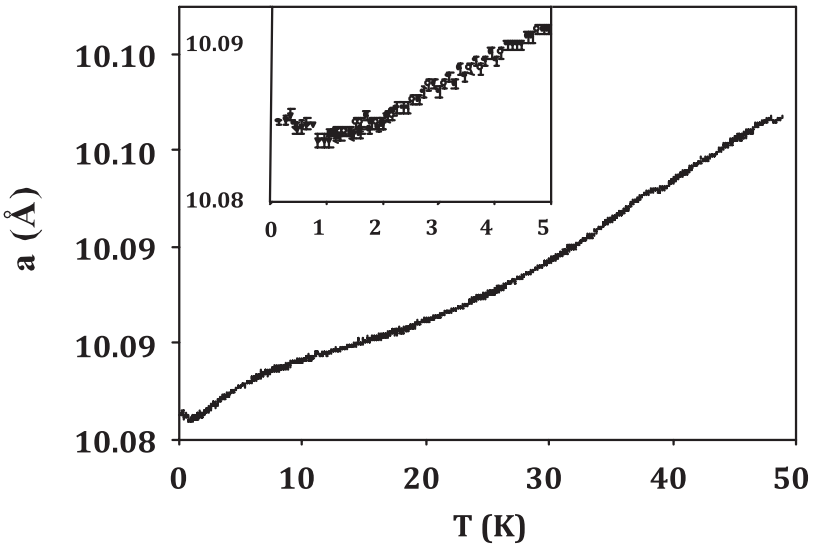

Fig. 3.7: Variation of the lattice parameter as a function of temperature for KOs_2O_6; the inset is the expanded low temperature regime. Data collections in 10–500 K run (as open circles) longer period, low-temperature, below 10 K, data collections (as filled circles)and second data collection 2–12 K (as filled triangles). The curve fitted to 10–500 K data represents the best fit using a Grüneisen-type behaviour.

Tab. 3.4: 1.5 K structure model 1 for KOs_2O_6 and extracted key distances and angles a=10.0889(1)Å, $Fd\bar{3}m$, $R_{wp} = 4.26\%$, $R_p = 3.03\%$. K–O × 12 [3.0915(9)]Å. Os–O × 6 [1.9092(3)Å], and Os–O–Os [137.81(5)°]

name/site	x	y	z	$U_i/U_e \times 100Å^2$	site occupancy
K 8b	$^3/_8$	$^3/_8$	$^3/_8$	2.95(11)	1
Os 16c	0	0	0	1.16(3)	1.0
O1 48f	0.31820(9)	$^1/_8$	$^1/_8$	1.40(4)	1.0

Tab. 3.5: 1.5 K structure, model 2, for KOs_2O_6, a = 10.0889(1)Å, $F\bar{4}3m$, ordered potassium ions. $R_{wp} = 4.29\%$, $R_p = 3.04\%$

name/site	x	y	z	$U_i/U_e \times 100Å^2$	site occupancy
K 4c	0.25	0.25	0.25	5.32	1.0
K 8b	0.5	0.5	0.5	1.08	1.0
Os 16e	0.8766(3)	0.8766(3)	0.8766(3)	1.20	1.0
O1 24f	0.1920(6)	0.0	0.0	1.85	1.0
O1 24g	0.5554(6)	0.25	0.25	0.98	1.0

support this model over model 1 investigated within $Fd\bar{3}m$.

Disordering of the potassium from 4c, Table 3.5, to 16e Table 3.6 (model 3) resulted in a more reasonable ADP for this ion but no improvement in profile fit. Overall the absence of reflections requiring a reduction in symmetry to $F\bar{4}3m$ and the inability to improve the profile fit by modeling in this space group supports $Fd\bar{3}$m as the best description of the KOs_2O_6 structure at low temperature.

Fig. 3.8 shows the experimental profiles between 67° and 69° 2θ for the 1.5 K data

Tab. 3.6: 1.5 K structure model 3 for KOs_2O_6, a = 10.0889(1)Å, $F\bar{4}3m$, disordered potassium ions. $R_{wp} = 4.32\%$, $R_p = 3.07\%$

name/site	x	y	z	$U_i/U_e \times 100Å^2$	site occupancy
K 16e	0.2678(7)	0.2678(7)	0.2678(7)	3.12	0.25
K 8b	0.5	0.5	0.5	0.6	1.0
Os 16e	0.8768(3)	0.8768(3)	0.8768(3)	1.21	1.0
O1 24f	0.1929(6)	0.0	0.0	1.62	1.0
O1 24g	0.5561(5)	0.25	0.25	1.26	1.0

and the data between 10 and 475 (summed every 25 K). The inset shows the calculated profile in this region based on the model and coordinates previously proposed [99]. All data, experimental and theoretical, were scaled so that the adjacent reflection at 2θ = 67°, (hkl = 531), is of identical intensity. As can be seen from these profiles, there is no evidence of a concerted phase change or lowering of symmetry from $Fd\bar{3}m$ to $F\bar{4}3m$. Indeed, Le Bail extractions, varying just profile parameters, carried out on data sets collected at between 1.5 and 475 K in $Fd\bar{3}m$ and $F\bar{4}3m$ showed no significant variation in the extracted profile fit factors confirming that the space group needed to describe the structure across this whole temperature range remains unchanged. No difference in the extracted Le Bail profile fit parameters between $F\bar{4}3m$ and $Fd\bar{3}m$ was observed at any temperature.

3.4 Thermal Evolution of the Cell and Cation Displacement in AOs_2O_6

PND data analysis for all three materials was undertaken in the $Fd\bar{3}m$ space group using the standard β-pyrochlore description. Least squares refinement gave a good fit to the data and allowed extraction of the structural model independent parameters such as the lattice parameter. Fig. 3.7, Fig. 3.9, Fig. 3.10 show plots of the lattice parameters as a function of temperature for the three materials AOs_2O_6, A= K^+, Rb^+, and Cs^+. Structure refinements of $RbOs_2O_6$ and KOs_2O_6 from neutron diffraction data, described in the previous section, showed that cubic lattice symmetry is preserved down to 2 K, but the cell parameters reveal an unexpected and remarkable change of behaviour in the region 5–20 K. From all the data collected, the unit cell shows a positive thermal expansion above T = 20 K but below this, the cell shrinks with increasing temperature (Fig. 3.7, Fig. 3.9). This negative volume expansion was not seen for $CsOs_2O_6$ and is unprecedented in this family of oxides. No unusual structural changes in the metal-to-oxygen bond distances are observed, and it is thought that the anomalous expansion is associated either with local, static displacements of the alkali metal cation, which occur below 80 K, or with low phonon modes recently appeared in literature [6, 95]. The behaviour is associated with the size of the A cation (Fig. 3.11), and became more pronounced for A = K^+, than for A = Rb^+.

Further analysis of the diffraction data from KOs_2O_6 therefore centred on possible origins of this effect and all the further modeling was undertaken in the conventional pyrochlore space group. At the higher temperatures of 100–500 K, with high thermal

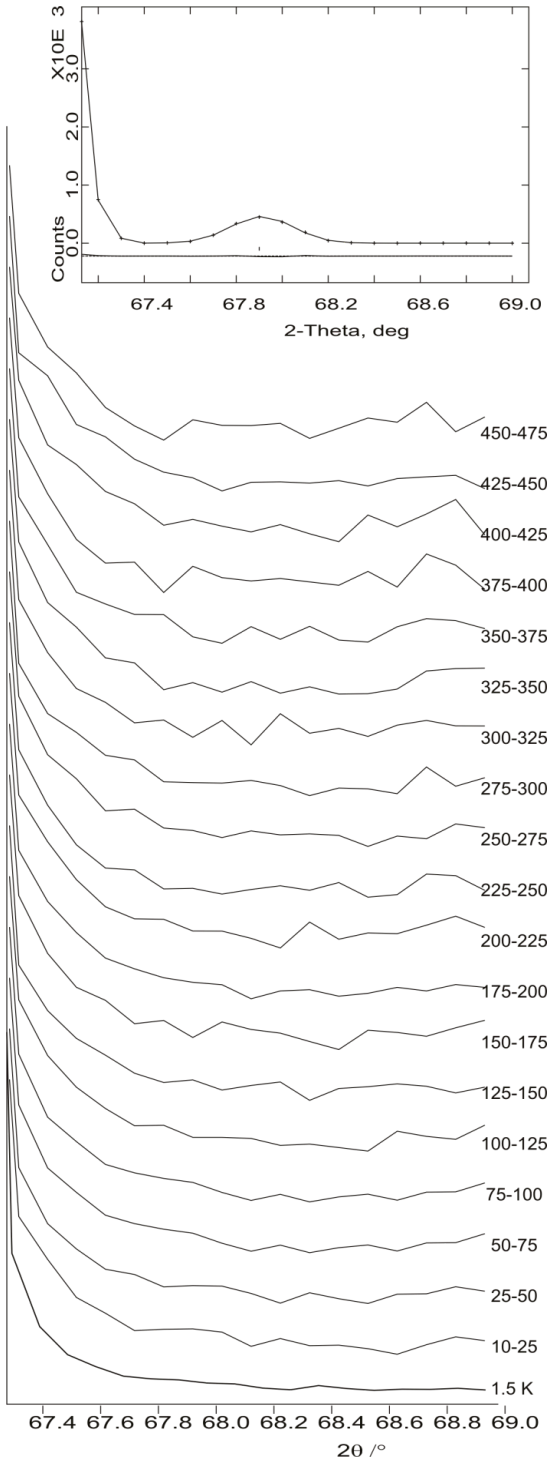

Fig. 3.8: Powder neutron diffraction data from KOs_2O_6 in the angular range of 67.1°–69° 2θ corresponding to the expected position of the (600) reflection in $F\bar{4}3m$. The inset shows the calculated powder pattern in this region based on the model of Schuck *et al* [71].

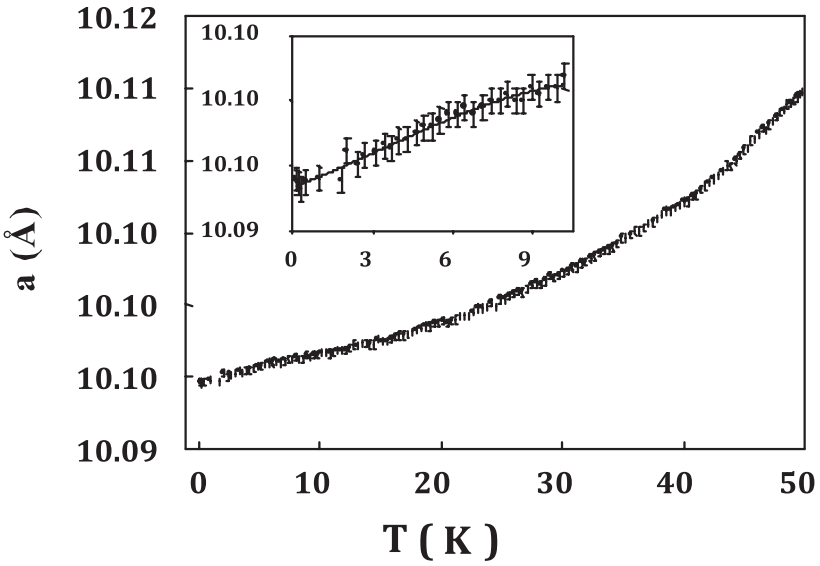

Fig. 3.9: Variation of the lattice parameter as a function of temperature for $RbOs_2O_6$. The inset is the expanded low temperature regime.

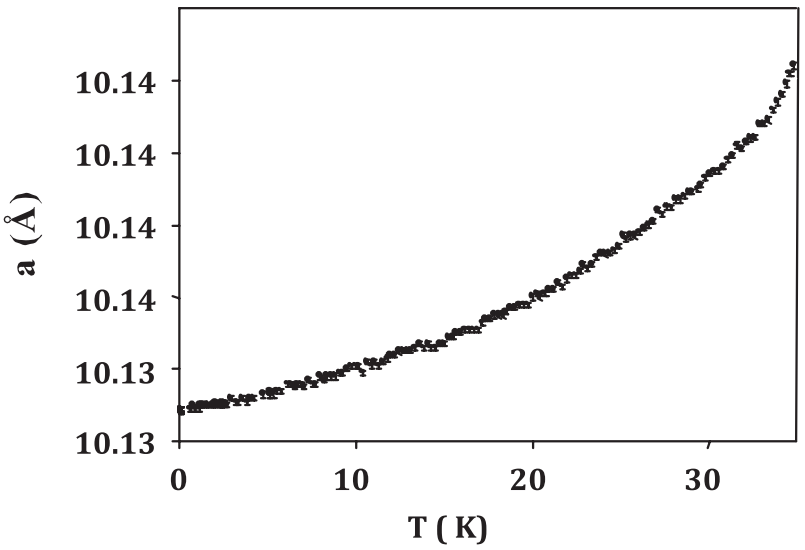

Fig. 3.10: Variation of the lattice parameter as a function of temperature for $CsOs_2O_6$.

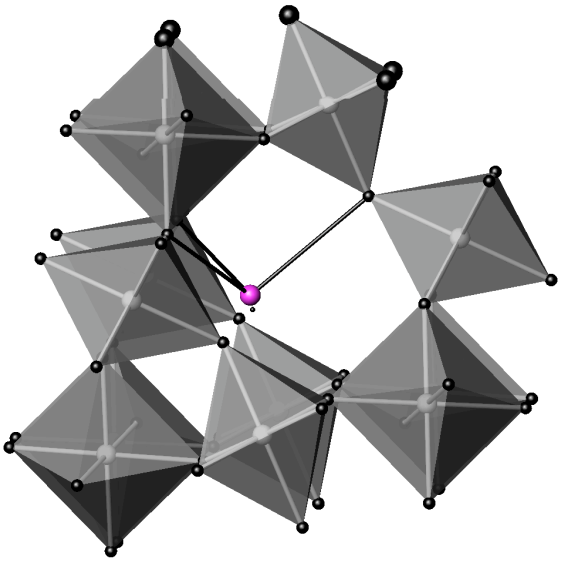

Fig. 3.11: Structure model demonstrating the displacement of the potassium ion (shaded sphere) with coordination to oxygen shown from the central 8*b* site (•). Shaded polyhedra are OsO_6.

motion of the species present, the profiles were best fitted using the standard $Fd\bar{3}$m pyrochlore description (denoted as model 1, Sn. 3.3) with a high atomic displacement parameter for potassium which represents very well the thermal motion of the potassium ion within the large cavity surrounding 8*b*, Table 3.4. At low temperatures, therefore, the best model involved a static disordered displacement of the potassium ion from 8*b* to 32*e* with a site occupancy of $\frac{1}{4}$. In this model (model 4), Table 3.7 summarises the coordinate description showing a significant displacement (magnitude of 0.23 *Å*) of the potassium ion from the central position Fig. 3.11; on this site, this also results in a much lower ADP for the ion. Comparison of the profile fits achieved with models 1 and 4 to the 1.5 K data set showed a small improvement in the profile fit factors (Table 3.4 and Table 3.7). It should be noted that these two models are effectively similar representation of the scattering density of KOs_2O_6 at low temperature. The stable refinement of a significant displacement of the potassium ion, and a reduced far more realistic atomic displacement parameter for potassium supports model 4 as a better representation of KOs_2O_6 at low temperature. Fig. 3.12 shows the final, excellent fit achieved to the diffraction data profile.

In order to investigate any change in the suitability of these models as a function of temperature, a SEQGSAS [84] refinement of the structure using the individual data

Tab. 3.7: 1.5 K structure model 4 for KOs_2O_6 and extracted key distances and angles a =10.0889(1)Å, $Fd\bar{3}m$, R_{wp}= 4.13 %, R_p = 2.88 % K–O × 6 [2.941(18)×3, 3.26(22)×3, and 3.361(31) ×3 Å], Os–O ×6 [1.9103(2) Å, and Os–O–Os 137.86 °.

name/site	x	y	z	$U_i/U_e \times 100Å^2$	site occupancy
K 32e	0.3591(20)	0.3591(20)	0.3591(20)	0.2113	0.25
Os 16c	0	0	0	1.16(3)	1.0
O1 48f	0.31811(9)	$^1/_8$	$^1/_8$	1.38(4)	1.0

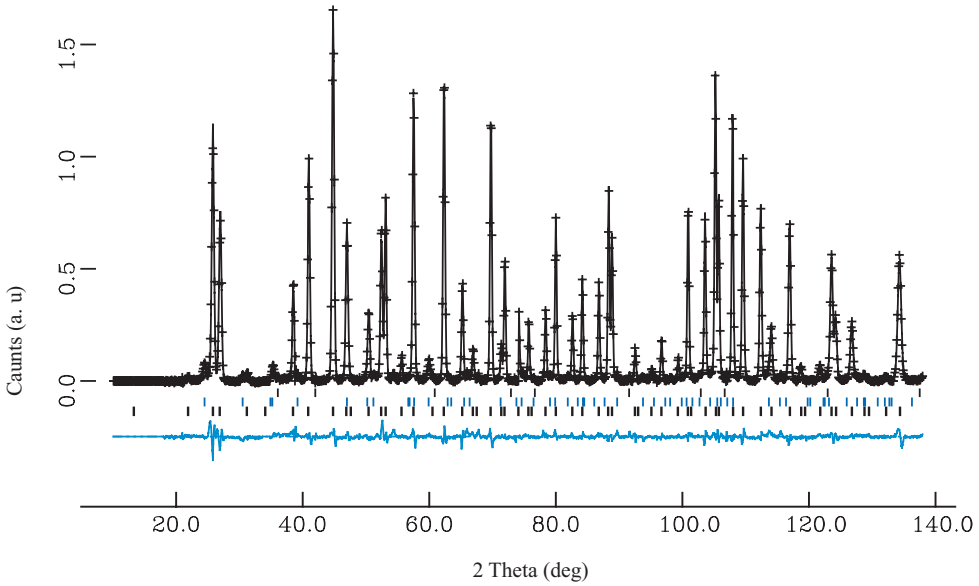

Fig. 3.12: Profile fit obtained to the 1.5 K data set obtained from KOs_2O_6 (1200 s, model 4) data set. Cross marks are observed intensities, upper continuous line is the calculated profile, and lower continuous line is the difference. Tick marks, from top to bottom, are calculated reflection positions for vanadium (sample can), OsO_2 and KOs_2O_6 respectively.

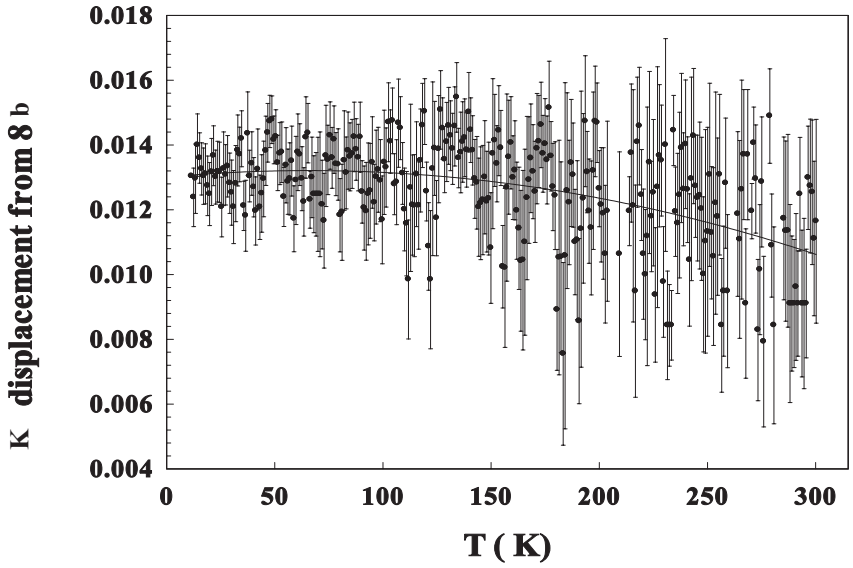

Fig. 3.13: The refined coordinate displacement of K^+ from the 8*b* site in model 4 as a function of temperature.

sets from 1.5 to 275 K was undertaken using model 4 as the starting point. Fig. 3.13 shows the extracted potassium ion displacement from the 8*b* position and Fig. 3.14 shows this ion's ADP as a function of temperature. As the temperature is raised, the magnitude of this static displacement shows a tendency to decrease with an increasing esd while the extracted atomic displacement parameter markedly increases so that structural description effectively becomes indistinguishable from model 1 above about 80 K. Indeed, for data sets collected above 80 K, model 4 could be used to fit the profiles, generating identical fit factors to model 1 with fewer refinable parameters. It is noteworthy that this change in preferred model occurs in the same temperature range where the plateau is reached in the lattice parameter variation. This implies that the confinement of the potassium ion to one side of the cavity may occur on cooling below approximately 80 K and result in a marked rapid decrease in lattice parameter. The process seems to be complete by around 10–20 K where the lattice parameter, see the inset of Fig. 3.7, levels out and then slightly expands on cooling further to 1.5 K.

For $RbOs_2O_6$, similar behaviour is observed though the deviations in the lattice parameter variation are not as strong as with the potassium analogue. The lattice parameter is again almost invariant below 10 K before an initial relatively rapid increase between 10 and 50 K; a weak plateau exists between 50 and 100 K before more normal

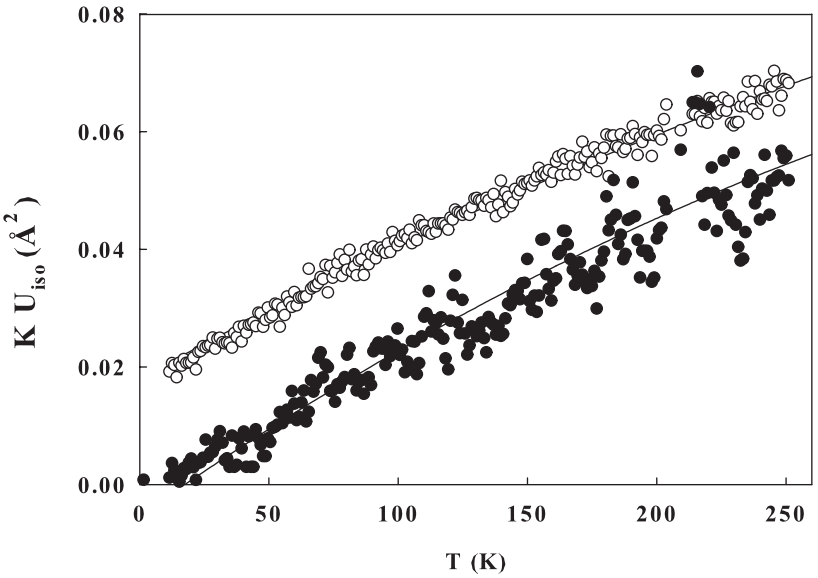

Fig. 3.14: U_i as a function of temperatures for potassium in model 1 (open circle) and model 4 (filled circle)

expansion at higher temperatures. From the study reported in Sn. 3.3, the structure of $RbOs_2O_6$ can be successfully modeled in the $Fd\bar{3}m$ description between 2 and 450 K though with a somewhat higher (compared to those of osmium and oxygen) atomic displacement parameter for rubidium. Following the observation of a refinable off-centre displacement for potassium in KOs_2O_6, we investigated whether a similar displacement could be determined for rubidium in $RbOs_2O_6$ using the data collected here at 1.5 K and in our previous D2B experiment on this compound, Sn. 3.3 [101]. Structure refinements displacing Rb to the 32*e* site (x,x,x) produced only a very marginal improvement in profile fit, a slight reduction in this atom's ADP, and a value of 0.3685 for x showing that the displacement of this species probably occurs but is not crystallographically significant in that is it is less than two esds from the central site at $x = 0.375$. However, it seems likely that the variations in lattice parameter in $RbOs_2O_6$ below 50 K result from a similar behaviour to that observed with KOs_2O_6, and localised static displacements of the rubidium ions to the 32*e* sites occur on cooling between 25 and 10 K. It is noteworthy that the temperature at which the static displacements of the A-type cation start to occur (reflected in a more rapid decrease in the lattice parameter) is lower for Rb^+ (around 50 K compared to around 80 K for K^+). The structural changes that occur in $RbOs_2O_6$ as a function of temperature are thus intermediate between those of

the potassium and cesium analogues with a weaker but observable effect below ∼50 K. Data from the A = Cs system showed typical Grüneisen-type behaviours, in excellent agreement with the value previously reported using other neutron diffraction data [3].

The behaviours of the structures of the AOs_2O_6 phases as a function of temperature reflect the ionic sizes of the A^+ ions. For A = Cs the behaviour is classical between 2 and 350 K with a variation in lattice parameter that can be well fitted using simple Grüneisen theory though with a small overall thermal expansion parameter indicative of a rigid osmium-oxygen framework. For A = K the lattice parameter behaviour as a function of temperature is much more complex indicating some structural changes on cooling from room temperature. Analysis of these data indicate that at low temperatures, between 80 and 20 K, the rattling of the potassium ion is gradually frozen out with the ion coordinating strongly to one side of the cavity; hopping of potassium ions between the off-centre sites is likely to occur in this temperature range and may still slowly occur below 20 K. In this analysis of polycrystalline material, this trapping of the cation seems to occur randomly leaving the $Fd\bar{3}m$ description with statically disordered potassium ions as the best model. It is possible that in single crystals such displacements of the potassium ions could occur in a more concerted manner in portions of the crystal leading to domains of lower symmetry. If such domains were large enough then single crystal diffraction studies might show extra reflections consistent with the lower symmetry of the ordered regions.

The more enhanced displacement which the A ions undergo in this family as its size decreases is attributed to the weak bonds of these A ions into structure. A, *de facto*, has six shorter bonds to oxygen and a further twelve interactions with oxygens at longer distances. Comparison of these structures with those in α-pyrochlores is important for explaining many behaviours. In the α-pyrochlore $Hg_2Os_2O_7$ [102] the A-type cations (Hg) have eight bonds to oxygen; two short interactions to the channel oxygen, O', at 2.215 *Å* and six to O of the OsO_6 octahedra at 2.601 *Å*. The evolution of the ADPs for the sites in the α system show only small increases for Hg, Os, O and O' (by a factor of 2 typically) between 12 K and RT. Thus the behaviours of the ADPs of the A-type cations in $Hg_2Os_2O_7$ and AOs_2O_6 are very different and point to a very weakly bound A-type cation in the β-pyrochlore.

Consideration of the cation site in the β-pyrochlore structure shows that it is very

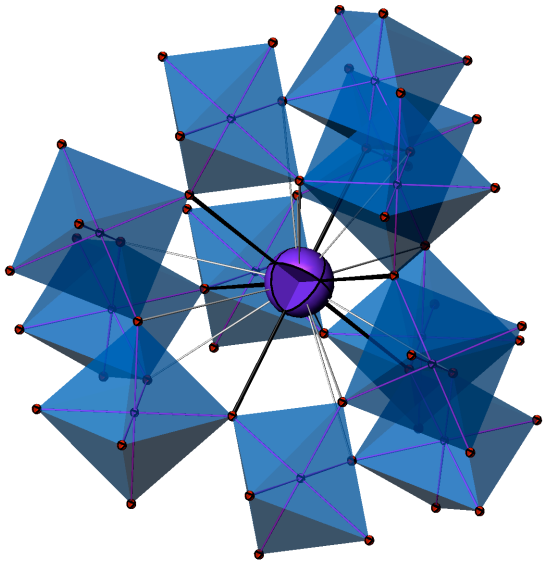

Fig. 3.15: The rubidium ion site in $RbOs_2O_6$ showing its coordination to the OsO_6 octahedra. The six octahedral interactions are shown in black and the 12 longer ones in grey.

weakly bound in the structure. From the least square refinements, carried out on D20 data, the cesium ion has, in $CsOs_2O_6$ has six bonds to oxygen at 3.133(5) *Å* and a further twelve interactions with oxygen at 3.633(5) *Å* (Fig. 3.15) whereas in $RbOs_2O_6$ the rubidium ion has six bonds to oxygen at 3.114 *Å* and a further twelve interactions with oxygen at 3.623 *Å* (Fig. 3.15). Potassium bounds oxygen at 2.965(2) *Å*, 3.272(7) *Å*, and 3.374(3) *Å*.

The OsO_6 framework remains very rigid over the temperature range 2–300 K. The slower thermal expansions of the potassium and rubidium materials compared to $CsOs_2O_6$ are noteworthy. In each case the thermal expansion is relatively small as reflected in the low average thermal expansion parameters for these materials between 10 and 350 K with $\alpha = 2.19 \times 10^{-6}$ K^{-1} (K), 2.28×10^{-6} K^{-1} (Rb), in excellent agreement with the value reported previously using other neutron diffraction data of $\alpha = 2.0 \times 10^{-6}$ K^{-1} (K), and 2.69×10^{-6} K^{-1} (Cs) (*cf.* a typical α for a perovskite oxide of 10×10^{-6} K^{-1} and 8.1×10^{-6} K^{-1} in Al_2O_3 [103]).

The Os–O bond length does not vary significantly remaining at 1.9122 ± 0.0005 *Å* between 2 K and 300 K for cesium, 1.9111 ± 0.0007 *Å* between 2 K and 300 K for rubidium and 1.9103 ± 0.0003 *Å* between 2 K and 300 K for potassium. A more detailed investigation is presented in Sn. 3.4.1. The deviation from the idealised pyrochlore framework structure, which has oxygen on the 48*f* site with $x = 0.3125$, pro-

duces a small distortion of the OsO_6 octahedron with Os–O–Os angles which are again almost invariant with temperature (88.24(6)° at 2 K and 88.26(6) at 300 K). The Rb–O bond lengths increase in length only very marginally between 2 K (6× 3.114 and 12× 3.6216 *Å*) and 300 K (6× 3.117 and 12× 3.6239 *Å*) though this expansion, ($\sim 2 \times 10^{-6}$ K^{-1}), is in line with the overall thermal expansion parameter. A further origin of the small expansion in this material derives from an increase (straightening) of the Os–O–Os bond angle which increases monotonically from 138.35(8)° at 10 K to 138.58(9)° at 300 K. Intriguingly the Os–O–Os bond angle also increases marginally on cooling from 10 K to 2 K (from 138.35° to 138.55°) though this change, based on a few data, lies almost within the esds for these values. This behaviour, however, may be linked with the superconducting transition.

3.4.1 KOs_2O_6 Negative Thermal Expansion

The low temperature, 1.6–25 K, structure of KOs_2O_6 has been investigated in detail in the current section. Powder neutron diffraction studies have allowed us to probe the structure of polycrystalline KOs_2O_6 below its critical temperature. In this section, results are further interpreted through thermodynamical relationship to recent spectroscopic observations [86, 6, 87, 88, 104, 105] which highlighted the crucial role played by the combination of the crystal structure at low temperature and electronic properties.

While the superconducting mechanism remains controversial, the anharmonic rattling motion of K^+ ions in an oversized cage constructed from KOs_2O_6 units has been suggested to enhance superconductivity. Thus superconductivity in KOs_2O_6 is normally discussed in terms of the coupling of the rattling phenomenon [38, 106], and frustration [1]; a further transition possibly involving the potassium ions freezing to an ordered state at T∼7.5 K has also been observed in single crystal samples [90]. However the link between superconductivity below 9.6 K, the transition at ∼7.5 K, and the crystal structure of KOs_2O_6 remains unclear as there are few direct probes of the true structure that can be easily applied at T< 12 K.

The polycrystalline KOs_2O_6 used for the structural study, here reported, was produced by a solid state reaction. Details of the synthetic procedure were reported previously (Sn. 3.2).

PND measurements, for this investigation, were performed on the D2B and D20 powder diffractometers at the Institute-Laue-Langevin in Grenoble (λ = 1.594 *Å* and

1.359 $\AA$ for D2B and D20 [85] respectively). For both instruments 1.5 g of KOs_2O_6 was sealed in a vanadium can and cooled in a standard ILL Orange Cryostat to below 4 K. The high resolution D2B data, from the large angular range $24 < 2\theta < 150^\circ$, was used initially to obtain a potentially higher-quality, structural model at a few low temperature points; data sets were collected at 3.4 K, 4 K, 6 K, 8 K, 10 K, 15 K and 25 K for 2 hours each. Data were collected on the D20 diffractometer every 1 K from 4 K to 25 K. Data are collected more rapidly on this higher flux instrument allowing more temperatures to be sampled although the inherent lower resolution of this instrument leads to slightly higher errors on some extracted profile, atomic and atomic displacement parameters. Note that these new data collected on D20 at very low temperatures were obtained from a larger sample of KOs_2O_6 and with substantially longer count times than in the study described in Sn. 3.4, leading to significantly reduced error bars compared with that study which was carried out over a much larger temperature range.

All data were analysed through Rietveld profile refinements using the GSAS/EXPGUI suite of programs [84, 98]. Low temperature D2B data were initially refined in the space group using the standard beta-pyrochlore description, with K fixed on the 8b sites ($\frac{3}{8}$, $\frac{3}{8}$, $\frac{3}{8}$) Os on the 16c sites (0, 0, 0) and O on 48f (x,$\frac{1}{8}$, $\frac{1}{8}$). The structure refinement proceeded smoothly and converged rapidly to acceptable R-factors (R_{wp} = 5.21%, R_p = 3.94 %, χ^2 = 4.40) with the inclusion of cell parameters, peak shape profiles, atom positions and ADPs. The pseudo-Voigt peak shape function option was chosen and the background was fitted using a cosine Fourier series function. Accurate extracted parameters for this refinement showed an abnormally large ADP value for the K-site, as expected from the literature [93]. However, as shown in a previous section (Sn. 3.4) high ADPs at such low temperatures are much more likely to be ascribed to static positional displacements of K cation along the [111] directions rather than high thermal motion. This behaviour was investigated by fitting the diffraction profile using the alternative model originally proposed by us in which the potassium ion is allowed to displace from the central 8b site onto a 32e site (x,x,x), $x \sim 0.364$. The quality of the fit to the profile for this model was slightly better (R_{wp} = 5.17 %, R_p = 3.94 %, χ^2 = 4.33) and, more significantly, yielded much smaller atomic displacement parameters for the K^+ ion, yielding a value of a similar magnitude to those obtained for the other atoms in this structure at this temperature. At this stage it was decided to apply the two models to the full range of D20 and D2B data; model 1 with K fixed on the 8b sites ($\frac{3}{8}$,$\frac{3}{8}$,$\frac{3}{8}$) was investigated first. Extracted profile (lattice parameter, peak shape), positional and displacement parameters were analysed from the models used to fit the

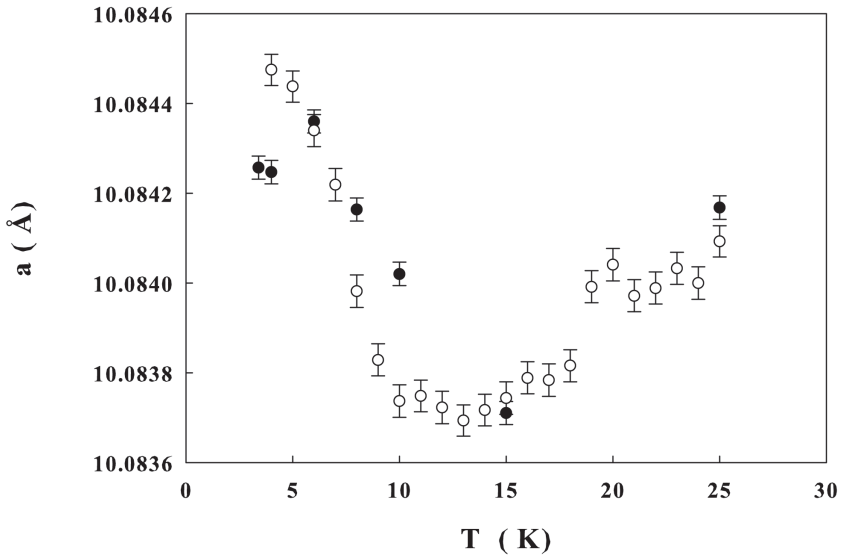

Fig. 3.16: Variation of the lattice parameter of KOs_2O_6 between 1.6 and 25 K. D20 - open circles, D2B filled circles. To allow for instrumental errors the D2B data were scaled to ensure equivalence at 6 K, dividing extracted values by 1.0008.

22 data sets collected on D20 between 4 K and 25 K at 1 K intervals and on D2B at the seven temperatures studied. Fig. 3.16 and Fig. 3.17 summarise the key changes seen over this temperature range; for other variables *e.g.* the oxygen x coordinate, no significant variation was observed. Fig. 3.16 shows the lattice parameter variation between 3.6 and 20 K and demonstrates that below 10 K, that is the critical temperature for this material, KOs_2O_6 shows significant negative thermal expansion (NTE) with α of -2.35 $\times$ 10^{-5} at 6 K. Note that the variation in lattice parameter is almost structural model independent, so identical trends was seen for data analysed with and without a displaced potassium ion.

Also significant was the variation seen in the potassium ADP when this ion was fixed on the 8*b* site. The magnitude of this atom's extracted ADP, displayed in Fig. 3.17 (filled circle), is almost three times that of the same atom when is displaced onto the near 32*e* site (square). Potassium was refined anisotropically on the 32*e* site and this ion's AADP formally decreased to 10 K before increasing. It it is unlikely that the observed increase in this extracted AADP in this model is associated with an increase in thermal motion on cooling and it therefore supports very strongly the hypothesis that the extracted AADP represents an attempt to model a static displacement; this average displacement, from the 8*b* site either increases in magnitude below T_c or could

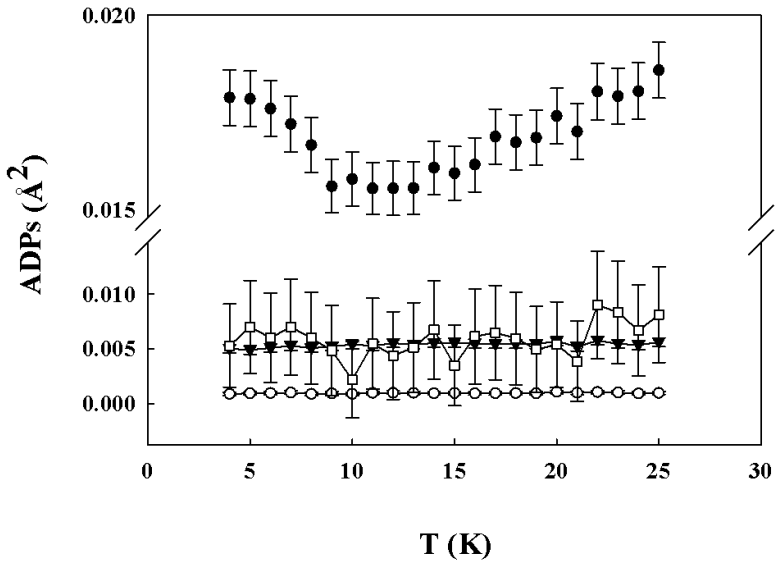

Fig. 3.17: Variation of the potassium ADP when assigned to the 8*b* site-filled circle, and AADP when assigned to the 32*e* site - square, Os- open circles and O triangles as a function of temperature. D20 data only

involve a change in position, which is even more poorly fitted using a potassium ion on the 8*b* site, thus producing an increasingly larger extracted ADP. Such a locking of the potassium ion position or a new type of local ion displacement would also be consistent with the observed negative thermal expansion, vide infra. Therefore the model proposed previously, with the potassium ion displaced onto the 32*e* site, was developed further.

All data sets from D20 and D2B were analysed with potassium displaced and disordered ($\frac{1}{4}$ site occupancy) from the 8*b* site onto the 32*e* site (x,x,x) with x<0.375. For all temperatures this model refined stably and involved local displacements for the potassium ions of about $\sim$0.2 *Å* at 3.5 K, a more plausible representation of K^+ within the cage.

In this model the potassium site ADP is reduced to values very similar to those of the osmium and oxygen atoms and all, as would be expected at such low temperatures, are almost invarient across the temperature range studied. The magnitude of the displacements of the potassium ions along [111] are very similar to those found previously (Sn. 3.4) and its plot, over the temperature range considered, is illustrated in Fig. 3.18.

The OsO_6 framework remains more or less rigid over the temperature range 15-

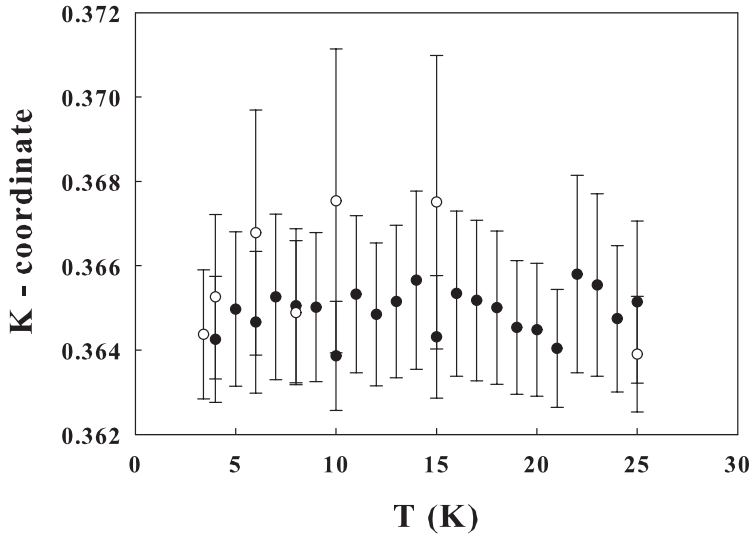

Fig. 3.18: Potassium ion coordinate, x, for the 32e site (x, x, x); D20 data filled circles and D2B data open circles.

300, and in the same temperature region as the negative linear expansion (2-10 K), the Os–O bond length shows a small decrease from at 1.9082(5) *Å* at 2 K to 1.9077(7) *Å* at 10 K, see Fig. 3.19.

Which circumstances favour this contraction occurring is still not certain but it is likely that, even at low temperatures, vibrational contributions play an important role in the thermodynamic properties with the structure adjusting itself to minimize the lattice energy. Recently, NMR [96] and electronic structure investigations [106, 107], validated the *ab initio* calculation of Kuneš *et al.* [4] which addressed the unconventional lattice dynamics of KOs_2O_6 to the large anharmonic vibrations of the K^+ ion. This strong anharmonicity of the lattice has been established [108, 109] to depend on the low-energy phonon modes due to the displacement of the K^+ towards one side of the cage of oxygen atoms. In order to investigate this further the thermal expansion and heat capacity (HC) behaviours were studied in the range 3.4 to 12 K.

HC, for this study, was measured (Sn. 2.3.5) on the same polycrystalline potassium osmate sample as was used for the neutron diffraction work. The heat capacity of a sample consisting of larger crystals, grain size of at least 100μm, was also measured. The heat capacity data obtained from the polycrystalline sample were presented

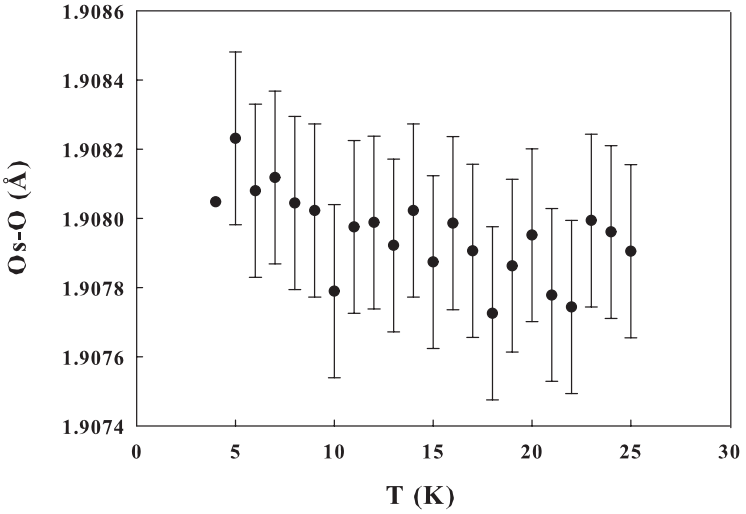

Fig. 3.19: Variation of structural parameter Os–O bond length as a function of temperature

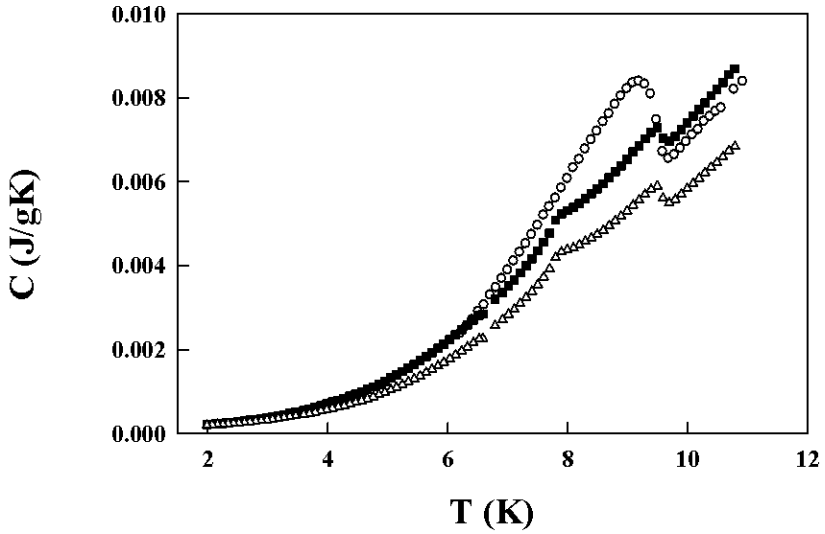

Fig. 3.20: Heat capacity of polycrystalline KOs_2O_6 (open circle) and KOs_2O_6 crystals, grain size of at least 100μm in zero field (triangle) and 9 at Tessla (square) between 2.8 and 12 K.

in Fig. 3.20 (empty circle) and shows a peak at the critical temperature of 9.6 K but with no evidence of a further phase transition observed at around 7.5 K. An anomaly instead, is observed in HC measurement conducted on crystals. The peak appears in the same temperature region as evidenced by previous work and becomes stronger as the applied magnetic field is increased, as evidenced in Fig. 3.20 [6]. The 7.5 K peak in the heat capacity is phonon mediated [6, 95], and is not shown in the HC of the polycrystalline KOs_2O_6 as the phonons, due to the long mean free path at this temperature, will be scattered at grain boundaries for crystals of the order of μm or less, negating the phonon contribution to specific heat. Although the HC peak is not shown in the polycrystalline sample on which we have performed the current structural study, phonon contributions are still very important in driving the anomalous lattice expansion shown by this material in the 5-20 K region. If the NTE is phonon driven, heat capacity measurement can give important information about the thermal expansion of the cell through the relationship found by Grüneisen [100].

Through

$$\gamma = \frac{\alpha_v V}{C_v K} \tag{3.1}$$

where γ represents the *Grüneisen parameter* which relates the bulk mudulus K (Eqn. 3.2) to the volume V and to the specific heat at constant volume Cv, the HC data collected can be used to probe possible origins of the unusual thermal expansion behaviour of the unit cell. The values of K were calculated from the elastic constant recently published by Katrych *et al.* [110] and as the frequency, v, of the vibrational modes decreases, the volume of the material will decrease and will have a negative value.

$$K = -(V)\left(\frac{\partial P}{\partial V}\right)_T \tag{3.2}$$

Fig. 3.21 shows the plot of the calculated thermodynamic Grüneisen parameter as a function of the temperature. It closely follows the behaviour of α; similar behaviour on either side of the the superconducting transition temperature is known, as in for example MgB_2. Interestingly, coupling of the HC data with the lattice expansion coefficients gives a minimum in the same temperature region where Tp = 7.5 K was recently reported [89] and which is likely to have its origins in a structural transition, although its origins have remained unclear until now.

From the structural data, detailed at the beginning of the current section, any further

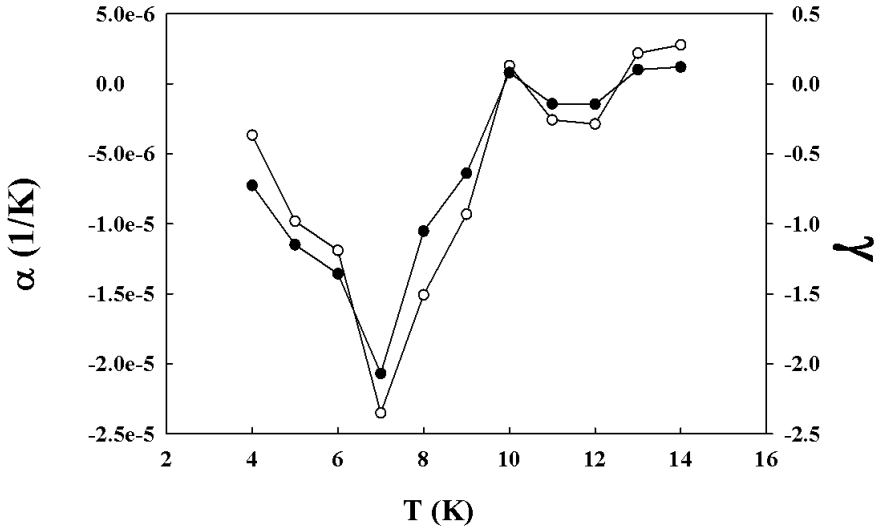

Fig. 3.21: Temperature dependence of the thermal expansion coefficient, α, (filled circle) and calculated temperature dependence of the Grüneisen parameter, γ, for KOs_2O_6 (empty circle).

displacements of the potassium ion from the (x,x,x) site are too small to be unambiguously determined but they are evident in the increased potassium AADPs and negative thermal expansion that occurs below 7.5 K. Therefore any changes occurring at the minimum (7.5 K) must be structurally extremely subtle but it is likely to involve small structural changes such as a further potassium ion shift to lower symmetry site, *e.g.* to 96*g* site. Techniques such as single crystal X-ray or neutron diffraction applied at 4 K or Magic Angle Spinning Nuclear Magnetic Resonance (MASNMR) may be able to probe such subtle changes below 10 K in KOs_2O_6.

Very similar structural behaviours have been observed in other materials where delocalisation or de-trapping of an atom from split and partially occupied sites occurs as a function of temperature. In Ba_6Ge_{25} the structure at low temperature is modelled with barium atoms on split sites whose separation varies markedly as a function of temperature while at around room temperature a fully ordered model can be used. The transition between these models occurs between 250 and 200 K and is associated with negative thermal expansion of the material; the structural effects in this material are associated with a marked drop in the electrical conductivity.[111]

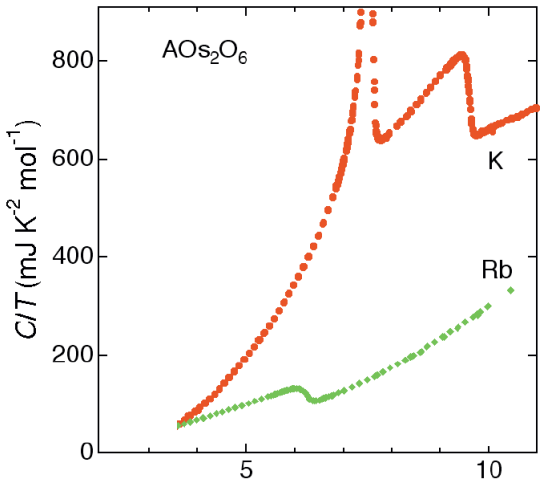

Fig. 3.22: Heat capacity of single crystal KOs_2O_6 (red circle) and polycrystalline $RbOs_2O_6$ (green diamond) as reported by Hiroi *et al.* [6]

3.5 Magnetisation

The magnetisation for the superconducting β-osmates described in this section is shown in Fig. 3.20 and Fig. 3.22 [6]. The anomaly in the heat capacity of KOs_2O_6, was only observed on HC measurement conducted on a sample consisting of larger crystals (grain size) of at least 100μm, as earlier described in Sn. 3.4.1 and shown in Fig. 3.20. The magnitude of heat capacity above T_c is very different among the compounds earlier described and this must be due to the difference in lattice contributions depending on to the specific frequency of the rattling motion of the alkali ions; electronic contributions to the specific heat of such similar structures should be similar. The peak appears in the same temperature region as reported in recent studies [6, 95]. This is graphically showed in Fig. 3.22 that reports the HC of both KOs_2O_6 single crystal and $RbOs_2O_6$ [6]. On the other hand, detailed description of VSM analyses and considerations on $RbOs_2O_6$ and $CsOs_2O_6$ described in this chapter can be found in the PhD thesis work of Mr C.S. Simon [112].

3.6 Conclusions

The structure of β-pyrochlore AOs_2O_6 between 2 K and 300 K consists of a rigid framework of OsO_6 octahedra described by the centrosymmetric space group $Fd\bar{3}m$ throughout the temperature range. The A ions are very weakly bound into the framework and show strong thermal motion on their sites. This behaviour is strongly cor-

related with the A cationic ionic radius size and is more enhanced for rubidium and potassium osmate. Thermal expansion of the material, as a result of the increased ionic motion, is thus abnormally small for a complex oxide. Such bond length increases are unnecessary, particularly for potassium, as the environment it occupies at 2 K readily accommodates any increase in the local thermal motion.

Although the crystal chemistry is very similar for the three members of the family, the low temperature physical properties of KOs_2O_6 appear be quite different from the other two members of the β-pyrochlore osmate superconductors, and can be associated with the thermal motion of the alkali metal ion in the big cavities.

At very low temperatures, the structures of the β-pyrochlores AOs_2O_6 for the smaller cations A are best described in terms of disordered localized A-type cations. For KOs_2O_6, a local displacement of the potassium ion starts to become apparent below 80 K and is complete above T_c. Thus, any discussion of the structure and derived properties of the superconducting pyrochlore osmate phases should employ a structural model with locally displaced alkali metal cations. At high temperatures above 80 K a model with full rattling of the A-type cations around a central pyrochlore cavity position best describes the structure.

Low temperature structural investigation found pronounced anomalies in the variations in the lattice parameter through the superconducting transition region. On cooling from 10 K to 3.6 K the material undergoes expansion which seems to be associated with further displacements and locking of the potassium ion positions in this temperature range at 7.5 K.

The results of the analysis of associated thermodynamics, through Grüneisen parameters, extracted from specific heat measurements on the corresponding powders and the diffraction data, highlight the crucial role played by the combination of the crystal structure at low temperature and electronic properties and can be viewed as a further confirmation that strong anharmonicity generates low temperature structural instability in this compound which results in the peak in the heat capacity at 7.5 K for larger grain crystals.

4. ALKALI METAL EXCHANGE IN THE AOs$_2$O$_6$ (A = K) SYSTEM

The study of the β-pyrochlore osmates [1, 2, 3], has been extended in this chapter to the synthesis of two new materials derived from KOs_2O_6. Results from the previous chapter, which highlighted the variability in the members of the osmate family represented a valid starting point that (i) motivated the investigation of osmium pyrochlores with lithium and sodium on the A site of the structure, possibly enhancing the interesting properties of the KOs_2O_6 parent compound, and (ii) directed to the synthesis of the two new materials. Apart from giving a further overview to the chemistry of an interesting family of materials, the study undertaken in this chapter will draw attention to how the changes in cation size, chemical composition and charge influences their properties.

This chapter will cover briefly the description of synthesis that produced the two successful compounds, $AA'Os_2O_6$ ($A' = Li^+, Na^+$) together with investigation of their structure. The synthesis of such compounds was little explored in the literature due to the high thermal instability of the starting material KOs_2O_6, for which solid state reactions as well as several other synthesis methods, proved inadequate. Due to this instability, modification of the KOs_2O_6 structure was attempted by chemical substitution in 'milder' conditions, *i.e.* anhydrous ionic exchange.

The ability to exchange the A-type cation in pyrochlores is well known and this can lead to the synthesis of metastable materials that are otherwise inaccessible. The replacement of a proportion of the A ions in AOs$_2$O$_6$ by alkali metal ions of smaller ionic radius has been largely restricted to the KOs_2O_6 compound. Ion exchange on KOs_2O_6 could be attempted because of its relatively open channels formed by corner-sharing OsO_6 octahedra which form the pyrochlore three-dimensional network. These result in large cavities in which the K^+ ions are accommodated. Because of this channel-structure the exchange of the A cations with a range of smaller cations can be attempted in solution, allowing the synthesis of compounds whose formation

is precluded by direct synthesis. Thus, starting from KOs_2O_6, partially exchanged $K_{1-x}Li_yOs_2O_6$ and $K_{1-x}Na_zOsO_6$ were synthesised. They can be classified as having a mixed cation type on the A site. Although the aim was to modify KOs_2O_6, to produce a compound with higher T_c, interesting features have been studied in the course of the work and will be covered in this chapter. Much importance will be dedicated to the investigation of the local rearrangement of the cations following the synthetic process. A comparison of the two materials is given, and the magnetic behaviour of the phases interpreted. This resulted in further insight into the effect of structure change upon the superconductive properties of Os-based pyrochlore systems. Characterisation techniques used include PXD and PND for cation and anion location; energy dispersive X-ray measurements (EDX) provided qualitative monitoring of the stoichiometry of reaction product whilst quantitative contribution to the data was given by elemental analyses (EA) and TGA.

4.1 Experimental

4.1.1 Synthesis

The structural changes induced by the insertion of smaller cations were investigated through the analysis of the products of a wide range of synthetic methods and reaction conditions; these included anhydrous, aqueous and in melts ion exchange processes, as well as solid state reactions, which are detailed in the Table 4.1 and Table 4.2. The starting material for all of the ion exchange reactions was KOs_2O_6 ($\sim$ 0.5 g), a = 10.08389(22) $\AA$, synthesised as described in Sn. 3.2. This section contains an overview of the synthetic set up that led to the final compounds which will be characterised in the following sections by the techniques stated above.

Synthesis of $LiOs_2O_6$ and $NaOs_2O_6$ by solid state reaction, as well as *via* several other conditions and media was not easy due to the high thermal instability of the starting material KOs_2O_6. Although solid state syntheses in open and closed systems were attempted, ion-exchange was found to be the most appropriate route for modification of the structure of the pure potassium compound and synthesis of compounds similar to the precursor. Ion exchange of KOs_2O_6 was expected because of the channel structure formed by the OsO_6 octahedra and because of the weak interaction of the ion with

the framework, that allows K^+ to move along the 4 [111] directions.

The lithium sources used for the reactions were varied; these included LiCl (Aldrich, >99,5% purity), $LiNO_3$ (Aldrich, >99,5% purity) and $LiBF_4$ (Aldrich, >99,5% purity), whereas for the synthesis of the targeted sodium analogue NaCl (Aldrich, $>99,5\%$ purity) and $NaNO_3$ (Aldrich, >99,5% purity) were employed. The temperature chosen for each synthesis considered the decomposition temperatures of the starting materials used in the reaction. For the anhydrous syntheses both lithium and sodium precursors were dried and moved to a glove box, filled with N_2. All handling was undertaken in strictly dry 2 ppm H_2O atmospheres, in order to reduce the hydration energy term that may dominate the reaction preventing high cation uptake. Reactions, that resulted in the synthesis of final compounds, were carried out in a closed system using appropriate dry solvents (ethanol and acetone from Fluka, and methanol previously distilled in the laboratory) to dissolve LiCl and NaCl (and in which KCl, which could be formed, was less soluble; in these solvents, they were used to shift the equilibrium towards the synthesis of desired $LiOs_2O_6$ and $NaOs_2O_6$ phases). Experimental conditions of attempted ion-exchange on KOs_2O_6, as well as the final phases obtained, are listed in Table 4.1 and Table 4.2. The ion exchange processes in melts, were carried out using an excess of metal nitrate, in air, at temperatures slightly higher than the corresponding melting point of each chloride salt. In all of these reactions K^+ was not easily exchanged by Na^+ and Li^+ and two features were soon evident from the X-ray patterns: i) a decrease in the intensities of the diffraction for the KOs_2O_6 and ii) an increase in the intensity of the peaks related to the second phase OsO_2 present in the initial reaction batch. This was soon attributed to the decomposition of the framework which, in air, gave the more stable Os(IV) and Os(VIII) oxides. Prolonged heating periods ($>$ 96 h) resulted in almost complete decomposition of the KOs_2O_6 phase. These features confirmed the inadequacy of the route for obtaining the β-osmate. Reactions of Table 4.1 and Table 4.2, carried out in open systems, were washed from the alkali metal chloride solution, dried ∼350 K in an oven, and monitored by X-ray diffraction on a daily basis; EDX was also used on the most interesting compounds. Interestingly, the reaction carried out in solutions of metal nitrates or metal chlorides yielded very similar results for both the lithium and for the sodium phase. In fact, preliminary, room temperature investigations on the resulting polycrystalline phase showed a clear splitting in the X-ray diffraction patterns, indicating the generation of two phases, one indexable to the starting material and the other exhibiting the characteristic peaks of

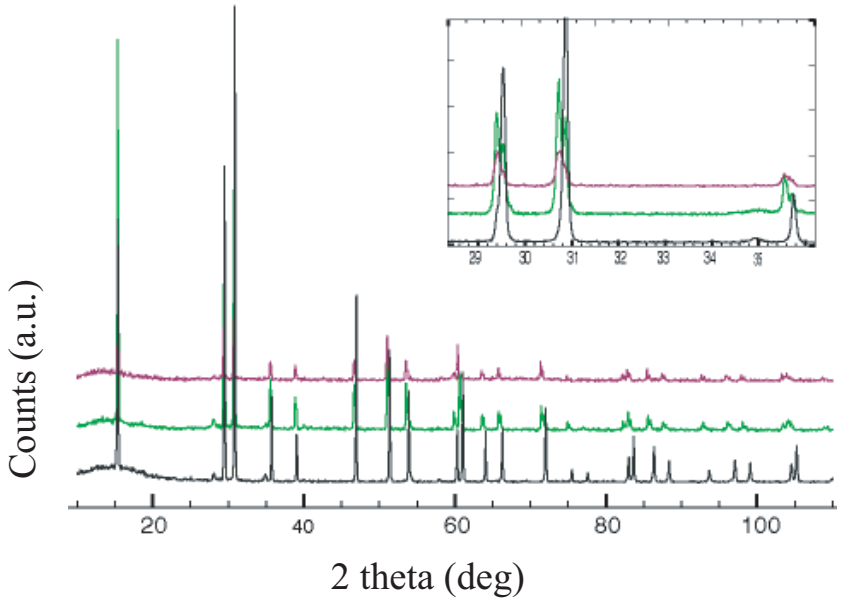

Fig. 4.1: X-ray diffraction pattern for the ion-exchange reaction of KOs_2O_6 and LiCl in water after two cycles. The black diffraction pattern represents the KOs_2O_6 used as the precursor, the green colour shows the X-ray pattern of the polycrystalline material obtained after the first cycle of the reaction, 24 hours, and pink after 48 hours. The inset expands the 2θ region between 25-40°, highlighting the pronounced decomposition of the potassium phase.

an osmate pyrochlore of bigger cell (Fig. 4.1), which turned out to be an hydrated potassium phase.

The lack of success in synthesising the targeted $LiOs_2O_6$ and $NaOs_2O_6$ by direct methods was attributed to the small ionic radii of lithium and sodium which fall out of the average range yielding to pyrochlore-type osmate compounds [5], but it also reflects the ability of the K^+ atoms to move out from the channel cavities facilitating the entrance of the smaller atoms to counterbalance the negatively charged framework.

Tab. 4.1: Synthesis conditions of attempted routes for the ion exchange of KOs_2O_6 to produce targeted $LiOs_2O_6$.

Method	Solvent/Conditions	Exchanging agent (Ea)	Ea : KOs_2O_6 ratio	Temp (K)	Duration (h)	Phase Obtained
Aqueous	Water	LiCl	Excess	323	96	$KOs_2O_6{\cdot}nH_2O$, OsO_2,OsO_4.
Aqueous	Water	LiCl + C.E.*	Excess	313	96	$KOs_2O_6{\cdot}nH_2O$, OsO_2.
Aqueous	Water	$LiNO_3$	Excess	313	96	$KOs_2O_6{\cdot}nH_2O$, OsO_4,OsO_2.
Anhydrous	Dry Ethanol (N_2 atmosphere)	LiCl + C.E. +	Excess	313	96	KOs_2O_6, $K_xLi_yOs_2O_6$,OsO_2.
Anhydrous	Dry Acetone (N_2 atmosphere)	LiCl + C.E. +	Excess	313	96	$K_{1-x}Li_yOs_2O_6$, OsO_2
Melt	Air	$LiBF_4$	1:1	590	48	$KOs_2O_6{\cdot}nH_2O$ OsO_2,OsO_4,Li^+F^-
Solid-state	(ampoule/vacuum)	LiCl	1:1	400	72	KOs_2O_6 OsO_2,OsO_4, $KOsO_4$

*C.E. = Crown Ether(18-Crown-6).

Tab. 4.2: Synthesis conditions of attempted routes for the ion exchange of KOs_2O_6 to produce targeted $NaOs_2O_6$

Method	Solvent/Conditions	Exchanging agent (Ea)	Ea : KOs_2O_6 ratio	Temp (K)	Duration (h)	Phase Obtained
Aqueous	Water	NaCl	Excess	323	96	$KOs_2O_6{\cdot}nH_2O$, OsO_2,OsO_4.
Aqueous	Water	NaCl + C.E.	Excess	313	96	$KOs_2O_6{\cdot}nH_2O$, OsO_2.
Aqueous	Water	$NaNO_3$	Excess	313	96	$KOs_2O_6{\cdot}nH_2O$, OsO_4,OsO_2.
Anhydrous	Dry Methanol (N_2 atmosphere)	NaCl + C.E. +	Excess	313	96	$K_{1-x}Na_zOs_2O_6$, OsO_2
Melt	Air	$NaNO_3$	1:1	$\sim$ 590 K	48	
Solid-state	(ampoule/vacuum)	NaCl	1:1	400	72	KOs_2O_6 OsO_2,OsO_4, $KOsO_4$

*C.E. = Crown Ether(18-Crown-6).

The best conditions to introduce lithium into the KOs_2O_6 structure were achieved using LiCl (as exchanging salt), crown ether, and dry acetone (as solvent). Methanol was substituted to dissolve sodium chloride. The use of water as the solvent or solid state methods was found to be very aggressive and caused decomposition of the host, see Table 4.1 and Table 4.2 while the synthesis of the pyrochlore containing sodium was obtained only after two steps, the analogue containing lithium, and characterised in Sn. 4.1.4 by neutron diffraction, was obtained after 3 steps.

The initial reaction mixture which produced the final products, characterised in Sn. 4.1.4, contained chloride salts (0.06 g), KOs_2O_6 (0.6 g), previously dried at 573 K overnight under nitrogen, and 18-crown 6 ether (1 g, 99%). Dry reactants were transferred to a Schlenk tube and mixed in the dry box. The reaction was carried out under a nitrogen atmosphere, at ∼313 K using solvents able to dissolve the salts and with the expectations that KCl, less soluble in both solvents used, would favour the cation substitution process shifting the equilibrium towards the synthesis of the desired compounds. The solution batch was refreshed every 36 hours to help the exchanging process. The solid phase was separated from the anhydrous solution of salt by settling and filtration. PXD, 10-110°, 2θ, 0.02° step size, and chemical analysis were employed for monitoring the progress of the reaction.

Crown ether 18-crown-6 was used in the reactions for its known ability to form stable complexes with alkali metals and to speed up the kinetics of the reactions [114, 115]. The reactions between the molecule and the salt, in fact, occur much more rapidly than they do in two phase systems. The 18-crown-6 has high affinity for the potassium cations as its ligand cavity has similar size to the ionic radius of the guest; this affinity for potassium also contributes towards its toxicity. The resulting cation often form salts that are even soluble in nonpolar solvents as they are brought together into organic solution from the solid phase. LiCl dissolves in low-polar solvents like acetone whereas methanol was chosen for the Na-exchange reaction; the choice was dictated by the very low solubility of NaCl in acetone despite the possibility for methanol to enter the structural cavities. Synthesis were carried out considering several factors affecting crown ether chemistry. The ion-macrocycle association process depends on several factors but, especially, on the nature of the solvent. The solvating ability of the solvent, indeed, plays a key role in different complexation reactions (as there is generally an inverse relationship between solvent polarity and binding constant K_s in that solvent). The more polar is the solvent, the more effectively it can compete with the ligand for the cation, contributing to the lowering of the binding. Methanol

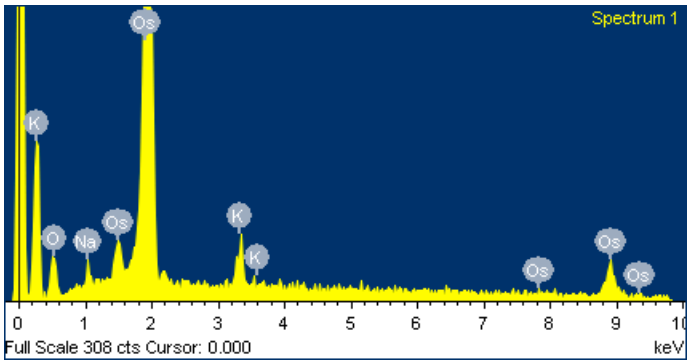

Fig. 4.2: Counts versus keV for the ion-exchange reaction obtained by KOs_2O_6, NaCl and crown ether.

would have been the best choice, as it represents a middle ground in polarity and can accommodate both metal salts and organic ligands. However the choice of acetone, as opposed to methanol was made for the 'lithium' reaction as methanol could easily enter the structure cavities hindering the exchanging process. Acetone, however, is a solvent of relatively high solvating ability which can compete with the crown ether for the lithium ion.

Progress of the anhydrous ion exchange reactions was monitored at each stage by PXD, EDX, and EA.

EDX measurements were used complimentarily due to the insensitivity of the PXD technique to the lighter atoms. These analyses suggested that part of the potassium was removed from the structure and was either replaced by lithium or sodium or to form vacancies. For the reaction carried out in the presence of LiCl, and after the third step, about 50% of the K was removed as the K: Os ratio increased from :2.6 to 1:5.4, whereas, in the reaction carried out with NaCl after the second step only the 23% of potassium left the structure, evidenced by the K: Os ratio that increased from 1: 2.6 to 1: 4.1.

The values agreed remarkably well with refined neutron occupancies for K and Li as will be shown in Sn. 4.1.4. Fig. 4.2 shows the EDX spectra collected for $K_{1-x}Na_zOs_2O_6$; as can be seen from the spectrum, sodium was detected.

The lithium and sodium content inserted into the structures was determined by elemental analysis (Medac Limited Laboratories, Egham, UK). Chemical analyses gave the empirical formulae of $K_{0.45}Li_{0.5}Os_2O_6$ and $K_{0.69}Na_{0.67}Os_2O_6$. Note that, for both materials, the contribution of OsO_2 as an impurity was roughly estimated on the basis of the phase fraction obtained from X-ray diffraction profiles, as well as full occupancy of the oxygen site.

The oxygen stoichiometries of the samples were determined by TGA following reduction of the osmates ($\sim$15 mg samples) to constituent oxides and osmium metal under a 5% hydrogen/nitrogen gas mixture over the temperature range 293-1173 K. Analyses for each sample were repeated until concordant results were obtained within the range of experimental error ($\pm$ of the oxygen content). TGA results confirmed in both structures a fully occupied site for oxygen. It appeared that the oxygen stoichiometry was not affected by the constituent on the A site and that no additional vacancies were formed on removal of potassium from the structure.

4.1.2 Magnetisation

In the compounds where K^+ was exchanged by Li^+ and Na^+, an increase in the critical temperatures, T_c, was expected following the inverse relationship between the ionic radius of the alkali metal and the superconductive temperature manifested by the members of the parent family AOs_2O_6. This did not occur.

The superconducting temperature, T_c, of substituted samples is systematically lower than in the undoped samples and this is shown in Fig. 4.3. The figure reports the T_c of starting material and of the two compounds obtained by metal chlorides exchange between 0 and 300 K. The T_c of KOs_2O_6 decreased to $\sim$7 K after the exchange with sodium and to $\sim$4 K after the exchange with lithium. The reason for the significant deterioration of the superconducting temperature following the substitution of $\sim$50% in $K_{1-x}Li_yOs_2O_6$ and $\sim$30% in $K_{1-x}Na_zOsO_6$ of potassium ions on the A site of the pyrochlore KOs_2O_6 ions could be either related to the relocation of the smaller alkali metal cation to smaller site, which is expected following the exchange process, or to the amount of potassium removed from the structure. These may cause a lowering in the alkali metal ion motion and, hence, a decrease of the strong anharmonicity of K^+ in the OsO_6 cage, which appears to play an important part in the superconductivity of the starting compound [106, 108].

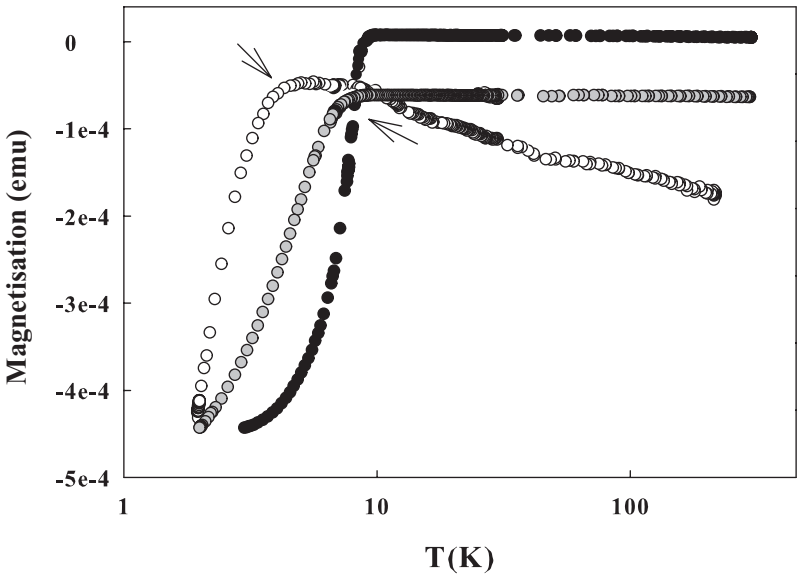

Fig. 4.3: Temperature dependence of the T_c for KOs_2O_6 (black filled circle) and for the two derived compounds, $K_{0.45}Li_{0.5}OsO_6$ (open circle) and $K_{0.69}Na_{0.67}OsO_6$ (grey filled circle).

4.1.3 PXD Structure Refinement of $K_{1-x}Li_yOs_2O_6$ and $K_{1-x}Na_zOs_2O_6$

Primary structural details of the two new-formed phase were obtained using powder PXD. Data on the samples where collected in the 2θ range as described previously (Sn. 2.3.1). A rather simple pattern implying a high symmetry was observed, as it was expected from simulated powder pattern diffraction pattern. A preliminary Le Bail fit, therefore, varying just profile parameters, was carried out on the set of data collected at room temperature (RT) to check if the space group of the originator $Fd\bar{3}m$, could still describe the lattice of the two new phases. Careful inspection of the diffraction profiles showed no obvious extra reflections due to symmetry reduction [71], confirming the space group needed to describe the structure. Both X-ray powder patterns appeared very similar (see Fig. 4.5 and Fig. 4.4), and could be indexed on the basis of a cubic unit cell of $a\sim10$ $\AA$. The analysis confirmed that a single phase pyrochlore could be obtained by ion exchange.

Initial RT cell investigations, for both new samples synthesised, was therefore started using the model which represented the starting material at that temperature, and described in the previous chapter, (the standard β-pyrochlore description in $Fd\bar{3}m$ with Os at 0, 0, 0, K at $\frac{3}{8},\frac{3}{8},\frac{3}{8}$ and O at $x,\frac{1}{8},\frac{1}{8}$). Inspection of data showed the presence of a small level (∼5% for lithium phase and slightly bigger, ∼10%, for the sodium compound) of OsO_2 impurity which was fitted using literature data [116], cell con-

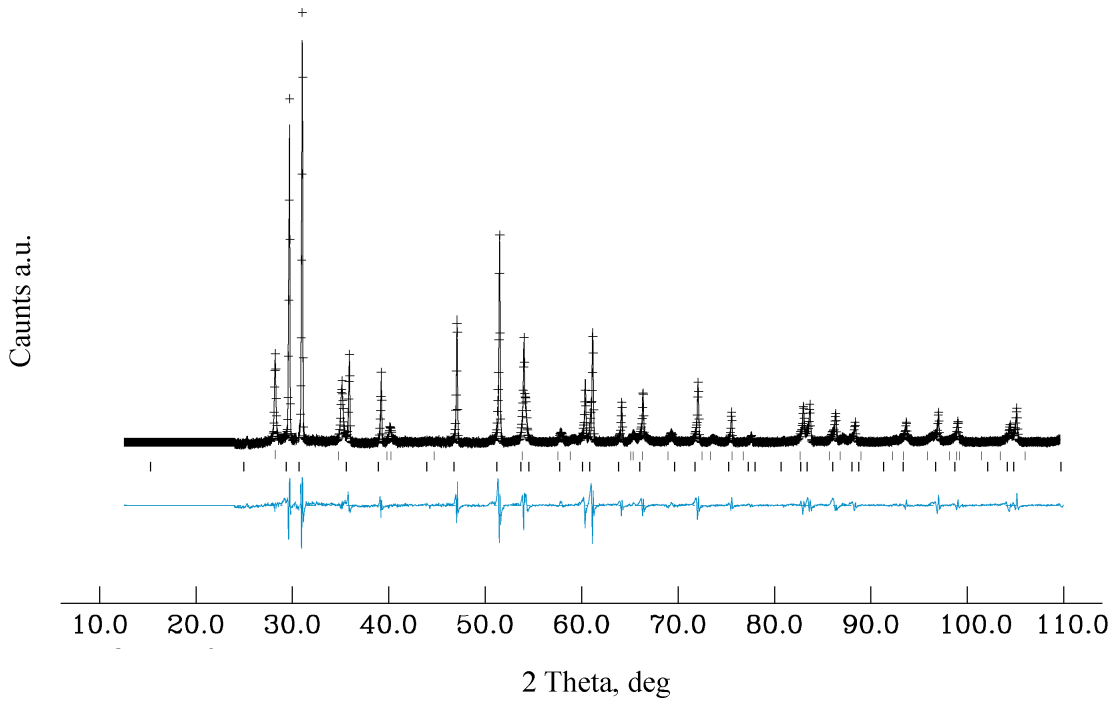

Fig. 4.4: Le Bail fit to the diffraction data for the reaction carried out in methanol and sodium chloride and crown ether, after two cycles. Cross marks are observed intensities, upper continuous line is the calculated profile, and lower continuous line is the difference. The tick marks show the peak position.

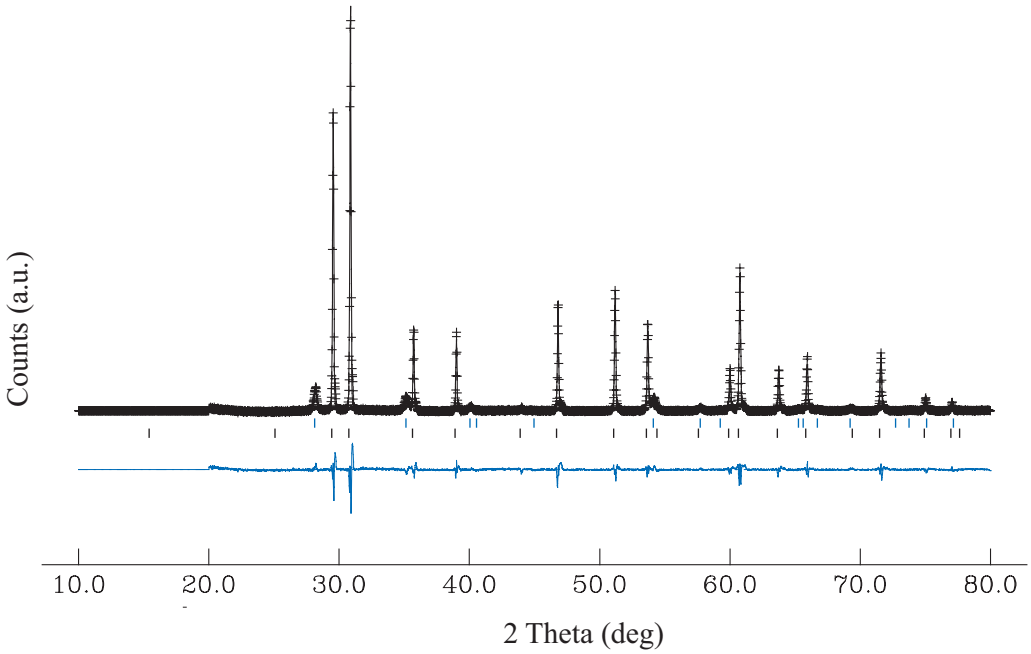

Fig. 4.5: Observed, calculated and difference Le Bail diffraction profiles for $K_{1-x}Li_yOs_2O_6$. The tick marks show the peak positions.

stant and phase fraction. Initial stages of the refinement proceeded smoothly with the variation of cell parameters, peak shape profile, cell constant and phase fraction, which along with the refinement of the isotropic atomic displacement parameters (ADPs), resulted in the expected improvement in the least-squares fit. The model used for both compounds fitted all the peaks observed and converged rapidly to reasonable R factors (Table 4.4 and Table 4.3). Alkali metal occupancies were not refined at this stage. Partial substitution of the potassium ion by lithium and sodium was expected, on the basis of EDX and EA measurements. These techniques showed that, following the exchange processes, almost half of the potassium originally present in KOs_2O_6 was substituted by the smaller lithium whereas the exchange reaction carried out in presence of NaCl only removed 0.3 of the initial potassium, though incorporated a larger amount of sodium with respect to lithium. This feature was soon confirmed by the least squares refinement when the potassium fraction, initially set to unity, was left to refine, even though the contribution of this light atom to the osmate diffraction pattern could only be roughly estimated. In the lithium phase, its occupancy, decreased soon to 0.55, indicating that part of K^+ moved away from the structure. The potassium ADP refined to a large value, a possible consequence of the partial occupancy of the site. Lithium atoms were not included in the initial refinements, due to the small X-ray scattering factors associated with this atom. Despite the missing intensity, both models revealed an adequate representation of the type-structure. In the sodium potassium osmate, though, the fraction of potassium steadily refined to 0.67 and showed also quite reasonable ADP value. Based on chemical analysis and the refined values from PXD refinements (Table 4.4 and Table 4.3), it was possible to estimate the structures of the two new osmates as $K_{1-x}Li_yOs_2O_6$ and $K_{1-x}Na_zOs_2O_6$. The compounds contain two different cations on the A site. X-ray instrumental detection limits could not help, at this stage, in the appropriate determination of cation occupancies and siting but PXD revealed indexing of the unit cell and identification of the space group.

4.1.4 Powder Neutron Diffraction

Taking into account the limitations of PXD, for refinement of the position of light atoms in the presence of heavily scattering metals, high resolution PND represented an important tool for identifying the position of the lithium and sodium within the OsO_6 framework and their possible distribution over the range of temperature investigated. Data were collected on the high-resolution, constant wavelength ($\lambda = 1.59432\AA$) pow-

Tab. 4.3: Model of $K_{1-x}Li_yOs_2O_6$ refined by PXD, a =10.13558(3)Å, $Fd\bar{3}m$, R_{wp}= 6.13%, R_p=5.68%, χ^2 = 7.82

Atom name/site	x	y	z	$U_i/U_e \times 100\ Å^2$	site occupancy
K 8*b*	0.375	0.375	0.375	7.29(4)	0.55
Os 16*c*	0	0	0	1.23(3)	1.0
O1 48*f*	0.3169(9)	$\frac{1}{8}$	$\frac{1}{8}$	1.38(4)	1.0
Li	-	-	-	-	-

Tab. 4.4: Model of $K_{1-x}Na_zOs_2O_6$ refined by PXD, a =10.22073(5)Å, $Fd\bar{3}m$, R_{wp}= 5.53 %, R_p= 4.63%, χ^2 = 7.21

atom name/site	x	y	z	$U_i/U_e \times 100\ Å^2$	site occupancy
K 8*b*	0.375	0.375	0.375	6.93(2)	0.67
Os 16*c*	0	0	0	1.146(1)	1.0
O1 48*f*	0.3165(8)	$\frac{1}{8}$	$\frac{1}{8}$	1.91(3)	1.0
Na 16*d*	0.5	0.5	0.5	2.7(13)	0.33

der diffractometer D2B at the I.L.L, Grenoble. Approximately 0.5 g of sample was placed into a 5 mm diameter vanadium can, and cooled at 2 K in a standard orange cryostat. To avoid any uptake of water into the pyrochlore frameworks the samples were loaded in a N_2 dry box. The powder pattern was collected over the range 2θ = 10-150° with a collection period of 4 h. Three additional patterns were collected at 15, 100 and 300 K.

$$K_{1-x}Li_yOs_2O_6$$

In Chapter 3, Sn. 3.4, a new model that better described the displacement of the potassium from the ideal central site and that resulted in a lower ADP value for this atom was proposed and fully discussed. On the basis of the study discussed in Sn. 3.4 on KOs_2O_6, therefore, a selection of models (within the $Fd\bar{3}m$ space group) were considered to investigate the structure of $K_{1-x}Li_yOs_2O_6$ and to model the A-ion motion in the surrounding of the 8*b* site at low temperature. Models implied the distribution of the A cations over 8*b*, 32*e* and 16*d* sites. Final profiles fits, coordinate parameters and atom occupancies are reported in Table 4.5. Structural refinements, on the neutron data collected, were carried out using the Rietveld method (Sn. 2.2.3). The atomic

positions used as the starting point for the refinement were the metal and oxide coordinates reported for KOs_2O_6 by Hiroi *et al.* [1] from powder neutron diffraction studies, with Os (0, 0, 0) and O (x, $\frac{1}{8}$,$\frac{1}{8}$). For data analysis, the scattering of OsO_2 could not be neglected, therefore the OsO_2 impurity was included in the refinement as a second phase. The non-framework cations (K^+ and Li^+) were not considered at the initial stage of the refinement. After initial refinement of scale factors, lattice parameters and background, the model, including only framework atoms led to a fit of R_{wp} = 6.87%, R_p = 5.34%, χ^2 = 8.85. In addition to the expected discrepancies between observed and calculated intensities, inspection of the diffraction pattern identified strong peaks in several regions (see pattern of Fig. 4.6) of the spectrum which were addressed as instrumental artifacts and thus removed from the refinement as excluded regions. Instrumental peaks reappeared also in the neutron data set used for structural determination of the structure of $K_{1-x}Na_zOs_2O_6$ as they were collected at the same experimental time. 6 background terms were fitted using a cosine Fourier series function, as well as a pseudo-Voigt peak shape. Discrepancies between observed and calculated intensities confirmed that there were additional atoms in the model that were not taken into account. Therefore, nuclear density around the cavity of the framework, where Li^+ and K^+ ions were likely to be found, was explored using difference Fourier maps. Peak searches identified electron density missing around the ideal potassium site and along the principal axes at approximately 0.1 *Å* from the central site. The potassium was, therefore, added to the structural refinement at coordinates $\frac{3}{8}$, $\frac{3}{8}$,$\frac{3}{8}$ as from the model proposed by Hiroi *et al.* [1], and after few refinement cycles lithium was also introduced on the 32*e* site, ∼0.08 *Å* away from K^+, as suggested from the nuclear density difference maps. ADPs parameters for Li^+ and K^+ site were, initially, constrained to be equal and their occupancies fixed at values suggested by EA, with an overall value of 1. Therefore, the variable positional parameter x of the lithium and potassium ions were refined at a time and fixed. Then, their ADPs were refined one at the time and finally uncoupled and refined isotropically together with the position of the two alkali metals in the next four refinement cycles to give the final values listed in Table 4.5. Lithium refined steadily to a 32*e* site x, x, x resulting in a concomitant reduction of the ADPs of all the atoms in the cell. The structure refinement using the 2 K data in $Fd\bar{3}m$ proceeded smoothly, with the introduction of cell parameters, peak shape profiles, and, along with the refinement of atom positions and isotropic ADP, resulted in a significant improvement in the least-square fit. Much more satisfactory convergence was achieved at this stage and the ADPs of the lithium and potassium cation sites showed a signif-

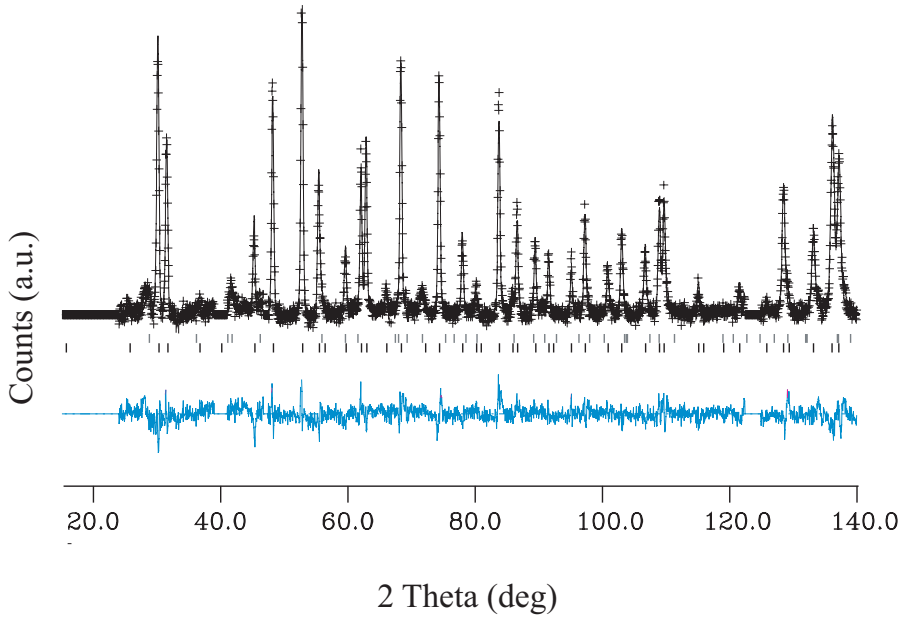

Fig. 4.6: Profile fit obtained to the 2 K data obtained from refinement of KOs_2O_6. Cross marks are observed intensities, upper continuous line is the calculated profile, and lower continuous line is the difference. Tick marks, from top to bottom, are calculated reflection positions for OsO_2 and KOs_2O_6

icant decrease, yielding values of a similar magnitude to those obtained for atoms in this structure at 2 K. Final ADPs for all the atoms of the cell are shown in Fig. 4.7. This model produced satisfactory bond lengths as well (Fig. 4.9). Careful inspection of the profile fit achieved at this stage showed no obvious extra reflections or tetragonal peak splitting as reported for KOs_2O_6 and $RbOs_2O_6$ by Schuck *et al.* [71, 72]. The final refined parameters obtained are listed in Table 4.5, derived bond lengths and angles of interest in Table 4.7, whereas the final fit to the 2 K data is shown in Fig. 4.6.

In the osmate family, high values of the ADP of the A cation are a characteristic feature [93] associated with the rattling of this small ion in an oversized cage [4]. In the pure KOs_2O_6, off-centre displacement of K^+ ions along the [111] decreased the high value associated with the ion. High ADP for lithium in $K_{1-x}Li_yOs_2O_6$ did not exclude the possibility of similarities with the precursor. Thus, to probe this hypothesis, the lithium was allowed to displace from the site previously refined onto the adjacent 96g

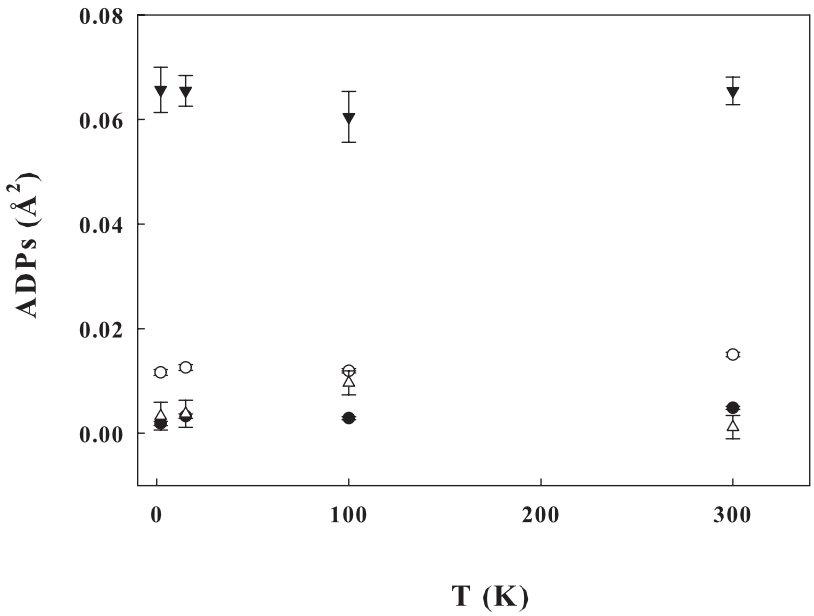

Fig. 4.7: Variation of the K ADP, assigned to the 8*b* site (open triangle), Os (filled circles) and O (open circles) and Li, assigned to the 32*e* (filled triangles) as a function of temperature. Estimated standard deviations (esds) shown as error bars.

and 16*d* sites, with the overall site occupancy constrained to be equal to the level of lithium displaced from the adjacent 32*e* site. In these descriptions, although the occupancy was initially fixed at a value given by the EA and the positional parameter x for lithium was refined only in alternate cycles with its ADP, the ADPs of all the atoms refined to unreasonably high values and resulted in highly unstable refinements even with the highest level of damping.

Comparing results confirmed the model involving local displacements for the Li^+ atoms of about 0.08 $\AA$ from the ideal site and with K^+ sitting at coordinate $\frac{3}{8}$, $\frac{3}{8}$,$\frac{3}{8}$ (see Fig. 4.9), as the more plausible representation for this cation in the pyrochlore cage.

The combined use of X-ray and neutron powder diffraction data coupled with EA measurements allowed the description of the distribution of cations within the pyrochlore channels and of the structural formula as K_{1-x} $Li_yOs_2O_6$. This description was, therefore, used as the starting point for neutron diffraction data collected at the next temperature. To ensure consistency the same variables and background points were used for data collected at each temperature pointE. The model was confirmed as the best depiction of the scattering density of K_{1-x} $Li_yOs_2O_6$, describing the ther-

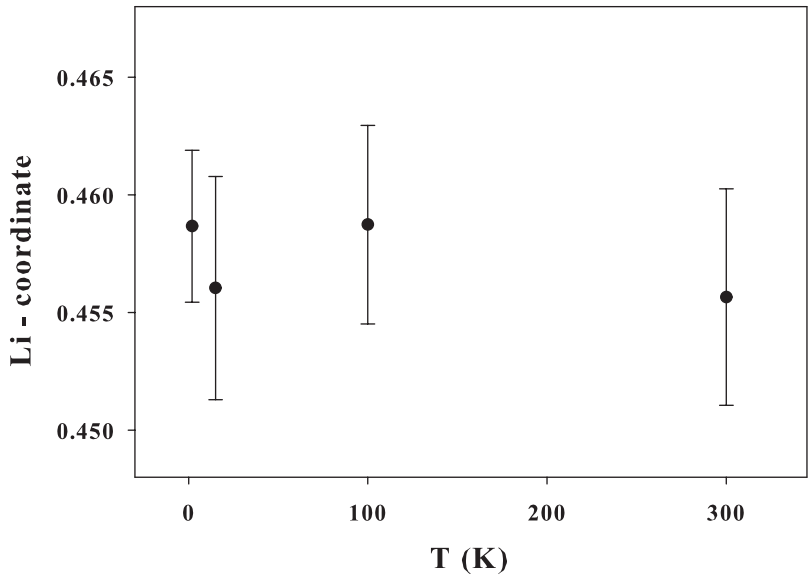

Fig. 4.8: Temperature variation of the lithium ion coordinate, x, for the 32e site (x, x, x) in $K_{0.5}Li_{0.5}Os_2O_6$. (Esds shown as error bars.)

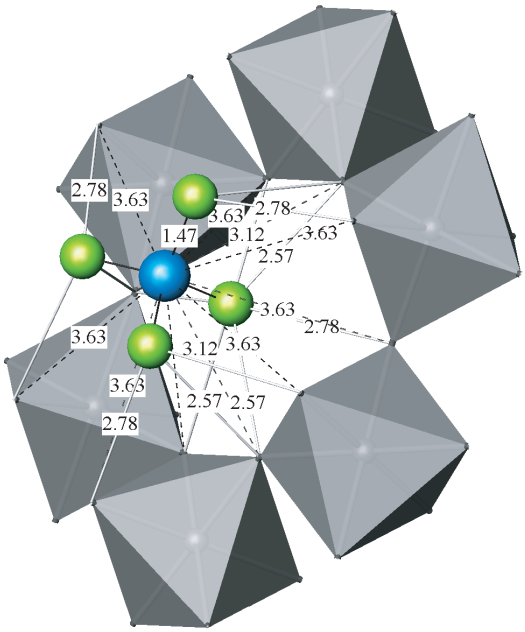

Fig. 4.9: Crystal structure at 2 K of the β-pyrochlore $K_{0.5}Li_{0.5}Os_2O_6$ demonstrating the displacement of the lithium onto the 32e site, the potassium ion on the central site, 8b, and the octahedral OsO_6 network.

Tab. 4.5: Model of $\mathrm{K_{1-x}Li_yOs_2O_6}$ refined by PND, space group $Fd\bar{3}m$. Esds in parentheses.

		2 K	**15 K**	**100 K**	**300 K**
K	*site*	**8*b***	**8*b***	**8*b***	**8*b***
	x	0.375	0.375	0.375	0.375
	Occ	0.5	0.5	0.5	0.5
	Ui/Ue × 100	5.77(3)	0.21(3)	1.26(4)	1.30(27)
Li	*site*	**32*e***	**32*e***	**32*e***	**32*e***
	x	0.4587(4)	0.4572(3)	0.4588(3)	0.4556(5)
	Occ	0.125	0.125	0.125	0.125
	Ui/Ue × 100	6.46(6)	6.54(3)	6.05(7)	6.54(4)
O	*site*	48*f*	48*f*	48*f*	48*f*
	x	0.3167(1)	0.3167(2)	0.3165(5)	0.3168(1)
	Occ	1.0	1.0	1.0	1.0
	Ui/Ue × 100	1.07(7)	1.25(4)	1.25(9)	1.54(5)
Os	site	16*c*	16*c*	16*c*	16*c*
	x	0	0	0	0
	Occ	1.0	1.0	1.0	1.0
	Ui/Ue × 100	0.19(2)	0.32(1)	0.36(6)	0.56(1)
a		10.1346(2)	10.14181(1)	10.13511(3)	10.13560(5)
χ^2		3.98	5.29	5.52	4.10
$\mathbf{R}_{wp}$		4.26%	4.73 %	4.02%	3.79%
$\mathbf{R}_p$		3.56%	3.63 %	3.06%	2.84%

mal motion of the cations through the temperature range investigated giving reasonable bond lengths for all the atoms. The K^+ coordinates were identified at each temperature as (0.375, 0.375, 0.375) whereas the lithium shift in positional parameter x over the 32e site is reported Fig. 4.8. The plot describes a lithium atom that is locked into its initial position. Profile fit parameters, numbers of refined ADPs obtained are summarised in Table 4.5. It is noteworthy to observe that the refined occupancy of potassium and lithium produces a stoichiometry in good agreement with that determined from EA analysis of this material which gave its final formula as $K_{0.5}Li_{0.5}Os_2O_6$.

$$K_{1-x}Na_zOs_2O_6$$

PND refinements of the second compound, derived from the potassium osmate pyrochlore, was started in the β-pyrochlore description, $Fd\bar{3}m$ by introduction of the Os (0, 0, 0) and O (x, $\frac{1}{8},\frac{1}{8}$) coordinates. Several regions were excluded as likely instrumental artefacts. Background was fitted with a 8 term, Fourier series function with a pseudo-Voigt peak shape, in the range 24–140° 2θ. Initial iterations in the refinement included background parameters, the histogram scale factor, peak shapes, and lattice parameter. Although the X-ray diffraction pattern evidenced missing scattering density, due to the fact that both the K^+ and Na^+ cations were not initially introduced in the refinement, the least square fit proceeded smoothly and gave profiles fit of R_{wp} = 5.67%, R_p = 4.14%, χ^2 = 7.67. A first difference Fourier mapping allowed the location of a significant electron density in proximity of the central site and at coordinate $\frac{1}{2},\frac{1}{2},\frac{1}{2}$, corresponding to the same region where nuclear density was found by refinement of the PXD data. The two missing atoms were, therefore, introduced into the refinement. Due to evidence of missing intensity between the 8b and the 16d positions, the potassium was initially introduced on the central site at $\frac{3}{8},\frac{3}{8},\frac{3}{8}$, excluding any potassium on the same site partially occupied by the Na^+. Na^+ and K^+ ADPs were constrained to be equal and their occupancies fixed at values suggested by EDX, with an overall value of 1.3. An aluminium impurity phase and OsO_2 impurity were also included in the refinement. The structure refinement using the 2 K data in $Fd\bar{3}m$ proceeded smoothly, and the introduction of cell parameters, peak shape profiles, along with the refinement of atom positions and isotropic temperature factors, resulted in a significant improvement in the least-squares fit. The model with K^+ on the central site and Na^+ at coordinate $\frac{1}{2},\frac{1}{2},\frac{1}{2}$ refined to R_{wp} = 3.39%, R_p = 2.08%, χ^2 = 5.51. Careful inspection of the diffraction pattern confirmed the compound belonged to the space group $Fd\bar{3}m$

and did not show any other extra reflections, as reported for KOs_2O_6 by Schuck *et al.* [71].

The final refined parameters are listed in Table 4.6 while derived bond lengths and angles of interest are shown in Table 4.8. However, as for KOs_2O_6, the ADP associated with the A site in this atom in this description, refined to a large value and presuming similarities with the precursor, displacement off-centre (along the four [111] directions) was, hence, allowed. This cation position displacement refined steadily to a 32e site x, x, x and resulted in a concomitant reduction of the potassium and sodium ADPs compared to those found with the model described above. To further investigate if possible correlation factors (between cation displacement and ADPs) may have contributed to the improvement in the profile fit achieved with this second description, and to obtain a more realistic distribution of the smaller cations, a partially constrained iterative model was adopted at the outset. The position of the potassium and of the sodium atoms and the ADPs of the atoms of the cell were refined one at a time and only finally uncoupled and refined isotropically together in the next refinement cycles to give the final values listed in Table 4.6.

Much more satisfactory convergence was achieved at this stage and the ADPs of the sodium and potassium cation sites showed a significant decrease compared to the refined values achieved with the potassium assigned to a 8b site. Improvements obtained with this second model were expected as the concomitant occupation of the 8b and the nearby 16d (2.2 $\AA$ away one from the other) would result in a rise of the free energy level of the two ions of interest. A close inspection of the refined parameters, obtained when the potassium is allowed to displace from the central site along the adjacent site, suggested also that this description was more appropriate in terms of bond distances. Although these two models are effectively a similar depiction of the scattering density of $K_{1-x}Li_yOs_2O_6$ at 2 K, the steady refinement of the potassium ions, the more reasonable ADP values obtained for this atom and sodium, and the corresponding improvement in the least squares refinements, proved this model as a better representation of the cation distributions in $K_{1-x}Li_yOs_2O_6$. The refined structure for this compound is in line with the description of the pure potassium pyrochlore which sees the confinement of the potassium ion to one side of the bigger 32e position in the structure cavity. It should be noted that the occupational parameters for sodium and potassium, which were initially constrained to give 1.3, as from elemental analysis, were refined and produced a steady model. The sodium and potassium content

Tab. 4.6: Model of $\mathrm{K_{1-x}Na_zOs_2O_6}$ refined by PND, space group $Fd\bar{3}m$. Esds in parentheses.

		2 K	**15 K**	**100 K**	**300 K**
K	*site*	**32*e***	**32*e***	**32*e***	**8*b***
	x	0.3469(5)	0.3475(2)	0.3704(2)	0.375
	Occ	0.33	0.33	0.33	0.33
	Ui/Ue × 100	3.588(1)	5.73(4)	5.81(2)	7.2(7)
Na	*site*	**16*d***	**16*d***	**16*d***	**16*d***
	x	0.5	0.5	0.5	0.5
	Occ	0.35	0.35	0.35	0.355
	Ui/Ue × 100	5.93(2)	6.33(2)	8.28(8)	9.42(4)
O	*site*	48*f*	48*f*	48*f*	48*f*
	x	0.3156(1)	0.3162(4)	0.31680(1)	0.31692(1)
	Occ	1.0	1.0	1.0	1.0
	Ui/Ue × 100	1.14(4)	1.11(8)	1.47(4)	1.67(2)
Os	site	16*c*	16*c*	16*c*	16*c*
	x	0	0	0	0
	Occ	1.0	1.0	1.0	1.0
	Ui/Ue × 100	0.122(2)	0.13(5)	0.31(6)	0.47(7)
a		10.20889(1)	10.2085961)	10.20980(1)	10.22037(5)
χ^2		2.66	2.83	3.37	4.43
$\mathbf{R}_{wp}$		3.17%	3.25 %	4.02%	3.94%
$\mathbf{R}_p$		2.48%	2.56 %	3.55%	2.65%

estimated from the model was in very good agreement with elemental analyses.

The refined structure could no longer be described as a 'β-type'. It presents, in fact, the same cation arrangement of an *inverse* (β-pyrochlore) and the 16*d* site partially occupied as in a conventional $\mathrm{A\square B_2O_6\square}$ *defect*-type pyrochlore. The different conditions used for the doping of $\mathrm{KOs_2O_6}$ with sodium chloride lead to an increase in the alkali metal content in the structure, compared to the parent $\mathrm{K_{0.5}Li_{0.5}Os_2O_6}$ system, and this additional sodium was essentially accommodated by an increased occupancy of the 16*d* site which can allow up to 2 cations per unit cell. This second model was, therefore, used as the starting point for neutron diffraction data collected for the next temperature. Profile fit parameters, atom positions and refined ADPs obtained are summarised in Table 4.6. A representation of the structure at 2 K is shown in Fig. 4.10.

As the temperature was raised above 100 K and up to 300 K, the thermal motion of the cations in the structure increased further and the representation used to describe the scattering density at low temperature became less adequate to represent the cation density in the cage. This was evidenced by refining each set of data, collected at temperature higher than 2 K, using both models earlier described to investigate the cell at 2 K. Although the description with K on the 32*e* and Na on the 16*d* represented at its best the scattering density of this sodium derived pyrochlore in the temperature range between 2 and 100 K, at T = 300 K the least square fit become slightly worse. The potassium ADP increased and, at the same time, its standard deviations in this region become so large that was not really possible to determine whether this trend was a significantly better experimental description of the scattering density of the cell compared to the model with potassium on its ideal site, described in Table 4.6. The significant variation in the sodium and potassium ADPs when this last ion is fixed on the ideal site between 2 and 300 K is displayed in Fig. 4.11. The magnitude of the K^+ ion's extracted ADP is almost double (open circle) that of the same atom displaced off-centre (filled circle). The same trend is manifested by the sodium atom which has an ADP that increased according to the model investigated. The higher ADP value for this atom, compared to potassium, was expected as a result of the partial occupancy of the smaller 16*d* site($< \frac{1}{4}$).

Assuming a similar behaviour to the parent $\mathrm{KOs_2O_6}$, the site occupancy of K^+ was left to refine and a decrease in the occupancy value from 0.18 to 0.08 was registered. Such a changing in the level of potassium on the 32*e* site soon foreshadowed a possible high temperature redistribution of potassium from the position occupied by the atom at

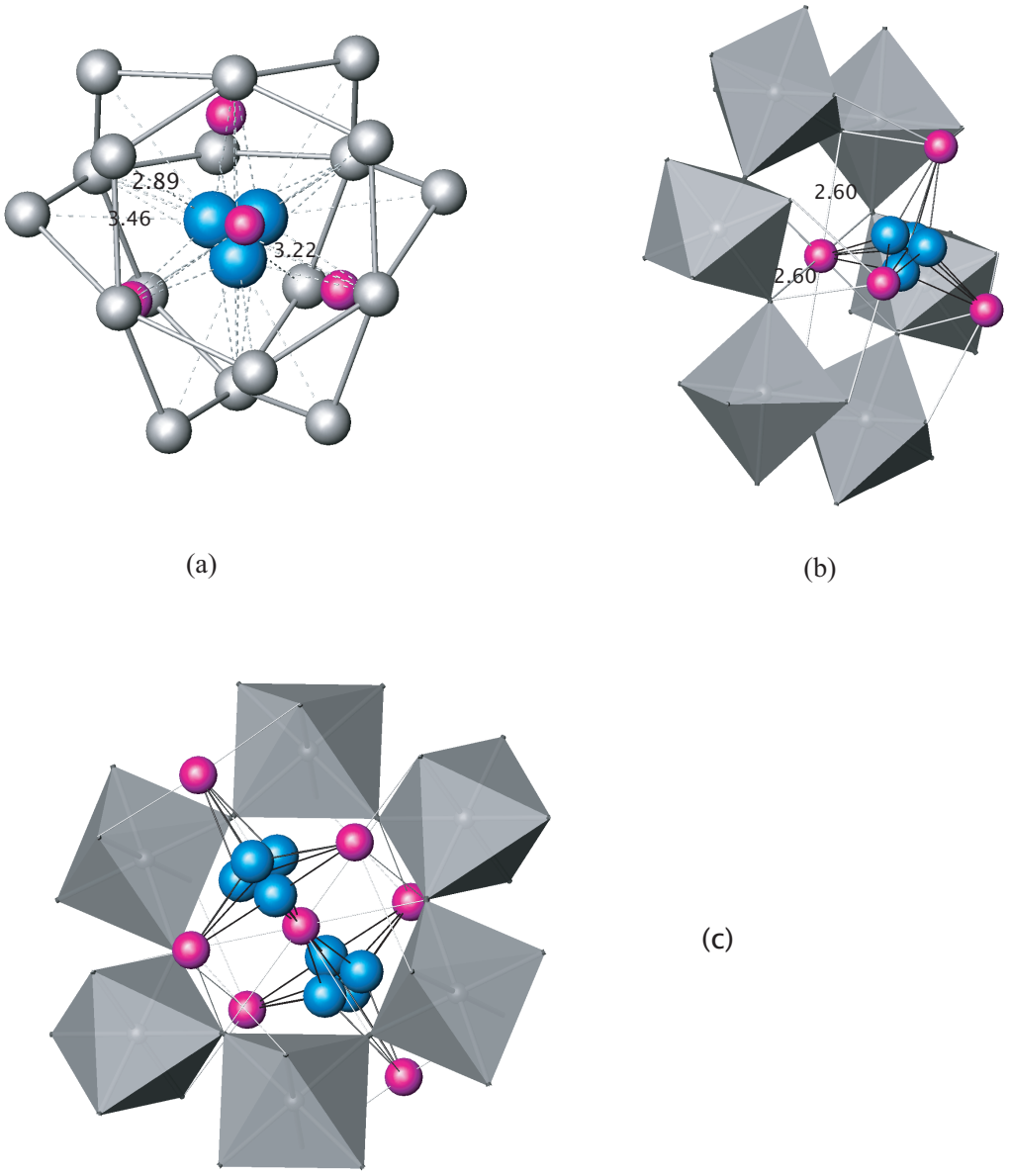

Fig. 4.10: Crystal structure of the defect pyrochlore $K_{0.6}Na_{0.7}Os_2O_6$, as from structure model at 2 K, showing the A and A' cation arrangement around the 8b site and 16d site. (a) Spacial representation around the structure cavity formed by 18 oxygens (grey spheres) showing the off-centre displacement along the the four [111] directions of the potassium atom (blue) and the three different K–O bond distances to oxygens (esds ommitted in the diagram, range from 0.02 to 0.04). Purple spheres represent sodium atoms. (b) Coordination environment of both potassium and sodium to oxygen showing the octahedral network. Bond lengths refer to Na–O distances (esds 0.04). (c) Cavity density as seen along the [110] directions showing the hexagonal hole and the cations coordination. As the temperature increases up to 300 K, the potassium shifts onto the ideal site for this atom and its structure coordination become very similar to that of the potassium in the mixed K-Li phase; Na^+ maintains its former position.

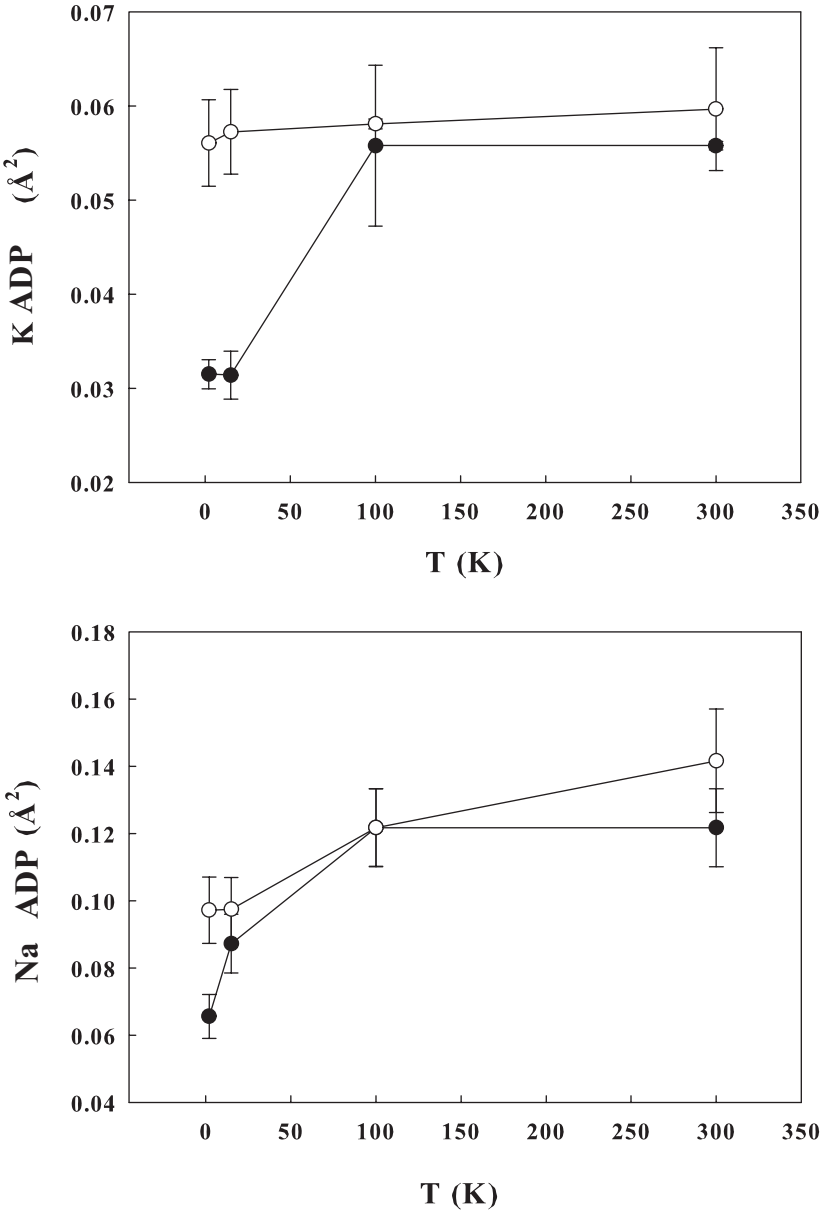

Fig. 4.11: Variation of K and Na cations ADPs for $K_{1-x}Na_zOs_2O_6$ when K was assigned to the 8*b* site, open circle, and when Na was assigned to the 32*e* site, filled circle, as a function of temperature. Esds are shown as error bars.

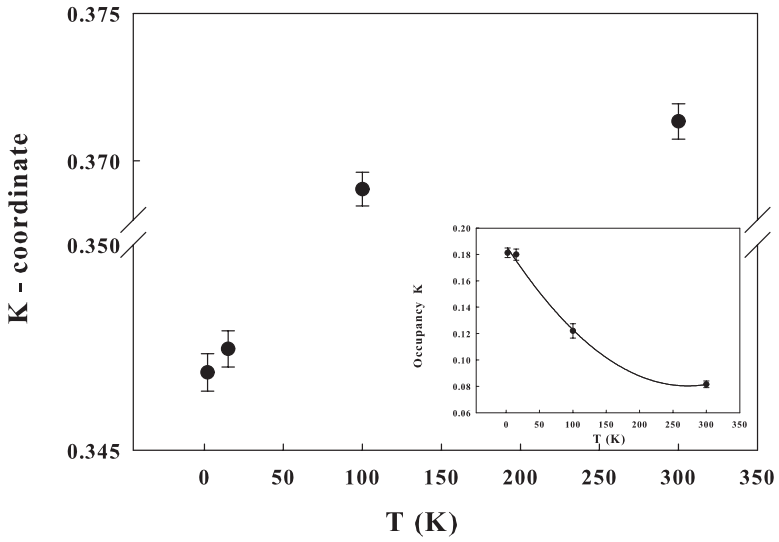

Fig. 4.12: The refined positional coordinate x for K^+ on the 32e site as a function of temperature in $K_{1-x}Na_zOs_2O_6$. The insert reports the variation as a function of temperature in the refined site occupancy parameter for this ion. Esds are shown as error bars.

lower temperature. The more logical rearrangement at RT would see potassium sitting on the ideal central site. Potassium was then relocated at coordinate $\frac{3}{8},\frac{3}{8},\frac{3}{8}$, this cation redistribution improved the final fit and better modeled also its thermal factors, see Table 4.6. This improvement in the R factors, coupled with a reduction in the occupancy of the site occupied by K^+ ions confirmed the latest model, which also uses a minimal number of refinable parameters, as the best description of the structure at 300 K. Final lattice parameters, R factors, fractional coordinates and ADPs parameters are listed in Table 4.6 while selected bond lengths and bond angles are listed in Table 4.8 .

Fig. 4.12 shows the variation with temperature of the potassium displacement. It increases linearly with temperature over the region of temperature investigated, whereas the inserted plot represents the variation in potassium level on the 32e site, linked to the potassium on the 8b obtained when this is varied freely. The potassium site occupancy on the 32e site decreased towards zero in line with this change. This represented the most realistic statistical distribution of potassium density from the 32e to the 8b site.

4.2 Discussion

In an attempt to dope the superconductor KOs_2O_6 and synthesise the unknown compounds $Li_2Os_2O_6$ and $Na_2Os_2O_6$, which could possibly show higher T_c, two new partially exchanged potassium osmates were produced, $K_{0.5}Li_{0.5}Os_2O_6$ and $K_{0.7}Na_{0.6}Os_2O_6$. The products with the limiting stoichiometry described above could not be obtained by conventional solid state methods, as the products did not crystallise in the desired material but in 'mild' ion exchange conditions.
A combination of EA and diffraction studies confirmed, within experimental error, the stoichiometry of two phases in the osmate family, $K_{0.5}Li_{0.5}Os_2O_6$ and $K_{0.7}Na_{0.6}Os_2O_6$, recognizing that (i) these two new compounds had two different cations on the A site, (ii) that the pyrochlore-type structure was maintained throughout. The cubic lattice symmetry and space group of precursor, KOs_2O_6, was preserved in both compounds although $K_{0.7}Na_{0.6}Os_2O_6$ differs from the lithium derivative in that it is a defect-type and not a β-pyrochlore type.

The determination of the structural details of the two new compounds was facilitated by the detailed knowledge of KOs_2O_6 that maintained its overall feature, even if partially exchanged, in that K^+ moves in the surrounding of the high symmetry site. Studies conducted on the previous chapter were invaluable for the potential structural complexities of the resulting ion-exchange phases, deriving from the fact that (i) the structure contained two cations on the A site, the distribution of which over the two possible set of sites was not immediately apparent; (ii) if different-sized cations are accommodated onto a larger A site, they may be displaced off-centre. After the removal of a small portion of K^+ from the precursor, a meaningful assignment of the scattering density could be obtained only by small displacement of the potassium ion ($\sim$0.02 $\AA$) away from the 8b site. This relocation better described the energy of the alkali metal cations and also led to a better bonding environment for all the atoms, typical of those found in pyrochlores (see Fig. 4.10). For grater exchange levels of the potassium ion, on the other hand, the ideal central site became a more stable position, as happen for $K_{0.5}Li_{0.5}Os_2O_6$, see Fig. 4.9.

The exchanged portion of atoms thus moves off their ideal positions which can be rationalised in light of electrostatic Coulomb-type interaction. In $K_{0.5}Li_{0.5}Os_2O_6$, the lithium cation was stabilised only after a displacement $\sim$0.17 $\AA$ from the high symmetry position which lies at the centre of the tetrahedron identified by the 4 near-neighbours, whereas for $K_{0.7}Na_{0.6}Os_2O_6$, Coulomb-type interaction between Na^+ were

minimised only on the 16*d* site.

Indeed, the pyrochlore phase formation strongly depends on the ionic radii of the *A* and *B* cations (with the structure generally being stable for ionic radius ratio values between 1.46 and 1.80 *Å*), but also other factors (such as electronegativity of cations) played an important role in the stabilisation of the final structure [117]. An idea of the interaction between the atomic orbitals of the precursor KOs_2O_6 and of the other two known members of the β-pyrochlore family, $RbOs_2O_6$ and $CsOs_2O_6$ was given by Kuneš, Jeong and Pickett, who studied in detail the electronic properties of this family and found that, in the β-osmate pyrochlore lattice, the alkali ions do not mix with the *d* state of Os and that they contribute as donors of an electron, becoming a source of an electrostatic potential [38]. The ion size, and hence its formal charge, becomes a very important factor that determines the site that the *A* atom will occupy, which will be pushed away from the vertices toward the centre of the tetrahedra they form, due to the electrostatic repulsions between the outer alkali ion orbitals and the orbitals of the four neighboring alkali ions.

The energy surface and deformation potential for the K–K ions distances was calculated and a dynamical instability of K^+ was found with energy minimised only after a displacement of the K ions by 0.65 *Å* from the ideal position toward the four [111] directions. For the first time not only the energy of the known AOs_2O_6 β-pyrochlore was calculated but also the energy of a fictitious $NaOs_2O_6$ compounds. While a very flat energy surface was found for K^+, even after a large shift, the high symmetry position of coordinate, $\frac{3}{8},\frac{3}{8},\frac{3}{8}$, was found to be unstable for Na^+, concluding that this crystal structure might not have been stable for the smaller alkali cations Na^+ and Li^+ simply because they do not stay near the ideal site. The electrostatic repulsions of the four neighboring alkali ions are more pronounced for the bigger alkali metal which orbitals are less localised than the 2*p* of Na. Further observations by Saniz and Freeman [118] showed that the *s* character in $NaOs_2O_6$ falls from 73%, to 31% in KOs_2O_6 and 23% $RbOs_2O_6$, to reach the 11% in $CsOs_2O_6$ whereas, at the same time, the *p* character rises from 16% $NaOs_2O_6$ to 31% in KOs_2O_6 and 38% $RbOs_2O_6$ to 55% in $CsOs_2O_6$ which explains the pronounced difference between the mixed K/Na phase and the K osmate pyrochlore in terms of cation distribution.

From all the data refined (see Table 4.5 and Table 4.6) the unit cell showed typical positive thermal expansion across the full range of temperatures investigated. For the phase partially exchanged by sodium, the variation in lattice parameter was almost

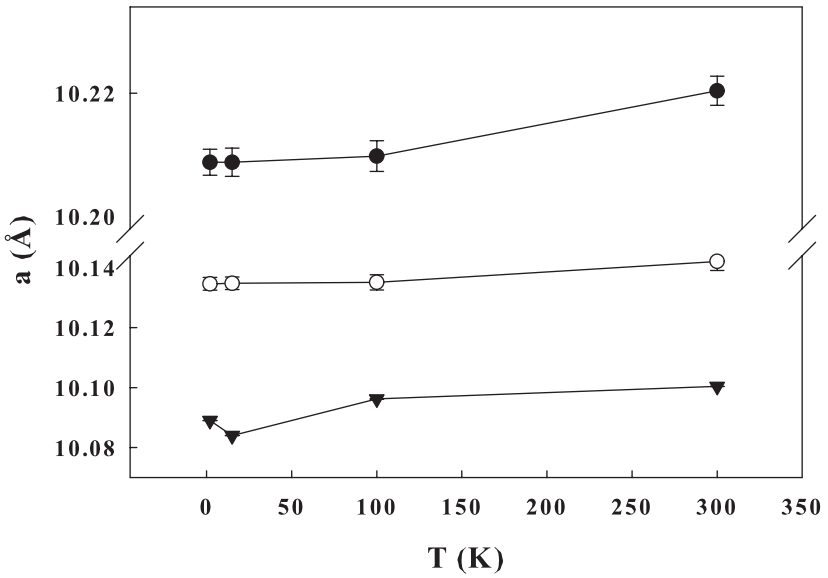

Fig. 4.13: Variation in the unit cell parameter a of KOs_2O_6, filled triangle, $K_{0.5}Li_{0.5}Os_2O_6$, open circles and $K_{0.7}Na_{0.6}Os_2O_6$, filled circles, with temperature. Esds are shown as error bars.

structural model independent, so identical trends were seen for data analysed with and without displaced potassium ions. It is noteworthy to observe how this increase in a occurred in the same temperature range where the pure potassium osmate exhibited a negative volume expansion, as it is shown in Fig. 4.13.

A linear increase with increasing the ionic radius of the cation introduced can be noticed. Since the Na^+ ion has a larger radius than Li^+, the lattice parameter of the sodium substituted KOs_2O_6 was also bigger than the lithium exchanged KOs_2O_6, an obvious consequence of the size of the A cation but also a function of the degree of substitution. A remarkable feature resulting from this plot is that the cubic lattice parameter of the two derived osmate compounds are larger than that of the parents pyrochlore osmate AOs_2O_6 (A = Cs, Rb, K) which a reported a nearly linear relationship when plotted against the ionic radius. As the potassium was exchanged with cation of smaller sizes, a linear decrease in the lattice length was expected due to the smaller size of Na^+ and Li^+. Final findings did not comply with this expectation and the KOs_2O_6 lattice parameter was found to be smaller than the exchanged phases. The linear relationship manifested by AOs_2O_6 suggested that the smaller values of the lattice parameter of AOs_2O_6 were dependent on the occupancy of the the A cations of the same site, which caused the structure to contract, whereas presence of two dif-

ferent cations (K^+Na^+ and K^+Li^+) resulted in a relaxation of the OsO_6 framework. Previously published data on the pyrochlore series $ANbW_2O_6$ and $A_2NbW_2O_6$ (A = Na, K, Rb, Cs) [119] showed similar lattice parameter trends to the derived osmate pyrochlore reported. In the niobium-tungstate series the a of the sodium compound was found much bigger than of the other three members of the family. This behaviour was attributed to the occupancy of the smaller 16d site by the Na^+ ions which appears to be the cause of the relaxation of the cell, whereas the cell contracts for A = K, Rb, Cs. The relaxation, hence, can account for the larger values of these two AA' osmates compared to the pure A osmates. It is plausible, therefore, to assume that the structural change is not only due to the size effect of the alkali metal ions but also to the interaction which determines the stabilisation of the alkali metal into a specific site and that makes the structure to contract or relax. The site occupied by the cation can, thus, contribute to the overall relaxation of the lattice with concomitant increase the lattice parameter.

Over the range of temperatures examined, the shift of K and A' cations, in both compounds, influences only in part the expansion of the OsO_6 framework. This evidences a small overall thermal expansion parameter in the range 2–300 K, the result of the small variation of the single variable parameter for O x (see Table 4.5 and Table 4.6), which reflects the small Os–O bond length variation. Selected bond distances and angles for the two new exchanged osmate compounds are shown in Table 4.7 and Table 4.8. Comparison of these values with bond distances in the pure AOs_2O_6 indicate a small deviation from the idealised pyrochlore framework, in excellent agreement with the value reported previously in Sn. 3.4 of Chapter 3. The Os–O bond length does not vary significantly remaining between 1.9141(7) $\AA$ (for the lithium exchanged potassium) and 1.9261(7) $\AA$ (for the sodium exchanged one), whereas the Os–O bond length value ranged from 1.9092(3) $\AA$ (for pure potassium), 1.9099(7)$\AA$ (for rubidium) and 1.9122(2) $\AA$ for cesium at the same temperature. The deviation from the idealised pyrochlore framework structure, which has oxygen on the 48f site with x = 0.3125, produces a small distortion of the OsO_6 octahedron with Os–O–Os angles nearly invariant with temperature as showed by small variations, almost within the estimated standard deviations, for these values (Table 4.7 and Table 4.8).

A schematic representation of the cation density in the structures obtained by ion exchange is presented in Fig. 4.9 and Fig. 4.10. The first highlights the coordination

Tab. 4.7: Derived bond lengths and angles of interest from PND models describing $\mathrm{K_{1-x}Li_yOs_2O_6}$ between 2 and 300 K, $Fd\bar{3}m$. The smaller O–Os–O angle defines the main rectangular cross section of the octahedra and the Os–O–Os angle characterises the staggered Os–O chain of the underlying pyrochlore lattice.

T/K	Os–O (Å)	∠ O–Os–O (Å)	∠ O–Os–O (Å)	∠ Os–O–Os (Å)
2	1.9141(7)	91.52(8)	88.48(8)	138.89(4)
15	1.9151(6)	91.69(7)	88.32(1)	138.88(3)
100	1.9144(7)	91.66(7)	88.34(7)	138.78(8)
300	1.9114(6)	91.74(7)	88.26(7)	138.58(10)

Tab. 4.8: Derived bond lengths and angles of interest from PND models describing $\mathrm{K_{0.7}Na_0.6Os_2O_6}$ between 2 and 300 K, $Fd\bar{3}m$.

T/K	Os–O (Å)	∠ O–Os–O (Å)	∠ O–Os–O (Å)	∠ Os–O–Os (Å)	
	2	1.9261(7)	91.49(8)	88.51(6)	138.99(5)
	15	1.9245(7)	91.52(8)	88.49(1)	139.85(3)
	100	1.9246(8)	91.58(7)	88.48(6)	139.36(8)
	300	1.9259(8)	91.59(7)	88.52(7)	139.47(10)

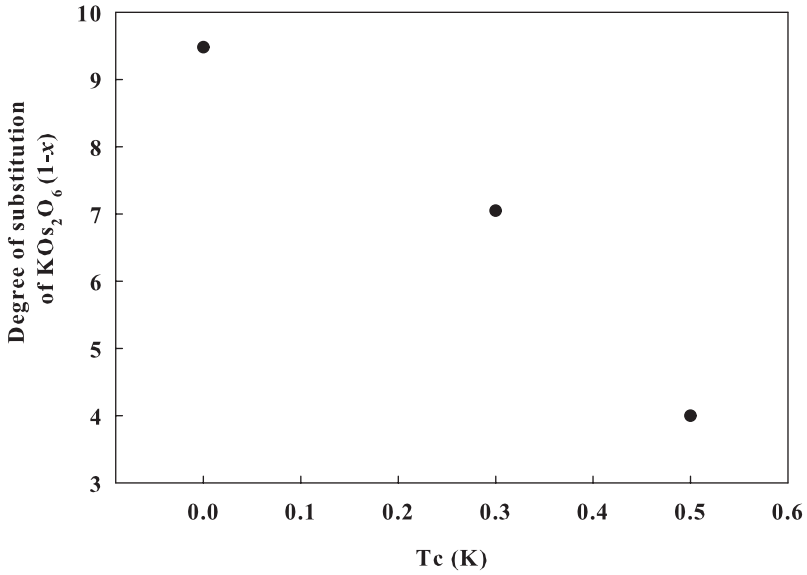

Fig. 4.14: Critical temperatures, T_c, for the superconductor KOs_2O_6 as a function of the degree of substitution. Figure shows the systematic decrease in T_c which occurs in the doped osmate compounds described in the course of the chapter.

environments of lithium and potassium cations from refinement of the neutron data earlier described in Sn. 4.1.4, with K and Li in the ratio 0.5:0.5 distributed on the ideal central site over the 32*e* site. Considering the immediate coordination of the the *AA'*-cations, these are surrounded by a puckered ring of 6 oxygen atoms; lithium is coordinated to oxygen at 2.57(2) *Å* and 2.78(1) *Å* while potassium is coordinated by K–O at [2.29(4)×3, 3.20(2)×3, and 3.32(2)×3 *Å*]. The cation coordination of Na and K ions in $K_{0.7}Na_{0.6}Os_2O_6$ is reported in Fig. 4.10, which describes the statistical distribution at 2 K of the K^+, displaced off-centre onto the 32*e* and Na^+, partially populating the 16*d* position. *A,A'* bond lengths to the framework oxygens, extracted from PND data described in Sn. 4.1.4, are shown in *Å*.

Magnetic measurements conducted on the two derived potassium pyrochlores, plotted in Fig. 4.3, showed that the superconducting temperature of substituted samples was systematically lower than in the undoped analogues. The larger superconductivity loss of Li-exchanged and the Na-exchanged sample relative to the pure potassium osmate, in magnetic field, and *A* and *A'* cation occupancy suggested that this change was highly correlated to the removal of portions of potassium from the cell rather than to the relocation of the smaller cation to adjacent sites.

The prevailing change at T_c was associated with a decrease of the U_{iso} of the potassium, while the framework atoms remained essentially unmodified. This decrease could be seen as the consequence of the counterbalance between the overall negative charge that the framework inherited following the substitution of the bigger potassium ions by smaller alkali metals and the positive charge of the cations which reduces energy vibrations of K^+. These findings, bring further evidence to the importance of the special combination of ionic radius suitability, site and the large amplitude of vibrations of this ion in dictating the properties of KOs_2O_6.

4.3 Conclusions

The effect of partial replacement of the K^+ ions on the structure of KOs_2O_6 pyrochlore by insertion of lithium and sodium ions was investigated. Two new materials were obtained. Initial reactions along with chemical, structural and properties changes that accompany the substitution were investigated. These studies showed that the exchanging process did not affect the pyrochlore main connectivity, which remained almost invariant throughout although some differences between these structure were identified. At very low temperatures the structures of these two new compounds differ slightly in the motion of the *A'*-type cation.

The structure of β-pyroclore AOs_2O_6 between 2 K and 300 K consists of a rigid framework of OsO_6 octahedra described in centrosymmetric $Fd\bar{3}m$ throughout the temperature range. The A ions are very weakly bound into the framework and show strong thermal motion on their sites. Although the crystal chemistry is very similar for the two members of the family, in the lithium exchanged compound the high temperature structural behaviours associated with the thermal motion of the alkali metal ion in the big cavities appears be quite different for from the sodium one and from the pure potassium. This behaviour is strongly correlated with the A radius size, the lattice interactions and the degree of potassium exchange. At very low temperatures, the structures of the K-Na pyrochlore for the smaller cation A is best described in terms of disordered localised A-type cations, similarly to the pure potassium osmate. At high temperatures above 100 K a model with the A-type cations around a central pyrochlore cavity position best describes the structure. This displacive disorder in the A site of the osmate analogs appears to be restricted to the K-Na phase only.

Results of this study are relevant to a better understanding of the interactions existing between mobile species and the surrounding framework and concluded a static displacive disorder in the A portion of the structure.

The analysis of associated magnetic properties conducted on these polycrystalline samples and the diffraction data, clearly showed that the doping significantly degraded the superconductive properties of both exchanged compounds. This highlights the crucial role played by the combination of the potassium size and the strong anharmonicity that this ion generates at low-temperature and confirms KOs_2O_6 once again as the most interesting material of this family-type of compounds.

5. HYDRATION, STRUCTURAL BEHAVIOUR AND PROPERTIES OF THE β-POTASSIUM PYROCHLORE OSMATE

Incorporation of water is a common phenomenon in structures like the defect pyrochlore family that have cavities where easily exchangeable or mobile species reside. The structures of a number of materials of this type have been studied and of note are the work of Barnes *et al.* [120] who investigated the structural changes that occur as water is absorbed, including studies as a function of pressure. In these materials as the moles of water, n, increases the potassium ions become displaced to the 16d site with water molecules occupying 32e sites and coordinated to the potassium ions. In $NaW_2O_6.nH_2O$ a similar structural model has been determined with the sodium ion 7-coordinate to framework oxygen and the oxygen of the water molecule present in the pyrochlore channels [121].

The structural and compositional evolution of one hydrated member of the family of osmium defect pyrochlores obtained from KOs_2O_6 together with its superconducting properties is reported in this chapter. KOs_2O_6 in moist air, or by contact with water during washing, absorbs water molecules into the structure influencing its properties. This sample has been studied as a function of temperature up to 580 K. The sensitivity of the osmate pyrochlores to water is also alluded to in the literature [89]. Despite this, methods of producing pure bulk polycrystalline material have involved washing with water to remove the commonly formed $AOsO_4$, A = K, Rb, Cs, impurities, followed by drying at 373 K. Furthermore, single crystals have often been handled in air allowing for incorporation of water at least into the surface of the material. This volume expansion due to insertion of water has not been observed for any of the β-pyrochlore $RbOs_2O_6$ and $CsOs_2O_6$ phases synthesised and reason was ascribed to the bigger size of Rb^+ and Cs^+ ions, which do not leave room for the water oxygen (O_w) to be accommodated within the structure cavities. The rubidium and the cesium derivative do not hydrate, even on washing the second phases with aqueous solution. On the basis of these observations, the discussion focused essentially on the KOs_2O_6 phase.

Crystallographic studies using a combination of X- ray and neutron powder diffraction were carried out on these phases to determine the distribution of cations within the pyrochlore channels and the effect of inserted water on this distribution. The combined use of these techniques represents a powerful methodology for obtaining a detailed structure analysis. These structural descriptions are correlated with the measured superconducting properties. Variable temperature powder neutron and X-ray diffraction show that an increase in lattice parameter occurs when water enters the pyrochlore structure; the water molecules are located in the α cages displacing a portion of the potassium ions to adjacent sites. On removing water the lattice parameter and structure revert to those of the normal β-pyrochlore crystallographic description. Hydration has the effect of reducing the onset of superconducting behaviour from a critical temperature of 10.25 K in fully dry KOs_2O_6 to 9.75 K in $KOs_2O_6{\cdot}0.12H_2O$.

5.1 Synthesis and Experimental Procedure of KOs_2O_6

Polycrystalline KOs_2O_6 was prepared by reaction of appropriate quantities of high-purity oxide OsO_2 (0.862g, 99,99%, Alfa Aesar) and of KO_2 (0.138g, Aldrich). These materials were ground together thoroughly in a Nitrogen dry box (N_2 glove box $<$ 2ppm H_2O), pressed into a pellet and placed into a silica ampoule together with a small gold tube containing 0.13 g of Ag_2O to create an oxidizing atmosphere. The tube was sealed under vacuum and heated to 723 K at a rate of 100 $K{\cdot}h^{-1}$ and maintained at this temperature for 16 h before furnace cooling. Bulk, polycrystalline KOs_2O_6 synthesised at 723 K was found to be purer than samples synthesised at lower temperatures (623 -703 K), while attempts to obtain materials at higher temperatures were unsuccessful as only the phases $KOsO_4$, OsO_2 and Os were detected as products. Bulk KOs_2O_6 can be reliably synthesised using this method but is not single phase and contains small amounts of OsO_2 ($\sim$5%), $KOsO_4$ ($\sim$20%) and OsO_4 (visibly observed as coating the wall of the tube and some crystallites). OsO_4 is highly toxic and evaporates rapidly from the product at room temperature in a stream of air. $AOsO_4$ phases, A = K, Rb, Os, can be removed by washing with water or other polar solvents. Various alternative washing regimes were used in this study as summarised in Table 5.1, including the use of dimethylformamide (DMF) which dissolves $KOsO_4$ while also having a molecular diameter too large to enter the pyrochlore structure. A sample (sample 'E'), consisting of a mixture of phases, was studied 'as-made'; for this sample all handling

Tab. 5.1: $KOs_2O_6{\cdot}nH_2O$ phases synthesis conditions, cell parameter and superconducting transition temperature T_c.

Sample	Sample description	Washing agent	Drying T and conditions	a (Å), PXD at 298 K	T_c
A	Hydr.1	Stirred with water 1 hour	298 K air	10.1202(2)	9.8(1)
B	Hydr.2 Neutr.sample	Stirred with water 30 minutes	350 K air	10.1106(3)*	10.0(1)
C	Part hydrated	Stirred with DMF, water washing	298 K air 598 K/N_2	10.0882(5)	10.1(1)
D	Dried.Exposed to air and dried	Not washed Not washed	598 K/N_2	10.0828(12)	10.2(1)
E	Dry box	Not washed	-	10.0795(2)	10.2(1)

*PND

was undertaken in strictly dry conditions with the sealed reaction tube opened in the dry box.

X-ray powder diffraction patterns for all samples were collected at room temperature (RT), over a 2θ range of 10-110° with a step size of 0.02° over 15 hours under dried nitrogen. Profiles indicated that for all the washed samples the main observed peaks could be indexed using a cubic cell with $a{\sim}10$ Å with the space group $Fd\bar{3}m$; a few very weak peaks ($I/I_0 < 0.04$) could be assigned to OsO_2. Accurate lattice parameters were obtained by fitting the profile using GSAS using the standard crystallographic description of the pyrochlore structure and varying only the profile parameters. For the unwashed samples additional peaks from $KOsO_4$ were observed in profile and accurate lattice parameters for the pyrochlore phase present in these materials were again extracted using profile fitting, with a second phase added to the modeling process to account for the $KOsO_4$ phase reflections. A 3 g sample was obtained by combining the products from several syntheses under identical conditions and using a washing scheme equivalent to sample 'B' and this was used for powder neutron diffraction studies.

Neutron diffraction data were recorded on the high flux D20 diffractometer at the Institut Laue-Langevin, Grenoble in the 2–500 K temperature range using a cryofur-

nace. Data were collected in the 2θ =10–150° range with a wavelength λ= 1.868 *Å*; a continuous ramp rate of $1 K \cdot min^{-1}$ was used. A longer (1 hour) data set was collected initially at 2 K. The sample was loosely sealed inside a vanadium can with a small header space.

5.2 Structure Analysis

Analysis of the various powder diffraction data sets was undertaken by the Rietveld method using the GSAS program; this program also allows the rapid analysis of a large number of variable temperature data sets using the SEQGSAS option. Initial analysis of the powder neutron diffraction data collected from sample 'B' ($KOs_2O_6 \cdot nH_2O$) used the standard coordinate description for the β-pyrochlore structure in $Fd\bar{3}m$ with Os (0, 0, 0), *A* ($\frac{3}{8}$, $\frac{3}{8}$, $\frac{3}{8}$) and O (x, $\frac{1}{8}$, $\frac{1}{8}$). Single crystal X-ray diffraction studies on KOs_2O_6 carried out by Schuck *et al.* [71] revealed Bragg peaks that violated $Fd\bar{3}m$ symmetry between 100 K and 400 K and the structure was thus reported to be *non-centrosymmetric* with space group $F\bar{4}3m$. Inspection of the data collected from $KOs_2O_6 \cdot nH_2O$ at 2 K, and at all other temperatures, showed no measurable intensity associated with the *002*, *024* or *006* reflections (see for example Fig. 5.1), supporting the $Fd\bar{3}m$ description rather than $F\bar{4}3m$ for this hydrated material.

An initial refinement of the structure using the 2 K data converged rapidly using the simple $Fd\bar{3}m$ KOs_2O_6 crystallographic model; cell parameters, peak shape profiles, atomic positions and thermal displacement parameters were sequentially added to the refinement which converged smoothly to yield acceptable R-factors (R_{wp}=3.95%, R_p=2.81%, χ^2 = 4.34). This model was then used as a basis for a SEQGSAS analysis of the remaining data sets from the temperature range 2–500 K. Preliminary analysis of the data extracted from the variable temperature range data centred on the extracted lattice parameter, the potassium site atomic displacement parameter (ADP_{iso}) and the background. Fig. 5.2(a) summarises the variation in lattice parameter between 2 and 500 K; between 2 and 350 K a normal monotonic increase in the a lattice parameter is observed before a significant drop between 350 and 450 K after which the cubic cell parameter starts to increase again. This drop in cell parameter was associated with a significant decrease in the background level (and also decreases in the extracted thermal displacement parameters associated with potassium, Fig. 5.2(b)). The former is

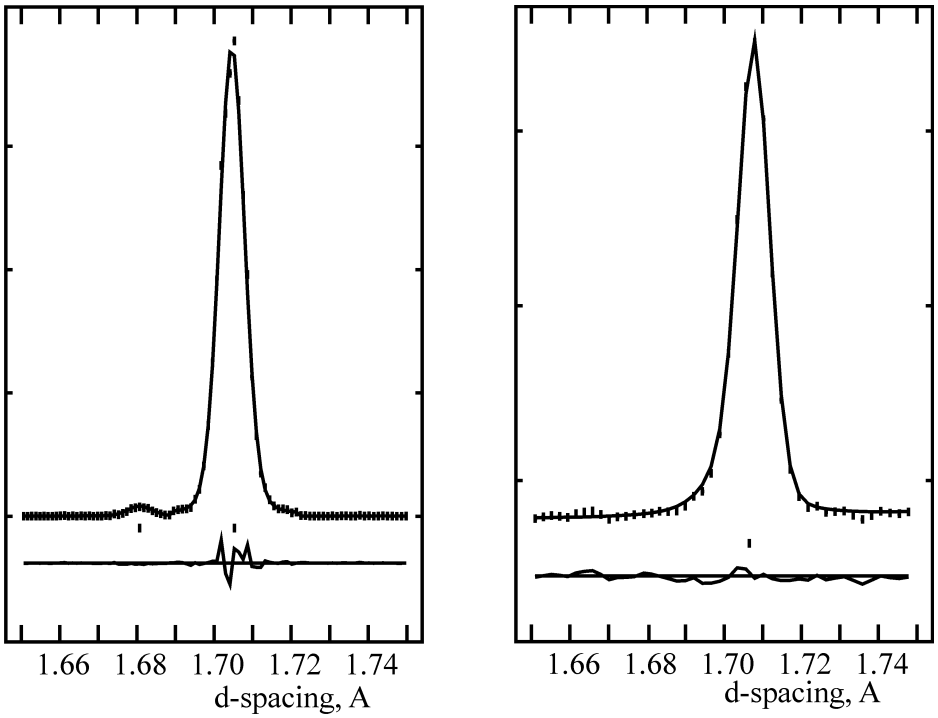

Fig. 5.1: Calculated, left, using Schuck's $F\bar{4}3m$ model [71], and observed, right 2 K, profiles for $KOs_2O_6{\cdot}nH_2O$ between 1.65 and 1.75 *Å* for data collected on D20. The calculated profile shows the *600* reflection at 1.6806 *Å* which is not visible in the experimental data from the hydrated $KOs_2O_6{\cdot}nH_2O$.

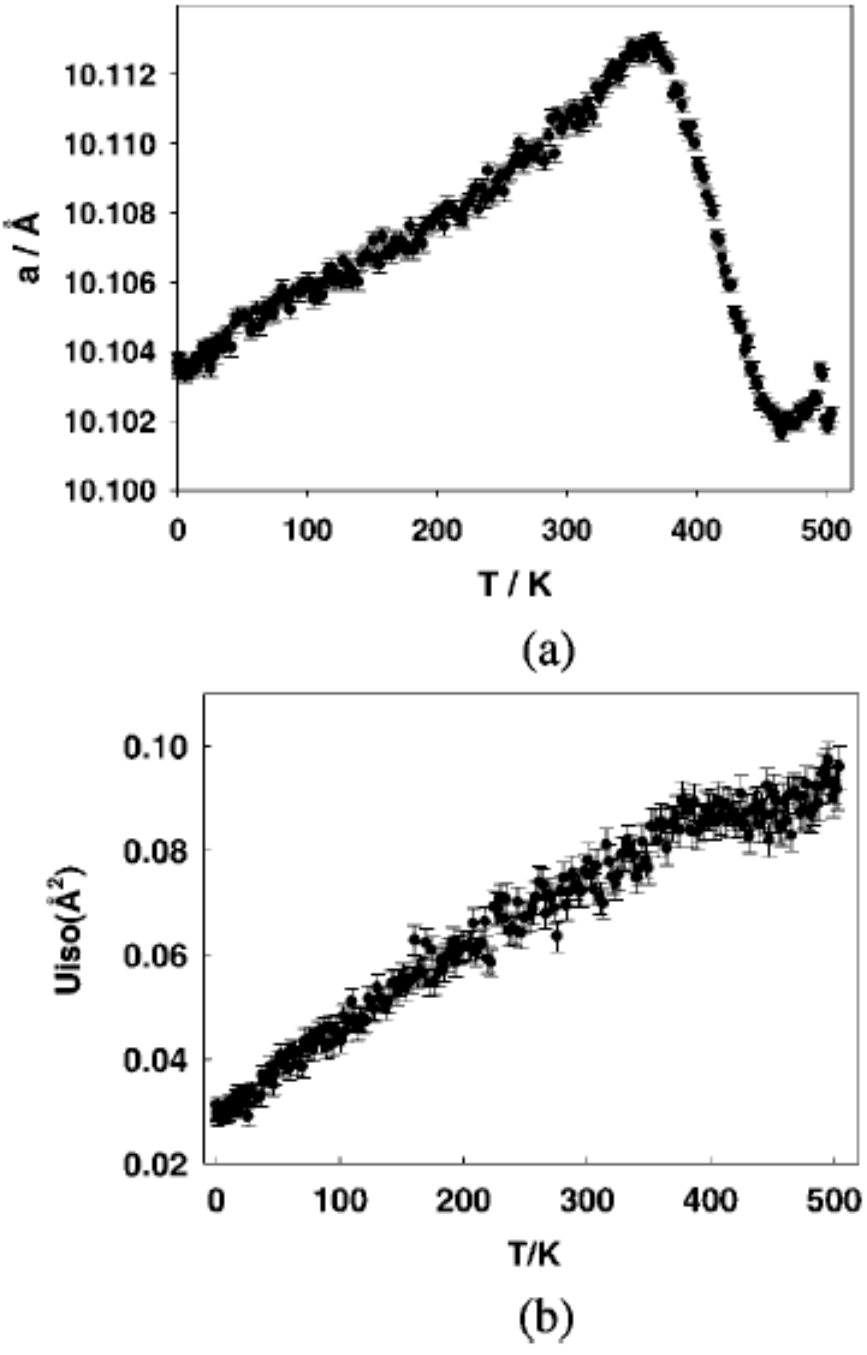

Fig. 5.2: (a) Lattice parameter, *a* (*Å*), as a function of temperature as determined from profile fitting of the neutron powder diffraction data. Estimated standard deviations (esds) are shown as bars. (b) Variation in extracted potassium ADP as a function of temperature. Both figures are related to the structure refinement using the simple β-pyrochlore based structure of KOs_2O_6.

indicative of a decrease in hydrogen content in the material and concomitant reduction of the large incoherent scattering associated with this isotope. A likely explanation of these behaviours, particularly when associated with the thermogravimetric analysis, Sn. 5.2.1, is that water is lost from the pyrochlore channels between 350 and 450 K and the correct description of the washed osmate pyrochlore, in the temperature interval $<$ 350 K, is $KOs_2O_6{\cdot}nH_2O$; based on the thermogravimetric analysis of the sample $n \sim 0.1$, therefore, a new structural model was constructed to represent the hydrated phase.

Previous work [120] on hydrated beta pyrochlores indicated that as water enters the structure the potassium ion shifts from the 8*b* site to the 16*d* site with the water oxygen position at 32*e* with $x{\sim}0.42$. The 2 K data powder neutron diffraction data were analysed further with this model in mind. Structure refinements were undertaken with just the osmate octahedra portion of the structure description and difference Fourier maps were calculated to determine the scattering density within the pyrochlore channels around the 16*d* and 8*b* sites. Possible sites for the missing scattering density were found, as expected, at the 8*b* site, with weaker features at adjacent 32*e* sites ($x \sim 0.32$) and around the 16*d*. Therefore a model was constructed with potassium allowed to occupy both the 8*b* and 16*d* sites (with the total model potassium level constrained to represent KOs_2O_6 with water oxygen introduced to the 32*e* sites at (0.32, 0.32,0.32) again with the overall site occupancy constrained to be equal to the level of potassium displaced from the adjacent 8*b* site. No attempt was made to include hydrogen atom positions due to the low water content and the therefore small hydrogen scattering factor. This model is similar to that used by Barnes *et al.* [120] to describe hydrated phases in the $ANbWO_6{\cdot}nH_2O$ (*A*= K, Rb) systems and reflects the likely structural changes that occur when water enters the structure where it occupies a site close to the original potassium site (8*b*) displacing a portion of it to a position close to the 16*d* site. In order to reduce the number of refinable variables in the Rietveld analysis and allow stable refinement, the displaced potassium was fixed on the 16*d* site at $\frac{1}{2}$, $\frac{1}{2}$, $\frac{1}{2}$, and its atomic displacement parameter (ADP_{iso}) also fixed at 0.08 $\AA^2$.

Given the proximity of the potassium ion on the 8*b* sites and the oxygen on the *32e* site ($x{\sim}0.32$) these atoms were constrained to have the same ADP. All other positional parameters and thermal parameters were allowed to refine. The refinement converged satisfactorily giving the structure description for $KOs_2O_6{\cdot}nH_2O$ summarised in Table 5.2 and Table 5.3; the extracted fit factors were R_{wp} = 3.82%, R_p = 2.71%, χ^2 = 4.07 showing a small improvement over the simple β-pyrochlore model originally

used and further supporting this more realistic structure model though there was a small increase in the number of crystallographic variables. Fig. 5.3 shows the profile fits achieved using the simple β-pyrochlore model and the improved model with water oxygen and partially displaced potassium. The refined level of water oxygen produces a stoichiometry with $n = 0.08$, *i.e.*$KOs_2O_6{\cdot}0.08H_2O$, in good agreement with that determined from thermogravimetric analysis (TGA) of this material of 0.11 (see Fig. 5.6). Fig. 5.4 shows a representation of this hydrated structure.

This structural model was then used in the SEQGSAS refinement to analyse the full temperature range of data from 2K–350K. Once the material began to lose water as evidenced by the change in lattice parameter and TGA the model was adjusted to allow the fractional occupancy of the water oxygen site to vary freely with concomitant and linked variations in the potassium levels on the 8*b* and 16*d* sites. This model showed a decrease in potassium level on the 16*d* site (and linked water oxygen on the 32*e* site) with the site occupancy falling from 0.040(6) at 350 K to 0.000(6) at 450 K; the potassium site occupancy on the 8*b* site increased towards unity in line with this change and is reported in Fig. 5.5. This represents the expected loss of water from the structure and transfer of potassium from the 16*d* to the 8*b* site.

Once water was fully removed from the structure the crystallographic description was found to revert to one with full occupancy of the 8*b* site by potassium. The normal β-pyrochlore description and a model based on this simple description was thus used for the analysis of the remainder of the variable temperature data sets from 460 to 500 K. Note that while single crystal data for as-prepared, single crystal, anhydrous KOs_2O_6 [71, 99] indicate a cell symmetry of $F\bar{4}3m$, our data show no evidence for this crystallographic description. However, it is unlikely that we would be able to distinguish the two models due to the large thermal motion of the potassium ions at these temperatures, and only insignificant differences in the diffraction intensities. Fig. 5.10 (a-e) summarises the key extracted structural information from the powder neutron diffraction study.

5.2.1 Thermogravimetric Analysis (TGA)

TGA experiments on two hydrated samples 'A' and 'C', shown in Fig. 5.6, showed that the mass losses between 323K and 573K during heating were 0.42% and 0.17% respectively. The fully hydrated sample showed a further sharp increase in mass loss starting at around 523 K whilst for the partially hydrated sample a similar weight loss

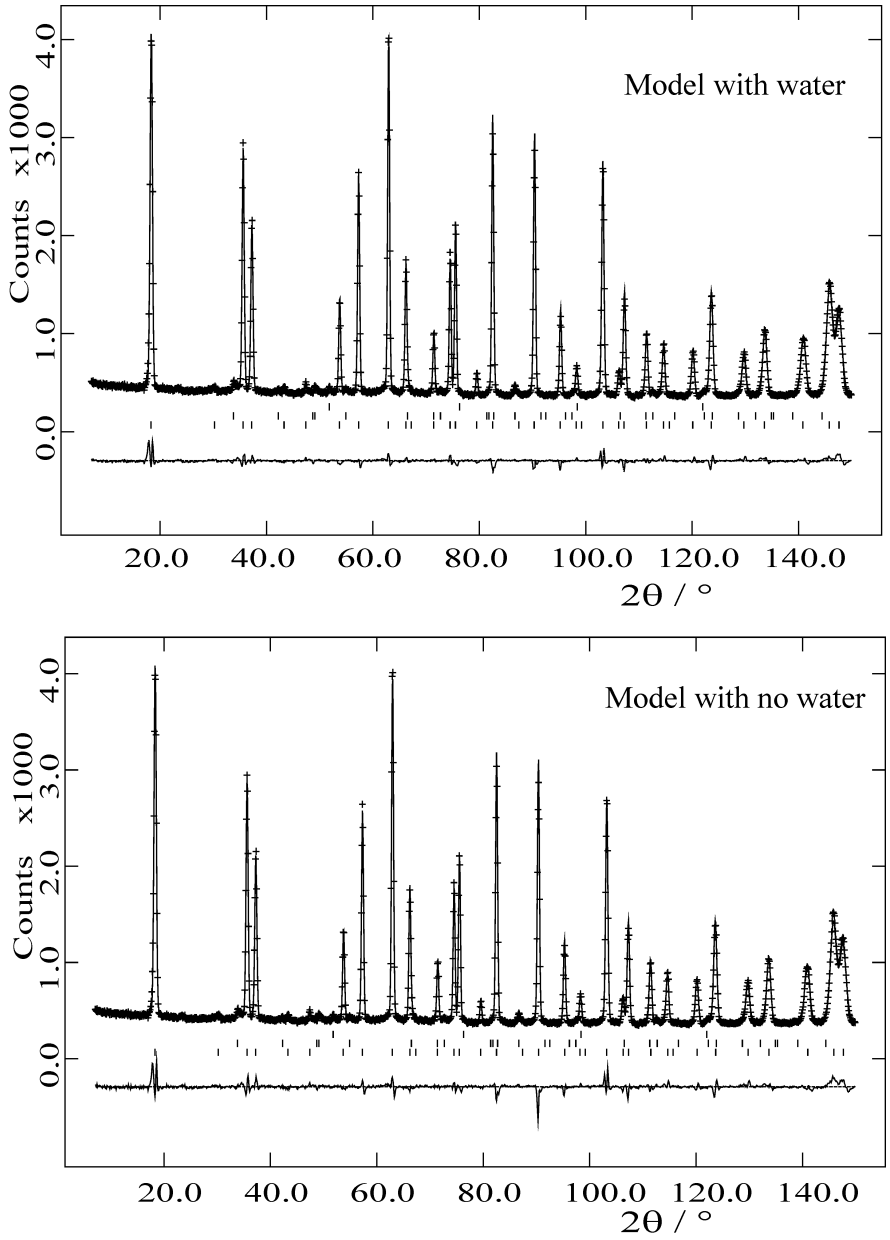

Fig. 5.3: Upper: profile fit achieved using the model summarised in Table 5.2. Lower: the poorer profile fit to the same experimental data using the simple β-pyrochlore structure description. Crosses are observed data, upper continuous line is the calculated profile, and lower continuous line is the difference. Tick marks show the reflection positions.

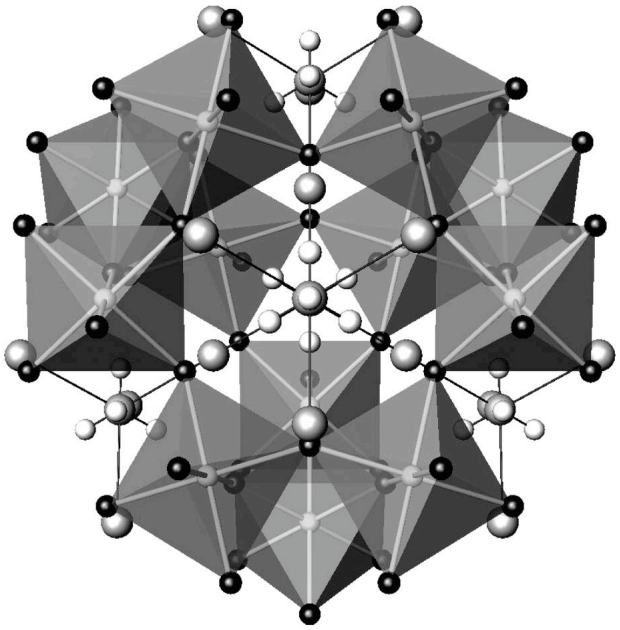

Fig. 5.4: β-pyrochlore based structure of $KOs_2O_6{\cdot}nH_2O$ showing the partially displaced potassium ions and associated water oxygen position.

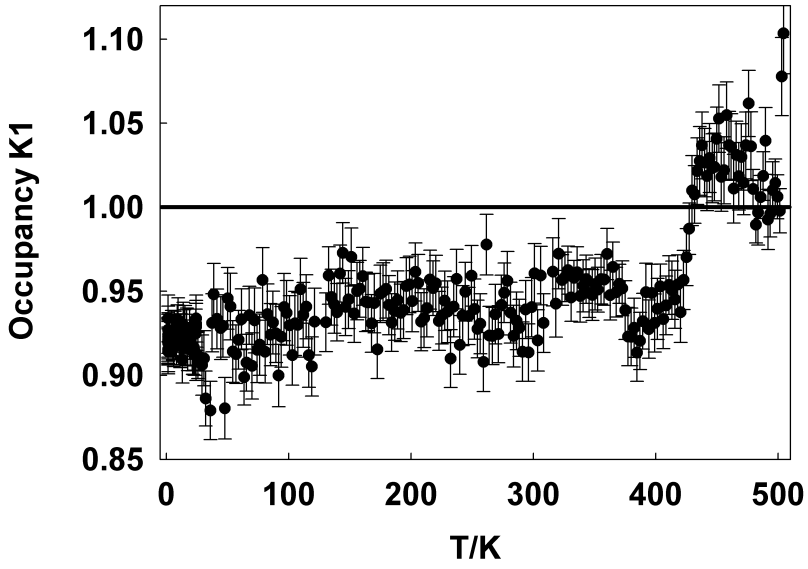

Fig. 5.5: Variation as a function of temperature in the refined site occupancy parameter for the K_1, 8*b*, position. Estimated standard deviations are shown as error bars.

Tab. 5.2: 2 K structure model 2 for $KOs_2O_6{\cdot}0.08H_2O$. Space group $Fd\bar{3}m$ KOs_2O_6, a = 10.10363(19). Esds in parentheses.

(a)Structural model					
name/site	x	y	z	$U_i/U_e \times 100\AA^2$	site occupancy
K_1 8*b*	$\frac{3}{8}$	$\frac{3}{8}$	$\frac{3}{8}$	2.22(10)	0.924(11)
Os 16*c*	0	0	0	0.10(2)	1.0
O_f 48*f*	0.31715(11)	$\frac{1}{8}$	$\frac{1}{8}$	0.51(5)	1.0
K_2 16*d*	$\frac{1}{2}$	$\frac{3}{8}$	$\frac{3}{8}$	8.00	0.038(6)
O_w 32*e*	0.326(7)	0.326(7)	0.326(7)	2.22(10)	0.022(3)

Tab. 5.3: Extracted key distances ($\AA$) and angles (deg) in $KOs_2O_6{\cdot}0.08H_2O$

(b) Bond Distances and Angles		
atoms	multiplicity	bond length/bond angle
K_1–O	×6	3.1104(11)
K_1–O	×12	3.61968(19)
Os–O	×6	1.9106(4)
O–Os–O	×3	91.86(4)
O–Os–O	×3	88.14(4)
K_2–O	×6	2.5697(8)
K_2–O_w	× 6(both sites occupied at low levels)	2.067(7)

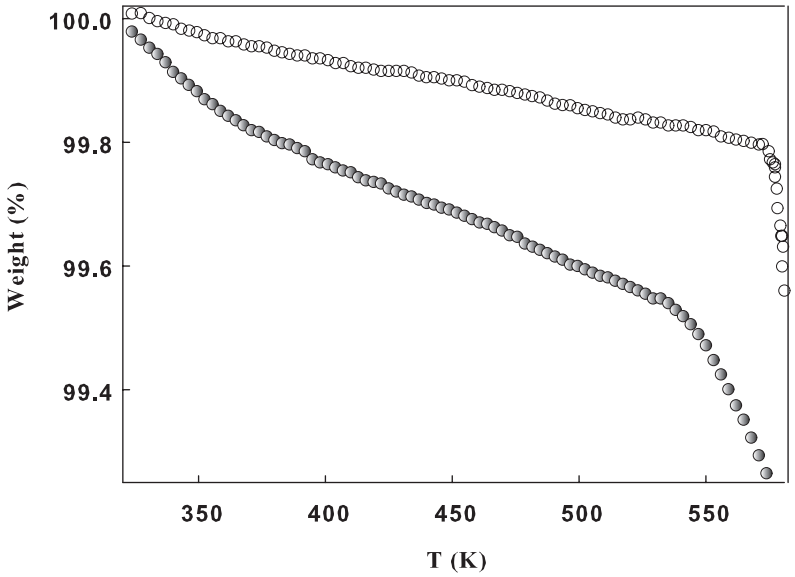

Fig. 5.6: TGA data for the fully hydrated (sample A, open circles) and partially hydrated KOs_2O_6 (sample C, filled grey circles).

occured starting around 573 K. These large additional weight loses could have a number of origins. Residual volatiles trapped within the samples such as OsO_4 or $KOsO_4$ may have been evolved or more likely it is due to decomposition of the pyrochlore phase through loss of potassium oxides or disproportionation and loss of OsO_4.

Extra peaks that appeared in the powder PXD patterns of samples repeatedly heated to 500 K and which occured with simultaneous broadening and weakening of the pyrochlore reflections confirmed this decomposition. Considering just the mass loss between 323 and 530 K, which corresponds to the temperature range where significant changes in the lattice parameter occured in both X-ray and neutron diffraction data, the water content in the structure for the fully hydrated sample correspond to 0.11 mol, *i.e.* $KOs_2O_6{\cdot}0.11H_2O$ whilst for the partially hydrated sample it is around half of the amount. As already pointed out, the former value is consistent with the stoichiometry obtained from the refined site occupancy factors of the similar sample used for NPD analysis, though the great instability of the phases seen on heating further above 530 K in flowing argon means that the values should be treated with some caution.

5.2.2 Superconducting Properties

VSM data were collected for all samples, 'A-E'; Fig. 5.7 shows data from key samples over the lowest temperature portion where the materials become superconducting. The

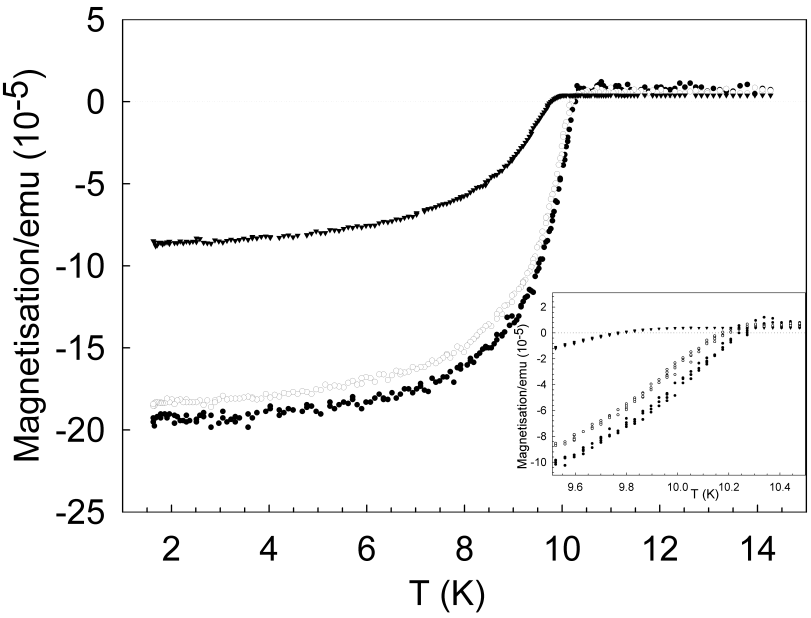

Fig. 5.7: Overall magnetisation of the materials for 'D' dried (filled circles), 'C' (stirred with DMF and washed briefly with water, open circles) and 'A' (fully hydrated, filled triangles) samples. Inset: expanded view around 10 K.

data appear to show a correlation between the level of hydration and the superconducting transition of the material, with T_c lowering as more water is incorporated into the structure. Determined onset T_c's for 'A', 'C' and 'D' were 9.8(1) K, 10.1(1) K and 10.2(1) K respectively.

5.2.3 Variable Temperature X-ray Analysis in an Open System

PXD data sets were collected from sample 'C'. These were fitted in a similar method to the neutron diffraction data sets using SEQGSAS but due to the reduced sensitivity of the X-ray method to potassium and oxygen in this system, just a simple osmate framework model in $Fd\bar{3}m$ was used to fit the data and extract the variation of the lattice parameter as a function of temperature on both heating and cooling cycles between 298 and 580 K (as shown in Fig. 5.7). Values obtained on heating showed similar variation as those seen with the powder neutron diffraction data with a contraction centred around 450 K. On cooling the lattice parameter of the thermally dehydrated phase contracts, producing a room temperature value significantly smaller than the hydrated starting material and consistent with the value of an anhydrous as-prepared KOs_2O_6 phase, sample 'E'.

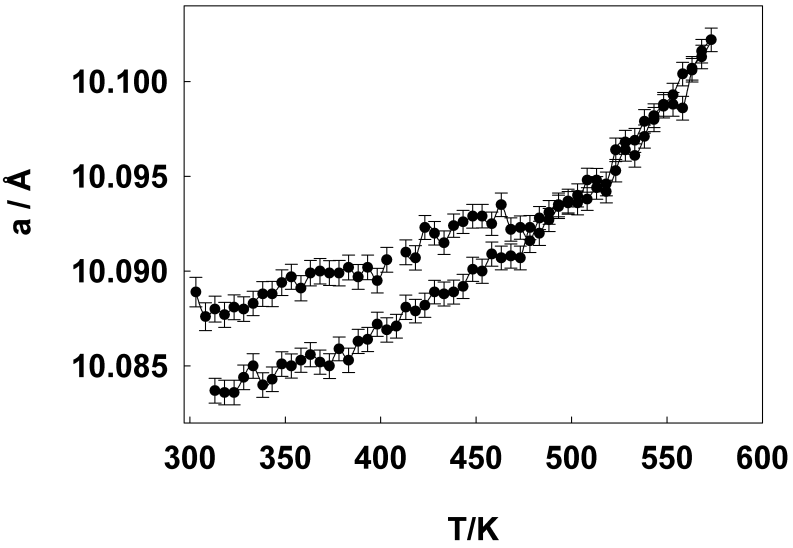

Fig. 5.8: Lattice parameter of $KOs_2O_6{\cdot}0.11H_2O$, $n \sim 1$, samples as a function of temperature from PXD displaying variation of a on heating and cooling in flowing N_2

5.2.4 Discussion

The observed increase in lattice parameter on washing potassium osmate pyrochlores with water reflects the incorporation of water into the pyrochlore channels. The magnitude of this increase of 0.04(1) *Å* is smaller than that observed in other potassium β-pyrochlores *e.g.* $KNbWO_6$ where the lattice parameter increases by around 0.20 *Å* for the addition of one mole of water into the material. This indicates only partial hydration in the osmate materials. Washing the samples in DMF alone produced no increase in lattice constant, consistent with this observation. The hydration dehydration is initially fully reversible, though cycling through this process by heating to above 575 K was found to result in slow degradation of the material with loss of crystallinity and appearance of additional phases. Thus comparison of variable temperature powder neutron diffraction data from the hydrated phase and an anhydrous phase, Fig. 5.9, shows that once the material is fully dehydrated the lattice parameter reverts to that of a heated sample of anhydrous KOs_2O_6.

The mode of incorporation of water into the superconducting potassium osmate pyrochlores parallels that seen in other β-pyrochlores. That is as water is inserted into the pyrochlore channels it displaces the potassium ion from the 8*b* site to 16*d* site. In the $KOs_2O_6{\cdot}0.11H_2O$ system this cation-shift mechanism seems to occur only partly,

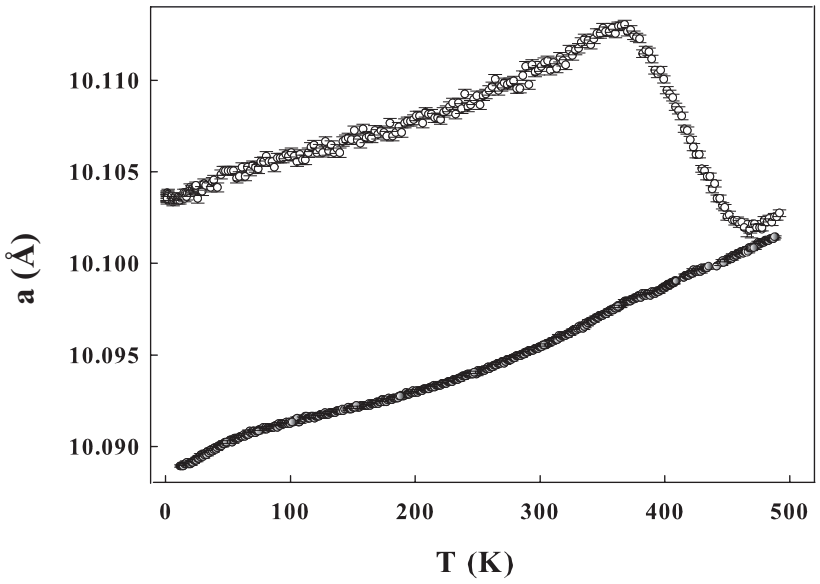

Fig. 5.9: Comparison of the lattice parameter variation of hydrated $KOs_2O_6{\cdot}0.11H_2O$, open circles, and anhydrous KOs_2O_6, filled circles, as a function of temperature between 2 K and 550 K from powder neutron diffraction data.

limiting the level of water incorporated. The origin of this effect is unclear and attempts to further increase the water content through, for example, extended periods of stirring with water produces materials with a maximum water content of n (in $KOs_2O_6{\cdot}nH_2O$, approaching 0.2) and result in increasing sample degradation. This may reflect the ease with which osmium (5.5+) can be reduced thus undergoing a slow redox reaction with water. Another effect might be the smaller lattice parameter of the KOs_2O_6 ($a \sim 10.1$ Å) system compared with $KTaWO_6$ ($a \approx 10.3$ Å) impeding water molecule and potassium ion diffusion along the pyrochlore channels.

Indeed comparison of the various potassium β-pyrochlores that form fully hydrated phases $AB_2X_6{\cdot}H_2O$ show that hydration is limited to those with large lattice parameters for the anhydrous material; thus, $K(Ta,Nb)WO_6$ and $KNiCrF_6$ ($a \sim 10.24$ Å) [59] form a hydrated $KNiCrF_6{\cdot}H_2O$ ($a = 10.45$ Å) [58], but for phases such as $K(Ti_{0.5}Te_{1.5})O_6$ ($a = 10.06$ Å) [122] hydrated phases are unknown.

When water does enter the β-pyrochlore structure it is accommodated in the larger cavities surrounding the 8*b* site. However, this position is originally fully occupied by potassium though the site is effectively larger than that required by the ionic radius and coordination demands of this ion. Thus the ion may be locally displaced or show high ADPs associated with the ion *rattling* [99, 93, 38]. Even so there is insufficient room for the water molecule to share this 8*b* centred cavity with a potassium ion and

a proportionate level of potassium is displaced to the 16*d* site to accommodate the inserted water.

The thermal variations of key positional, bond length, angle and atomic displacement parameters are summarised in Fig. 5.10(a)-(e). The framework oxygen, O, *x* coordinate is the only variable, in combination with the lattice parameter, that defines the geometry of the osmium–oxygen framework and potassium–oxygen distances of the standard $Fd\bar{3}m$ β-pyrochlore description. Between 2 K and 350 K for $KOs_2O_6{\cdot}0.08H_2O$ this *x*-coordinate is almost invariant showing only a small, insignificant (within esds), decrease which translates in combination with the increase in lattice parameter over this temperature range into the expected small increase in Os–O distance (Fig. 5.10(c) and derived Os–O–Os bond angle (Fig. 5.10(d)) as the material expands. Between 350 and 450 K there is a marked increase in the O *x* coordinate which occurs simultaneously with contraction of the lattice as water is lost from the structure. The Os–O distance is almost invariant over this temperature range but the Os–O–Os bond angle contracts significantly as the OsO_6 octahedra tilt allowing the structure to contract and coordinate more strongly to the potassium ion on the K_1 site (Fig. 5.10(e)). This behaviour is also reflected in the potassium ion displacement parameter which plateaus in this region presumably as a result of the volume of the local coordination site decreases. Above 450 K the dry KOs_2O_6 material starts to demonstrate normal expansion of the pyrochlore framework with the Os–O, K_1–O distances and the Os–O–Os angle all increasing.

The effect on the superconducting properties in the $KOs_2O_6{\cdot}nH_2O$ system seems to be a slight degradation in both T_c and superconducting volume. Thus T_c falls from 10.2 K in totally dry materials to 9.8 K for$KOs_2O_6{\cdot}nH_2O$ ($n \approx 0.2$). Interestingly, the value for our anhydrous polycrystalline material handled totally in the absence of moisture (sample 'E') is slightly higher than previously reported values for KOs_2O_6 (Table 1). The decrease in T_c could have two compositional/structural origins. Incorporation of water results in a small increase in lattice parameter and the value of T_c shows an inverse correlation with lattice constant in the series AOs_2O_6 (A = Cs, Rb, K). Alternatively the *rattling* of the smallest potassium ions on the 8*b* sites has been proposed as a reason for the highest T_c value for this osmate derivative in the series A = K, Rb, Cs. That is low lying phonons are associated with the ratting potassium ion located in a highly anharmonic potential and this gives rise to anomalous electron scattering and strong-coupling superconductivity [104]. Incorporation of water into the KOs_2O_6 structure will affect the *rattling* of potassium ions/nature of the low lying phonons as

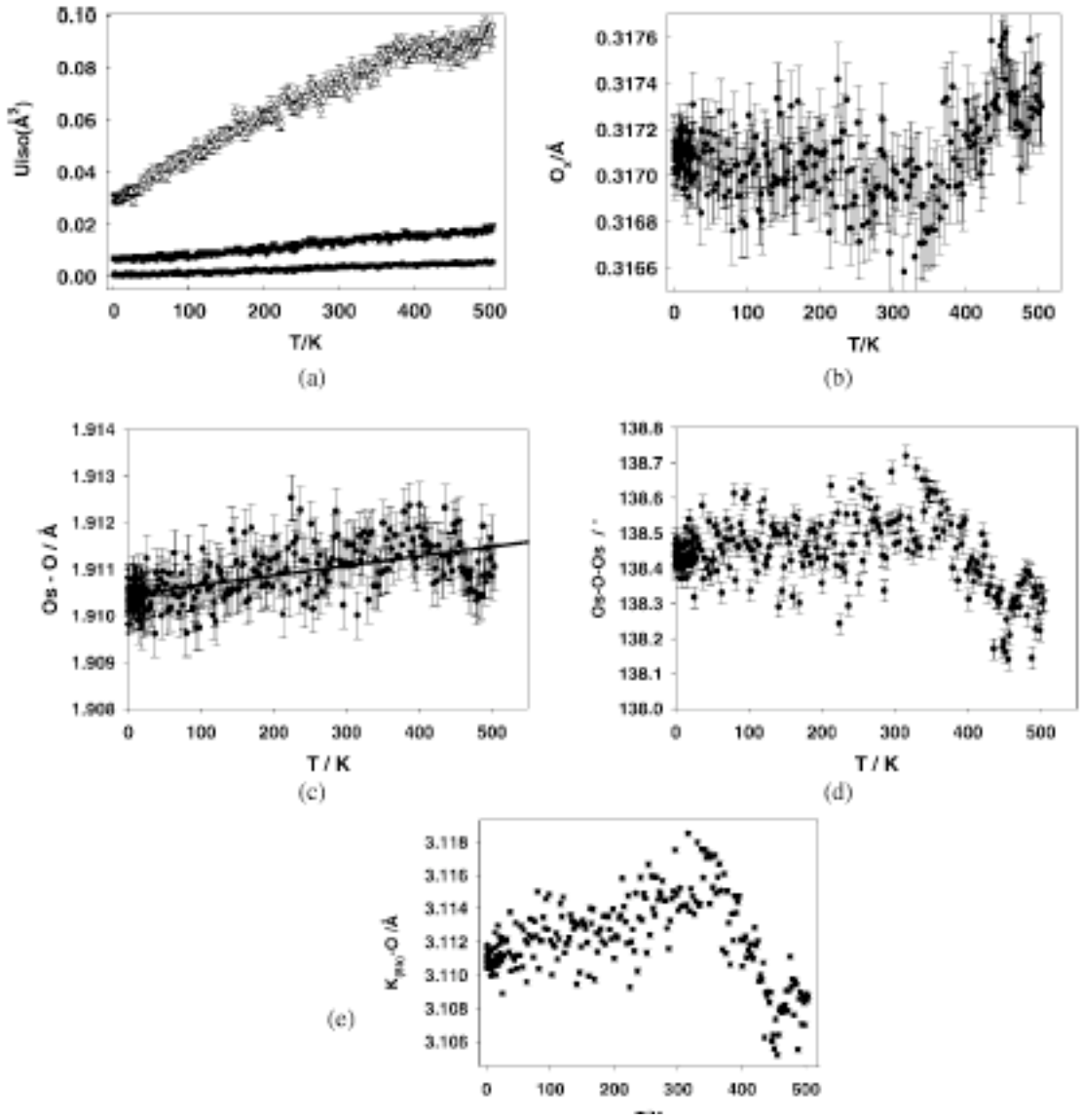

Fig. 5.10: a-e.Variation of various structural parameters as a function of temperature: (a) Uiso (*Å*) ADPs for K1 (O), Os (b) and O1(1); (b) framework oxygen (O1) *x* coordinate, (c) Os–O' distance, (d) Os–O'–Os bond angle, and (e) K1-O' distance.

a result of both the displacement of the potassium ions and the partial occupation of the normal potassium ion sites by water molecules. By quenching a number of the low-energy phonons a decrease in T_c might be expected in such a strongly-coupled superconductor [123]

Finally, no evidence for reduction in symmetry from $Fd\bar{3}m$ to $F4\bar{3}m$ in $KOs_2O_6H_2O$ has been found. Schuck *et al.* [71] maintain that their samples of anhydrous KOs_2O_6 show evidence of symmetry breaking to $F4\bar{3}m$ in high intensity single crystal X-ray diffraction studies while Hiroi *et al.* [123] find no evidence of such behaviour in their single crystals. The study from previous chapter, Sn. 3.3, confirmed no evidence of a reduction from $Fd\bar{3}m$ symmetry in the anhydrous polycrystalline materials, but disordered displacements of potassium ions within the pyrochlore cavity that can be fully modeled in $Fd\bar{3}m$. It is possible that differences in preparative methods may be the origin of these results. In our partially hydrated samples further disorder results from the partial incorporation of water and the formation of 'averaged' structures formed from hydrated and anhydrous domains; again this can be modeled well in $Fd\bar{3}m$. The sensitivity of KOs_2O_6 to water uptake should be noted and it is likely that single crystals as well as polycrystalline material will rapidly take up some water into their surface layers even in moist air. This may affect the measured properties and structures of KOs_2O_6 phases unless water has been scrupulously avoided.

5.3 Conclusions

The present structural study, along with previous studies, has enhanced our understanding of defect osmium pyrochlores in two respects. First, if hydration occurs the expansion of the lattice occurs. Second, if the *A*-type cation counterbalancing the negative charge coming from the framework is sufficiently small, displacements occur. The extent of this displacement strongly depends on the ion size of the cation, site availability and charge interaction within the channel.

A small amount of hydration has the effect of reducing the onset of superconducting behaviour and increasing the cell volume. On removing water the lattice parameters, the structure and properties revert to those of the crystallographic description earlier described.

6. EFFECT OF HYDRATION ON ION-EXCHANGED PHASES DERIVED FROM KOs_2O_6

The effect of introducing water into the superconducting KOs_2O_6 compounds has opened the study on the influence of water on the structure, as well as T_c, of the osmate pyrochlore. The main purpose of this chapter is to present a systematic study on the effect of water insertion and cation distribution on the structures and their relationship with properties of the osmate defect pyrochlore family. Study of water interactions in this system could add important information to the understanding of the physical behaviours of the osmate system. The structural and compositional evolution of three hydrated members of the family of osmium pyrochlores obtained from KOs_2O_6 is reported. To facilitate the reader, they will be discussed separately depending on the cation composition of the *A* site, so the monovalent $A^+A'^+$ cation site compound, $AA'OsO_6{\cdot}nH_2O$ (A^+ = K and A'^+ = Li^+ and Na^+) will be discussed first, where the divalent A^{2+} (A^{2+} = Ba^{2+}) site cation, $Ba(OsO_6)_2{\cdot}H_2O$ will be fully characterised later.

6.1 $AA'OsO_6{\cdot}nH_2O$ (A^+ = K and A'^+ = Li^+ and Na^+)

Experimental

The *AA'* materials, derived from the potassium osmate pyrochlore by ion-exchange, have been fully studied and characterised by powder neutron diffraction (PND) in Chapter 4. $AA'OsO_6$ phases are hygroscopic and quickly hydrate in air to form $AA'OsO_6{\cdot}nH_2O$. Therefore, to study how the inserted water affected the distribution of cations within the pyrochlore channels and the superconductivity, the two new compounds, were exposed to air for 48 hours before PND measurements were carried out. On the basis of similarities of the crystal structure type and properties, both $AA'OsO_6{\cdot}nH_2O$ materials will be discussed together.

Initial X-Ray diffraction patterns were collected on the two new hydrated members

of the osmate family at room temperature as described in Sn. 2.2.2 in the 10–110°, 2θ range. X-ray data were only used for checking for phase changes and for decomposition of the phases. Refinements were not attempted due to the low quality of the data, which does not allow determination of the water molecules and the cation positions and light cations.

Powder neutron diffraction (PND) data were collected on the D1A diffractometer, see Sn. 2.3.1, at the ILL, at 2 K using the constant wavelength λ = 1.909 *Å* over the 2θ range = 10–150°, over a period of 4–5 hours. The powdered samples were placed into a 5-mm diameter vanadium can and cooled to 2 K in a standard cryostat.

Structure Analysis

Neutron data for both compounds were refined by the Rietveld method using the GSAS/EXPGUI suite of programs [84, 98]. Preliminary examination of the data showed no evidence for forbidden (002), (024) or (006) reflections associated with the violation of the *d*-glide extinction rules of $Fd\bar{3}m$, which means that *0kl* (k + l ≠ 4n) and *00l* (l≠ 4n) should not be seen in the diffraction measurements. Therefore, all the work on the two derived potassium structures was carried out in the centrosymmetric $Fd\bar{3}m$ space group. After hydration, no other significant change in the X-ray diffraction patterns of these compounds was observed apart from the increasing of the lattice parameter by 2-3%; this means that the hydration process does not affect the structures.

In the literature [44, 124], water oxygen of hydrated pyrochlore phases have been described by many authors as occupying the 32*e* Wyckoff site, next to the central position. This insertion into the structure, often causes the displacement of the mobile *A* site cation from the 8*b*/32*e* site to the 16*d* site. The tendency has also been confirmed for the hydrated KOs_2O_6 for which O_w density at $(x, x, x) \sim 0.32$, with a site occupancy of 0.020(3), was found.

Displacements in cubic pyrochlores with oxygen deficient networks is a very common feature and was first highlighted by a Groult *et al.* [66] in 1982 when he pointed out that the 8*b* site represents the centre of a plateau of relatively constant electrostatic potential and not an electrostatic minimum.

Studies from the previous chapters showed that *A* and *A'* cations can occupy, along

the pyrochlore framework, three possible positions: (i) on 8*b* site (occupancy = 1), (ii) on the 16*d* site ($\frac{1}{2}$ occupancy), (iii) or on an intermediate position ($\frac{1}{4}$ occupancy), 32*e*.

Therefore, with this in mind, starting with $K_{0.7}Na_{0.6}Os_2O_6{\cdot}nH_2O$, two preliminary models were investigated to identify eventual changes in the *A* and *A'* cation position when compared to the corresponding dry phases. Initial refinement, identified as model 1, was based on the structural description constructed to represent the related non-hydrated phase, described earlier in Chapter 4, with Os (0, 0, 0), O (x, $\frac{1}{8}$, $\frac{1}{8}$), *A'* on the 16*d* site and *A* at approximately 0.35 (x, x, x) and a second model, model 2, where the potassium sits on the 8*b* site at coordinates ($\frac{3}{8}$, $\frac{3}{8}$, $\frac{3}{8}$) and the smaller sodium is on the 16*d* site ($\frac{1}{2}$, $\frac{1}{2}$, $\frac{1}{2}$), similar to the model discussed in section Sn. 5.2 of the previous chapter to describe hydrated phase of $KOsO_6{\cdot}nH_2O$. Of these, although the missing intensity and incoherent scattering coming from the H atoms, due to the fact that H_2O was not included in the refinement, the second representation (model 2) was noticeably better, providing a much more improved fit to the data (R_{wp} = 4.80 %, R_p = 3.16 %, χ^2 = 4.16) compared to the first model (R_{wp} = 6.6%, R_p = 5.7%, χ^2 = 5.23) and much lower atomic displacement parameter (ADP) for both *A* and *A'* implying a better assignment of density distribution within the framework. The other choice with either *A* and *A'* on a variable 16*d* site was excluded *a priori* due to the instability of the atomic position and the negative isotropic ADPs confirming an inadequate depiction of the structure. For these reasons the second model (2) was chosen as a starting point for the determination of water molecule position into the pyrochlore cage.

An initial difference Fourier mapping allowed location of missing atoms, on an 8*b* equivalent position at coordinate (0.125, 0.625, 0.125). The density was attributed to the oxygen of the water (O_w). Additional cycles, including the newly located water oxygen atoms in the refinement, significantly improved the fit (R_{wp} = 4.33 %, R_p = 3.12 %, χ^2 = 3.40). Further peak searches in the difference Fourier map enabled unambiguous location of protons on the 48*f* site, off centred toward the 8*a* at coordinate (0.125, 0.49,0.125). Fig. 6.1 shows the profile fit achieved to the data using model 2 after the incorporation of water into the structural model. The final fit statistic reached R_{wp}= 2.98 %, R_p = 2.37 %, χ^2 = 1.61. From this model and based on thermogravimetric analysis (TGA), Sn. 6.1, it was possible to locate water molecules inside the $K_{0.7}Na_{0.6}Os_2O_6{\cdot}nH_2O$ cell and to describe the cations' displacement around the pyrochlore cavities giving the structure description for $K_{0.7}Na_{0.6}Os_2O_6{\cdot}0.3H_2O$ summarised in Table 6.1.

This structure solution was consequently applied to the phase $K_{0.5}Li_{0.5}Os_2O_6{\cdot}nH_2O$.

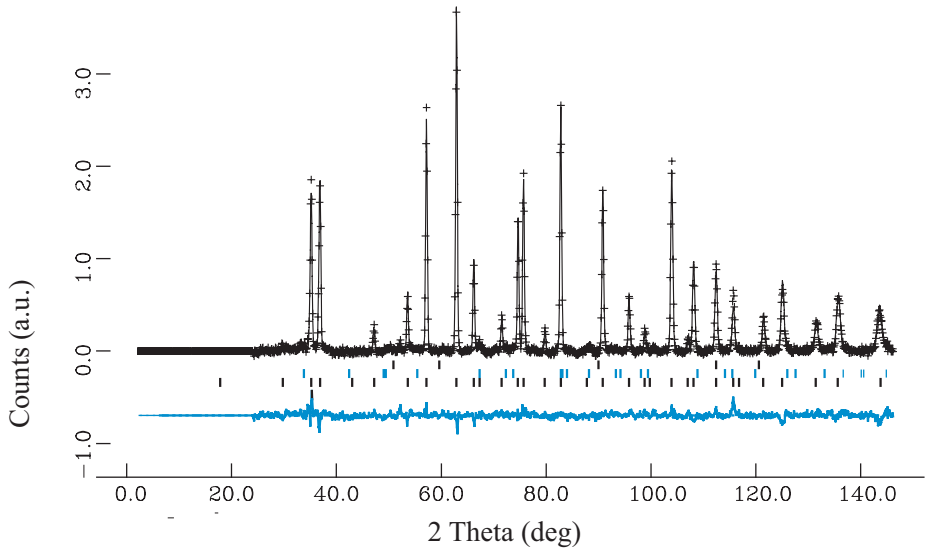

Fig. 6.1: Profile fit achieved for $K_{0.7}Na_{0.6}Os_2O_6{\cdot}0.3H_2O$ using the model summarised in Table 6.1. Observed data are indicated as crosses, upper continuous line is the calculated profile, and lower continuous line is the difference. Tick marks, from top to bottom, are calculated reflection positions for vanadium (sample can), OsO_2 and KOs_2O_6 respectively.

Tab. 6.1: 2 K PND structure model 2 for $K_{0.7}Na_{0.6}Os_2O_6{\cdot}0.3H_2O$. Space group $Fd\bar{3}m$, a = 10.2263(3) $\AA$. Estimated standard deviations (esds) in parentheses.

atom name/site	x	y	z	$U_i/U_e \times 100\AA^2$	site occupancy
K 8*b*	$\frac{3}{8}$	$\frac{3}{8}$	$\frac{3}{8}$	3.1(2)(10)	0.7
Os 16*c*	0	0	0	0.10(2)	1.0
O 48*f*	0.3172(6)	$\frac{1}{8}$	$\frac{1}{8}$	1.15(5)	1.0
Na 16*d*	$\frac{1}{2}$	$\frac{1}{2}$	$\frac{1}{2}$	2.87(3)	0.35
Ow 8*b*	$\frac{3}{8}$	$\frac{3}{8}$	$\frac{3}{8}$	7.2(8)	0.29
H 48*f*	$\frac{1}{8}$	0.4948(8)	$\frac{1}{8}$	4.7(3)	0.1(2)

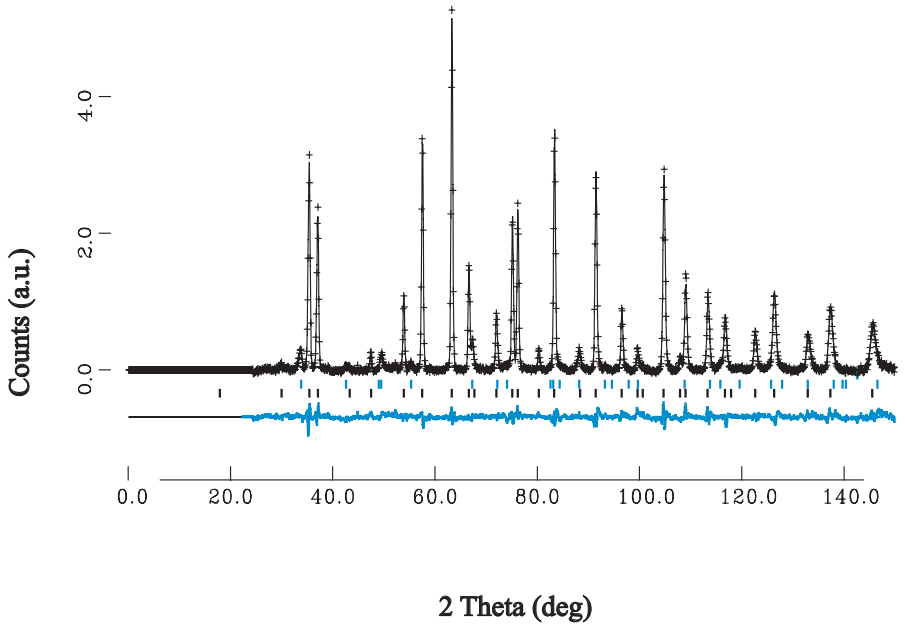

Fig. 6.2: Profile fit achieved for $K_{0.5}Li_{0.5}Os_2O_6{\cdot}nH_2O$ using the model summarised in Table 6.2. Observed data are indicated as crosses, upper continuous line is the calculated profile, and lower continuous line is the difference. Tick marks, from top to bottom, are calculated reflection positions for vanadium (sample can), OsO_2 and KOs_2O_6 respectively.

After initial refinement of scale factors, lattice parameters and the background, the model, including only K and Li and the framework atoms, led to a fit of R_{wp} = 5.84%, R_p = 3.84%, χ^2 = 7.95. Discrepancies between observed and calculated intensities confirmed that there were additional atoms in the model not taken into account. Difference Fourier maps were therefore calculated. Missing density was identified as additional water oxygen and added to the structural refinement at coordinate ($\frac{3}{8}$, $\frac{3}{8}$, $\frac{3}{8}$) on the 8*b* position. The fit factors improved significantly to R_{wp}=4.58%, R_p=3.43%, χ^2 = 4.89 with a further decrease to R_{wp} = 3.30 %, R_p = 2.62%, χ^2 = 2.53 after the addition of H atoms to the model. The final refined parameters are listed in Table 6.2.

A combination of TGA (see Sn. 6.1) and PND refinements allowed the crystal structure of $K_{0.5}Li_{0.5}Os_2O_6{\cdot}0.36H_2O$ to be fully described. All the refined occupancies and ADP were refined independently and simultaneously without any constraints. ADP values for both hydrated materials were reported in Table 6.1 and Table 6.2 as U_i/U_e. In addition, the refined Na and Li ions content was in good agreement with the microanalysis measurements reported in Chapter 4.

Tab. 6.2: 2 K PND structure for $K_{0.5}Li_{0.5}Os_2O_6{\cdot}nH_2O$. Space group $Fd\bar{3}m$, a = 10.1696(1) Å. Esds in parentheses.

Atom name/site	x	y	z	$U_i/U_e \times 100\text{Å}^2$	site occupancy
K 8*b*	$\frac{3}{8}$	$\frac{3}{8}$	$\frac{3}{8}$	6.32(5)	0.5
Os 16*c*	0	0	0	0.25(5)	1.0
O 48*f*	0.3154(3)	$\frac{1}{8}$	$\frac{1}{8}$	1.31(4)	1.0
Li 16d	$\frac{1}{2}$	$\frac{1}{2}$	$\frac{1}{2}$	6.15(5)	0.125
Ow 8*b*	$\frac{3}{8}$	$\frac{3}{8}$	$\frac{3}{8}$	5.51(5)	0.36
H 48*f*	$\frac{1}{8}$	0.5011(9)	$\frac{1}{8}$	5.87(3)	0.1(4)

Thermogravimetric Analysis

TGA performed on the two-hydrated potassium derivative evidenced the masses loss between 323 K and 623 K on heating in flowing nitrogen. Observation of bands at approximately 1650 and 3500 cm^1 in their Infra-red (IR) spectra confirmed the presence of water either on the surface or trapped in the structure. The decompositional weight decreases were, respectively, 0.06 wt% and 0.24 wt% leading to the chemical composition of $K_{0.7}Na_{0.6}Os_2O_6{\cdot}0.32H_2O$ and $K_{0.5}Li_{0.5}Os_2O_6{\cdot}0.37H_2O$. The values for the H_2O content confirmed the expected stoichiometry, agreeing well with the predicted values ($\sim$ 0.3 and $\sim$ 0.36 moles) from neutron data. There is a noticeable variation in water content as a function of the *A'* cation size within this range. The Li compound displayed a higher level of hydration. This was expected to happen due to the replacement of a larger amount of potassium by the smaller lithium, which leaves more room for water to be incorporated. Water is eliminated in several steps and this is consistent with what was previously seen for the pure hydrated potassium osmate pyrochlore. The initial mass loss occurs around 343–353 K and is observed in both samples, independent of the cation on the *A* site. This is probably due to weakly bound surface water. A further amount of more tightly bound water is lost between 373 and 623 K due to water contained within the tunnel of the β-pyrochlore channels. A large additional weight loss, occurring about 623 K for the sodium compound and at about 600 K for the lithium one, is likely to be due to the partial decomposition of the pyrochlore phase and elimination of OsO_4. This highlights the low thermal stability of these phases on heating above $\sim$600 K. Broadening and weakening of the pyrochlore peaks on the powder patterns collected on the samples after heat treatment confirmed this behaviour.

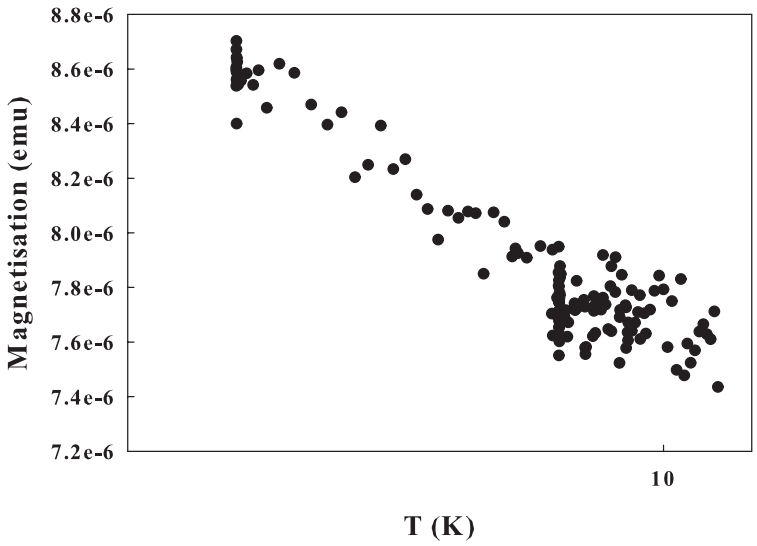

Fig. 6.3: Temperature dependence of the magnetic susceptibility of the polycrystalline $K_{0.7}Na_{0.6}Os_2O_6{\cdot}0.3H_2O$

Magnetic Characterisation

The magnetic behaviour of $K_{0.7}Na_{0.6}Os_2O_6{\cdot}0.3H_2O$ (reported in Fig. 6.3) and $K_{0.5}Li_{0.5}Os_2O_6{\cdot}0.36H_2O$ (reported in Fig. 6.4) was determined in the temperature range 2–10 K. Magnetisation measurements of both polycrystalline compounds did not manifest any superconductivity above 2 K, in contrast to what was found for the β-pyrochlore $KOs_2O_6{\cdot}0.08H_2O$. This can possibly mean that the absence of superconductivity in these partially exchanged compound is a consequence of the higher concentration of water in the structure which, preventing the rattling of the *A* cations, degrades the superconductivity manifested by the correspondenting dry materials.

Discussion

In moist air *AA'*OsO_6 phases absorb water molecules into the structure to produce $K_{0.7}Na_{0.6}Os_2O_6{\cdot}nH_2O$ and $K_{0.5}Li_{0.5}Os_2O_6{\cdot}nH_2O$ $0.3<n<0.36$. This insertion is associated with increases in lattice parameter and concomitant migration of *A* and *A'* to different sites. For the compound containing sodium, the magnitude of this increase of 0.02(1) *Å* is comparable to that observed in potassium β-pyrochlores while it almost doubles in the case of the compound containing lithium 0.035(2). Smaller size cations allow a larger amount of water to be inserted with consequent increasing of

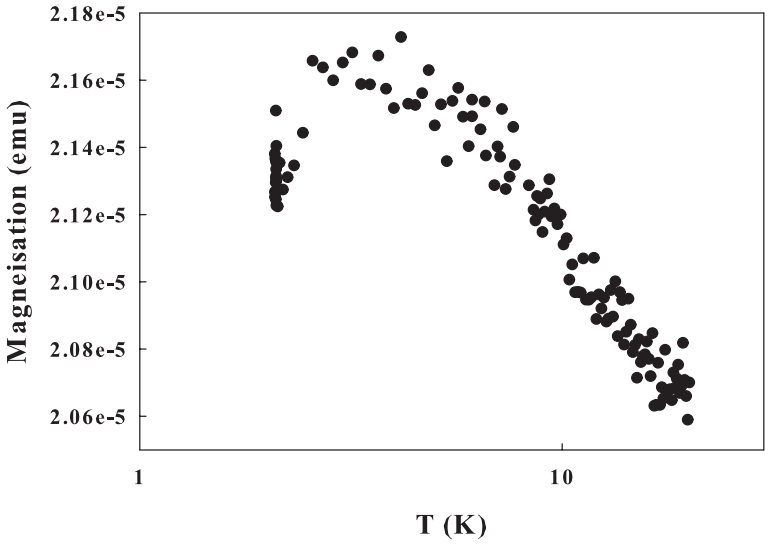

Fig. 6.4: Temperature dependence of the magnetic susceptibility of the polycrystalline $K_{0.5}Li_{0.5}Os_2O_6.0.36H_2O$

the lattice parameter. Water molecules, even those located in the channels, are only weakly bound to the framework and water is lost on heating above 500 K. Although the insertion of water is fully reversible (as the lattice parameters assume their original values once water is removed from the structure) the hydration-dehydration process results in slow degradation of the material with loss of crystallinity and enhancement of the OsO_2 second phase ($\sim$20 %).

In these materials the most intriguing feature is the easy and fast cation rearrangement of the non-framework atoms to accommodate the inserted water, which oxygen (O_w) atom does not sit on the *32e* site as previously found for the pure potassium osmate but it occupies a site equivalent to the 8*b*. Occupation of the central site by a water molecule is made possible by the fact that this site it is only partially occupied by potassium ions; so there is enough room for both atoms to share the middle of the cavity and minimize the energy of the system.

The mode of incorporation of water into the osmate structure confirms the important role played by interaction of species within the crystal lattice which, through migration, rearrange to decrease the lattice energy. Their orientation is obviously determined by the electrostatic interaction between the H_2O molecule and the

AA'OsO_6 network. In the dry analogue K sits on the 32*e* Wyckoff site. After insertion of water into the β-pyrochlore channels, a new partly occupied sites appear in close proximity to the statistically distributed O_w site due to the *A* cations' migration to an adjacent site. K^+ finds accommodation on the 8*b* position where the Na^+ species occupy the smaller 16*d* site $(\frac{1}{2}, \frac{1}{2}, \frac{1}{2})$ at the bottleneck between 2 cavities. Water hydrogens were found on the 48*f* site, slightly off-centered toward the large unoccupied 8*a* sites at coordinates (0.125, 0.49, 0.125) pointing toward the oxygens of the framework, as expected on electrostatic grounds [66]. The distribution of *A* and *A'* cations in $K_{0.7}Na_{0.6}Os_2O_6{\cdot}0.3H_2O$ is similar to the one in $K_{0.5}Li_{0.5}Os_2O_60.36H_2O$ and both appear to deviate from the proposed cation siting for pure hydrated potassium osmate. The structure, therefore, to accommodate the inserted water, minimises the energy only after displacements of the K ion along the [111] channels and the smaller alkali cations Na^+ and Li^+ move far from their ideal high symmetry sites.

The thermal variations of key positional, bond length, angle and atomic displacement parameters for the two compounds are summarised in Table 6.1 and Table 6.2, respectively. The oxygen positional parameter, *x*, which defines geometry of the osmium-oxygen framework is low compared to the value found for the $KOs_2O_6{\cdot}nH_2O$ oxide (see Sn. 5.2 of this work). The low value of *x* results from the expansion of the Os–O_6 polyhedra since the length of Os–O bonds is dependent on both *a* and *x*. The strength of the Os–O bond influences the lattice stability which is reduced as the lattice expands. A decrease in *x* will counterbalance this effect. At 2 K for both *AA'*$OsO_6{\cdot}nH_2O$, this *x*-coordinate, varies only by a small value and appears not to be affected by the marked increase in lattice parameter manifested by the Na-phase. Furthermore, it appears that due to the water insertion Li–O, Na–O, K–O bonds are considerably shorter than would normally be observed for the corresponding anhydrous phases and the framework is forced to expand resulting in the observed volume increase.

The positions of the sodium/lithium, potassium and water molecules are illustrated in Fig. 6.5. In $K_{0.7}Na_{0.6}Os_2O_6{\cdot}0.3H_2O$, the potassium ion, indicated as a blue sphere, has six bonds to framework oxygens at 3.167(2) *Å* and a further twelve interactions with oxygens at 3.667(3) *Å*. The sodium/lithium (green spheres), sitting on the 16*d* site, occupies the middle of a hexagonal chair formed by six framework oxygen (grey spheres) at 2.615(2) *Å* from O and 2.214(1) *Å* from O_w, which shares the 8*b* position with the potassium. The water molecules are linked to the O by weaker hydrogen

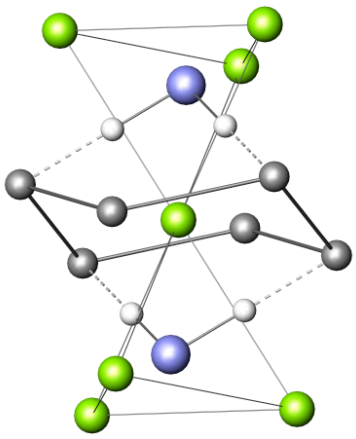

Fig. 6.5: *A* (blue sphere) *A'* (green spheres) and framework oxygen atom (dark grey spheres) coordination in *AA'*OsO_6 hydrated materials. Water molecule shares sites with *A*, in the ideal central site. Hydrogens atoms coordination to framework oxygens is shown (white spheres).

bonds, with O–H bond lengths of 1.792(1) *Å* and H–O_w of 1.372(1) *Å*. The Na–O_w bond length is 2.214(3) *Å*, in good agreement with the characteristic Na–O distance expected.

When lithium partially replaces potassium ions in the β-pyrochlore structure, the resulting structure is very similar to the representation of the previously described sodium phase. If water enters the structure, its O_w shares site 8*b*, with the potassium. The site is located in the centre of a large spherical cavity formed by eighteen oxygen atoms; six of them at 3.149(1) *Å* from K/O_w and additional twelve at 3.646(5) *Å*. Hydrogens from the water molecule are directed towards the framework oxygens at distance of 1.891(1) *Å*, indicating that there is weak hydrogen bonding between water and framework, as previously seen in the sodium derivative. The potassium cations pushes the Li^+ ions, which partially occupy the two 16*d* sites at coordinates $(\frac{1}{2},\frac{1}{2},\frac{1}{2})$, 1.916(4) *Å* away from the framework oxygens arranged in a chair conformation, with O atoms in equatorial positions and O_w oriented axially to the plane made by the six framework oxygens. The Os–O distance is similar to the distance observed in $K_{0.7}Na_{0.6}Os_2O_6 \cdot_0 .3H_2O$, as expected.

In general, the relatively high ADPs of O_w, compared to O, and H suggest that

both atoms are not static at fixed positions despite the fact that water motion is frozen at 2 K and they might be due to the fact the O_w positions (8 Wyckoff sites) and H (48 Wyckoff sites) are partially-occupied. The K–O_w distance is 2.314(1) *Å* in good agreement with the characteristic K–O distance. These results permit us to draw a picture of the mobility of the cations within the cavities of the rigid β-pyrochlore cage to allow water into the cavities. Hydration involves water molecule diffusion through the structure hole. It is worth noting that when water enters the pyrochlore structure, the *A* and *A'* positions for the lithium phase differ significantly from the positions occupied in dry phase. In the dry sodium analogue, at the same temperature, the potassium ion is located on the 8*b* site, in the centre of the cage, where sodium ions are located on the 16*d*. In the lithium derived compound, the potassium occupies the central site, whereas the lithium cation sits in the vicinity of the 16*d* position ∼ (0.45,0.45,0.45).

A hydrated osmium pyrochlore containing only sodium cations and obtained by a melt method was recently published [125]. The compound, identified with the formula $Na_{1.4}Os_2O_6{\cdot}H_2O$, has been described as a defect pyrochlore with the oxidation state of osmium reduced from +5.5 (starting KOs_2O_6) to + 5.3. This compound shows some similarities and some differences when compared to the mixed K and Na osmate discussed previously. Both compounds behave similarly in terms of properties displayed whilst structurally the *A* cation site in $Na_{1.4}Os_2O{\cdot}H_2O$ is not the same as that in the $K_{0.7}Na_{0.6}Os_2O_6{\cdot}\ 0.3H_2O$ compound described in this Chapter, as the sodium cations were modelled in the large 32*e* site in the vicinity of the 16*d* site. Oxygen atoms of the water molecules reside on the same site in the vicinity of the 8*b* position. The reasons for that this difference can be numerous, from the size of the *A* cations occupying the crystallographic sites to the amount of water which entered the structure. We have seen so far how important these variables are in determining the cation siting around the pyrochlore cage. What is important in this study is the fact that it reinforces what has been outlined so far about the importance of water in deteriorating the superconductive properties of the KOs_2O_6 pyrochlore. Furthermore, the author affirmed that in 10 preliminary samples at early experimental stages, with different molar quantities of Na and water were characterised. However, none of those showed superconductivity above 2 K. This represents a further confirmation to what was stated at the end of the preceding chapter, specifically that the decreased T_c displayed by $K_{0.7}Na_{0.6}Os_2O_6$ could be a result of either the removal of K from the structure which destabilises the superconducting rattling of K^+ within the β structure or on the variation in the oxida-

tion state of the Os of +5.5.

Conclusions

An increase in the unit cell volume of the two host pyrochlores was observed, at 2 K, which was interpreted as the result of insertion of water in the channel of the sodium potassium and lithium potassium osmium pyrochlore. If the 8*b* site is fully occupied, H_2O sits in the α cages (32*e*) displacing a portion of the potassium ions to adjacent sites (16*d*). When the centre of the cavity is only partially occupied by potassium ions, then water shares a site with the central cation. The displaced ions in this case, are the smaller Na^+ and Li^+ ions which are accommodated on smaller secondary sites. Hydration, hence, leads to a closer packing of species within the structures reducing its superconducting rattling. Once again, hydration was confirmed to have a negative effect on the superconductivity of the osmate pyrochlore compounds

6.2 $A(Os_2O_6)_2{\cdot}H_2O$ ($A^{2+} = Ba^{2+}$)

Ba-based osmium oxide pyrochlore was synthesised for the first time from the K-osmate starting material by ion-exchange method. To our knowledge this is the first barium pyrochlore belonging to the osmate family to be synthesised. It is known that AOs_2O_6-type osmate pyrochlores are formed in the case where the *A* cation is a large monovalent metal such as Cs^+, Rb^+, K^+ [1, 2, 3]. According to previous study [126], a wide range of A^{2+} cations can be introduced into the β-pyrochlore structure with synthesis easily achieved by ionic exchange methods removing the limits on the possibilities of ionic substitution in this family determined by the unsteadiness of the framework at high temperature. Thus, the synthesis of a new pyrochlore oxide containing barium and osmium was attempted. Based on the ionic radius of the barium cation, which compares well with that of potassium, Ba^{2+} should combine easily with osmium species to form pyrochlore-type compounds, possibly displaying the interesting properties of the KOs_2O_6 parent compound.

The target material was successfully synthesised as single phase material through ion exchange methods in a water medium, with the expectation that $BaCl_2$ being slightly more soluble in water than KCl (37.5 g/100 ml *versus* 34 g/100 ml at 300 K) and larger in size would favor the cation substitution process and would compete with O_w for the occupation of the *3*2e or 8*b* sites, depending on the amount of water inserted. PND analysis, EDX and TGA confirmed the structure to belong to the β-type pyrochlore. The composition was identified as $Ba(OsO_6)_2{\cdot}H_2O$. Defect pyrochlores with charge of *A* +2 are known in literature and they were synthesised for the first time by ionic exchange methods by Chernorukov *et al.*[126].

Experimental

Black polycrystalline $Ba(OsO_6)_2{\cdot}nH_2O$ was obtained by ionic exchange using KOs_2O_6, the synthesis of which was fully described in the previous chapter Sn. 3. The ion-exchange was accomplished after a 2 step treatment in which 0.5 g of KOs_2O_6 starting material was left stirring for about 2 weeks in a 2 M $BaCl_2$ (99.8 %, Sigma Aldrich) solution. $BaNO_3$ could also have been used as both salts were appropriate for the ion-exchange. The solution was refreshed every 48 hours to maintain a maximum concentration gradient. The resulting powder was filtered off and washed thoroughly with distilled water to remove the exchanged cations left in solution and dried at ∼363 K in

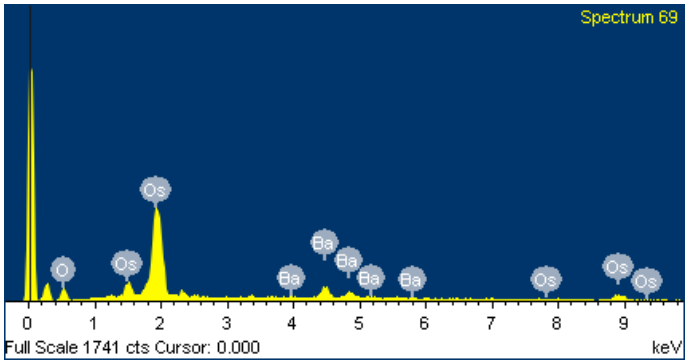

Fig. 6.6: EDX spectrum (Counts vs keV) for $Ba(OsO_6)_2{\cdot}nH_2O$ obtained by ion-exchange reaction and showing the incorporated cation species Ba^2.

a dry oven, for 2 hours before PXD analysis was carried out on the sample. The process always occurs with incorporation of water atoms into the structure cavities.This helps the lattice to maintain charge balance and stabilises the structure. Successful syntheses of these phases depended on the ease which the framework displays in exchanging counterions present in the cavities and on the ability of the inserted ions to displace the initial one. A direct solid state route was not attempted due to the relative instability of the OsO_6 framework which easily oxidises on heating above 400 K to form OsO_4 and BaO.

Energy Dispersive X-ray Microanalysis

Energy dispersive X-ray microanalysis confirmed completion of the exchange reaction as no detectable potassium X-ray spectrum was observed. The osmium peaks, in Fig. 6.6, do not overlap with those of the divalent barium across the energy range, particularly at lower energies where the more intense peaks provide the $Ba(OsO_6)_2{\cdot}nH_2O$ accurate information for quantitative analysis and it gave a rough estimate of the average Ba:Os = metal ratio of 1:2. The proportion of oxygen was calculated rather than measured due to the poor ratios provided by this method in the presence of heavy atoms. The compound was thus labeled as $Ba(OsO_6)_2{\cdot}nH_2O$ assuming a fully occupied framework.

Thermogravimetric Analysis

Thermogravimetric analysis, carried out at 5 °/min up to 700 K evidences well-defined weight losses from Fig. 6.7. The TGA profile indicated two different weight losses

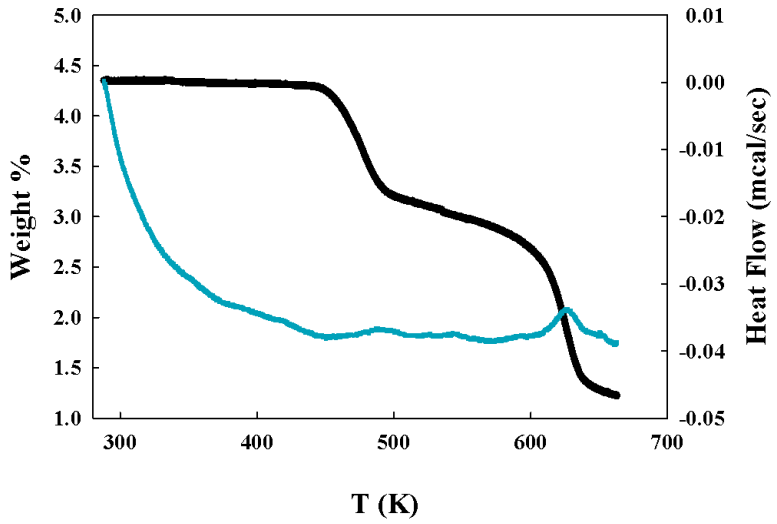

Fig. 6.7: Thermogravimetric (TG and DSC) analysis for $Ba(OsO_6)_2{\cdot}H_2O$

characterised by two different weight/temperature slopes. The first weight loss region ranges from room temperature to 373 K and was associated with the release of surface water. Water in interstitial cavities is lost in the temperature range of 373-423 K. Weight losses associated with water content (~ 0.12 w%) evidences a fully exchanged material containing one water molecule, giving a standard formula of $Ba(OsO_6)_2{\cdot}H_2O$. The Differential Scanning Calorimetric (DSC) curve profiles also showed an exothermic reaction at higher temperatures (peaks at 440 K and 625 K). X-ray diffraction patterns, collected after thermal analysis, did not resemble that of the $Ba(OsO_6)_2{\cdot}H_2O$ pyrochlore but rather a mixture of BaO and OsO_2 oxides.

Structure Analysis

PXD patterns, collected at RT indicated that the main observed peaks could be indexed using a cubic cell, $a \sim 10$ *Å*, consistent with the space group $Fd\bar{3}m$. Neutron diffraction data were recorded on the high flux D20 diffractometer at the ILL, Grenoble, at a temperature of 2 K using a standard orange cryostat over a period of 1 hour. Data were collected in the 2θ =10–150 ° range with a wavelength λ = 1.868 *Å*. The sample was loosely sealed inside a vanadium can with a small header space. The level of hydration of the compound was obtained by thermogravimetric measurement.

Analysis of the various powder diffraction data sets was undertaken by the Rietveld

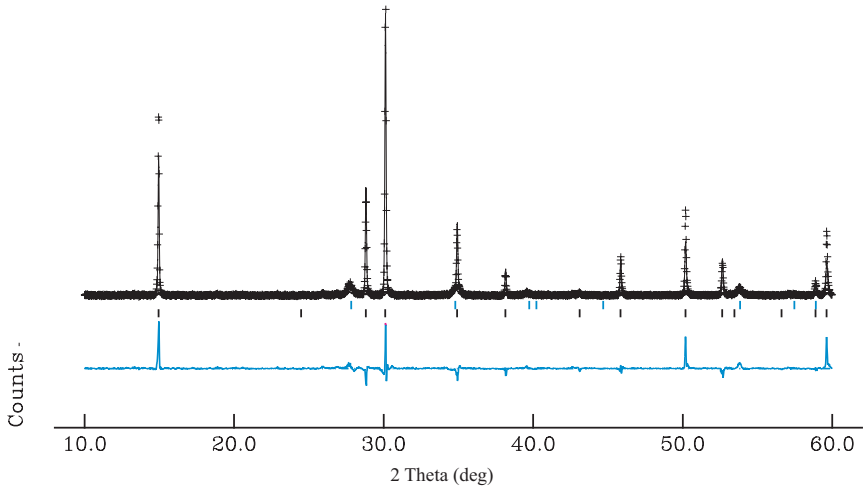

Fig. 6.8: Profile fit obtained to the PXD data set of $Ba(OsO_6)_2H_2O$. Cross marks are observed intensities, upper continuous line is the calculated profile, and lower continuous line is the difference. Tick marks, from top to bottom, are calculated reflection positions for OsO_2 and $Ba(OsO_6)_2{\cdot}H_2O$

method using the GSAS/EXPGUI program, and started on the basis of the barium tungstate pyrochlore structure, $A^{2+}(W^{5+}O_6)_2{\cdot}H_2O$, described by Chernorukov *et al.* [126], in the standard β-pyrochlore space group $Fd\bar{3}m$. Inspection of data showed the presence of a small level ∼5% of OsO_2 impurity deriving from KOs_2O_6, starting material, which was fitted using literature data [116]. Initial stages of the refinement proceeded smoothly with the variation of cell parameters, peak shape profile, cell constant and phase fraction, which along with the refinement of the isotropic atomic displacement parameters (ADPs), resulted in the expected improvement in the least-squares fit. The model used for the compounds fitted all the peaks observed and converged rapidly to reasonable R factors (see Table 6.3). The plot of the profile fit (reported in Table 6.8) soon showed that exchange of potassium by barium atoms, and the insertion of water, was accompanied by an increase of the intensity of the *222* Bragg reflection and decrease of the *311* Bragg peak. The relatively larger intensity change suggested this is not due to the preferred orientation of powder but a substantial deviation in the occupancy of the metal ions. X-ray analysis also suggested the 16*d* site, due to its multiplicity, as possible position for the Ba^{2+} atoms and the 32*e* as being occupied the the water oxygen.

This description was therefore used as a starting point for PND study, which was

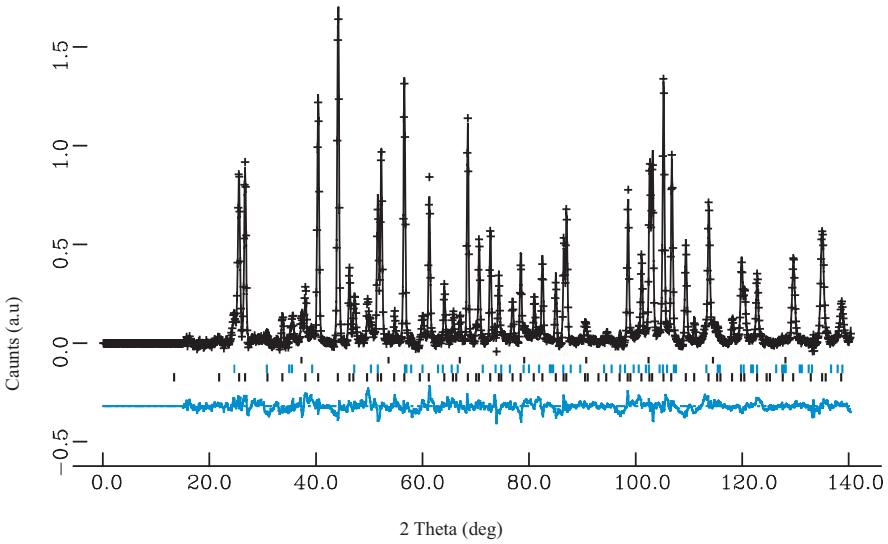

Fig. 6.9: Profile fit obtained to the PND data set of $Ba(OsO_6)_2H_2O$. Cross marks are observed intensities, upper continuous line is the calculated profile, and lower continuous line is the difference. Tick marks, from top to bottom, are calculated reflection positions for V, OsO_2 and $Ba(OsO_6)_2{\cdot}H_2O$

undertaken on data collected at 2 K. In this model (model 1), water atoms were not included at the starting point of the refinement. The dissimilarity between the observed and calculated intensities, evidenced by the diffraction pattern at this stage, are a result of the missing H_2O atoms that were not included in the refinements. Therefore, a difference Fourier map was carried out with the intent of identifying the position of water oxygen in the pyrochlore cavity. Refinement fit factors improved significantly following the introduction of O_w into the structural model (with R_{wp} = 2.73 %, R_p =1.60 %, χ^2 = 16.05) decreasing to R_{wp} =1.89 %, R_p =1.31 %, χ^2 = 7.63) and went further down after a second difference Fourier map that allowed the location of hydrogen atoms (R_{wp} = 1.44%, R_p = 1.12%, χ^2 = 4.46). Fig. 6.9 illustrates the fit for PND data after final refinement. The details of the refinement parameters are summarised in Table 6.4 and selected interatomic distances are in Table 6.5.

To confirm the model as the best description of the new formed phase, two additional models were investigated. In a second model (model 2), the barium was allowed to partially occupy the 16*d* and 8*b* site with O_w refined onto the 32*e*. This representation provided some minor discrepancies and an unacceptable negative ADP for the barium (which was allowed to refine on the 8*b* site), for the osmium atom, as well as a higher than expected value of *x* for the framework oxygen, which would correspond to an increase of the level of distortion in the OsO_6 octahedra.

Tab. 6.3: XRD structure model for $Ba(OsO_6)_2H_2O$. Space group $Fd\bar{3}m$, a = 10.2811(6). Esds in parentheses

Atom name/site	x	y	z	$U_i/U_e \times 100\AA^2$	site occupancy
Ba 16*d*	$\frac{1}{2}$	$\frac{1}{2}$	$\frac{1}{2}$	4.3(6)	0.25
Os 16*c*	0	0	0	3.32(2)	1.0
O 48*f*	0.3132(9)	$\frac{1}{8}$	$\frac{1}{8}$	0.5(7)	1.0

Tab. 6.4: 2 K PND structure model 1 for $Ba(OsO_6)_2{\cdot}H_2O$. Space group $Fd\bar{3}m$, a =10.28303(2). Esds in parentheses.

Atom name/site	x	y	z	$U_i/U_e \times 100\AA^2$	site occupancy
Ba 16*d*	$\frac{1}{2}$	$\frac{1}{2}$	$\frac{1}{2}$	0.44(2)	0.25
Os 16*c*	0	0	0	0.20(2)	1.0
O 48*f*	0.31386(2)	$\frac{1}{8}$	$\frac{1}{8}$	0.42(7)	1.0
Ow 32*e*	0.34432(5)	0.34458(7)	0.34458(7)	2.68(2)	0.25
H 48*f*	$\frac{3}{8}$	$\frac{3}{8}$	0.5110(5)	7.2(3)	0.33(6)

Tab. 6.5: Extracted key distances ($\AA$) and angles (deg) in the 2 K PND structure model 1 for $Ba(OsO_6)_2{\cdot}H_2O$

Bonding toms	Bond length/Bond angle
Os–O	1.9328(5)
O–Os–O	90.55(6)
O–Os–O	89.45(4)
Ba–O	2.6397(2)
Ba–O_w	2.1081(8)
Ba–O_w	2.773(8)
O_w–H	1.17(1)
O–H	1.80(1)

Further refinement,using a third model (identified as model 3) was also attempted allowing the water oxygen to sit on the 8*b* site displacing the barium on the 32*e* site. This last representation gave a poor fit and confirmed a very ADP for the barium (0.76(2)). Among the three models, the first refinement investigated provided a much better fit to the data as well as very low ADPs for all the atoms and was considered the best way to describe the $Ba(OsO_6)_2 \cdot H_2O$ structure.

6.2.1 Magnetic Characterisation

Magnetisation measurements were carried out on the novel $Ba(OsO_6)_2 \cdot nH_2O$ in order to explore magnetic properties. They clarified absence of superconductivity above 2 K. This is shown in Fig. 6.10. The hydration likely plays a significant role in destroying the possible superconductivity.

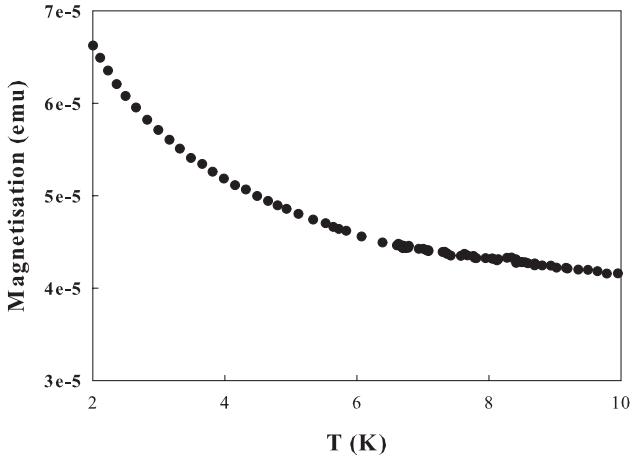

Fig. 6.10: Temperature dependence of the magnetic susceptibility of the polycrystalline $Ba(OsO_6)_2.H_2O$

6.2.2 Discussion

The tendency to exchange the more labile cations has been reported for several pyrochlores; A complete *A* cation exchange can be fully achieved also for the KOs_2O_6 compounds. The conventional ionic exchange method of dissolving chloride salts in water has been confirmed as a successful procedure leading to the synthesis of a new osmate defect pyrochlore. According to EDX, thermogravimetric analysis, and Rietveld refinements the new as formed material was confirmed to have the formula

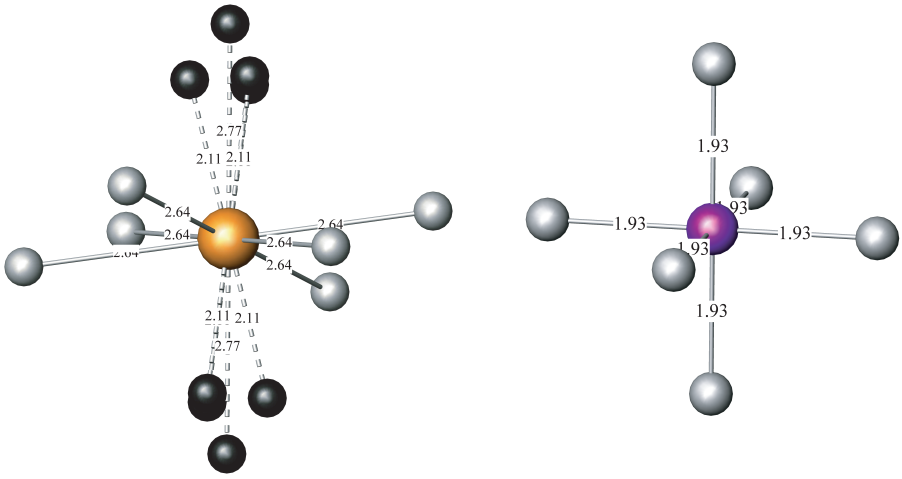

Fig. 6.11: Left: Coordination around barium on the 16*d* site, shown as orange spheres in $Ba(OsO_6)_2{\cdot}H_2O$; grey spheres are framework oxygens and black spheres identify O_w on the 32*e* site. Right: Coordination around the osmium (purple sphere)

$Ba(OsO_6)_2{\cdot}H_2O$. It, clearly, retains the defect structure composition. The only example in the literature of defect pyrochlore with *A* site cations that have a charge higher than +1 and a defect-type structure is the family $A^{2+}(W^{5+}O_6)_2{\cdot}H_2O$ where A^{2+} = Ca, Sr and Ba and *B* (in the oxidation state +5) = Nb or Ta.

Preliminary Rietveld analysis on the powder neutron data from $Ba(OsO_6)_2{\cdot}H_2O$ indicate that the Ba^{2+} is displaced from the ideal 32*e*/8*b* site, where potassium is found, to the 16*d* positions, the site that *A* occupies in a conventional defect pyrochlore. Fig. 6.11 illustrates the $Ba(OsO_6)_2{\cdot}H_2O$ cation coordination. Os atoms form the pyrochlore lattice just as in an ordinary β-pyrochlore osmium oxide, while Ba atoms are located in the α-cages made of OsO_6 octahedra exactly in the middle of the puckered ring of six oxygens, with two oxygens contributing from the waters. Barium insertion leads to the expansion of the BiO_6 ochtahedra which results in the cell parameter of *a* = 10.3807(4) *Å* larger than that found for the hydrated potassium compound. This can either be a consequence of the larger size of the barium or a consequence of the full hydration.

Effective bonding between the framework cages and Ba atoms provides rather regular ADPs for all atoms; also for the oxygen of the framework, which generally has

rather high ADP in this pyrochlore type compounds. The temperature dependencies of the ADPs scale with the atom masses as can be seen from Table 6.4. Thus no special rattling effect is expected for Ba-atoms. A likely explanation is that, when water is inserted into this structure-type, the close packing of species due to electrostatic interaction within the cavity also slows this phenomenon and once again, highlights the important role that water plays in degrading or overturning the superconductivity characteristic of this family of compounds. The presence of one molecule of water per unit formula, which preferentially fully occupies the ideal 8*b* site, relocated Ba^{2+} ions to the smaller *16d* positions inhibiting the superconducting rattling of the *A* cation that is believed to play an important role in establishing the superconductivity. The introduction of Ba^{2+} ions and water molecules, hence, places the cage under expansive stress as a result of the inserted water which fully occupies positions along the (110) plane and causes relocation of the *A* cation on the *16d* site. Ba cation refines well onto the *16d* site although, because of its ion radius, (slightly larger than is ideal for this site) it would be expected to occupy the bigger 32*e*. We can easily understand, however, that the site although being slightly smaller for Ba^{2+} it is considerably closer than any other site available within the framework giving Ba–O distances of 2.64(1) *Å*.

The expectation of an enhanced superconductivity than KOs_2O_6 failed as the new compound did not show any trace of superconductivity above 2 K. Besides, it is suggested that T_c goes up efficiently by replacing the *A* atom by a smaller ion size as superconducting critical temperature (T_c) increases depending on the *A* atom mass from 3.3 K (*A* = Cs) to 6.4 K (Rb), and to 9.6 K (K) [3].The description in the earlier sections, in part validates what was outlined in the previous chapters about the extremely importance of *A* cation size for preservation of the original crystallographic structure of KOs_2O_6.

6.3 Conclusions

A complete ion exchange in KOs_2O_6 was successfully achieved. The Ba-based Os oxide pyrochlore was synthesised for the first time and its structure and magnetic properties studied. Two additional hydrated osmium oxides adopting a pyrochlore-type structure were also synthesised and investigated.

The framework although unstable at temperatures above 500 K does keep its nature in solution and tends to behave as a host for the incorporation of small cation or

molecule. If the ion-exchange is carried out in water or species are left in air, H_2O molecules will fill the framework cavities depending on the room available. Considerable work has been devoted to establish the exact location of species within the framework and interaction of these species: surface and hydration water that fill intramolecular cavities, and O groups taking the place of the potassium.

Starting from the pure potassium phase through the partial exchanged potassium to the fully exchanged phase, it can be stated that when water enters the pyrochlore structure, the water molecules are strongly directed to the centre or toward the four windows of the big cavity formed by the rigid pyrochlore framework. Water molecules play an important role in the packing of the crystalline lattice of the hydrated pyrochlore osmate, both because it participates in hydrogen bonds linking anions and also, through its lone-pair orbitals, it can act as a suitable ligand for the cations of the structure. This can be the cause of the reduced *rattling* of the *A* cations in the cavity of the new hydrated materials when compared to the precursor potassium osmate, which relates to the superconductive properties of the material.

Although conclusions from the previous chapter on the superconductor KOs_2O_6 suggested that a small degree of hydration does not destroy the superconductivity, the hydrated phases obtained by ion-exchange and fully discussed in the present chapter do not act as superconductors above 2 K. This is probably because they accommodate much more water than $KOs_2O_6{\cdot}_{0.08}H_2O$ [97], totally erasing the superconductivity of the β-pyrochlore originator.

7. STOICHIOMETRIC SECOND AND THIRD-ROW TRANSITION METAL PYROCHLORES

As part of a detailed study of the structural properties of metal pyrochlores, materials containing transition second and third transition rows metals oxides (TM) in combination with rare earth oxides were synthesised and investigated. The interest in such combinations of oxides, which can be described by the formula $R_2B_2O_6O'$ or $R_2B_2O_7$ (R = rare earth and B = Ru, Ir and Mo) comes from the interesting magnetic features arising when both R and B are occupied by magnetic ions, the electrons of which (f of rare earths, d of TM and coupling between f and d) can form structures that support geometrical frustration in three dimensions [30, 31, 32], magnetic ordering, and can result in interesting phenomena, such as the anomalous Hall effect in $Nd_2Mo_2O_7$ [33], the underscreened Kondo effect in $Pr_2Ir_2O_{7.7}$ [34] or superconductivity in $Cd_2Re_2O_7$ [35]). These recently discovered properties are very interesting from the electronic point of view [5] but are also still very poorly understood. The structural investigation, hence, is expected to improve the understanding of the structure-properties interactions in these systems for which the electronic state is often the result of subtle coupling between electronic and structural degrees of freedom deriving from the intermediate character between localized and itinerant orbitals.

The analysis of these compounds was undertaken with the two-fold objectives of: i) studying their structure, so as to describe their structural trends, and to establish any variation within the group of R cations, with particular emphasis on the relationship between cell size and the value of the variable oxygen positional parameter, x and ii) identifying possible structural changes associated with the use of different TM cations on the B site. In this chapter, these studies are well illustrated by three examples: the ruthenate, the iridate and molybdate families of α pyrochlore that have been reported to display a wide variety of properties ranging from metallic to semiconducting to non metallic states depending on the rare earth cation forming the R_2O' sublattice. Pyrochlore compounds containing Ru^{4+} have gained great importance as

conductors [9, 10] and for their catalytic activity [16]. Studies published by Kannan *et al.* [127] and Goodenough and co-workers [128] demonstrated that the Ir^{4+} pyrochlores are stable oxygen reduction catalysts with well established and important magnetic properties. Recently, Yanagishima and Maeno showed that polycrystalline samples of $R_2Ir_2O_7$ exhibit a metal-insulator transition where the metallic state was found for R = Nd, Pr, Sm, and Eu, and a non metallic state was observed for those with an R cation with smaller radius [129]. By contrast the Mo^{4+} system undergoes magnetic transitions from a spin-glass (SG) insulating state to ferromagnetic metallic state (FM) [17, 18] as the R cation is varied.

In all these structures, the wide variety of properties displayed are likely due to the fact that their bandwidths depend strongly on the ionic radius of the trivalent R^{3+} ions through B–O–B bond bending [130]. The B^{4+} metal cation has four electrons in nearly degenerate t_{2g} orbitals, and their combination with the f electrons of the rare earth cation is essential in determining the properties of the final compound.

7.1 Experimental

7.1.1 Synthesis

Oxides of composition $R_2B_2O_6O'$ were prepared by conventional solid state routes and involved heating the opportune amount of the respective pre-dried oxides, with rare earth sesquioxides R_2O_3 and BO_2 (all with purity of higher than 99.5%). The heating procedure was important for removing any moisture and to oxidise the rare earth to the stoichiometric composition. Each sample was weighed in the correct ratio and intimately mixed in an agate mortar, pressed into pellet and fired, in alumina crucibles in air, at temperatures indicated in the following synthetic tables with several intermediate re-grindings. After cooling to room temperature, the samples were crushed into powder, reground, repressed and reheated until the reaction was complete. It was very important to form pellet of the materials to minimise iridium loss through volatilisation. Additional heat treatment at higher temperature caused the pyrochlore phase to dissociate. The reaction conditions, taking accounts of starting materials, amount, and reaction times and temperatures are detailed in Table 7.1 and Table 7.2 , Table 7.3 and Table 7.4. The following four tables summarise a number of attempts to prepare mixed-metal ruthenate, iridate, molybdate α-pyrochlores. These preparations were attempted in order to investigate the effect of the ionic size of the metal cations

Tab. 7.1: Part Ia: Synthesis conditions of successful and attempted routes that led to the synthesis of the $R_2Ru_2O_6O'$ (R= Y, Dy) investigated in the current chapter

Target compound	Starting materials (g)	annealing T (K)	Annealing Time (Day)	Reaction Time (Day)	Reaction T (K)	Phases Obtained
$Y_2Ru_2O_7$	Y_2O_3 (0.459)+ RuO_2 (0.541)	1123	1	2	1473	$Y_2Ru_2O_7$ + Y_2O_3
$Y_2Ru_2O_7$	Y_2O_3 (0.459)+ RuO_2 (0.541)	1123	1	3	1473	$Y_2Ru_2O_7$ + Y_2O_3
$Y_2Ru_2O_7$	Y_2O_3 (0.459)+ RuO_2 (0.541)	1123	1	4	1473	$Y_2Ru_2O_7$ + Y_2O_3
$Y_2Ru_2O_7$	Y_2O_3 (0.459)+ RuO_2 (0.541)	1123	1	5	1473	$Y_2Ru_2O_7$ + Y_2O_3
$Y_2Ru_2O_7$	Y_2O_3 (0.459)+ RuO_2 (0.541)	1173	1	5	1473	$Y_2Ru_2O_7$ + Y_2O_3
$Y_2Ru_2O_7$	Y_2O_3 (0.459)+ RuO_2 (0.541)	1223	1	5	1473	$Y_2Ru_2O_7$ + Y_2O_3
$Y_2Ru_2O_7$	Y_2O_3 (0.459)+ RuO_2 (0.541)	1273	1	5	1473	$Y_2Ru_2O_7$ + Y_2O_3
$Y_2Ru_2O_7$	Y_2O_3 (0.459)+ RuO_2 (0.568)	1273	1	5	1473	$Y_2Ru_2O_7$ + Y_2O_3
$Y_2Ru_2O_7$	Y_2O_3 (0.459)+ RuO_2 (0.568)	1273	1	5	1473	$Y_2Ru_2O_7$ + Y_2O_3
$Y_2Ru_2O_7$	Y_2O_3 (0.459)+ RuO_2 (0.568)	1273	2	5	1473	$Y_2Ru_2O_7$ + Y_2O_3
$Y_2Ru_2O_7$	Y_2O_3 (0.459)+ RuO_2 (0.595)	1273	3	5	1473	$Y_2Ru_2O_7$ + Y_2O_3
$Y_2Ru_2O_7$	Y_2O_3 (0.459)+ RuO_2 (0.568)	1273	4	5	1473	$Y_2Ru_2O_7$ + Y_2O_3
$Y_2Ru_2O_7$	Y_2O_3 (0.459)+ RuO_2 (0.568)	1273	4	6	1473	$Y_2Ru_2O_7$ + Y_2O_3
$Y_2Ru_2O_7$	Y_2O_3 (0.459)+ RuO_2 (0.568)	1273	4	7	1473	$Y_2Ru_2O_7$ + Y_2O_3
$Eu_2Ru_2O_7$	Eu_2O_3 (0.569)+ RuO_2 (0.431)	1123	1	2	1473	$Eu_2Ru_2O_7$ + Eu_2O_3
$Eu_2Ru_2O_7$	Eu_2O_3 (0.569)+ RuO_2 (0.431)	1123	1	3	1473	$Eu_2Ru_2O_7$ + Eu_2O_3
$Eu_2Ru_2O_7$	Eu_2O_3 (0.569)+ RuO_2 (0.431)	1123	1	4	1473	$Eu_2Ru_2O_7$ + Eu_2O_3
$Eu_2Ru_2O_7$	Eu_2O_3 (0.569)+ RuO_2 (0.431)	1123	1	5	1473	$Eu_2Ru_2O_7$ + Eu_2O_3
$Eu_2Ru_2O_7$	Eu_2O_3 (0.558)+ RuO_2 (0.431)	1173	1	5	1473	$Eu_2Ru_2O_7$ + Eu_2O_3
$Eu_2Ru_2O_7$	Eu_2O_3 (0.558)+ RuO_2 (0.431)	1223	1	5	1473	$Eu_2Ru_2O_7$ + Eu_2O_3
$Eu_2Ru_2O_7$	Eu_2O_3 (0.558)+ RuO_2 (0.431)	1273	1	5	1473	$Eu_2Ru_2O_7$ + Eu_2O_3
$Eu_2Ru_2O_7$	Eu_2O_3 (0.558)+ RuO_2 (0.431)	1273	1	5	1473	$Eu_2Ru_2O_7$ + Eu_2O_3
$Eu_2Ru_2O_7$	Eu_2O_3 (0.558)+ RuO_2 (0.452)	1273	1	5	1473	$Eu_2Ru_2O_7$ + Eu_2O_3
$Eu_2Ru_2O_7$	Eu_2O_3 (0.459)+ RuO_2 (0.452)	1273	2	5	1473	$Eu_2Ru_2O_7$ + Eu_2O_3
$Eu_2Ru_2O_7$	Eu_2O_3 (0.459)+ RuO_2 (0.452)	1273	3	5	1473	$Eu_2Ru_2O_7$ + Eu_2O_3
$Eu_2Ru_2O_7$	Eu_2O_3 (0.459)+ RuO_2 (0.452)	1273	4	5	1473	$Eu_2Ru_2O_7$ + Eu_2O_3
$Eu_2Ru_2O_7$	Eu_2O_3 (0.459)+ RuO_2 (0.452)	1273	4	6	1473	$Eu_2Ru_2O_7$ + Eu_2O_3
$Eu_2Ru_2O_7$	Eu_2O_3 (0.459)+ RuO_2 (0.452)	1273	4	7	1473	$Eu_2Ru_2O_7$ + Eu_2O_3
$Eu_2Ru_2O_7$	Eu_2O_3 (0.459)+ RuO_2 (0.471)	1273	4	7	1473	$Eu_2Ru_2O_7$ + Eu_2O_3

and of the trivalent ions on structure and properties of the final pyrochlores obtained.

The synthesis of the molybdate phases was conducted in sealed quartz tubes following the procedure described by Manthiram and Gopalakrishnan [131] to avoid the oxidation of the MoO_2 into oxidation states different from 4^+. For the successful synthesis of the compounds of such a family, high-purity powders of R_2O_3 and MoO_2 (previously prepared by the reduction of MoO_3 in presence of Mo at 1073 K in an evacuated and sealed quartz tube) were mixed according to the amounts reported in Table 7.3, and pressed into a pellet. The pellet was broken into pieces and put in a quartz tube, which was then, evacuated and sealed. The evacuated tube was heated to 1473 K for 48 h before the pellet was taken out, reground and repelletised, and the heat treatment repeated. The process was continued until the reaction was complete and the PXD pattern contained only peaks indexable to a cubic single-phase material. Not all the syntheses of the targeted compounds were successful, and failure was mainly a consequence of the higher reaction temperatures required by the synthetic process, which the quartz tube could not support and that resulted in insufficient temperatures to bring

Tab. 7.2: Part II: Synthesis conditions of successful and attempted routes that led to the synthesis of the $R_2Ru_2O_6O'$ (R= Yb, Dy and Nd) investigated in the current chapter

Target compound	Starting materials (g)	annealing T (K)	Annealing Time (Day)	Reaction Time (Day)	Reaction T (K)	Phases Obtained
$Yb_2Ru_2O_7$	Yb_2O_3 (0.597)+ RuO_2 (0.403)	1123	1	2	1353	$Yb_2Ru_2O_7$ + Yb_2O_3
$Yb_2Ru_2O_7$	Yb_2O_3 (0.597)+ RuO_2 (0.403)	1123	1	2	1383	$Yb_2Ru_2O_7$ + Yb_2O_3
$Yb_2Ru_2O_7$	Yb_2O_3 (0.597)+ RuO_2 (0.403)	1123	1	2	1423	$Yb_2Ru_2O_7$ + Yb_2O_3
$Yb_2Ru_2O_7$	Yb_2O_3 (0.597)+ RuO_2 (0.403)	1123	1	3	1473	$Yb_2Ru_2O_7$ + Yb_2O_3
$Yb_2Ru_2O_7$	Yb_2O_3 (0.597)+ RuO_2 (0.403)	1123	1	4	1473	$Yb_2Ru_2O_7$ + Yb_2O_3
$Yb_2Ru_2O_7$	Yb_2O_3 (0.597)+ RuO_2 (0.403)	1123	1	5	1473	$Yb_2Ru_2O_7$ + Yb_2O_3
$Yb_2Ru_2O_7$	Yb_2O_3 (0.597)+ RuO_2 (0.425)	1173	1	5	1473	$Yb_2Ru_2O_7$ + Yb_2O_3
$Yb_2Ru_2O_7$	Yb_2O_3 (0.597)+ RuO_2 (0.447)	1173	1	5	1473	$Yb_2Ru_2O_7$ + Yb_2O_3
$Dy_2Ru_2O_7$	Dy_2O_3 (0.586)+ RuO_2 (0.416)	1123	1	2	1383	$Dy_2Ru_2O_7$ + Yb_2O_3
$Dy_2Ru_2O_7$	Dy_2O_3(0.586)+ RuO_2 (0.416)	1123	1	5	1423	$Dy_2Ru_2O_7$ + Yb_2O_3
$Dy_2Ru_2O_7$	Dy_2O_3 (0.586)+ RuO_2(0.416)	1123	1	5	1473	$Dy_2Ru_2O_7$ + Yb_2O_3
$Dy_2Ru_2O_7$	Dy_2O_3 (0.586)+ RuO_2 (0.437)	1173	1	5	1473	$Dy_2Ru_2O_7$ + Yb_2O_3
$Nd_2Ru_2O_7$	Nd_2O_3 (0.558)+ RuO_2 (0.442)	1123	1	2	1473	$Nd_2Ru_2O_7$ + Nd_2O_3
$Nd_2Ru_2O_7$	Nd_2O_3 (0.558)+ RuO_2 (0.442)	1123	1	3	1473	$Nd_2Ru_2O_7$ + Nd_2O_3
$Nd_2Ru_2O_7$	Nd_2O_3 (0.558)+ RuO_2 (0.442)	1123	1	4	1473	$Nd_2Ru_2O_7$ + Nd_2O_3
$Nd_2Ru_2O_7$	Nd_2O_3 (0.558)+ RuO_2 (0.442)	1123	1	5	1473	$Nd_2Ru_2O_7$ + Nd_2O_3
$Nd_2Ru_2O_7$	Nd_2O_3 (0.558)+ RuO_2 (0.442)	1173	1	5	1473	$Nd_2Ru_2O_7$ + Nd_2O_3
$Nd_2Ru_2O_7$	Nd_2O_3 (0.558)+ RuO_2 (0.442)	1223	1	5	1473	$Nd_2Ru_2O_7$ + Nd_2O_3
$Nd_2Ru_2O_7$	Nd_2O_3 (0.558)+ RuO_2 (0.442)	1273	1	5	1473	$Nd_2Ru_2O_7$ + Nd_2O_3
$Nd_2Ru_2O_7$	Nd_2O_3 (0.558)+ RuO_2 (0.464)	1273	1	5	1473	$Nd_2Ru_2O_7$ + Nd_2O_3
$Nd_2Ru_2O_7$	Nd_2O_3 (0.558)+ RuO_2 (0.464)	1273	1	5	1473	$Nd_2Ru_2O_7$ + Nd_2O_3
$Nd_2Ru_2O_7$	Nd_2O_3 (0.459)+ RuO_2 (0.464)	1273	2	5	1473	$Nd_2Ru_2O_7$ + Nd_2O_3
$Nd_2Ru_2O_7$	Nd_2O_3 (0.459)+ RuO_2 (0.464)	1273	3	5	1473	$Nd_2Ru_2O_7$ + Nd_2O_3
$Nd_2Ru_2O_7$	Nd_2O_3 (0.459)+ RuO_2 (0.464)	1273	4	5	1473	$Nd_2Ru_2O_7$ + Nd_2O_3
$Nd_2Ru_2O_7$	Nd_2O_3 (0.459)+ RuO_2 (0.464)	1273	4	6	1473	$Nd_2Ru_2O_7$ + Nd_2O_3
$Nd_2Ru_2O_7$	Nd_2O_3 (0.459)+ RuO_2 (0.464)	1273	4	7	1473	$Nd_2Ru_2O_7$ + Nd_2O_3
$Nd_2Ru_2O_7$	Nd_2O_3 (0.459)+ RuO_2 (0.486)	1273	4	7	1473	$Nd_2Ru_2O_7$ + Nd_2O_3

Tab. 7.3: Synthesis conditions of successful and attempted routes that led to the synthesis of the $R_2Mo_2O_6O'$ (R= Y, Gd, Dy Sm, Nd) investigated in the current chapter

Target compound	Starting materials (g)	annealing T (K)	Annealing Time (Day)	Reaction Time (Day)	Reaction T (K)	Phases Obtained
$Y_2Mo_2O_7$	Y_2O_3 (0.531)+ MoO_2 (0.469)	1073	1	2	1173	$Y_2Mo_2O_7$ + $Y(MoO_4O)_3$
$Y_2Mo_2O_7$	Y_2O_3 (0.531)+ MoO_2 (0.469)	1123	2	3	1623	$Y_2Mo_2O_7$ (orthorombic)+ Y_2O_3
$Y_2Mo_2O_7$	Y_2O_3 (0.531)+ MoO_2 (0.469)	1123	2	2	1623	$Y_2Mo_2O_7$ + Y_2O_3
$Y_2Mo_2O_7$	Y_2O_3 (0.266)+ MoO_2 (0.234)	1123	2	3	1623	$Y_2Mo_2O_7$ (cubic)+ Y_2O_3
$Y_2Mo_2O_7$	Y_2O_3 (0.266)+ MoO_2 (0.251)	1123	2	3	1623	$Y_2Mo_2O_7$ (cubic)+ Y_2O_3
$Nd_2Mo_2O_7$	Nd_2O_3 (0.558)+ MoO_2 (0.432)	1073	1	2	1173	$Nd_2Mo_2O_7$ + $Nd(MoO_4O)_3$
$Nd_2Mo_2O_7$	Nd_2O_3 (0.558)+ MoO_2 (0.432)	1073	1	2	1223	$Nd_2Mo_2O_7$ + $Nd(MoO_4O)_3$
$Nd_2Mo_2O_7$	Nd_2O_3 (0.558)+ MoO_2 (0.432)	1123	2	3	1623	$Nd_2Mo_2O_7$ (orthorombic)+ Nd_2O_3
$Nd_2Mo_2O_7$	Nd_2O_3 (0.558)+ MoO_2 (0.432)	1123	2	4	1623	$Nd_2Mo_2O_7$ + Nd_2O_3
$Nd_2Mo_2O_7$	Nd_2O_3 (0.558)+ MoO_2 (0.432)	1123	2	5	1623	$Nd_2Mo_2O_7$ (cubic)+ Nd_2O_3
$Sm_2Mo_2O_7$	Sm_2O_3 (0.558)+ MoO_2 (0.432)	1123	1	2	1223	$Sm_2Mo_2O_7$ + $Sm(MoO_4O)_3$
$Sm_2Mo_2O_7$	Sm_2O_3 (0.558)+ MoO_2 (0.432)	1123	2	3	1623	$Sm_2Mo_2O_7$ (orthorombic)+ Sm_2O_3
$Sm_2Mo_2O_7$	Sm_2O_3 (0.558)+ MoO_2 (0.432)	1123	2	4	1623	$Sm_2Mo_2O_7$ (orthorombic) + Sm_2O_3
$Sm_2Mo_2O_7$	Sm_2O_3 (0.558)+ MoO_2 (0.432)	1123	2	5	1623	$Sm_2Mo_2O_7$ (cubic)+ Sm_2O_3
$Gd_2Mo_2O_7$	Gd_2O_3 (0.586)+ MoO_2 (0.414)	1123	2	3	1623	$Gd_2Mo_2O_7$ (orthorombic)+ Gd_2O_3
$Gd_2Mo_2O_7$	Gd_2O_3 (0.586)+ MoO_2 (0.414)	1123	2	4	1623	$Gd_2Mo_2O_7$ (orthorombic) + Gd_2O_3
$Gd_2Mo_2O_7$	Gd_2O_3 (0.586)+ MoO_2 (0.414)	1123	2	5	1623	$Gd_2Mo_2O_7$ (orthorombic) + Gd_2O_3
$Gd_2Mo_2O_7$	Gd_2O_3 (0.586)+ MoO_2 (0.414)	1123	2	7	1673	$Gd_2Mo_2O_7$ (cubic)+ Gd_2O_3
$Gd_2Mo_2O_7$	Gd_2O_3 (0.586)+ MoO_2 (0.421)	1123	2	7	1673	$Gd_2Mo_2O_7$ (cubic)+ Gd_2O_3
$Gd_2Mo_2O_7$	Gd_2O_3 (0.293)+ MoO_2 (0.207)	1123	2	7	1673	$Gd_2Mo_2O_7$ (cubic)+ Gd_2O_3
$Dy_2Mo_2O_7$	Dy_2O_3 (0.593)+ MoO_2 (0.407)	1123	2	3	1623	Dy_2MoO_5 + MoO_2
$Dy_2Mo_2O_7$	Dy_2O_3 (0.593)+ MoO_2 (0.407)	1123	2	3	1673	Dy_2MoO_5 + MoO_2
$Dy_2Mo_2O_7$	Dy_2O_3 (0.593)+ MoO_2 (0.407)	1123	2	5	1673	Dy_2MoO_5 + MoO_2
$Dy_2Mo_2O_7$	Dy_2O_3 (0.593)+ MoO_2 (0.407)	1123	2	7	1673	Dy_2MoO_5 + MoO_2
$Dy_2Mo_2O_7$	Dy_2O_3 (0.296)+ MoO_2 (0.203)	1123	2	3	1623	Dy_2MoO_5 + MoO_2
$Dy_2Mo_2O_7$	Dy_2O_3 (0.296)+ MoO_2 (0.407)	1123	2	3	1673	Dy_2MoO_5 + MoO_2
$Dy_2Mo_2O_7$	Dy_2O_3 (0.296)+ MoO_2 (0.407)	1123	2	7	1673	Dy_2MoO_5 + MoO_2

Tab. 7.4: Synthesis conditions of successful and attempted routes that led to the synthesis of the $R_2Ir_2O_6O'$ (R= Y,Eu and Nd)

Target compound	Starting materials (g)	annealing T (K)	Annealing Time (Day)	Reaction Time (Day)	Reaction T (K)	Phases Obtained
$Y_2Ir_2O_7$	Y_2O_3 (0.531)+ IrO_2 (0.469)	1123	1	2	1123	$Y_2Ir_2O_7$ + Y_2O_3
$Y_2Ir_2O_7$	Y_2O_3 (0.531)+ IrO_2 (0.469)	1123	1	3	1123	$Y_2Ir_2O_7$ + Y_2O_3
$Y_2Ir_2O_7$	Y_2O_3 (0.531)+ IrO_2 (0.469)	1123	2	5	1123	$Y_2Ir_2O_7$ + Y_2O_3 + Ir
$Y_2Ir_2O_7$	Y_2O_3 (0.531)+ IrO_2 (0.469)	1123	2	5	1173	$Y_2Ir_2O_7$ + Y_2O_3 + Ir
$Y_2Ir_2O_7$	Y_2O_3 (0.531)+ IrO_2 (0.469)	1123	2	5	1223	$Y_2Ir_2O_7$ + Y_2O_3 + Ir
$Y_2Ir_2O_7$	Y_2O_3 (0.531)+ IrO_2 (0.469)	1123	2	2	1273	$Y_2Ir_2O_7$ + Y_2O_3 + Ir
$Y_2Ir_2O_7$	Y_2O_3 (0.265)+ IrO_2 (0.234)	1123	2	5	1223	$Y_2Ir_2O_7$ + Y_2O_3 + Ir
$Nd_2Ir_2O_7$	Nd_2O_3 (0.572)+ IrO_2 (0.429)	1123	1	2	1123	$Nd_2Ir_2O_7$ + Nd_2O_3+ IrO_2
$Nd_2Ir_2O_7$	Nd_2O_3 (0.572)+ IrO_2 (0.429)	1123	1	3	1123	$Nd_2Ir_2O_7$ + Nd_2O_3
+ IrO_2 $Nd_2Ir_2O_7$	Nd_2O_3 (0.572)+ IrO_2 (0.429)	1123	2	4	1123	$Nd_2Ir_2O_7$ + Nd_2O_3
$Nd_2Ir_2O_7$	Nd_2O_3 (0.572)+ IrO_2 (0.429)	1123	2	5	1123	$Nd_2Ir_2O_7$ + Nd_2O_3 + Ir
$Nd_2Ir_2O_7$	Nd_2O_3 (0.572)+ IrO_2 (0.429)	1123	2	5	1273	$Nd_2Ir_2O_7$ + Nd_2O_3 + Ir
$Eu_2Ir_2O_7$	Eu_2O_3 (0.569)+ IrO_2 (0.431)	1123	1	2	1123	$Eu_2Ir_2O_7$ + Eu_2O_3 + IrO_2
$Eu_2Ir_2O_7$	Eu_2O_3 (0.569)+ IrO_2 (0.431)	1123	1	3	1173	$Eu_2Ir_2O_7$ + Eu_2O_3
$Eu_2Ir_2O_7$	Eu_2O_3 (0.569)+ IrO_2 (0.431)	1123	2	4	1173	$Eu_2Ir_2O_7$ + Eu_2O_3 + Ir
$Eu_2Ir_2O_7$	Eu_2O_3 (0.569)+ IrO_2 (0.431)	1123	1	5	1173	$Eu_2Ir_2O_7$ + Eu_2O_3 + Ir

the reactions to a completion. Only synthesis of yttrium, neodymium, gadolinium and samarium molybdate pyrochlores were completed as these systems required temperatures below 1670 K. The long-term heating with regrinding at the relatively high temperature ensured that steady-state conditions had been achieved. For R = Dy only a mixture of R_2MoO_5 and MoO_2 was obtained even after prolonged annealing. The heavier lanthanides may form $R_2Mo_2O_7$ structures at higher temperatures but these could not be reached with the quartz tubes as the quartz melted and heavily interacted with the pellet.

7.1.2 Structure Analysis

PXD patterns were collected to identify the phase and purity of the polycrystalline products. Structural analysis was performed on good quality polycrystalline samples of $R_2B_2O_6O'$ (B = Ru, Ir, Mo). The majority of the data were collected over a 2θ-range 10–110°, with a step size of 0.02° for a period of 15 hours. PND data, when possible, were collected using the high-resolution time-of-flight (TOF) data on the HRPD (Sn. 2.22) diffractometer at the ISIS facility, Rutherford Appleton laboratory. Data were collected on *circa* 3g of sample sealed in a 5 mm vanadium can with a time-of-flight of 30-130 μs, for 12 hours at 2 K and 298 K. Crystal structures were determined by the Rietveld method [45], using the GSAS/EXPGUI suite of programs [98], as described in Sn. 2.2.3. Where the presence of a very small amount of rare earth oxide

was detected, this was included as a second phase in the Rietveld refinement. The initial parameters of the pyrochlore phases $R_2B_2O_6O'$ were taken from the literature.

PXD Structure Refinement of $R_2Ru_2O_6O'$ (R=Y, Dy, Eu, Nd)

These phases crystallised with body centred symmetry in the space group $Fd\bar{3}m$. The results of the X-ray diffraction measurements showed that not all the desired $R_2B_2O_6O'$ pyrochlores could be obtained as single-phase and that small amounts of rare earth oxides, used as starting materials, could be detected in the final products up to 5% (within the limits of the experimental technique). The first material produced as a pure phase material and investigated in terms of structure was $Y_2Ru_2O_6O'$. The starting structural model for the Rietveld refinement was that proposed by Greedan [132], space group $Fd\bar{3}m$ with all atoms at full occupancy. The trivalent Y^{3+} ion was situated on (0.5, 0.5, 0.5), ruthenium on (0, 0, 0), and the oxygen atoms O on (x, $\frac{1}{8}$, $\frac{1}{8}$) and O' on ($\frac{3}{8}$, $\frac{3}{8}$, $\frac{3}{8}$). After the introduction of the atoms (placed on the positions earlier described and at full occupancy) the refinement of the PXD data was started by varying background parameters, zero point, scale factors, the lattice parameter and peak shape. This soon resulted in a good fit to the data. The isotropic atomic displacement parameters (ADPs) were then varied, which greatly improved the quality of the fit. The yttrium ruthenium pyrochlore was iso-structural with the cubic parent pyrochlore material reported in [133] and had a cell parameter a = 10.13980(2) $\AA$ which lies close to the value reported by for the room temperature data. ADPs for the Y atom and for the O refined to very large values, whereas the ADPs of the two remaining atoms were rather low. High value of the ADP for the atom on the 16*d* and 48*f* sites are quite characteristic features for the α-pyrochlore phases and associable with the unusual coordination geometry of the 16*d* site [50] and with the degree of freedom that the oxygen has on this site. However, to probe that the high thermal motion was not originating either from a partial occupancy of the site or from a disordering of the atoms off the special positions, refinement of the occupancy of the Y atom was performed and displacement off site was allowed. The oxygen occupancy was also attempted despite the poor accuracy of X-ray techniques toward light atoms, but this did not show any particular feature attributable to deficiencies in the model. The Y and O atoms, therefore, in alternate cycles were allowed to move off their ideal site onto the adjacent 4-fold, 32*e* position with quarter occupancy. Attempts to refine Y and O' on the 32*e* sites invariably led to a worsening of the fit. The displacement of these atoms from the ideal position resulted in unrealistically

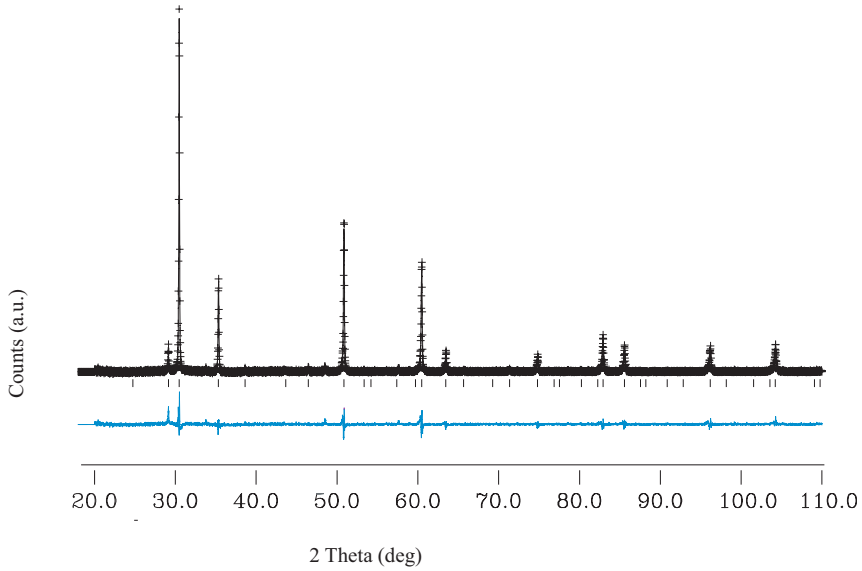

Fig. 7.1: Observed, calculated and difference X-ray powder diffraction profiles for $Y_2Ru_2O_6O$'. The short vertical lines below the profiles mark the position of all possible Bragg reflections for the pyrochlore phase.

high values and produced an unstable refinement after few cycles. In the final model, therefore, the occupancies of the Y atom and of the oxygen were allowed to stay at unity and on their ideal sites. Final refined atomic parameters are given in Table 7.5. From Table 7.5 the value for O x is ≈ 0.33 and compares well with the values of an ordered pyrochlore phase, whereas disorder would imply an x coordinate for the atom on the 48f site close to 0.375 (the value expected for a disordered-fluorite model). The profile fit is shown in Fig. 7.1 and reports the X-ray reflections for $Y_2Ru_2O_6O$' which are typical of α-pyrochlore compounds.

This first refinement represented the starting point for the other ruthenium phases that were successfully synthesised and investigated, Nd, Eu and Dy. It appeared soon that the neodymium, europium and dysprosium ruthenate pyrochlores were isostructural with the cubic $Y_2Ru_2O_6$, with cell parameters lying close to the value of $\sim$ 10 $\AA$ expected for cubic ruthenate pyrochlores, and which were strictly influenced by the ionic size of the trivalent element on the R site of the structure. These phases crystallised in the space group $Fd\bar{3}m$. Table 7.5 below provides a summary of the structure and cell parameters of the four materials studied within the same metal group.

Tab. 7.5: X-ray extracted structural parameters for the ruthenate pyrochlore, $R_2Ru_2O_6O'$ (R= Y, Nd, Eu, Dy), estimated standard deviations in parentheses. The crystal symmetry is cubic, $Fd\bar{3}m$. The atomic sites are R, 16d ($\frac{1}{2}, \frac{1}{2}, \frac{1}{2}$), Ru, 16$c$ (0, 0, 0), O (x, $\frac{1}{8}, \frac{1}{8}$), and O' ($\frac{3}{8}, \frac{3}{8}, \frac{3}{8}$).

	Y	Dy	Eu	Nd
Ionic radii (*Å*)	0.90	0.91	0.95	0.98
a (*Å*)	10.13980(2)	10.16815(2)	10.25311(1)	10.34143(3)
x (O)	0.33391(6)	0.33491(6)	0.33632(1)	0.33965(5)
Isotropic ADPs				
R	0.27(6)	0.25(4)	0.21(2)	0.19(2)
Ru	0.24(0)	0.25(7)	0.21(3)	0.17(3)
O	0.73(1)	0.81(1)	0.50(8)	0.46(3)
O'	0.56(1)	0.63(1)	0.32(2)	0.32(1)
Selected bond lengths and angle				
Ru–O (*Å*)	1.98(4)	2.00(1)	2.02(4)	2.04(5)
6 × R–O (*Å*)	2.46(1)	2.45(3)	2.47(1)	2.52(3)
2 × R–O' (*Å*)	2.19(5)	2.21(4)	2.22(1)	2.24(2)
Ru–O–Ru (°)	129.2(9)	129.1(1)	128.2(2)	129.3(1)
χ^2	1.69	2.52	2.56	4.44
R_{wp}(%)	2.12	2.32	2.38	3.89
R_p (%)	1.77	2.07	1.90	2.75

PXD Structure Refinement of $R_2Ir_2O_6O'$, (R=Y, Nd, Eu)

Refinement of the structure of the three $R_2Ir_2O_6O'$ pyrochlores was performed using the same starting structural coordinates as the cubic $Nd_2Ir_2O_6O'$ proposed by Lazarev *et al.*[134], space group $Fd\bar{3}m$. The refinements proceeded smoothly, with the variation of background parameters, zero point, scale factors, lattice parameter and peak shape, and soon resulted in satisfactory values for all sites at full occupancy. The ADP for the rare earth ions were high as expected and this was attributed to the site geometry rather than vacancies or disorder in the structure. All the sites were found to be fully occupied and any attempt to refine the occupancy did not produce occupancy values different from unity. All the least squares refinements produced acceptable fits and gave reasonable ADPs value for atoms of similar type. A summary of the atomic parameters is given in Table 7.6, together with selected bond distances of interest and statistical fit parameters. A graphical representation of these parameters is presented in Fig. 7.3; the trend of each parameter shows a monotonic increase as the ionic radius of the element *R* within the group increases.

PXD Structure Refinement of $R_2Mo_2O_7$ (R= Y, Gd, Sm, Nd)

Sintering of the samples, obtained according the procedure described in Sn. 7.1.1 led to hard, black polycrystalline products which were characterised by PXD. All the phases produced were found to contain impurity peaks associated with 5-10% of the MoO_2 starting material and a main $R_2Mo_2O_6O'$ pyrochlore phase (*R*= Nd, Sm, Gd), for the products obtained by heating the reaction mixtures between 1473 and 1673 K for several days. The strong reflections in the powder pattern of these phases could be indexed to a face-centred cubic lattice with a $\sim$10 $\AA$ (see Table 7.7), indicating that the cubic pyrochlore phases were formed only after several grindings and prolonged annealing at temperatures higher than 1473 K. Reactions carried out at temperature lower than 1473 K only produced patterns that contained several weak reflections which could not be indexed on the basis of the cubic structure but rather to an orthorhombic lattice .

The structural investigation of the molybdate phases started with the analysis of the $Y_2Mo_2O_6O'$ compound. The initial structural model for the full profile refinement was that proposed by Reimers *et al.* [135], with space group $Fd\bar{3}m$, and all the atoms at full occupancies. MoO_2 was introduced into the refinement as a second phase, and initial steps in the refinement included the variation of the scale factors, background, zero

Tab. 7.6: X-ray extracted structural parameters for the iridate pyrochlore of formula $R_2Mo_2O_6O'$ (R= Y, Gd, Sm, Nd), estimated standard deviations in parentheses. The crystal symmetry is cubic, $Fd\overline{3}m$. The atomic sites are R, 16d ($\frac{1}{2}, \frac{1}{2}, \frac{1}{2}$), Ir, 16$c$ (0, 0, 0), O (x, $\frac{1}{8}, \frac{1}{8}$), and O' ($\frac{3}{8}, \frac{3}{8}, \frac{3}{8}$)

	Y	Eu	Nd
Ionic radii (Å)	0.90	0.95	0.98
a (Å)	10.15510(5).	10.27311(1)	10.36859(9)
x (O)	0.33409(1)	0.33493(2)	0.33508(4)
Isotropic ADPs			
R	0.33(2)	0.31(5)	0.27(1)
Ir	0.21(3)	0.31(5)	0.23(1)
O	0.54(1)	0.69(3)	0.71(6)
O'	0.38(7)	0.43(1)	0.47(3)
Selected bond lengths and angle			
Ir–O (Å)	2.04(2)	2.04(4)	2.06(2)
6 × R–O (Å)	2.47(4)	2.48(1)	2.50(3)
2 × R–O' (Å)	2.24(5)	2.23(4)	2.24(5)
Ir–O–Ir (°)	127.9(9)	128.4(2)	128.6(1)
χ^2	1.57	2.56	3.44
R_{wp}(%)	1.32	3.38	4.79
R_p (%)	1.09	2.22	3.75

Tab. 7.7: X-ray extracted structural parameters for the molybdate pyrochlore of formula $R_2Mo_2O_6O'$ (R= Y, Gd, Sm, Nd),estimated standard deviations in parentheses. The crystal symmetry is cubic, $Fd\bar{3}m$. The atomic sites are R, 16d ($\frac{1}{2}, \frac{1}{2}, \frac{1}{2}$), Mo, 16$c$ (0, 0, 0), O (x, $\frac{1}{8}, \frac{1}{8}$), and O' ($\frac{3}{8}, \frac{3}{8}, \frac{3}{8}$).

	Y	Gd	Sm	Nd
Ionic radii (Å)	0.90	0.94	0.96	0.98
a (Å)	10.21242(1)	10.28732(2)	10.31865(1)	10.32972(2)
x (O)	0.33051(4)	0.33131(3)	0.33245(3)	0.33303(6)
Isotropic ADPs				
R	0.32(6)	0.27(4)	0.22(2)	0.21(9)
Mo	0.19(6)	0.23(7)	0.22(3)	0.19(3)
O	0.63(1)	0.71(1)	0.460(8)	0.33(3)
O'	0.39(2)	0.53(2)	0.32(6)	0.33(1)
Selected bond length and angle				
Mo–O (Å)	1.99(6)	2.03(4)	2.04(3)	2.06(5)
6 × R–O (Å)	2.51(1)	2.54(5)	2.60(8)	2.62(9)
2 × R–O' (Å)	2.21(1)	2.23(3)	2.25(3)	2.29(8)
Mo–O–Mo (°)	130.7(7)	131.5(7)	131.7(2)	132.0(2)
χ^2	2.54	1.74	1.27	1.17
R_{wp}	3.16	2.01	1.39	1.6
R_p	2.13	1.52	1.10	1.34

point displacement and lattice constant. The model produced an excellent fit, which further improved as soon as ADPs for each atom were varied. Refined positional and final profile fit parameters are listed below in Table 7.7.

This model was thus used as starting point for the analysis of the other members of the $R_2Mo_2O_6O'$ (R = Gd, Sm, Nd) molybdate family and confirmed that this model could be used to adequately describe the distribution of the cationic density in each structure. Final positional parameters, isotropic displacements and statistical parameters are listed in Table 7.7. Atomic parameters and O x values agreed closely with those reported in the literature by Moritomo *et al.* [136], Greedan *et al.* [137, 138] and Hubert [139, 140].

7.1.3 Powder Neutron Diffraction

The previously reported PXD measurements were expected to be relatively insensitive to the oxygen atom displacements and thermal vibrations, therefore variable temperature structural studies on two selected systems, described in the previous section, $R_2Ru_2O_6O$' and $R_2Ir_2O_6O$', were performed by high resolution PND in order to investigate, in detail, possible structural changes to the RO_8 and BO_6 polyhedra that may occur as a function of temperature. The phases for PND analysis were mainly chosen according to their purity, minor neutron absorbance and the availability of material at the time of the assigned neutron time.

PND Structure Refinement of $Y_2Ru_2O_6O$' and $Nd_2Ru_2O_6O$'

PND analysis of $Y_2Ru_2O_6$ and $Nd_2Ru_2O_6$ was carried out using the conventional cubic pyrochlore space group model ($Fd\bar{3}m$), described in Sn. 7.1.2. Since a small amount (less then 3%) of Y_2O_3 was detected in the sample, this second phase was included in the Rietveld refinement. Cell parameters obtained by the Rietveld refinement of the PND data, at room and low temperature on the two compounds investigated, agreed closely with those determined by PXD measurements. No evidence for extra reflections was observed in the low temperature data of both compounds with respect to the 298 K data, confirming that the phase remains cubic even at 2 K. The isotropic ADP for the oxygen atom O was slightly high ($\sim 0.50(8)$) and this may have indicated an oxygen deficiency. However, refining of the site occupancy for this atom gave a value of 1. The high quality of the data allowed the anisotropic ADPs to be varied for the atoms on the lower symmetry sites such as *R* and O. These parameters were refined simultaneously and the final values are reported in Table 7.10. Table 7.8 below provide a summary of the structure and cell parameters for the 2 K model discussed. The trend manifested by these two ruthenate pyrochlores belongs to the reported trends of the rare earth ruthenate pyrochlores reported in literature [132, 141].

This model was, therefore, used as starting point for structural refinement against neutron diffraction data collected for the next temperature in the heating section. To ensure consistency, the same variables and background points were used for data collected at each temperature. As the temperature was raised to 298 K, the thermal motion of the cations in the structure increased but the model used to describe the scattering density at low temperature was still adequate to represent the cation density within the cage for both $Y_2Ru_2O_6O$' and $Nd_2Ru_2O_6O$', and confirmed that neither changes

Tab. 7.8: Refined lattice parameters, atomic coordinates and ADPs, derived bond lengths and angle of interest for the models describing $Y_2Ru_2O_6O$' and profile fits achieved at 2 and 298 K, $Fd\bar{3}m$. Estimated standard deviations in parentheses (esds). The Ru–O–Ru angle characterises the staggered Ru–O chain of the underlying pyrochlore lattice.

	2 K	298 K
a (Å)	10.14399(1)	10.39041(2)
Ox	0.33510(4)	0.33522(5)
Ru–O (Å)	1.9903(3)	1.9853(3)
Ln–O (Å) (6 ×)	2.4526(4)	2.4507(4)
Ln–O' (Å) (2 ×)	2.19(6)	2.1950(5)
Ru–O–Ru (°)	128.9(3)	128.7(1)
χ^2	2.86	2.84
R_{wp}	6.78	6.76
R_p	5.77	5.75

in fractional occupancy of the atoms nor in their cation coordination. Selected refinement details, as well as important bond lengths and angles, are given in Table 7.8 and Table 7.9 whereas the final 2 K NPD fit for both compounds, is reported in Fig. 7.2

PND Structure Refinement of $Y_2Ir_2O_6O$'

Powder neutron diffraction data were collected using the high-resolution TOF, diffractometer. To improve the quality of the data taking into account the high neutron absorption cross section of iridium, the sample was loaded in a slab can, allowing a bigger surface area per amount of sample compared to the cylindrical vanadium sample can. Data were collected at 2 K and RT, each over a period of 12 hours for $Y_2Ir_2O_6O$'. The Rietveld refinement of the TOF diffraction data was performed using all data points between the time-of- flight range of 40-120 μs (2θ = 30-120).

In the early PXD structural study, Sn. 7.1.2, $Y_2Ir_2O_6O$' was described with a cubic pyrochlore cell. Cell parameters obtained from the previous analysis were thus imported into the starting model used for the structure refinement against the PND data. For these constant wavelength measurements the background was refined using a Voigt peak- shape function and the Gaussian and Lorentzian components were refined. Despite the lower quality of the data, due to neutron absorption effects by the Ir sample, the refinement in the conventional space group proceeded without incident

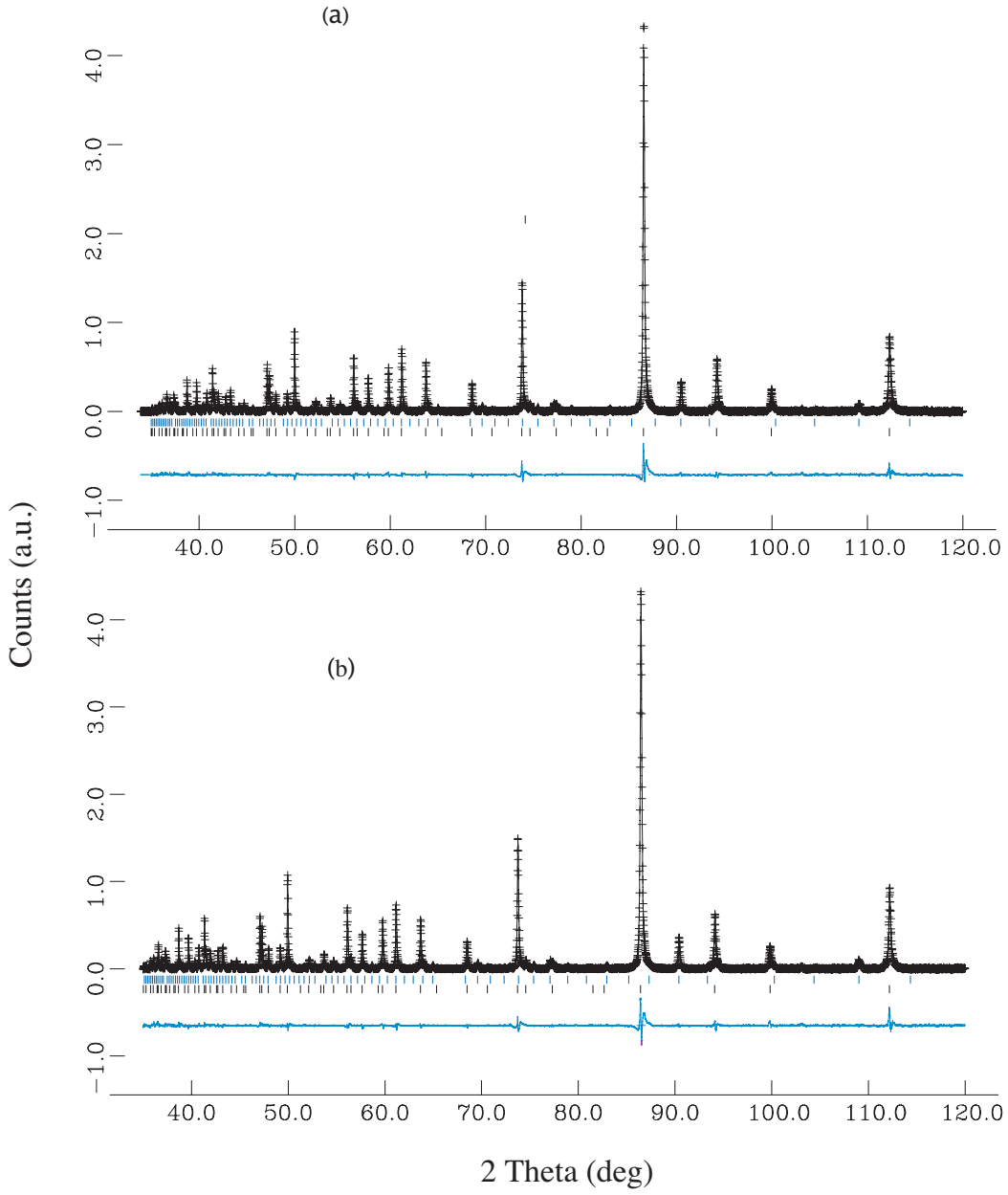

Fig. 7.2: Profile fit obtained to the 2 K NPD data for $Y_2Ru_2O_6O'$ (a) and $Nd_2Ru_2O_6O'$ (b). Cross marks are observed intensities, upper continuous line is the calculated profile, and lower continuous line is the difference. Tick marks, from top to bottom, are calculated reflection positions for the respective impurity (Y_2O_3 or Nd_2O_3), and for the main pyrochlore phase.

Tab. 7.9: Refined lattice parameters, atomic coordinates and ADPs, derived bond lengths and angle of interest for the models describing $Nd_2Ru_2O_6O'$ and profile fits achieved at 2 and 298 K, $Fd\overline{3}m$. Estimated standard deviations in parentheses. The smaller O–B–O angle defines the main rectangular cross section of the octahedra and the B–O–B angle characterises the staggered B–O chain of the underlying pyrochlore lattice.

	2 K	298 K
a (Å)	10.32915(3	10.34168(8)
Ox	0.32964(9)	0.32980(1)
Ru–O (Å)	2.01(5)	2.00(3)
Ln–O (Å) (6 ×)	2.53(7)	2.52(3)
Ln–O' (Å) (2 ×)	2.23(6)	2.22(5)
Ru–O–Ru (°)	128.9(7)	129.1(1)
χ^2	3.7	2.89
R_{wp}	5.78	5.46
R_p	4.37	4.98

Tab. 7.10: Atomic displacement parameters for $Y_2Ru_2O_6O'$ ($Å^2 \times 10^3$). Estimated standard deviations in parentheses.

T (K)	Atom	site	U_{11}	U_{22}=U_{33}	U_{12}=U_{13}	U_{23}
	Y	16*d*	2.65(1)	= U_{11}	0.40(2)	=U_{12}
	Ru	16*c*	1.63(2)	=U_{11}	-	=U_{12}
2	O	48*f*	5.07(1)	=U_{11}	0.0	0.20(4)
	O'	8*b*	2.13(4)	=U_{11}	-	-
	Y	16*d*	5.51(5)	=U_{11}	-0.24	=U_{12}
	Ru	16*c*	3.43(2)	=U_{11}	-	=U_{12}
298	O	48*f*	6.33(5)	=U_{11}	0.0	2.76(3)
	O'	8*b*	3.4(2)	=U_{11}	-	-

Tab. 7.11: Atomic displacement parameters for $Nd_2Ru_2O_6O'$ ($Å^2 \times 10^3$). Estimated standard deviations in parentheses.

T (K)	Atom	site	U_{11}	U_{22}=U_{33}	U_{12}=U_{13}	U_{23}
	Nd	16*d*	2.52(1)	= U_{11}	0.0	=U_{12}
	Ru	16*c*	1.41(2)	=U_{11}	-	=U_{12}
2	O	48*f*	4.7(9)	=U_{11}	0.0	1.46(4)
	O'	8*b*	2.2(7)	=U_{11}	-	-
	Nd	16*d*	6.98(8)	=U_{11}	0.0	=U_{12}
	Ru	16*c*	5.99(5)	=U_{11}	-	=U_{12}
298	O	48*f*	7.59(7)	=U_{11}	0.0	3.5(3)
	O'	8*b*	5.64(5)	=U_{11}	-	-

for the data collected on $Y_2Ir_2O_6O'$ at 2 K and the refinement converged to reasonable low R values (listed in Table 7.12).

The 2 K model was then applied to the RT data which was confirmed to be a rather good description of the structure of $Y_2Ir_2O_6O'$ and gave the expected trends for cell parameter, bond lengths and angles and thermal motion with *r* cation radius. These, together with the goodness of fit parameters reported in Table 7.12. It is noticeable that the differences in the final goodness of fit parameters obtained for these compounds reflected the quality of the data, rather than any inadequacies of the structural model , which resulted in sensible bond lengths and angles, confirming that the material adopts a regular pyrochlore structure.

7.2 Discussion

.

From the powder diffraction profiles analysed by the Rietveld method of the three different α pyrochlore families of interest, in which smaller trivalent rare earth cations were progressively substituted for ones of larger ionic radius size), the lattice constant, *a*, was found to increase linearly as the atomic radius of the trivalent *R* cation increased, in excellent agreement with literature records. At RT, all the structures investigated could be described in the $Fd\bar{3}m$ space group and adopted the regular pyrochlore structure with $a \sim 10\,Å$, as reported in Sn. 7.1.2. Each transition metal adopted a nearly regular octahedral coordination environment whereas the coordination around the *R* atom could be described as that of an axially compressed scalenohedron (along

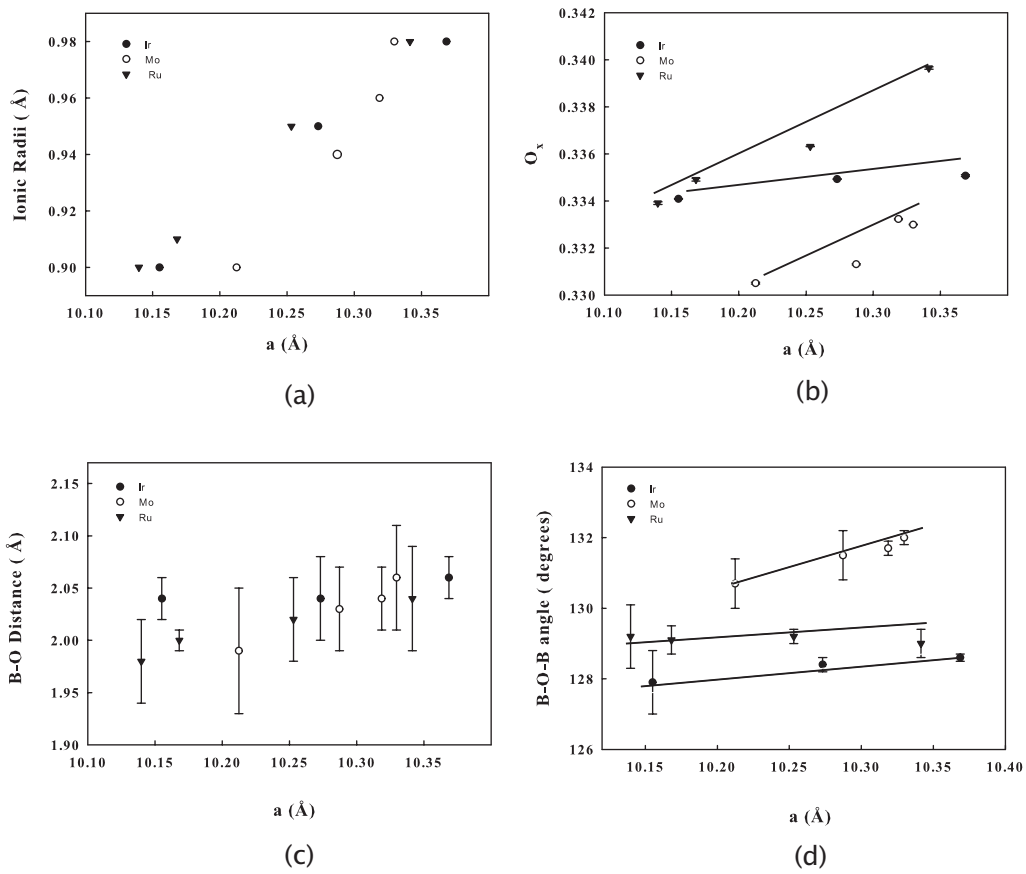

Fig. 7.3: (a) Variation of the cubic lattice parameter with ionic radii of the rare earth in the ruthenate, molybdate and iridate pyrochlore. (b) Variation of the oxygen positional parameter, x, with the cubic lattice parameter for the three series. (c) Variation of the B–O bond length as a function of a. Filled triangles identify the ruthenate family, filled circles the iridate pyrochlore and the open circles were used to identify the molybdate pyrochlores.

Tab. 7.12: Refined lattice parameters, atomic coordinates and ADPs, derived bond lengths and angle of interest for the models describing $Y_2Ir_2O_6O'$) and profile fits achieved at 2 and 298 K, $Fd\bar{3}m$. Estimated standard deviations in parentheses.

	2 K	298 K
a (Å)	10.15622(3)	10.30923(2)
x	0.33412(2)	0.33431(2)
B–O (Å)	2.04(3)	2.04(4)
6 × R–O (Å)	2.48(2)	2.49(1)
2 × R–O' (Å)	2.24(1)	2.24(3)
B–O–B (°)	128.0(1)	128.5(4)
χ^2	7.38	8.90
R_{wp}	6.49	7.71 %
R_p	5.55	6.37

a three-fold axis); In other words, each *R* atom can be described as a distorted eight fold coordination geometry, with six O atoms at longer and two additional at shorter distances Table 7.5, Table 7.6, Table 7.7.

The principal change in the structures was the increase of the *x* coordinate for O from the molybdate to the ruthenate compounds which also influences the degree of distortion around the oxygen-ion and the relative R^{3+}–O interaction as shown by changes in bond lengths. This value, O *x* which is also dependent on the refined *a* value, represents the only refinable atomic position. The refined positional coordinate O*x* trend systematically decreased with r_R, in excellent agreement with the size of the ionic radii of the element *R* present in the structure.

The accurate determination of the oxygen *x* coordinate become therefore of primary importance as its accurate position will give accurate *R*-O bond distances and important information about the properties of these compounds such as the *B*–O distance and the *B*–O–*B* angle are strongly influenced by the repulsion caused by the overlap between the filled shells of the *R* cation and the O^{2-} anions. The discussion in the chapter has been based mainly on experimental data obtained by PXD as the PXD data collections were as a complete series of compounds, allowing for more systematic analyses.

These pyrochlores, indeed, appeared to have structure and properties entirely de-

termined by the ionic radii of the chemical elements contained on their R cation. The extracted values for the O x parameter, obtained by X-ray diffraction, were reported in Table 7.5, Table 7.6, Table 7.7 and graphically plotted in Fig. 7.3(b). The plot does not show any unexpected trend and it suggests an approximately linear dependence between O x and the cell length a which is also reflected in the R–O and R–O' relationship. The values extracted compare well with those found in parent compounds but also with those of binary and ternary oxides containing the TM in the oxidation state +4.

As discussed in the introductory chapter the shorter R–O' bond length is only influenced by the value of a ($= a\sqrt{3/8}$) whereas both the R–O or B–O lengths depend on both the lattice parameter and O x. The B–O distance, showed in Fig. 7.3(c), keeps constant with the composition while the B–O–B angle between corner-shared octahedra is strictly influenced by the size of R^{3+} and becomes a very important parameter, which determines the degree of interaction between the near neighbours B spins and accounts for several effects on the electronic structure of these families earlier cited [142, 143]. The B–O–B angle ranges from $\sim$129° in $R_2Ru_2O_6O'$ to $\sim$131° in $R_2Mo_2O_6O'$ and $\sim$129° in $R_2Ir_2O_6O'$ and increases going down the period with increasing of the ionic radii of the elements and in good agreement with the bond length trend and bond angle trend of similar materials. These similarities to analogous compounds in the literature are further confirmation that the ordered models used for the PXD data to represent these α-phases, was correct and realistically described the atomic scattering density of the atoms in the cell. PND carried out only on a limited number of samples agreed closely with the PXD findings of Sn. 7.1.2, did not show any evidence of disorder or oxygen non-stoichiometry, and attributed the description of the structure in the ordered cubic pyrochlore and somehow addressed the high ADPs for R and O atoms to the degree of freedom that the structure allows. In fact, anisotropic refinement of the ADPs from TOF data for the $R_2Ru_2O_6O'$ showed rather high values for the R and the O atoms (as was found by isotropic refinement of PXD data) and highlighted an enhanced anisotropic displacement for both Y^{3+} and Nd^{3+} parallel to the [111] direction and very low vibration along the the $\bar{3}m$ axis. The O atom, on the other hand, displays an enhanced vibration in the [100] directions.

As clearly seen for all the powder diffraction data and for the different combinations of R, there was a general positive correlation between against r_R and the extracted

lattice parameter of the $R_2B_2O_6O$' pyrochlore described in Sn. 7.1.2 (see Fig. 7.3(a) where the lattice parameter a is plotted as a function of the ionic radius of the cations of the structure). In all the cases, the cubic lattice parameter showed a marked linear relationship with both the ionic radii from the rare earth on the R cation site,r_R, and from the ionic radius of the TM. Thus, the cell constant of $R_2Mo_2O_6O$' is larger than that found for R_2Ru_2 O_6O' consistent with the ionic radii size of the smaller Ru^{4+} (0.69 *Å vs* 0.62 *Å* [144]) and Nd_2Mo_2 O_6O' is larger than that found for the analogous neodymium ruthenate, $Nd_2Ru_2O_7$, in accord with the slightly larger ionic radius of Mo^{4+} 0.65 *Å* compared to Ir^{4+} 0.68 *Å* and Ru^{4+} 0.62 *Å*. This is consistent with the fact that the ionic radius of the Nd^{3+} is larger than that of the Y^{3+} ion.

7.3 Conclusions

The present structural study along with previous studies, has allowed a description of the structural trends of $R_2Ru_2O_6$, $R_2Ir_2O_6$ and $R_2Mo_2O_6$ pyroclores: All the phases could be described in terms of the ordered centrosymmetric $Fd\bar{3}m$ model throughout. The crystal chemistry appeared very similar for all the members of the three families and is strictly dependent on the ionic radius of the element on the R site. No obvious structural anomalies were identified with the use of different TMs on the B site, a possible consequence of the similarities in the band width of the B^{4+} metal cations which have four electrons in nearly degenerate t_{2g} orbitals. Thus the structures in all cases displayed R–O, B–O, bond distances and B–O–B angles increasing with increased ionic radius of the cation .

8. CONCLUSION AND FINAL REMARKS

A thorough understanding of the structural chemistry of many metal oxides is motivated by the desire of predicting their properties, essential for the design of new materials. Among these, the oxide pyrochlores offer a unique combination of highly symmetric structures and a wide range of properties closely related to the composition, electrical and crystallographic properties. The large body of experimental data investigated throughout this study shows satisfactory agreement and has enhanced the understanding of pyrochlores oxides in many respects:

1. low temperatures description of the structures of the β-pyrochlore KOs_2O_6 in terms of disordered localized *A*-type cations;

2. negative thermal expansion (NTE) reported for AOs_2O_6 (A = K and Rb) and correlated to thermodynamics through Grüneisen parameters (KOs_2O_6);

3. structural study of the evolution of KOs_2O_6 following water incorporation;

4. synthesis and characterisation of two new partial exchanged phases derived from KOs_2O_6, $K_{0.5}Li_{0.5}Os_2O_6$ and $K_{0.6}Na_{0.7}Os_2O_6$.

5. synthesis and characterisation a of a new exchanged $Ba(OsO_6)_2$ compound.

Conclusions in connection to features detailed above were drawn as follows:

- Many literature studies on the family of superconductors AOs_2O_6 suffered through consequences of experimental limitation detection. In this work, Rietveld powder-profile analysis on several powder neutron diffraction measurements offered a strong contribution that helped overcoming many of the sensitivity limitations experienced in PXD and allowed the structural investigation of local environments. The comparison of the cation arrangement as function of the ionic size, across the same *A*-cation group, permitted a quantitative assessment of the relative contributions from each structure to the superconductivity. On the basis of these, the superconducting state is strongly correlated with the *A* ionic radius

size that undergoes local displacement between 80 K and the proximity of the superconducting transition T_c. This view is further supported by pronounced anomalies in the variation in the lattice parameter through the superconducting temperature region. On cooling from 10 K to 3.6 K the material undergoes expansion which seems to be associated with further displacements of the *A*-type. This feature, firstly observed in this work, provides new insights into disentangling complexity in the yet poorly understood superconducting mechanism of osmate pyrochlores.

- The well known ability to exchange the *A*-type cation in pyrochlores has been thorough exploited through this study and led to the synthesis of metastable materials that were otherwise inaccessible. The replacement of a proportion of the *A* ions in AOs_2O_6 by alkali metal ions of smaller ionic radius has been largely restricted to the KOs_2O_6 compound. Ion exchange on KOs_2O_6 could be attempted because of its relative open channels formed by corner-sharing OsO_6 octahedra which form the pyrochlore three-dimensional network.

  The framework, therefore tends to behave as a host for the incorporation of small cations or molecules. If the ion-exchange is carried out in water or species are left in air, H_2O molecules enter the framework cavities depending on the room available. Although the ability of defect pyrochlores to absorb water is well documented in the literature, this feature and, most important, its influence on the physical properties of KOs_2O_6 was never considered before. Considerable systematic studies were devoted to establish the effect of water insertion and cation distribution on the structures and their relationship with properties of the osmate defect pyrochlore family. Findings showed that the substitution of different types of cations within a material, even when it maintains the same basic structure, have a strong impact on the superconducting properties of the bulk compound.

- The present structural study along with previous studies, has allowed a description of the structural trend of $R_2Ru_2O_6$, $R_2Ir_2O_6$ and $R_2Mo_2O_6$ pyroclores investigated: i) all the phases could be described in terms of the ordered centrosym-

metric $Fd\bar{3}m$ model. The crystal chemistry appeared very similar for all the members of the three families and is strictly dependent on the ionic radii of the element on the *R* site. No obvious structural anomalies were identified with the use of different TMs on the *B* site, possible consequence of the similarities in the electronic arrangement of the metal cation were investigated.

BIBLIOGRAPHY

[1] S. Yonezawa, Y.Muraoka, and Z.Hiroi, *J. Phys. Condens. Matter*, **16**, L9 (2004).

[2] S. Yonezawa, Y. Muraoka, Y. Matsushita, and Z. Hiroi, *J. Phys. Soc. Jpn.*, **73**, 819 (2004).

[3] S.Yonezawa, Y. Muraoka, and Z.Hiroi, *J. Phys. Soc. Jpn.*, **73**, 1655 (2004).

[4] J. Kuneš and W. E. Pickett, *Phys. Status Solidi (A)*, **203**, 2962 (2006).

[5] M. Subramanian, G. Aravamudan, and G. S. Rao, *Progr. Solid State Chem.*, **15**, 55 (1983).

[6] M. Yoshida, K. Arai, R. Kaido, M. Takigawa, S. Yonezawa, Y. Muraoka, and Z. Hiroi, *Phys. Rev. Lett.*, **19**, 197002 (2007).

[7] M. Subramanian, G. Aravamudan, and G. S. Rao, *J. Solid State Chem.*, **31**, 329 (1980).

[8] M. Straumanias and A. Draveniks, *J. Am. Chem. Soc.*, **71**, 683 (1949).

[9] G. E. Pike and C. H. Seager, *J. Appl. Phys.*, **48**, 5152 (1977).

[10] H. S. Horowitz, J. M. Longo, and H. H. Horowitz, *J. Electochem. Soc.*, **130**, 1851 (1983).

[11] F. Galasso and W. Derby, *Inorg. Chem.*, **1**, 71 (1965).

[12] J. Schooley, W. Hosler, and M. Cohen, *Phys. Rev. Lett.*, **12**, 474 (1964).

[13] V. Ginzburg, *J. Phys. USSR*, **10**, 107 (1946).

[14] D. Bernard, J. Pannetier, and J. Lucas, *Ferroelectrics*, **21**, 429 (1978).

[15] W. Cherry and R. Adler, *Phys. Rev.*, **72**, 981 (1948).

[16] R. G. Egdell, J. B. Goodenough, A. Hamnett, and C. Naish, *J. Chem. Soc. Faraday Trans. 1*, **79**, 893 (1983).

[17] N. Ali, M. Hill, and S. Labroo, *ibid*, **83**, 178 (1989).

[18] J. Greedan, M. Sato, N. Ali, and W. Datars, *J. Solid State Chem.*, **68**, 30 (1987).

[19] D. Bernard, S. L. Montagner, J. Pannetier, and J. Lucas, *Mater. Res. Bull.*, **6**, 75 (1971).

[20] R. Marchand, Y. Laurent, J. Guyader, P. L'Haridon, and P. Verdier, *J. of Eur. Cer. Soc.*, **8**, 197 (1991).

[21] F. Pors, R. Marchand, and Y. Laurent, *J. of Solid State Chem.*, **39**, 107 (1993).

[22] V. Dolgikh and E. Lavut, *Russ. J. Inorg. Chem.*, **36**, 1389 (1991).

[23] H. Gaertner, *Neues Jb. Mineralog. Geol. Palaontol., Beilage-Bd. Abt.*, **A 61**, 1 (1930).

[24] C. Cascales, J. Alonso, and I. Rasines, *J. Mater. Sci. Lett.*, **5**, 675 (1986).

[25] S. Ishida, F. Reng, and N. Takeuchi, *J. Am. Chem. Soc.*, **76**, 2644 (2005).

[26] K. Sickafus, L. Minervini, R. Grimes, J. Valdez, M. Ishimaru, F. Li, K. McClellan, and T. Hartmann, *Science*, **289**, 748 (2000).

[27] B. Saruhan, P. Francois, K. Fritscher, and U. Schulz, *Surf. Coat. Technol.*, **182**, 175 (2004).

[28] M. Subramanian, R. Subramanian, and A. Clearfield, *Solid State Ionics*, **15**, 15 (1985).

[29] I. Shaplygin and V. Lazarev, *Thermochim. Acta*, **33**, 225 (1979).

[30] A. P. Ramirez, *Annu. Rev. Mater. Sci.*, **24**, 453 (1994).

[31] R. Houtappel, *Physica*, **16**, 425 (1950).

[32] G. Wannier, *Phys. Rev.*, **79**, 357 (1950).

[33] Y. Taguchi, Y. Oohara, H. Yoshizawa, N. Nagaosa, and Y. Tokura, *Science*, **291**, 2573 (2001).

[34] S. Nakatsuji, Y. Machida, Y. Maeno, T. Tayama, T. Sakakibara, J. van Duijn, L. Balicas, J. N. Millican, R. T. Macaluso, and J. Y. Chan, *Phys. Rev. Lett.*, **96**, 087204 (2006).

[35] M. Hanawa, Y. Muraoka, T. Tayama, T. Sakakibara, J. Yamaura, and Z. Hiroi, *Phys. Rev. Lett.*, **87**, 187001 (2001).

[36] H. Sakai, K. Yoshimura, H. Ohno, H. Kato, S. Kambe, R. Walstedt, T. Matsuda, Y. Haga, and Y. Onuki, *J. Phys.: Condens. Matter*, **13**, L785 (2001).

[37] R. McCauley and F. Hummel, *J. Lumin.*, **6**, 105 (1973).

[38] J. Kuneš, T. Jeong, and W. Pickett., *Phys. Rev. B*, **70**, 174510 (2004).

[39] H. Nyman and S. Andersson, *J. Solid State Chem.*, **26**, 123 (1978).

[40] V. Isupov, *Kristallografiya*, **3**, 99 (1958).

[41] H. Hyman, S. Andersson, B. Hyde, and M. O'Keeffe, *J. Solid State Chem.*, **26**, 123 (1978).

[42] E. Stroganov, Y. Smirnov, V. Saltykova, and V. Markin, *Vestn. Leningr. Univ., Ser. 4: Fiz., Khim.*, **4**, 46 (1979).

[43] F. Jona, G. Shirane, and R. Pepinsky, *Phys. Rev.*, **98**, 903 (55).

[44] B. Darriet, M. Rat, J. Galy, and P. Hagenmuller, *Mater. Res. Bull.*, **6**, 1305 (71).

[45] H. Rietveld, *J. Appl. Crystallogr.*, **2**, 65 (1969).

[46] B. Chakoumakos, *J. Solid State Chem.*, **53**, 120 (1984).

[47] R. McCauley, *J. Appl. Phys.*, **51**, 290 (1980).

[48] E. Aleshin and R. Roy, *J. Am. Ceram. Soc.*, **45**, 18 (1962).

[49] J. Pannetier and J. Lucas, *Mater. Rrs. Rdl*, **5**, 797 (1970).

[50] A. W. Sleight, *Inorg. Chem.*, page 1704 (1968).

[51] Y. Shimakawa, Y. Kubo, and T. Manako, *Nature*, **53**, 379 (1996).

[52] J. Grins, M. Nygren, and T. Wallin, *Solid State Ionics*, **3/4**, 255 (1981).

[53] J. Grins, M. Nygren, and T. Wallin, *Mater. Res. Bull.*, **15**, 53 (1980).

[54] J. Pannetier, *J. Phys. Chem. Solids*, **34**, 583 (1973).

[55] J. Pannetier, *J. Phys. Chem. Solids*, **34**, 583 (1970).

[56] S. Yonezawa, Y. Muraoka, Y. Matsushita, and Z. Hiroi, *J. Phys. Soc. Jpn.*, **73**, 819 (2004).

[57] W. Baker, P. White, and O. Knop, *Canad. J. Chem.*, **54**, 2316 (1976).

[58] D. Babel, G. Pausewang, and W. Viebahn, *Z. Naturforsch., B: Anorg. Chem. Org. Chem.*, **22**, 1219 (1967).

[59] D. Babel, *Zeit. Anorg. Allg. Chem.*, **387**, 161 (1972).

[60] B. Wuensch, K. Eberman, C. Heremans, E. Ku, P. Onnerud, E. Yeo, S. Haile, J. Stalick, and J. Jorgensen, *Solid State Ionics*, **129**, 111 (2000).

[61] T. Hahn, Ed., *International tables for crystallography*, 4th ed. dordrecht: kluwer ed., 1996.

[62] J. Lian, L. Wang, J. Chen, K. Sun, R. Ewing, J. Farmer, and L. Boatner, *Acta Mater.*, **51**, 1493 (2003).

[63] R. Beyerlein, H. Horowitz, J. Longo, M. Leonowicz, J. Jorgensen, and F. Rotella., *J. Solid State Chem.*, **51**, 253 (1984).

[64] C. Michel, D. Groult, and B. Raveau, *J. Inorg. Nucl. Chem.*, **37**, 247 (1975).

[65] J. Pannetier, *Solid State Commun.*, **34**, 405 (1980).

[66] D. Groult, J. Pannetier, and B. Raveau, *J. Solid State Chem.*, **41**, 277 (1982).

[67] J. Alonso, C. Cascales, and I. Rasines, *Acta Crystallogr., Sect. C*, **45**, 3 (1989).

[68] H. Kobayashi, R. Kanno, Y. Kawamoto, T. Kamiyama, F. Izumi, and A. Sleight, *J. Solid State Chem.*, **114**, 15 (1955).

[69] Ismunandar, B. J. Kennedy, and B. Hunter, *J. Solid State Chem.*, **130**, 81 (1997).

[70] J. Yamaura and Z. Hiroi, *J. Phys. Soc. Jpn.*, **71**, 2598 (2002).

[71] G. Schuck, S. M. Kazakov, K. Rogacki, N. D. Zhigadlo, and J. Karpinski, *Phys. Rev. B*, **73**, 144506 (2006).

[72] K. Rogacki, G. Schuck, Z. Bukowski, N. D. Zhigadlo, and J.Karpinski, *Phys. Rev. B*, **77**(13), 134514 (2008).

[73] H. M. Rietveld, *Acta Cryst.*, **22**, 151 (1967).

[74] A. West, *Solid State chemistry and its Applications*, John Wiley Sons, 1984.

[75] G. Eisenman., *Biophys. J. Suppl.*, **2**, 259 (1962).

[76] F. Helfferich, *F. Ion Exchange*, McGraw-Hill: New York, 1962.

[77] W. Bragg, *Proc. Camb. Phil. Soc.*, **17**, 43 (1913).

[78] D. Mitchell and P. Powers, *Phys. Rev.*, **50**, 486 (1936).

[79] A. Cheetham and P.Day, *Solid State Chemistry: Techniques*, Oxford University Press, Clarendon Press, 1988.

[80] Bruker advantage x-ray solutions EVA, V10.1, 2004.

[81] International Centre for Diffraction Data, 12 Campus Boulevard, Newton Square, Pennsylvania 19073-3273, U.S.A.

[82] M. Buerger, *Contemporary Chrystallography*, McGraw-Hill, 1970.

[83] B. Willis and A. Pryor, *Thermal Vibrations in Crystallography*, Cambridge University Press (UK), 1975.

[84] A. C. Larson and R. B. V. Dreele, *Science*, **254**, 412 (1991).

[85] T. C. Hansen, P.F.Henry, H. Fischer, J. Torregrossa, and P. Convert, *Meas. Sci. Technol.*, **19**, 034001 (2008).

[86] T. Shimojima, Y. Shibata, K. Ishizaka, T. Kiss, A. Chainani, T. Yokoya, T. Togashi, X.-Y. Wang, C. T. Chen, S. Watanabe, J. Yamaura, S. Yonezawa, Y. Muraoka, Z. Hiroi, T. Saitoh, and S. Shin, *Phys. Rev. Lett.*, **99**, 117003 (2007).

[87] Y. Kasahara, Y. Shimono, T. Shibauchi, Y. Matsuda, S. Yonezawa, Y. Muraoka, and Z. Hiroi, *Phys. Rev. Lett.*, **96**(24), 247004 (2006).

[88] M. Bruhwiler, S. M. Kazakov, J. Karpinski, and B. Batlogg, *Phys. Rev. B*, **73**, 094518 (2006).

[89] Z. Hiroi, S. Yonezawa, J.-I. Yamaura, T. Muramatsu, and Y. Muraoka, *J. Phys. Soc. Jpn.*, **74**, 1682 (2005).

[90] Z. Hiroi, S. Yonezawa, and J. Yamaura, *J.Phys. Condens. Matter*, **19**, 145283 (2007).

[91] T. Muramatsu, S. Yonezawa, Y. Muraoka, and Z. Hiroi, *J. Phys. Soc. Jpn.*, **73**, 2912 (2004).

[92] Y. Shimono, T. Shibauchi, Y. Kasahara, T. Kato, K. Hashimoto, Y. Matsuda, J. Yamaura, Y. Nagao, and Z. Hiroi, *Phys. Rev. Lett.*, **98**, 257004 (2007).

[93] J.-I. Yamaura, S. Yonezawa, Y. Muraoka, and Z. Hiroi, *Journal of Solid State Chemistry*, **179**, 336 (2006).

[94] R. Galati, C. Simon, P. F. Henry, and M. T. Weller, *Phys. Rev. B*, **53**, 367 (2008).

[95] T. Hasegawa, Y. Takasu, N.Ogita, M.Udagawa, J.-I. Yamaura, Y. Nagao, and Z. Hiroi, *Phys. Rev. B*, **77**, 064303 (2008).

[96] H. Mutka, M. M. Koza, M. R. Johnson, Z. Hiroi, J.-I. Yamaura, and Y. Nagao, *Phys. Rev. B*, **78**(10), 104307 (2008).

[97] R. Galati, C. Simon, C. S. Knee, P. F. Henry, B. D. Rainford, and M. T. Weller, *Chem. Mat.*, **17**, 160 (2007).

[98] B. Toby, *J. Appl. Crystallogr.*, **34**, 210 (2001).

[99] G. Schuck, J. Karpinski, Z. Bukowski, and D. Chernyshov In *Jahrestagung der Deutsche Gesellschaft für Kristallographie*, 2006.

[100] E. Grunesein, Vol. 10 of *Handbuch der Physik*, Springer, Berlin, 1926.

[101] R. Galati, R. W. Hughes, C. S. Knee, P. F. Henry, and M. Weller, *J. Mater. Chem*, **17**, 160–163 (2007).

[102] J. Reading, S. Goordeev, and M. Weller, *J. Mater. Chem*, **12**, 646 – 650 (2002).

[103] F. S. Galasso, *Perovskites and High Tc Superconductors*, Gordon and Breach science Publishers, New York, 1990.

[104] Z. Hiroi, S. Yonezawa, Y. Nagao, and J. Yamaura, *Phys. Rev. B.*, **76**, 014523 (2007).

[105] I. Bonalde, R. Ribeiro, W. Bramer-Escamilla, J. Yamaura, Y. Nagao, and Z. Hiroi, *Phys. Rev. Lett.*, **98**, 227003 (2007).

[106] Y. Nagao, J. ichi Yamaura, H. Ogusu, Y. Okamoto, and Z. Hiroi, *J. Phys. Soc. Jpn.*, **78**, 064702 (2009).

[107] R. Saniz, J. Medvedeva, L. Ye, T. Shishidou, and A. J. Freeman, *Phys. Rev. B*, **70**, 100505 (2004).

[108] K. Hattori and H. Tsunetsugu, *J. Phys. Soc. Jpn.*, **78**(1), 013603 (2009).

[109] J. Chang, I. Eremin, and P. Thalmeier, *New J. Phys.*, **11**, 055068 (2009).

[110] S. Katrych, Q. Gu, Z. Bukowski, N. Zhigadlo, G. Krauss, and J. Karpinski, *J. Solid State Chem*, **182**, 428 (2009).

[111] M. Schmidt, P. G. Radaelli, M. J. Gutmann, S. J. L. Billinge, N. Hur, and S. W. Cheong, *J. Phys. Condens. Matter*, **16**, 7287 (2004).

[112] C. Simon *Synthesis, structure and characterisation of pyrochlore Materials* PhD thesis, Chemistry, Univeristy of Southampton, (2010).

[113] M. T. Weller, R. W. Hughes, J. Rooke, C. S. Knee, and J. Reading, *Dalton Trans.*, page 3032 (2008).

[114] C. Pedersen, *J. Am. Chem. Soc.*, **89**, 7017 (2002).

[115] C. J. Pedersen, *J. Am. Chem. Soc.*, **89**, 2495 (2002).

[116] P. Yen, R. Chen, C. Chen, Y. Huang, and K. K. Tiong, *J. Cryst. Growth*, **1-4**, 271 (2004).

[117] M. Subramanian, *Mater. Res. Bull.*, **25**, 107 (1990).

[118] R. Saniz and A. J. Freeman, *Phys. Rev. B*, **72**, 024522 (2005).

[119] D. W. Murphy, J. L. Dye, and S. M. Zahurak, *Inorg. Chem.*, **22**, 3679 (1983).

[120] P. Barnes, P. Woodward, L. Yongjae, T. Vogt, and J. Hriljac, *J. Am. Chem. Soc.*, **125**(15), 4572 (2003).

[121] G. J. Thorogood, B. J. Kennedy, and V. Luca, *Phys. Rev. B*, **385**, 91–93 (2006).

[122] A. A. Castro, I. Rasines, and X. Turrillas, *J. Solid State Chem.*, **80**, 227 (1989).

[123] K. Sasai, K. Hirota, Y. Nagao, S. Yonezawa, and Z. Hiroi, *J. Phy Soc. Jpn.*, **76**, 104603 (2007).

[124] D. Murphy, R. Cava, K. R. R. Roth, A. Santoro, S. Zahurak, and . J.L. Dyke 1986, 18-19, *Solid State Ionics*, **18-19**, 799 (1986).

[125] Y. Shi, A. Belik, M. Tachibana, M. Tanaka, Y. Katsuya, K. Kobayashi, K. Yamaura, and E. Takayama-Muromachi, *J. Phys.: Conf. Ser.*, **200**, 012185 (2010).

[126] E. Suleimanov, N. Chernorukov, and A. Golubev, *Russ. J. Inorg. Chem.*, **49**, 311 (2004).

[127] A. Kannan, A. Shukla, and S. Sathyanarayana, *J. Electroanal. Chem.*, **281**, 339 (1990).

[128] J. B. Goodenough, R. Manoharan, and M. Paranthaman, *J. Am. Chem. Soc.*, **112**, 2076 (1990).

[129] D. Yanagishima and Y. Maeno, *J. Phy Soc. Jpn.*, **70**, 2880 (2001).

[130] K. S. Lee, D. K. Seo, and M. H. Whangbo, *J. Solid State Chem*, **131**, 405 (1997).

[131] A. Manthiran and J. Gopalakrishnan, *Indian J. Chem.*, **19**, 1042 (1980).

[132] B. J. Kennedy, *Acta Cryst.*, **C51**, 790 (1995).

[133] B. Kennedy, *Physica B*, **241-243**, 303 (1998).

[134] V. Lazarev and I. Shaplygin, *Russ. J. lnorg. Chem.*, **23**, 163 (1978).

[135] J. Reimers, J. Greedan, and M. Sato, *J. Solid State Chem.*, **72**, 390 (1988).

[136] Y. Moritomo, S. Xu, A. Machida, T. Katsufuji, E. Nishibori, M. Takata, M. Sakata, and S.-W. Cheong, *Phys. Rev. B*, **63**, 144425 (2001).

[137] J. Greedan, M. Sato, X. Yan, and F. S. Razavi, *Solid State Commun.*, **59**, 895 (1986).

[138] M. Sato and J. E. Greedan, *J. Solid State Chem.*, **67**, 248 (1987).

[139] P. Hubert, *Bull. Soc. Chim. Fr.*, page 2385 (74).

[140] P. Hubert, *Bull. Soc. Chim. Fr.*, page 2463 (1975).

[141] M. Ito, Y. Yasui, M. Kanada, H. Harashima, S. Yoshii, K. Murata, M. Sato, H. Okumura, and K. Kakurai, *J. Phys. Soc. Jpn*, **69**, 888 (2000).

[142] J. Kanamori, *J. Phys. Chem. Solids*, **10**, 87 (1958).

[143] J. Goodenough, *Phys. Rev.*, **100**, 564 (1955).

[144] R. Shannon, *Acta Cryst. A*, **32**, 751 (1796).